Max-Planck-Institut für Polymerforschung

Max Planck Institute for Polymer Research

Assembling Nano-Objects with Polymers: From Hybrid Nanoarchitecture to Functional Materials

Dissertation

Zur Erlangung des Grades

´Doktor rerum naturalium (Dr. rer. nat.)

dem Fachbereich Chemie, Pharmazie und Geowissenschaften

der Johannes Gutenberg-Universität Mainz

Minghan Hu

Geboren in Nanning (China)

Mainz 2018

JOHANNES GUTENBERG UNIVERSITÄT MAINZ

JG|U

The thesis was carried out from December 2015 until December 2018 within the department of Prof. Dr. Katharina Landfester in the groups of Dr. Héloïse Thérien-Aubin and Dr. Markus B. Bannwarth at the Max-Planck-Institute for Polymer Research, Mainz.

Dekan: Prof. Dr. Dirk Schneider

Prodekan: Prof. Dr. Katja Heinze

Gutachter 1: Prof. Dr. Katharina Landfester

Gutachter 2: Prof. Dr. Michael Maskos

Date of oral examination: 29.01.2019

Declaration

I hereby declare that I wrote the dissertation submitted without any unauthorized external assistance and used only sources acknowledged in this work. All textual passages which are appropriate verbatim or paraphrased from published and unpublished texts, as well as all information obtained from oral sources, are duly indicated and listed in accordance with bibliographical rules. In carrying out this research, I complied with the rules of standard scientific practice as formulated in the statutes of Johannes Gutenberg-University Mainz to insure standard scientific practice.

……………………………

(Minghan Hu)

Contents

Abstract

In polymer-nanoparticles hybrids materials, functions can be imparted either through the clever design of new nano-building blocks or by gaining control over the manner those nano-building blocks organize. The main goal here was to develop new functional polymer-nanoparticles hybrid materials using both strategies. A new generation of functional materials was developed by expanding our library of functional nanoparticles and by the optimization of processing tools used to prepare hybrid materials by the assembly of nano-objects and polymers. In those new functional materials, function is conferred by the combination of chemical composition and structure.

In this thesis, two strategies have been used to fabricate assembled materials with new functions: 1) fabrication of new functional nano-building-blocks (nano-objects) and 2) processing of nano-building-blocks into hierarchical structured polymer/nanoparticle hybrid materials. To fulfill this goal, hybrid nanocapsules with damage self-reporting function (**Chapter 3.1**) and superparamagnetism (**Chapter 3.5**), disentangled single-chain polymer (**Chapter 3.2**), and inorganic nanoparticles with catalase-like activity and haloperoxidase-like activity (**Chapter 3.3 and Chapter 3.4, respectively**) have been synthesized and fabricated. Using processing methods allowing for the formation of complex hierarchical structures, such as Pickering emulsion followed by solvent evaporation (**Chapter 3.1**), electrospinning (**Chapter 3.2, 3.3, and 3.4**) or evaporation driven-assembly (**Chapter 3.5**) new functional materials based on the different nano-buildings blocks were prepared. The resulting nanoparticles/polymer hybrid materials, where functional nano-objects were dispersed in polymer matrices, were used to produce materials with "self-reporting", wound healing and anti-biofouling functions. Moreover, a new assembly method, which combined evaporation assembly and magnetic assembly, has been developed to generate

3D anisotropic microstructures with superparamagnetic function. These new assemblies were able to be remotely controlled by a magnetic field and could find potential applications in micro-robotics (**Chapter 3.5**).

With this work, it was clearly demonstrated how the combination of nanoparticle synthesis and processing methods can be used to prepare new functional materials with unique properties.

Zusammenfassung

In Polymernanopartikel basierten Hybridmaterialien, können Funktionen entweder durch ein cleveres Design neuer Nanobausteine oder durch die Kontrolle der Organisation solcher Nanobausteine eingeführt werden. Das Hauptziel hier war die Entwicklung neuer funktioneller Polymernanopartikel basierter Hybridmaterialien unter Verwendung dieser beiden Strategien. Eine neue Generation funktioneller Materialien wurde durch die Erweiterungen unserer Bandbreite funktioneller Nanopartikel und durch die Optimierung der Verarbeitungsmethoden zur Herstellung von Hybridmaterialien durch Anordnung von Nano-Objekten und Polymeren entwickelt. Diese neuen funktionellen Materialien erhalten ihre Funktion durch Kombination der chemischen Zusammensetzung und der Struktur.

In dieser Doktorarbeit wurden zwei Strategien verwendet, um angeordnete Materialien mit neuen Funktionen herzustellen: 1) Herstellung neuer funktioneller Nano-Bausteine (Nano-Objekten) und 2) Verarbeitung von Nano-Bausteinen zu hierarchisch strukturierten Polymernanopartikel basierten Hybridmaterialien. Um dieses Ziel zu erreichen, wurden Hybridnanokapseln, die selbstständig eine Beschädigung anzeigen (**Kapitel 3.1**) oder mit Superparamagnetismus (**Kapitel 3.5**), nicht-verschlaufte Polymereinzelketten (**Kapitel 3.2**) und anorganische Nanopartikel mit catalaseähnlicher sowie haloperoxidaseähnlicher Aktivität (**Kapitel 3.3 und 3.4**) synthetisiert und verarbeitet. Durch die Verwendung von Verarbeitungsprozessen wie Pickeringemulsiierung (**Kapitel 3.1**), Elektrospinnen (**Kapitel 3.2, 3.3 und 3.4**) oder verdampfungsgetriebene Anordnung (**Kapitel 3.5**) wurden neue funktionelle Materialien basierend auf unterschiedlichen Nanobausteinen hergestellt. Die resultierenden Nanopartikel/Polymer-Hybridmaterialien, bei denen Nano-Objekte in einer Polymermatrix

dispergiert sind, wurden zur Herstellung von Materialien mit "Selbstanzeige", Wundheilung und Anti-Biofouling verwendet. Darüber hinaus wurde eine neue Methode zur Anordnung entwickelt, bei der verdampfungsgetrieben Anordnung und magnetische Anordnung kombiniert werden, um dreidimensionale anisotrope Mikrostrukturen mit superparamagnetischer Funktion herzustellen. Diese neuen Anordnungen konnten durch ein magnetisches Feld ferngesteuert werden und könnten Anwendung in der Mikrorobotik finden (**Kapitel 3.5**).

Mit dieser Arbeit wurde klar gezeigt, wie die Kombination aus Nanopartikelsynthese und Verarbeitungsmethoden verwendet werden kann, um neue funktionelle Materialien mit einzigartigen Eigenschaften herzustellen.

1. Introduction

In the science fiction film "Fantastic Voyage", scientists developed a technology that can shrink a submarine to the size of a blood cell. This tiny submarine ventured through the human body to perform delicate surgery and repair the body damages. Nowadays, scientists use nanotechnology to bring this type of fictional stories into reality. Using nanotechnology, the size of the "submarine" is down to the nanometer range. These nano-objects can not only improve human health, but also impact many aspects of scientific and technological developments. For example, silver nanoparticles in fabric that can efficiently kill bacteria are widely used in wound dressing materials and odor-resistant clothing.[1] Nanoparticles have been used in solar cells to improve the efficiency of the energy harvesting.[2] Recently, scientists have developed wearable electronics with nanoparticles. Such electronic skin can be used for robots and prosthetic limbs, offering sensitivity to pressure, humidity, and temperature.[3]

Interestingly, instead of using single nanoparticle with a single function, assemblies of nanoparticles allow performing multiple tasks simultaneously or in sequence. Often, those assemblies display collective properties, new functions specific to complex assembled materials, that can be used in new functional devices. For example, multifunctional hybrid assemblies of magnetic and metal nanoparticles have been used for the separation of proteins[4,5] and the recovery of catalysts.[6] Moreover, assemblies of nanoparticles could show intriguing properties that are different from those of individual nanoparticles and corresponding bulk materials. Specific assembly of nanoparticles enables to couple and translate individual properties of nanoparticles to the desired macroscopic properties of new materials. For example, assembling of gold nanorods allows producing a plasmonic substrate with an excellent sensitivity that does not exist in single

nanorods,[7] which can be harnessed to design more sensitive diagnostic tools based on surface-enhanced Raman scattering.[8]

Therefore, it is essential to control the arrangement of nano-objects in order to allow the materials having desired properties and functions. Numerous approaches have been developed and used to produce assembled materials with various functions. The strategies of assembly nano-objects include template-assisted assembly, external field assisted assembly, and evaporation guided assembly.[9-11] Those different strategies lead to the different organization and alignment of nano-objects, resulting in bringing different functions to the assembled materials. In order to fabricate a material with on-demand functions, various nano-objects with desired functions have first to be synthesized and then precisely assembled into a programmable architecture. In this manner, the assembled materials can be used in a variety of applications such as coatings, sensing, and biomedical field.

Compared with the scientists in "Fantastic Voyage", we have not yet been able to shrink a macroscopic submarine to such a tiny size. Alternatively, scientists have developed various approaches for building "mini-submarine" with different architectures and functions. The nano-objects, which can be used as nano-building-blocks, have been desirably created and then been assembled into various structures on demanded. With the existing assembled structures of nano-objects, several functional materials have been fabricated. To further expand the library of functional materials prepared from the assembly of nano-objects and polymer, novel nano-objects need to be developed, processing methods need to be optimized and existing approaches can also be combined to generate a new generation of functional materials where function is imparted by the combination of chemical composition and structure.

2. State of the art

2.1 Synthesis of nanoparticles

The structure and properties of the nanoparticles, used as the building blocks for assembly, affect the property of assembled materials. Controlling the chemical composition of nanoparticles is the most straightforward manner to tune the property of nanoparticles. Different synthetic approaches lead to the formation of nanoparticles with different compositions. The three types of nanoparticles as specifically important in the framework of this thesis: polymer nanoparticles, inorganic nanoparticles, and hybrid polymer/inorganic nanoparticles.

2.1.1 Synthesis of polymer nanoparticles

Polymer nanoparticles can be produced either by preformed polymers or by the direct polymerization of monomers.[12-14] There are many methods to generate nanoparticles in the nanometer- and micrometer-size including miniemulsion, emulsion, microfluidic, and electrospraying. Among those, miniemulsion is the most versatile and general way to produce precursor nanodroplets in large scale with a variety of materials. These droplets act as the reactor for the polymerization and the confinement place for the formation of the polymer nanoparticles.

In general, the miniemulsion droplets are nanometer-size and stable in the continuous phase. To generate such droplets, two immiscible liquid phases are sheared with ultra-sonicators or homogenizers.[15] The nanodroplets are stabilized against coalescence and Ostwald ripening by the presence of surfactants and co-stabilizers.[16, 17] The surfactants are amphiphilic molecules that generate steric and/or electrostatic repulsion force at the droplets interfaces, resulting in preventing the coalescence of droplets. The co-stabilizer is a molecule with a low solubility in the continuous phase; the solubility of the co-stabilizer in the continuous phase also need to a much lower

solubility of the other molecules present in the dispersed phase. Therefore, the presence of a co-stabilizer builds up an osmotic pressure in the droplets to counteract the Laplace pressure that would otherwise result in the diffusion of the molecules forming the dispersed phase from smaller droplets to larger droplets.[15] The nanodroplets in miniemulsion can act as nanoreactors so that the reactions can take place in the droplet or at the droplet interface. **Figure 2.1** schematically illustrates the two general approaches of producing polymer nanoparticles by miniemulsion.
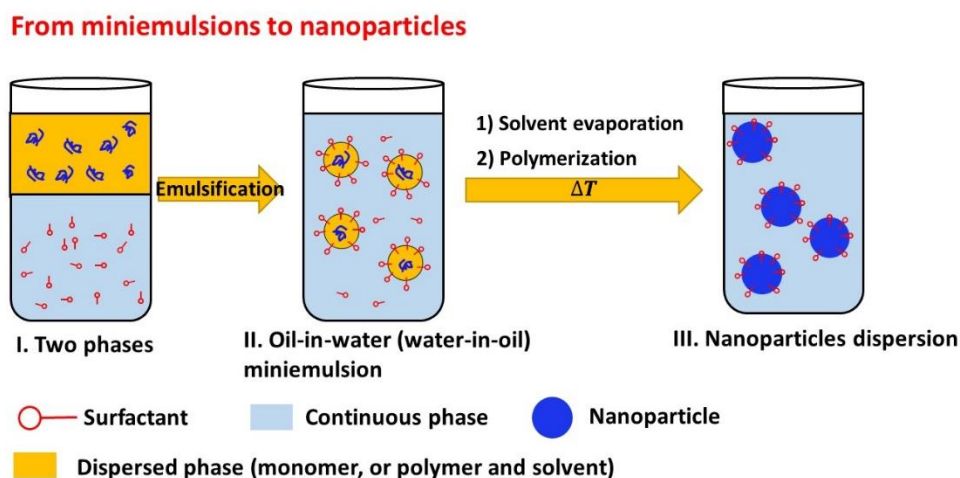
Figure 2.1 Production of polymer nanoparticles by miniemulsion process.

On one hand, polymer nanoparticles can be directly synthesized by the polymerization of monomers in the miniemulsion droplets.[18-20] Different types of polymerizations in miniemulsions droplets have been used to produce suspensions of homogeneous nanoparticles. Radical polymerization in dispersed phase has been used to successfully synthesized polystyrene, (**Figure 2.2a**),[21] polyacrylamide (**Figure 2.2b**),[22] polymethacrylates (**Figure 2.2c**),[23] and many other polymers nanoparticles.[24-26] Moreover, miniemulsion polymerization is not limited to radical polymerization, other types of polymerizations such as anionic polymerization and polyaddition can be performed in miniemulsion droplets. For example, polyamide-6 nanoparticles (**Figure 2.2d**) have been successfully obtained by anionic polymerization of ε-caprolactam in

4

heterophase using the miniemulsion process [27] Polyepoxide[28] and polyurethane (**Figure 2.2e**),[29, 30] nanoparticles have been produced by polyaddition polymerization in miniemulsion process. Additionally, protein nanoparticles (**Figure 2.2f**) were synthesized by a polyaddition reaction at the interface of nanodroplets in water-in-oil miniemulsions: the isocyanate groups of the cross-linker react with the hydroxyls and amines groups from proteins (hydroxyls and amines), resulting in the formation of water-insoluble nanocontainers with cross-linked polypeptide shells.[31-33]
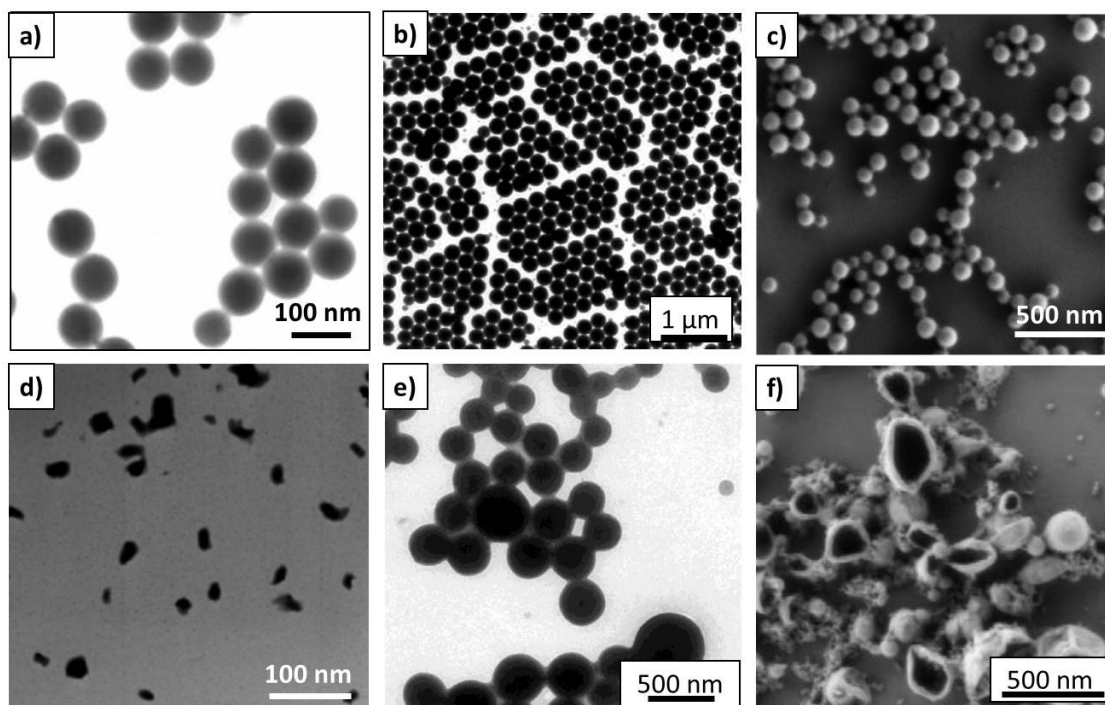
Figure 2.2 Electronic microscopic images of polymer nanoparticles: (a) polystyrene (adapted from ref. 21 with copyright 2005 John Wiley and Sons); (b) polyacrylamide (adapted from ref. 22 with copyright 2010 American Chemical Society); and (c) polymethacrylates nanoparticles produced by radical polymerization (adapted from ref. 23 with copyright 2010 John Wiley and Sons); (d) polyamide-6 nanoparticles produced by anionic polymerization (adapted from ref. 27 with copyright 2005 American Chemical Society); (e) polyurethane (adapted from ref. 29 with copyright 2001 John Wiley and Sons); and (f) protein nanocapsules produced by interfacial polyaddition polymerization (adapted from ref. 31 with copyright 2015 American Chemical Society).

On the other hand, evaporation of volatilized solvents in miniemulsion droplets is a generalized method for the preparation of polymer nanoparticles from preformed polymers.[34, 35] In this process, the polymers are dissolved in a solvent and the polymer solution is emulsified with another immiscible liquid in presence of a surfactant to form miniemulsion droplets. Afterward, the solvent is evaporated by heating the miniemulsion. Thus, the polymer inside the droplets can be solidified and nanoparticles are then obtained. In this manner, various types of polymers were successfully used to produce nanoparticles. For example, polylactide, poly(ε-caprolactone), and poly(lactide-co-glycolide) were used to produce biocompatible and biodegradable nanoparticles for biomedical applications.[36-38] In addition, it is possible to mix more than one type of polymer into miniemulsion droplets. During the process of solvent evaporation, the phase separation leads to the formation of Janus nanoparticles (**Figure 2.3**).[39, 40]
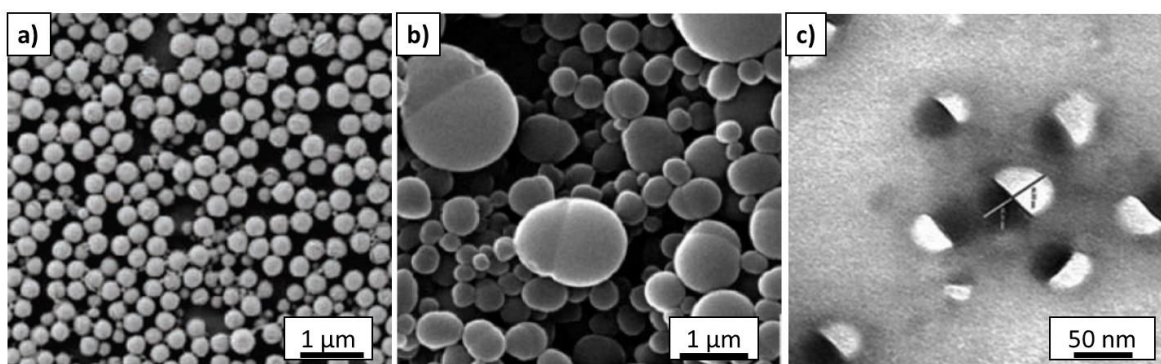

Figure 2.3 Electronic microscopic images of (a) polylactide nanoparticles (adapted from ref. 38 with copyright 2012 John Wiley and Sons); (b) polystyrene/poly(methyl methacrylate) Janus nanoparticles (adapted from ref. 39 with copyright 2008 American Chemical Society); and (c) polystyrene (dark)/polypropylene carbonate (white) Janus nanoparticles prepared by solvent evaporation (adapted from ref. 40 with copyright 2009 John Wiley and Sons).

Although miniemulsion-based techniques are almost a universal method to produce polymer nanoparticles, the polymer nanoparticles prepared from miniemulsion technique always need a

surfactant to stabilize the preformed droplets and fabricated nanoparticles. The surfactants are not always desirable in the final application of the nanoparticles and are maybe even harmful to the potential applications in some cases such as food industry and biomedicine. Therefore, additional purification steps are required to remove the surfactants in the nanoparticles suspensions. Alternatively, there are other surfactant-free methods such as surfactant-free emulsion polymerization[41] and electrospraying.[42-44] Electrospraying is a process where an electric field is used to produce and dry droplets of a polymer solution. In this process, a polymer solution is pumped out of a capillary nozzle and then an electric field is applied between the nozzle and a target. The difference of potential is used to accelerate the solution of polymer and leads to the elongation of the solution coming out of the nozzle and the formation of a jet.[45] The jet can further deform and split into unstable micro- or nano-droplets due to the high electrical forces. Once the droplets have detached from the main jet, the solvent in the droplets of polymer solution evaporates and then generate dense and solid particles at micro- or nanometer size are propelled towards the collector.[46] In electrospraying, the droplet sizes can be tailored by voltage and flow rate.[47] Furthermore, the morphology of nanoparticles can be tailored during the electrospraying process. For example, by controlling the molecular weight, concentration, and flow rate of polymer solution, spherical and ellipsoidal polymer particles have been produced[48] (**Figure 2.4**). The hollow microsphere with a single hole in its shell has been produced by coaxial electrospraying. Polymethylsilsesquioxane was used as a model shell material encapsulating a core of a volatile liquid, perfluorohexane, which was subsequently evaporated to produce the hollow spheres.[49]
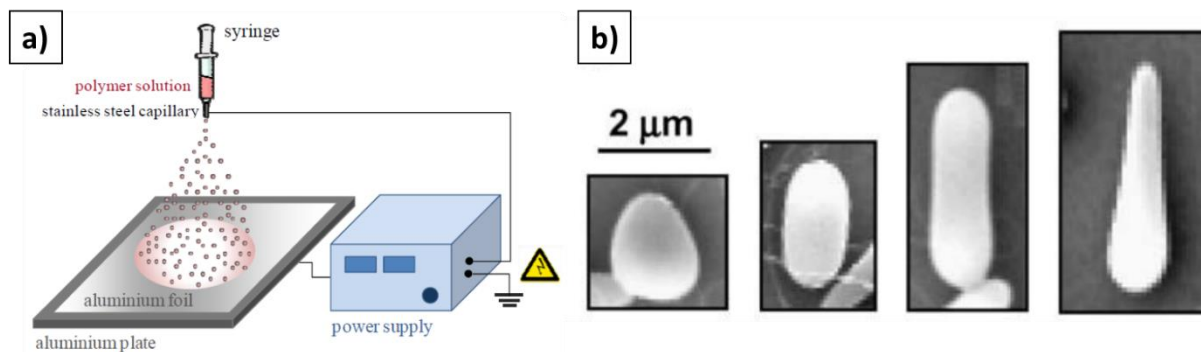
Figure 2.4 (a) Schematic picture of electrospraying process[46] (adapted from ref. 46 with open access article distributed under the Creative Commons Attribution License (CC BY 3.0)); (b) different morphologies of electrosprayed poly(lactic-co-glycolic acid) particles[48] (adapted from ref. 48 with copyright 2010 Elsevier).

2.1.2 Synthesis of inorganic nanoparticles

There are many synthetic strategies for producing inorganic nanoparticles with various composition, shape, and size. These methods are summarized and reviewed in the literature.[50, 51] In this thesis, the synthetic methods will be focused on those relevant to the formation of silica nanoparticles, cerium nanoparticles, and magnetic nanoparticles used in this study.

Silica nanoparticles are widely used in biomedical applications because of their biocompatibility.[51, 52] The most commonly used route for the synthesis of silica nanoparticles is the sol-gel method due to its ability to produce monodispersed with narrow-size distribution nanoparticles at mild conditions. Generally, the process involves hydrolysis and condensation of metal alkoxides ($Si(OR)_4$) such as tetraethylorthosilicate (TEOS, $Si(OC_2H_5)_4$)[53] or inorganic salts such as sodium silicate (Na_2SiO_3)[54] in the presence of acid (e.g. HCl) or base (e.g. NH_3) as catalyst. This method was first reported by Stöber.[55] This reaction in the sol-gel process is described as:

Sol process: hydrolysis of alkoxysilane

$$Si(OR)_4 + x(H_2O) \rightleftharpoons Si(OR)_{4-x}(OH)_x + x(ROH)$$
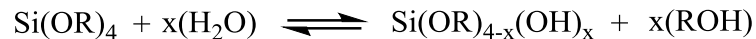
Gel process: condensation of hydroxysilanes

$$(RO)_3\text{-}Si\text{-}OH + HO\text{-}Si\text{-}(OR)_3 \rightleftharpoons (RO)_3\text{-}Si\text{-}O\text{-}Si\text{-}(OR)_3 + H_2O$$

Moreover, the silica nanoparticles can be mesoporous by the templating of the sol-gel method.[56] Generally, mesoporous silica nanoparticles are prepared in presence of the surfactant cetyltrimethylammonium bromide (CTAB) used as a liquid crystal templating agent, tetraethyl orthosilicate (TEOS) or sodium metasilicate (Na_2SiO_3) as the silica precursor, and an alkali as the catalyst. In this synthesis, when the concentration of surfactant is higher than the critical micelle concentration (CMC), micelles are formed. The silica precursors would then condensate at the surface of surfactant micelles and form silica wall around the surface of the micelles. After the removal of the surfactant, mesoporous silica nanoparticles are obtained with a specific surface area as high as 700 m^2/g, and with a pore size-tunable in the range of 1.6-10 nm (**Figure 1.5**).[52, 57]
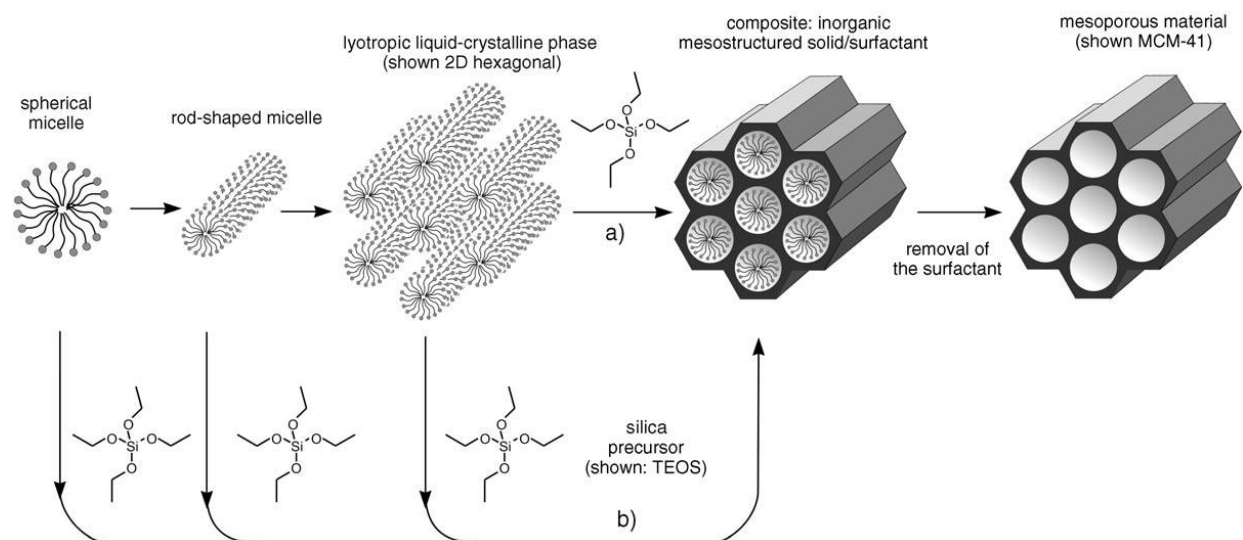

Figure 2.5 Formation of mesoporous silica materials by templating agents (Reproduced from ref. 52 with permission. Copyright 2012 John Wiley and Sons).

Recently, cerium oxides have been widely used in biomedical applications for reducing the oxidative stress generated by reactive oxygen species (ROS) in cells and tissues.[58, 59] Thanks to the Ce^{3+}/Ce^{4+} redox couple on the nanoparticle surface, it provides a biological activity that is similar to the activity of natural metallo-enzymes that use transition metal ions, e.g. Fe^{3+} and Cu^{2+}, to mediate the concentration of ROS. Therefore, the demand for cerium oxide nanoparticles is rapidly increasing.

Cerium oxide nanoparticles have been synthesized by the thermal decomposition of cerium precursor (e.g. cerium nitrate) in organic solvents[60] or in microemulsions[61]. The composition, surfactant, and the cerium source precursor are of importance in the final product morphology. By varying the NaOH concentration, reaction time, and precursor concentrations, CeO_2 nanoparticles with spherical, rod-like, cube-like, and spindle-like shapes have been obtained (**Figure 2.6**).[62, 63]
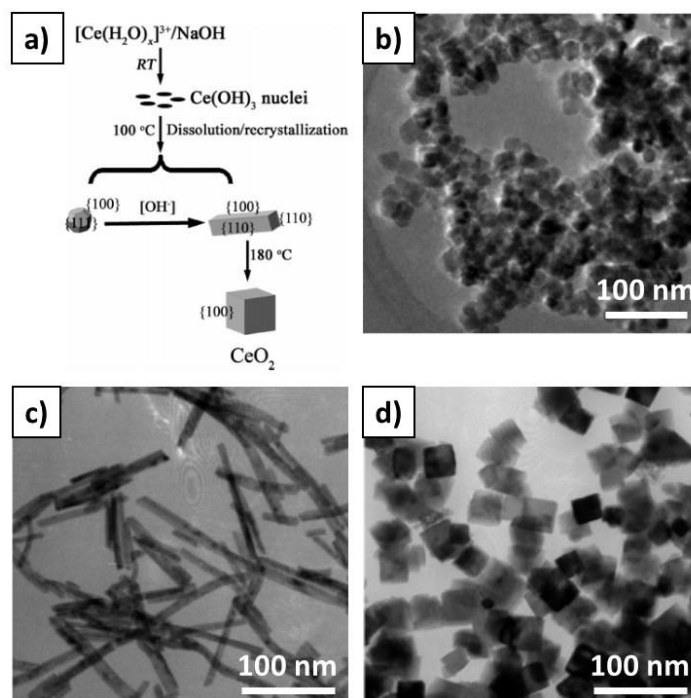

Figure 2.6 (a) Synthetic scheme of CeO_2 nanoparticles with different shapes. TEM images of CeO_2 (b) nanopolyhedras, (c) nanorods, and (d) nanocubes[63] (reproduced from ref. 63 with permission. Copyright 2007 American Chemical Society).

Magnetic nanoparticles are of great interest in a wide range of applications such as micro-actuators,[64, 65] magnetic separation,[66, 67] and drug delivery.[68, 69] These magnetic nanoparticles include metal oxides (Fe_3O_4 and γ-Fe_2O_3),[70, 71] spinel-type ferromagnets ($MnFe_2O_4$ and $CoFe_2O_4$),[72] pure metals (Fe and Co),[73, 74] and alloys ($CoPt_3$ and FePt).[75, 76] Both co-precipitation [77] and thermal decomposition[78] are techniques commonly used to synthesize high-quality magnetic nanoparticles in large amount. Co-precipitation is a facile and convenient way to synthesize Fe_3O_4 and γ-Fe_2O_3 from aqueous Fe^{2+}/Fe^{3+} salt solutions by the addition of a base at room temperature or at elevated temperature. The size, shape, and composition of the magnetic nanoparticles very much depend on the type of salts used (e.g. chlorides, sulfates, nitrates), the Fe^{2+}/Fe^{3+} salt ratio, the reaction temperature, the pH value and ionic strength of the media. With this synthesis, once the synthetic conditions are fixed, the quality of the magnetite nanoparticles is fully reproducible. Additionally, monodisperse magnetic nanocrystals with smaller size can be synthesized through the thermal decomposition of organometallic compounds in high-boiling organic solvents containing stabilizing surfactants. Besides these two methods, the other methods, such as microemulsion [79] and hydrothermal synthesis,[80] are also utilized to produce magnetic nanoparticles (**Table 2.1**).[81]

Table 2.1 Comparison of synthetic methods for magnetic nanoparticles. (Reproduced from ref. 81 with permission. Copyright 2007 John Wiley and Sons)

Synthetic method	Reaction temperature	Reaction time	Solvent	Size distribution	Shape controlling	Yield
Co-precipitation	20 – 90 °C	Minutes	Water	Relatively narrow	Not good	High
Thermal decomposition	100 – 320 °C	Hours - days	Organic solvent	Very narrow	Very good	High
Microemulsion	20 – 50 °C	Hours	Organic solvent	Relatively narrow	Good	Low
Hydrothermal synthesis	220 °C	Hours - days	Water-ethanol	Very narrow	Very good	Medium

2.1.3 Synthesis of inorganic/polymer hybrid nanoparticles

Inorganic/polymer hybrid nanoparticles have numerous applications including coatings, optical materials, and biomedical applications. Such hybrid nanoparticles provide very good processability and tunable mechanical properties because of the polymer components. Additionally, the inorganic part offers specific functionalities, e.g. magnetic responsive and catalytic activity, to the hybrid materials. Therefore, the hybrid nanoparticles have a unique synergetic effect coming from the different components. Depending on the synthetic strategy used, the hybrid material can be formed either be inorganic clusters encapsulated in a polymer matrix, inorganic particles forming a shell at the surface of polymer nanoparticles, or polymer chains grafted on an inorganic nanoparticle (**Figure 2.7**).
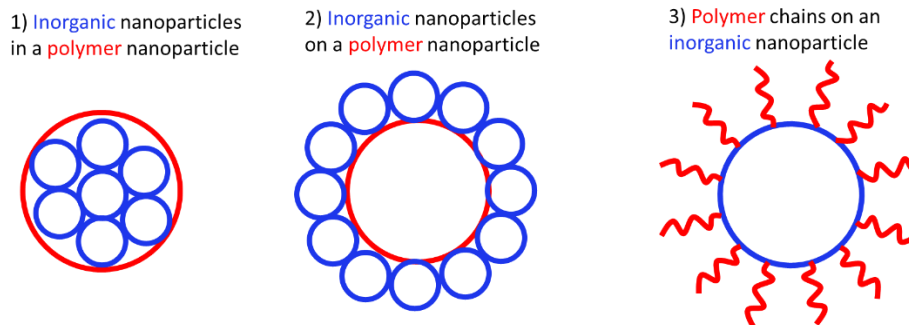
Figure 2.7 Different types of inorganic/polymer hybrid nanoparticles.

Miniemulsion can not be only used to prepare polymer particles but also hybrid particles. The inorganic nanocomponents are first mixed into the miniemulsion droplets, together with monomers or preformed polymers. After polymerization or solvent evaporation, the inorganic part is encapsulated inside the polymer nanoparticles.[37, 82] For example, biodegradable polylactide nanoparticles loaded with iron oxide particles were prepared by the combination of miniemulsion and emulsion/solvent evaporation techniques (**Figure 2.8a**).[37] This method shows the versatility possible when combining different polymer and inorganic nanoparticles. However, for some application purpose, e.g. catalytic application, the catalytic nanoparticles need to expose and stay on the outside of the hybrid nanoparticle to enable direct contact between the inorganic particles and the media and/or substrates.

There are two ways to position inorganic nanoparticles on the surface: either the *in situ* synthesis of inorganic nanoparticles on the surface of polymer nanoparticles or coating preformed inorganic nanoparticles on the surface of polymer nanoparticles. For example, the combination of *in situ* crystallization and miniemulsion process has been used to fabricate hybrid ceria/polymer nanoparticles. In this case, polystyrene and poly(methyl methacrylate) were prepared by miniemulsion copolymerization in the presence of different functional comonomers that provide carboxylic or phosphate groups. The functional groups of the comonomers generate a corona

around the polymer nanoparticles and serve as nucleating agents for the *in situ* crystallization of cerium oxide.[83] This technique has also been used to prepare an array of hybrid nanoparticles such as cadmium sulfide/polymer [84] and zirconium oxocluster/polymer [85, 86] hybrid nanoparticles. Some inorganic nanoparticles, such as silica [87] and titanium oxide [88] nanoparticle, can act as stabilizers to stabilize the emulsion droplets instead of, or in combination with, traditional surfactants. Such emulsions are called "Pickering emulsion".[89] By using Pickering emulsification, hybrid nanoparticles can be produced by using inorganic nanoparticles to stabilize droplets of monomers or polymers. For example, the raspberry-like nanoparticles were prepared by the combination of Pickering emulsion and solvent evaporation techniques (**Figure 2.8b**).[87] Pickering emulsification produces hybrid nanoparticles where the "surfactant", which is the inorganic nanoparticles, becomes one component of hybrid materials and is able to have functions such as magnetic responsive and catalytic activity.

Finally, hybrid nanoparticles can be prepared by the functionalization of the surface of inorganic nanoparticles with polymer chains. The preformed polymer chains can be grafted to the surface or a polymer chain can be grown *in situ* on the surface of inorganic nanoparticles.[90] In such hybrid nanoparticles, the polymer chains can control the interaction of inorganic nanoparticles, which is useful to tailor the behavior of the nanoparticles.[91, 92] For example, gold and palladium nanorods have been functionalized with polystyrene chains, allowing co-assembly linear chains with plasmonic properties.[93] Additionally, the polymer chains can act as surfactants to stabilize nanoparticles in aqueous solution and prevent aggregation. It is crucial for biomedical application. For example, biocompatible polymers such as polyethylene glycol and dextran have been used to control the reaction kinetics of cerium oxide nanoparticles. After the synthesis, the residual

polymer chains stay on the particles surfaces that can extend the circulation time in blood (**Figure 2.8c**).[94-97]
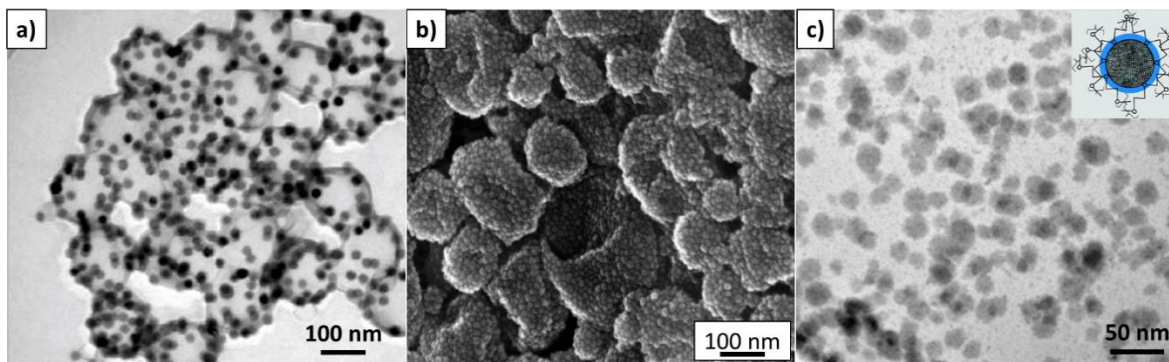

Figure 2.8 (a) TEM images of hybrid iron oxide/polylactide nanoparticles prepared by the combination of miniemulsion and solvent evaporation technique (adapted from ref. 37 with copyright 2009 John Wiley and Sons); (b) SEM images of hybrid silica/ poly(styrene-co-4-vinyl pyridine) nanoparticles prepared by the combination of Pickering emulsion and solvent evaporation technique (adapted from ref. 87 with copyright 2011 American Chemical Society); (c) TEM images of cerium oxide nanoparticles with poly(ethylene glycol) layer. The inset picture is the illustrated scheme of nanoparticles compositions (adapted from ref. 95 with copyright 2009 American Chemical Society).

2.2 Guided-assembly of nanoparticles

Organizing nanoparticles in specific architectures allow them to either harness their collective properties or provide a new way to formulating functional materials and allows novel possibilities to design functional devices. Moreover, by spatially controlling the orientation and spacing of nanoparticles in composites materials, the nanoparticle-based materials can perform multiple tasks simultaneously or in sequence. "Bottom-up" approaches are especially attractive to prepare composite materials. In these approaches, nano-building-blocks self-organized into the desired arrangement by their interactions or by the presence of external stimuli. Electrospinning, evaporation assembly and magnetic assembly are a few of those reliable and scalable techniques used to prepare nanocomposite materials.

2.2.1 Electrospinning

Electrospinning shows great potentials in assembling functional nanoparticles for the production of flexible 2D materials with a large surface-area, which are useful for water purification, wearable electronics, and medical applications. It is notable that during the electrospinning of anisotropic nanoparticles such as nanorods and nanowires, the nanoparticles can be aligned within the fibers to a certain extent to reduce Gibbs free energy.[98, 99] Thus, the electrospinning technique is not only a fabrication method, but also a simple and effective assembly method.

The electrospinning setup consists of four major components: a high-voltage power supply, a syringe pump, a nozzle, and a collector. The polymer fluid, i.e. polymer solution or polymer melt, is pumped out through the nozzle and it tends to form a spherical droplet. The applied high voltage generates charges at the surface of the droplet. The repulsion among these charges counteracts the surface tension and destabilize the spherical shape. The droplet then elongates into a conical shape when the repulsion force overcomes the surface tension. Because of the joint effect of the electric field and the repulsion among surface charges, the jet diameter continues decreasing until it starts to bend. Finally, the jet becomes ultrafine fibers because of the solvent evaporation or melt solidification (**Figure 2.9a**).[100, 101]

In order to assemble the nanoparticles within the electrospun fibers, the preformed nanoparticles are directly added into the polymer solution. Then the nanoparticles/polymer fibers are obtained by the electrospinning of the hybrid suspension. When the nanoparticles are uniformly distributed within the polymer solution, the nanoparticles/polymer fibers can be easily prepared. By varying the loading amount of nanoparticles, the properties of the fibrous materials can be tailored (**Figure 2.9b**).[99] The polymer scaffold provides protection and support for the nanoparticles (**Figure 2.9c**),[100] but the large surface area of polymer fibers also ensure the availability of the nanoparticles

to substrates outside the fibers. It is especially important for nanoparticles having catalytic functions. The catalytic activity and stability of nanoparticles can be preserved by immobilizing them into polymer fibrous materials. Compared with nanoparticles dispersions, polymer-embedded nanoparticles are more convenient for handling, continuous processing, and avoiding product contamination. For example, TiO_2 nanoparticles/polymer electrospun fibers showed better photocatalytic activity than nanoparticles themselves [102] and the electrospun Fe_3O_4 nanofibers showed a better peroxidase-like catalytic activity than commercial Fe_3O_4 nanoparticles.[103]
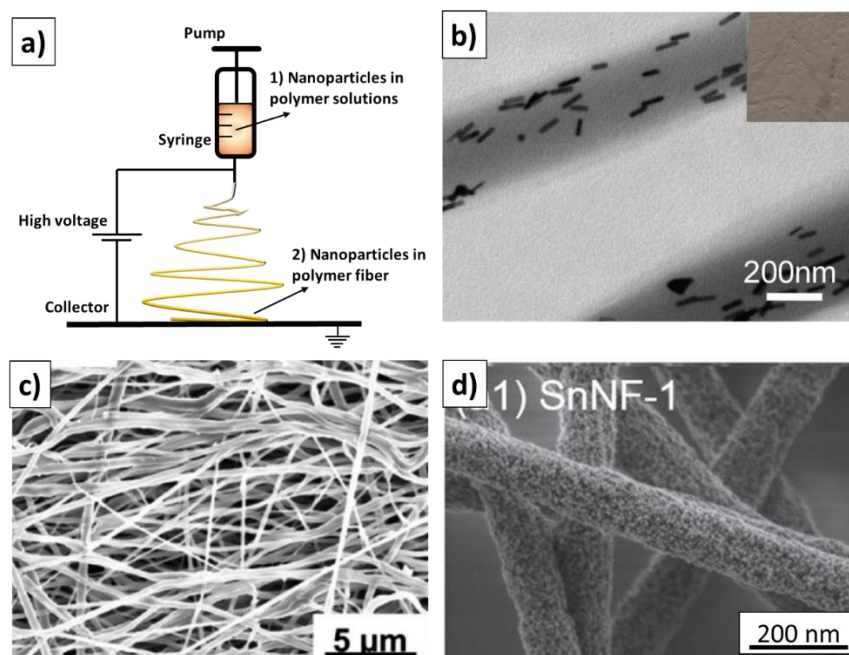
Figure 2.9 (a) Scheme of electrospinning process. (b) TEM image of gold nanorods/polymer membranes, the insect shows the color of the electrospun membrane (adapted from ref. 99 with copyright 2012 John Wiley and Sons); (c) SEM image of halloysite nanorods completely embedded in the polymer nanofibers (adapted from ref. 106 with copyright 2015 American Chemical Society); (d) SEM image of calcinated nanofibers containing SiO_2 and SnO_2 nanoparticles by using polymer nanofibers as templates[105] (adapted from ref. 105 with copyright 2017 IOPscience).

Moreover, multiple types of nanoparticles can be electrospun together to yield the multi-compartment fibers. For example, the multi-compartment fibers composed of silica nanoparticles and polystyrene nanoparticles have been fabricated by colloid-electrospinning. Afterward, the multi-compartment fibers were calcined at high temperature to remove the polystyrene nanoparticles and create porosity. The obtained fibers containing voids were subsequently broken *via* sonication to yield clustered silica rod.[104] Multi-component colloidal electrospinning has also been used to prepare hybrid materials by combining CeO_2 and SnO_2 nanoparticles with silica nanoparticles to form nanofibers with photocatalytic activity (**Figure 2.9d**).[105]

2.2.2 Evaporation guided assembly

The evaporation guided assembly method spatially controls the organization of the nanoparticles by the controlled evaporation of the solvent (water or other volatile components). This approach is a simple and robust platform for the assembly of colloidal nanoparticles. The nanoparticle assembly takes place at the three-phase-line of the meniscus of evaporating liquid, e.g. the droplet of the nanoparticle dispersion. The dispersed nanoparticles are transported to the edge of the liquid and they self-organize.[107, 108] The resulting assembled structures are strongly affected by the wetting property of the surface.[109] The wetting properties can be described by the contact angle (θ). The contact angle of a droplet on a solid surface depends on the interfacial tensions between the different phases (**Figure 2.10**) and is given by Young's equation: [110, 111]

$$\gamma_{SV} = \gamma_{SL} + \gamma_{LV} \cos \theta$$

where θ is the contact angle and γ is the interfacial tension between the solid (*S*), vapor (*V*) and liquid (*L*) phases, respectively.
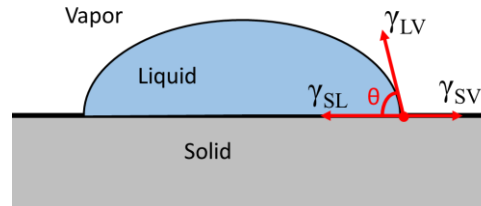
Figure 2.10 Wetting of a surface.

A well-known phenomenon of drying droplets of particles dispersion on the surface with low contact angle is the "coffee-ring effect".[112] Coffee-ring is a ring pattern caused by the drying of the coffee drop on the solid surface. The coffee-ring pattern originates from the capillary flow induced by the differential evaporation rates across the droplets: the liquid at the edge evaporates faster than the interior liquid. Thus, the interior liquid supplies the edge of evaporating liquid. The resulting edge-ward flow transports all the dispersed material to the edge. Based on this effect, many functional nanoparticle/polymer materials have been developed. For example, transparent conductive coatings have been obtained by drying the arrayed droplets of silver nanoparticles on the poly(ethylene terephthalate) substrate at room temperature. After evaporation of water, interconnected silver rings were formed. The interconnected rings are almost invisible to the naked eye. These rings are composed of self-assembled and closely packed silver nanoparticles, which make the fabricated coating electrically conductive.[113]

When droplets of nanoparticles dispersion evaporate on the surfaces with low wettability, e.g. superhydrophobic[114] or superamphiphobic surfaces,[115, 116] the nanoparticles arrange their positions in a confined droplet due to the high contact angle (usually > 150°) and low adhesion forces. In this case, the nanoparticles pack to form a mesoporous aggregate, called "supraparticle". The size of supraparticles can be tuned from several micrometers to millimeters by tuning the volume and concentration of the drying droplets (**Figure 2.11a-c**).[114] By mixing different types of nanoparticles dispersion in the droplets, single-component and multi-components can be obtained

on demand.[115] For example, the supraparticles made of Fe_3O_4, Pt and silica nanoparticles have been fabricated to use them as active swimmers in H_2O_2 solution. Additionally, the motion of the supraparticles can be steered by the external magnetic field because of the highly magnetic response of the Fe_3O_4 nanoparticles inside the supraparticles.[117]

Interestingly, the shape of the supraparticles can be tailored. The shape of droplets directly determines the shape of resulting supraparticles, which is spherical in most cases when drying droplets of nanoparticle suspensions on superhydrophobic and superamphiphobic surfaces. Hence, in order to tailor the final shape of the supraparticles, droplet geometry has to be changed during evaporation. The donut-like structure has been fabricated by drying the silica nanoparticles on the superhydrophobic surface.[118] During the evaporation, silica nanoparticles aggregate and form an elastic shell at the droplet. If the force of accumulated nanoparticles at the three-phase-line is strong enough, the droplet is pinned. Thus, the transversal shrinkage of the droplet is suppressed, resulting in exclusive shrinkage along the droplet height, i.e. droplet buckles. The similar buckling effect also has been reported by drying the polymer nanoparticles because of their aggregation during the evaporation. Through the addition of ions [119] or by adjusting pH value [116] of the droplet of nanoparticles dispersion, the nanoparticles can aggregate at the interfaces of the droplet to form a shell that causes droplet buckling during evaporation process (**Figure 2.11d-e**).
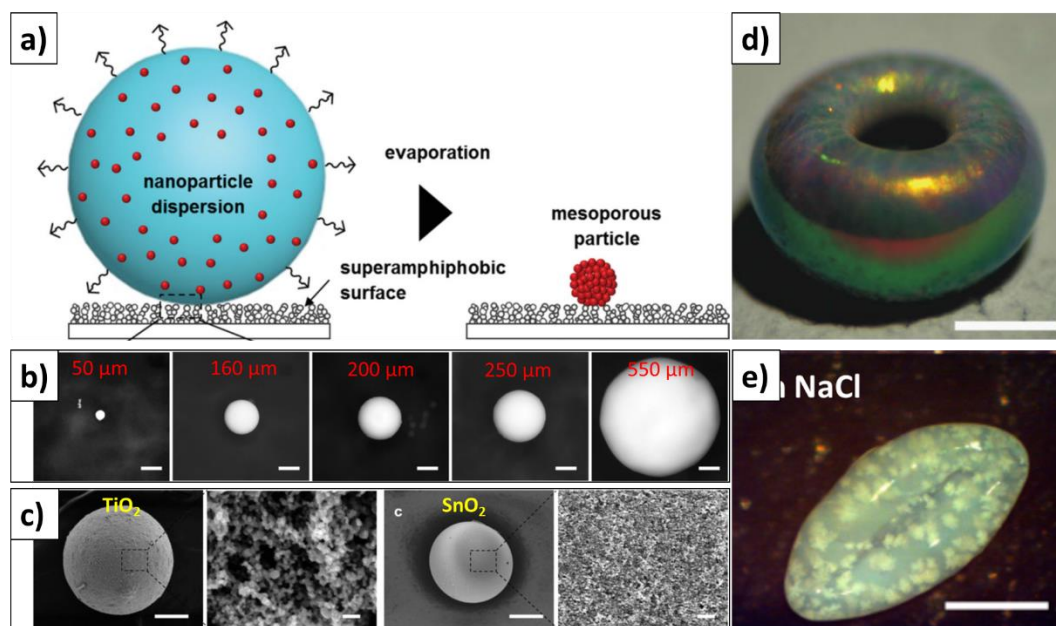
Figure 2.11 (a) Scheme of the fabrication of supraparticles by evaporation of nanoparticles dispersion on the superamphiphobic surface; (b) different size of TiO$_2$ supraparticles have been prepared by varying the concentration of nanoparticles droplets, scale bars are 100 µm; (c) SEM images of TiO$_2$ and SnO$_2$ supraparticles, scale bars are 100 µm (adapted from ref. 115 with copyright 2015 John Wiley and Sons); (d) doughnut shape of supraparticle fabricated by drying of droplet dispersion of silica and gold nanoparticles, scale bar is 500 µm (adapted from ref. 118 with copyright 2010 John Wiley and Sons); (e) boat-like supraparticle fabricated by evaporating of silica nanoparticles with 25 mM of NaCl, scale bar is 500 µm (adapted from ref. 119 with copyright 2014 John Wiley and Sons).

2.2.3 Magnetic assembly

Magnetic fields have been used to organize metal, metal oxide and hybrid nanoparticles in solution or on solid substrates.[120] The magnetic field provides enough driving force for the rapid assembly of colloidal nanoparticles within seconds. Moreover, magnetic assembly allows contactless manipulation of nanoparticles. More importantly, their strengths and spatial distributions can be

21

programmed macroscopically and microscopically, allowing the precise control over the nanoparticles organization from one single nanoparticle to the complete macroscopic assemblies.
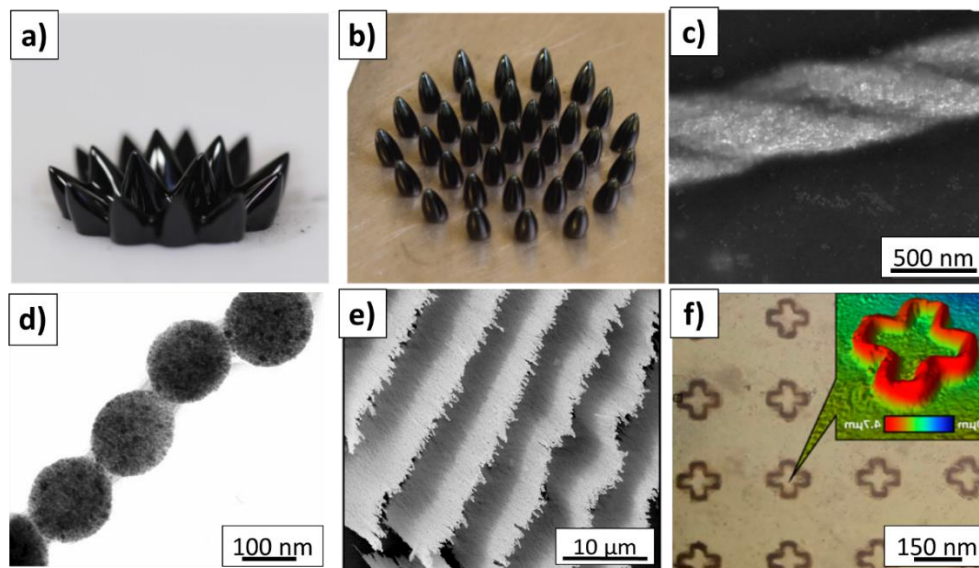
Figure 2.12 Different morphologies produced by magnetic assembly. (a) Rosensweig pattern on a glass substrate in the presence of a magnetic field. (b) Conical ferrofluid droplets generated on the superhydrophobic surface with an external vertical magnetic field (adapted from ref. 123 with copyright 2018 Elsevier); (c) helical assembled magnetic nanocubes by the magnetic assembly at the air/diethylene glycol interface (adapted from ref. 125 with copyright 2014 American Association for the Advancement of Science); (d) chain-like structure of assembled magnetic polymer nanoparticles (adapted from ref. 82 with copyright 2013 American Chemical Society); (e) Sheet-like structure assembled from $Fe_3O_4@SiO_2$ nanoparticles (adapted from ref. 129 with copyright 2013 American Chemical Society); (f) arbitrary microstructure assembled from Fe_3O_4 and $CoFe_2O_4$ nanoparticles and fixed by crosslinking with polymers (adapted from ref. 130 with copyright 2015 American Chemical Society).

The Rosensweig pattern[121] is a well-known macroscopic structure that is produced by applying a homogeneous magnetic field on a horizontal flat surface of magnetic fluid. (**Figure 2.12a**) It has the critical periodicity of $\lambda_c = \sqrt{\sigma/\rho g}$, where g is the gravitational acceleration, σ and ρ is the

surface tension and density of the magnetic fluid, respectively. Furthermore, the Rosensweig pattern can change to separated conical shape when the magnetic fluid is on the non-wetting surface (**Figure 2.12b**). Those transient patterns can reversibly switch back to the original state when the applied magnetic field is removed. [122, 123]

The microstructures of assemblies can be controlled or fixed by the manipulation of magnetic assembly either at the interfaces or in the solution.[82, 124] For example, magnetite nano-cubes have been assembled into arrays of helical superstructures by drying the nano-cubes at the solvent-air interface in the presence of a magnetic field. Different types of superstructures, including one-dimensional belts, as well as single, double, and triple helices, can be obtained by varying the density of nano-cubes and strength of the applied magnetic field (**Figure 2.12c**).[125]

Superparamagnetic nanoparticles do not have a permanent dipole, their size is so small that thermal fluctuations are enough to force the orientation of the dipole to tumble constantly. However, when an external magnetic field is applied, the magnetic dipole of the superparamagnetic nanoparticles will be aligned with the field and can subsequently be involved in dipole-dipole interactions between nanoparticles. Therefore, the nanoparticles are able to align with the direction of their magnetic moments to form the one-dimensional chains.[126] Such chain-like assemblies can be fixed by using curable polymers on the nanoparticles shells[82, 127] or by the encapsulation in silica layers[128] to form the nanofibers for further applications (**Figure 2.12d**). Furthermore, the chain-like structure can be developed into more complex structures such as sheet-like (**Figure 2.12e**)[129] or even to arbitrary shapes (**Figure 2.12f**).[130]

2.3 Applications of assembled hybrid materials

Hybrid materials made of nanoparticles and polymers have found application as a new generation of functional materials in an array of fields such as coatings, [131] biomedical applications[132] and sensing.[133, 134] Different approaches have been used to prepare various structures different dimensionalities (0D, 1D, 2D and 3D) and size ranges (nanoscopic, microscopic, and macroscopic).[9, 135]

2.3.1 Self-healing coatings

Coatings can protect metals against corrosion or ships from biofouling in order to prolong the lifetime of the materials.[136] However, small imperfections in the coatings can lead to a failure of the protective function. Hence, it is important to either repair or prevent the damages of coatings.

A straightforward method to repair coatings consists in embedding micro-/nanocapsules containing healing-agents inside the coating layer.[38, 137] Once a micro-damage occurs on a self-healing surface, by the mechanical stress from its environment, the release of a healing agent can be triggered by breaking the capsules embedded in the coating and can prompt the repair of the damaged area (**Figure 2.13a,b**). The miniemulsion technique provides a versatile platform for the fabrication of such nanocapsules with self-healing functions.[38] Various healing agents (monomers or crosslinkers) or corrosion inhibitors have been successfully encapsulated inside the polymer nanocapsules, showing the possibility of assembling them into polymer coating enabling self-healing.[38, 137]
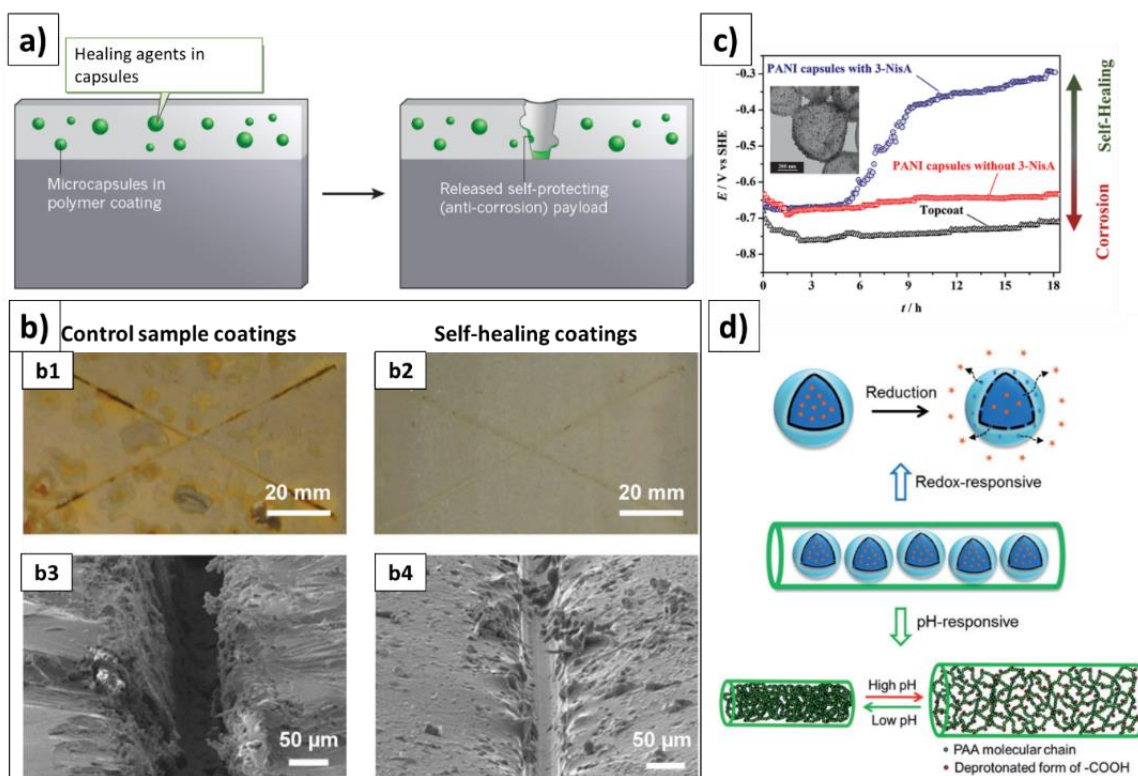
Figure 2.13 (a) Scheme of capsules-based self-healing coatings (adapted from ref. 149 with copyright 2016 Nature Publishing Group); (b) examples of self-healing coatings; b1) control sample, consisting of the epoxy vinyl ester matrix and an adhesion promoter, and b2) self-healing coating, consisting of a matrix, an adhesion promoter, microencapsulated catalyst, and phase-separated PDMS healing agent. SEM images of the scribed region of b3) the control coating and b4) the self-healing coating after healing (adapted from ref. 150 with copyright 2009 John Wiley and Sons); (c) corrosion potentials of different capsules monitored by scanning-Kelvin probe technique. The insect is the TEM images of gold nanoparticles coated polymer nanocapsules with self-healing agents (Adapted from ref. 139 with copyright 2013 John Wiley and Sons); (d) schematic illustration of the mechanism of redox- and pH-responsive release from nanofibers (Adapted from ref. 143 with the open access licensed under a Creative Commons Attribution 3.0 Unported Licence).

For example, monomers and catalysts can be separately encapsulated in different nanocapsules. Once the mechanical damage induces the breaking of the capsules, the monomer and catalyst can

be released and contact with each other, initiating polymerization to fill the damage gap.[138] Additionally, redox-responsive polymer nanocapsules have been used to encapsulated and specifically release the anti-corrosion agent when the metal corrosion initiates. (**Figure 2.13c**)[137, 139]

Besides the direct inclusion of micro-/nanocapsules into coatings, electrospinning is an alternative approach to make self-healing coatings. Electrospun fibers can encapsulate reactive agents used in self-healing coatings. Healing is initiated by mechanical damage to the coating causing the fibers to rupture and release their core materials into the damage region.[140, 141] These fiber networks offer not only the capability of encapsulating the healing agents, but also provide a way to produce hierarchical structures of multiple components. For example, redox-responsive silica nanocapsules containing an anti-corrosion agent have been synthesized by miniemulsion. Then, these nanocapsules have been assembled into polymer nanofibers by electrospinning.[101, 142] By using the pH-responsive polymer as fiber support, this nanocapsule-in-nanofiber hierarchical structure enhances the controlled release of the anti-corrosion agent. (**Figure 2.13d**) [143]

Electrospun fibers show great potential in the application of coatings. However, most fibrous membranes suffer from biofouling when they are used in aqueous environments. Biofouling is characterized as the nonspecific surface attachment of microorganisms and mammalian cells. To reduce the risk of biofouling, electrospun fibers require the ability to either reduce bio-attachment or to kill microorganisms.[144] Polymers with zwitterionic groups can prevent nonspecific protein adsorption and bacterial adhesion due to the electrostatically induced hydration. Thus, many zwitterionic polymers have been synthesized and electrospun to prepare anti-fouling coatings.[145, 146] Additionally, inorganic nanoparticles such as silver nanoparticles can efficiently kill

microorganisms. Using electrospinning, silver nanoparticles can be assembled with polymer fibers to fabricate the coatings with anti-fouling function.[147, 148]

2.3.2 Biomedical applications

Nanoparticles and their assemblies have been used for biomedical applications such as drug delivery and tissue engineering for decades.[52, 151, 152] The nanoparticles can be used as drug-transporter to deliver and targeted release cargos. In order to improve the efficiencies of delivery and release, various architectures of hybrid assemblies have been fabricated.[9, 10]

Because of the high biocompatibility and unique magnetic property, small magnetic nanoparticles (e.g. Fe_3O_4 nanoparticles below 30 nm shows superparamagnetism) have been used for targeted drug delivery.[5] An external magnetic field can be used as non-invasive tools to remotely control both the transport and the release of the drug. Additionally, superparamagnetic nanoparticles have been intensively used as contrast agents for magnetic resonance imaging (MRI) to trace the tumor position.[153, 154] By improving the size or clustering the nanoparticles, the MRI image quality can be significantly improved. For example, iron oxide nanoparticles have been assembled into chain-like structures with a protective biopolymer layer to increase the ability of the nanoparticles to circulate, target, and image tumors (**Figure 2.13a,b**).[155, 156]

Hierarchically assembling nanoparticles with encapsulated peptides into electrospun polymer fibers have been used for the sequence release of different complementary payloads, i.e. the nanoparticles were released from the nanofibers, and thereafter the peptides were released from the nanoparticles in a pH-responsive manner.[157] Besides targeted drug delivery, the hierarchical structures can be used for tissue engineering such as wound dressing materials and bone regeneration.[100] Wound dressing materials are designed to accelerate and improve the wound

healing process. They provide an environment that allows oxygen permeation, maintains moisture for materials diffusion, prevents infection, and promotes tissue formation. The assembled structure of nanofiber network exhibits high porosity, gas permeation, and offers a high surface-to-volume ratio.[158] These properties promote cell respiration, skin regeneration, and moisture retention, leading to a suitable candidate for wound dressing materials.[159] For example, silver nanoparticles have been synthesized and assembled in polymer nanofibers using electrospinning. The composite materials show very good biocompatibility, *in vitro* antibacterial ability and *in vivo* wound healing
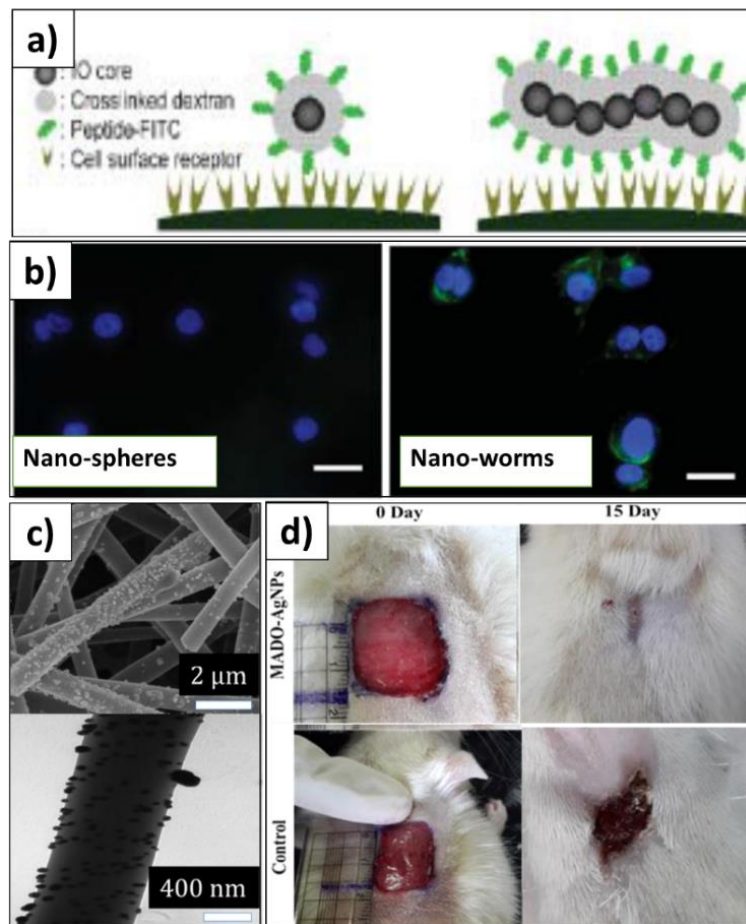

Figure 2.14 (a) Scheme illustrating the nano-worms have more interactions on cells surface than the nano-spheres (adapted from ref. 156 with copyright 2008 John Wiley and Sons); (b) fluorescence microscope images show that the interactions between cells (shown in blue) and nano-objects (spheres and worms, shown in green); scale bar is 20 mm (adapted from ref. 156 with

copyright 2008 John Wiley and Sons); (c) SEM and TEM images of polymer nanofibers coated with silver nanoparticles (adapted from ref. 160 with copyright 2015 American Chemical Society); (d) wound appearance at before and after treating with nanofibers with and without silver nanoparticles (adapted from ref. 160 with copyright 2015 American Chemical Society).

ability (**Figure 2.13c,d**). Additionally, polymer nanoparticles with antibacterial function have been assembled into polymer nanofibers and used as wound dressing materials. For example, the photoactive conjugated microporous polymer nanoparticles have been synthesized by miniemulsion polymerization and have subsequently been assembled into poly(vinyl alcohol) hydrogel nanofibers by colloid-electrospinning.[101] Such nanoparticle-in-nanofiber structure allows for a flexible combination of the properties of the nanoparticles and supporting nanofibers. Under the irradiation of visible light, the embedded photo-responsive polymer generate singlet oxygen which kills the bacteria but does not harm fibroblast cells. Therefore, the assembled material was able to inhibit biofilm formation, making the photoactive hydrogel membranes a promising candidate for active wound dressing materials.[161]

2.3.3 Other applications

Functional polymer/nanoparticle hybrids are finding applications in a variety of fields. In the design of optoelectronic devices, actuators and smart active matter to name a few. The fabrication of optoelectronic devices such as filters, pigments, antennas or waveguides heavily relies on the collective behavior of the assembled nanoparticles. For example, pigments having structural colors can be prepared by the assembly of nanoparticles.[133, 134] In this case, the color does not arise for the presence of dye molecules, but by the light interference observed when the light is reflected from highly periodical assembly of nanoparticles.[114] Such structural pigments have been prepared by the assembly of polystyrene nanoparticles into a crystalline structure by evaporation suspension droplet on the superhydrophobic surface. After drying, the resulting spherical "opal balls" show

colored rings originating from diffracted light from the curved supraparticle surface (**Figure 2.15a**). The assembled structures can, not only generate structural color for photonics but also, improve the optical signal by clustering/coupling the nanoparticles.[9, 91] For example, assemblies of metal nanoparticles (e.g. silver and gold) have been used for the sensing of molecules by surface-enhanced Raman scattering (SERS).[162] Compared to individual nanoparticles, assemblies show tenfold enhancement of SERS due to the coupling-induced enhancement of the local electromagnetic field.[91, 163, 164]
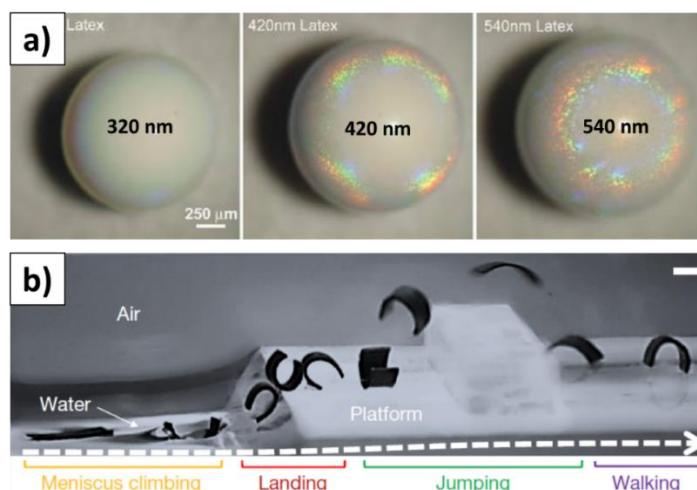
Figure 2.15 (a) Optical microscopy images of supraparticles made from drying of polystyrene nanoparticles with varying sizes (adapted from ref. 114 with copyright 2008 John Wiley and Sons); (b) The millirobot made from magnetic particles and silicon elastomer climbs up a water meniscus, lands on the solid platform, jumps beyond a standing obstacle, and walks away. Scale bar is 1 mm (adapted from ref. 167 with copyright 2018 Nature Publishing Group).

Micro-robotics is an increasingly popular topic in the 21st century and hybrid-assembled materials can offer the possibility of developing novel microbots that are multifunctional, power-efficient, compliant, and autonomous in ways akin to biological organisms.[165, 166] Polymer/nanoparticles hybrids have been used to prepare actuators, materials that in response to a stimulus creates a

movement. For example, the assembly of magnetic particles into silicone elastomer has been used to prepare soft magneto-elastic millimeter-scale robots able to swim inside and on the surface of liquids, climb liquid menisci, roll and walk on solid surfaces, jump over obstacles, and crawl within narrow tunnels (**Figure 2.15b**). [167] Superparamagnetic nanoparticles can also be assembled into polymers to form helical shapes by 3D print. Such helical magnetic polymer robots can move forward in the highly viscous environment, e.g. blood vessel, to transport the cargos and targeted released the cargos under the guiding of a magnetic field.[168, 169]

3. Results and discussion

The aim of this thesis is to develop new functional materials based on either the fabrication of new functional nano-building-blocks (nano-objects) or by the processing of nano-building-blocks into hierarchical structured polymer/nanoparticle hybrid materials. To fulfill this goal, hybrid nanocapsules (**Chapter 3.1**), polymer nanoparticles (**Chapter 3.2**), inorganic nanoparticles (**Chapter 3.3 and 3.4**), and hybrid nanoparticles (**Chapter 3.5**) with new functions have been fabricated. By assembling these functional nano-objects in polymer matrices, materials with "self-reporting", wound healing and anti-biofouling functions have been produced. Moreover, a new assembly method, which combined evaporation assembly and magnetic assembly, has been developed to generate 3D anisotropic microstructures with superparamagnetic function. These new assemblies were able to be remotely controlled by magnetic fields and could find potential applications in micro-robotics (**Chapter 3.5**).

In **Chapter 3.1**, silica/polymer hybrid nanocapsules have been fabricated by combining solvent evaporation and Pickering emulsion technique. The silica nanoparticles have been coated on the polymer shell and a latent dye has been encapsulated inside the polymer core. Upon mechanical damage, the dye was released from the broken capsules and upon contact with the silica nanoparticles was able to report the damage by the appearance of a blue color. Thus, nanocapsules with a "self-reporting" function were prepared. These nanocapsules have been successfully embedded into polymer coatings. Hence, whenever the coating was damaged, the capsules broke and highlighted the damaged area. As a second feature, the color development could be reversed and the discoloration occurred in presence of (self-)healing compounds which allow the end-user to follow the healing process. Thus, in a first step damages are being highlighted *via* color "switch-on" and, in a subsequent second step, a propagating healing reaction "switched-off" the damage

indicator dye. Coatings with such self-reporting nanocapsules allow for the monitoring the entire health-cycle of the materials, which is essential for prolonging the materials lifetime.

In **Chapter 3.2**, electrospraying technique has been used to fabricate polymer nanoparticles with minimal entanglements of polymer chains. Entanglement of polymer chains causes industrial problems during polymer processing owing to the difficulty of diffusion and movement of the polymer chains. This prevents the use of polymers with very high molecular weight by traditional processing methods such as extrusion. The objective, here, was to minimize polymer chain entanglement in linear polystyrene ($M_n = 1.1 \times 10^6$ g mol^{-1}). The polymer was dissolved at diluted concentration, well below the critical concentration of entanglement, and then electrosprayed. By drying very rapidly the polymer solution devoid of entanglements nanoparticles composed of ideally one single chain without or with few entanglements were formed.

In **Chapter 3.3**, spindle-shaped hematite (α-Fe$_2$O$_3$) nanoparticles have been prepared by forced hydrolysis of ferric chloride in water. These hematite nanoparticles show catalase-like activity by reducing H$_2$O$_2$ and producing O$_2$. Such catalase-like function is helpful for improving the wound healing process, which requires decreasing the amount of H$_2$O$_2$ and sufficient O$_2$. Therefore, hematite nanoparticles have been assembled into polymer nanofibers *via* electrospinning process, which is commonly used to generate high quality of nanofibrous wound dressing materials. On the one hand, the encapsulated hematite nanoparticles provided catalytic function to the nanofiber. On the other hand, the electrospun water-swellable polymer scaffold offered high water permeability and hydrophilic compounds to the embedded nanoparticles. When incubating fibroblasts at an H$_2$O$_2$ concentration of 50 μM (similar to the real wound environment), the catalytically active dressings efficiently reduced the H$_2$O$_2$ concentration and enabled sustained cell proliferation.

Thanks to such catalase-like activity, the hybrid nanofibrous gel could be used for improving the wound healing process.

In **Chapter 3.4**, anisotropic cerium oxide (CeO$_{2-x}$) nanorods have been synthesized by hydrothermal synthesis. These nanorods exhibit functional mimics of natural haloperoxidases that catalyze the oxidative bromination of Br$^-$ and H$_2$O$_2$ to HOBr. The generated HOBr, a natural signaling molecule, disrupted the bacterial quorum sensing, a critical step in biofilm formation. Therefore, such nanorods have the ability to combat biofouling. To endow the membranes with anti-biofouling function. The nanorods have been mixed with poly(vinyl alcohol) to generate nanofibrous structures *via* electrospinning. The embedded cerium oxide nanozymes act as a catalyst that can efficiently trigger oxidative bromination, as shown by haloperoxidase assay. Additionally, the embedded nanozymes enhanced the mechanical property of polymer mats, as shown by a single-fiber bending test using atomic force microscopy. The fabricated polymer mats with CeO$_{2-x}$ nanorods could be used to provide mechanically robust coatings and membranes with anti-biofouling properties.

In **Chapter 3.5**, a versatile and general assembly method has been developed to produce assembled microstructure with 3D anisotropic shapes and superparamagnetic function. By evaporating droplets of superparamagnetic nanoparticles suspension on superamphiphobic surfaces, mesoporous supraparticles can be produced. Furthermore, by tuning the concentration of ferrofluid droplets and controlling the magnetic field, barrel-like, cone-like, and two-towers-like supraparticles were obtained. These assembled supraparticles preserved the superparamagnetism of the original nanoparticles. Moreover, other colloids can easily be integrated into the ferrofluid suspension to produce, by co-assembly, anisotropic binary supraparticles with additional

functions. Additionally, the magnetic and anisotropic nature of the resulting supraparticles were harnessed to prepare magnetically actuable microswimmers.

3.1 Monitoring crack appearance and healing in coatings with damage self-reporting nanocapsules[†]

In this chapter, silica/ poly(methyl methacrylate) hybrid nanocapsules have been fabricated by combining solvent evaporation and Pickering emulsion technique. The silica nanoparticles have been coated on the polymer shell and a latent dye has been encapsulated inside the polymer core. Upon mechanical damage, the dye was released from the broken capsules and upon contact with the silica nanoparticles was able to report the damage by the appearance of a blue color. Thus, nanocapsules with a "self-reporting" function were prepared. These nanocapsules have been successfully embedded into polymer coatings. Hence, whenever the coating was damaged, the capsules broke and highlighted the damaged area. As a second feature, the color development could be reversed and the discoloration occurred in presence of (self-)healing compounds which allow the end-user to follow the healing process. Thus, in a first step damages are being highlighted *via* color "switch-on" and, in a subsequent second step, a propagating healing reaction "switched-off" the damage indicator dye. Coatings with such self-reporting nanocapsules allow for the monitoring the entire health-cycle of the materials, which is essential for prolonging the materials lifetime.

3.1.1 Introduction

Polymer coatings can act as a protective envelop around many materials to prolong their lifetime (*e.g.* prevent corrosion of metals[170, 171]) until exposure to environmental stress leads to damaging of the coating and impairment of its protective function.[172, 173] Hence, it is important to detect and repair damages as early as possible. But tiny (nano- or microscale) damages are hardly visible and common coatings do not possess the ability to autonomously highlight cracks to alert the user of an impending failure. To endow coatings with an autonomous damage-reporting function, dye-loaded microcapsules have been integrated in polymer coatings.[174] Upon mechanical damaging of the coating and contemptuous rupturing of the capsules, the released indicator dye can change its chemical structure *via* UV-light exposure,[175, 176] chemical reaction,[177-179] or physical aggregation[180, 181] to present a visible or fluorescent signal on the damaged spot. Besides, some bulk polymeric materials can change their color upon mechanical stress *via* chemical transformation of the polymers.[182-184] Thus, the micro-damage in the coating is autonomously highlighted to initiate maintenance of the coating.

Consequently, occurring damages in coatings can be reversibly healed by a number of well-established self-healing systems.[185-187] Thus, self-healing coatings can heal cracks by the dynamic formation of reversible chemical bonding,[188-195] by a covalent crosslinking polymerization of released monomers from microcapsules,[196-198] or by generating radicals during damage process which can initiate the repairing reaction.[199] The success of damage healing thereby depends on several factors like the distribution of self-healing agents within the coating, the environmental temperature or the size and depth of the damage. Thus, monitoring the success of damage healing is essential to guarantee the protective function of the coating and to indicate a required coating maintenance. Therefore, it is essential to visualize a damage that is not being healed with a self-

reporting system. However, when the irreversible damage reporting capsules described in the literature to date are combined with self-healing coatings, the capsules would highlight the crack even if it is being or has already been healed.[200] To enable simultaneous monitoring of damages in coatings and their self-healing, the optical damage-indication has to be made reversible. Currently, a hurdle is that the incorporated healing agents cannot deactivate the active indicator to turn off the optical signal. Therefore, it is crucial to create a system that cannot only turn on the signal to report the damage appearance, but can additionally turn off the signal to report that the damage is being healed.

In this chapter, a nanocapsule-based system was introduced for autonomously monitoring mechanical micro-damage appearance and healing in polymeric coatings. The damage appearance and healing monitoring system is schematically illustrated in **Figure 3.1.1**. First, a three-component nanocapsular system was designed a (**Figure 3.1.1a**), in which the damage-indicating dye is encapsulated within the protective polymer shell, which is further coated with a color developer. When the shell is mechanically broken, the released inactive dye (decolored form) becomes active (colored form) through reacting with the color developer. In this manner, the nanocapsules themselves autonomously report their destruction, which allows a spatial and functional separation from the surrounding medium and other capsules, enabling the universal use of such a self-reporting nanocapsule based system to indicate damages in various coatings (**Figure 3.1b**). As an additional feature, besides color indication, a defined second reaction between the color indication system and the surrounding medium can be implemented. Thus, the interactions between the dye and the color developer can be reversibly deactivated by different self-healing compounds or byproducts of self-healing reactions. Consequently, the self-reporting capsule-based system cannot only turn on the optical signal for sensing the crack in coatings, but can also

turn off the signal by interacting with healing agents to highlight only the damages that are not being healed.
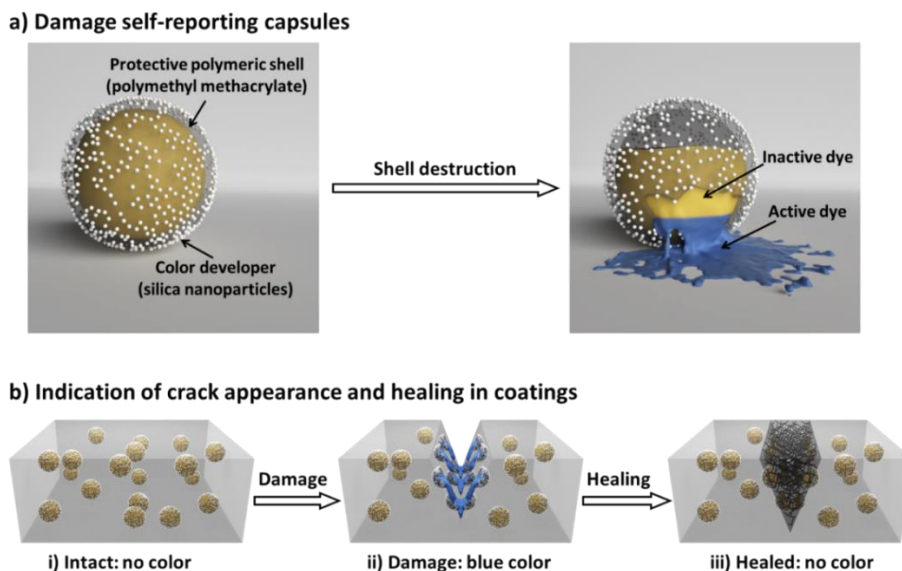
Figure 3.1.1 (a) Schematic illustration of a damage self-reporting capsule. The colorless damage-indicating dye (CVL) is encapsulated in a silica-coated polymer shell. When the capsule shell is broken, the released dye is developed through interaction with silica to give a deep blue color (CVL$^+$). (b) Damage self-reporting capsules embedded in waterborne polymer coating to indicate crack-appearance and self-healing (i-ii). When a mechanical damage occurs, the dye is released and locally reacts with the color developer at the ruptured capsules surface to highlight the damaged spot *via* a colorimetric indication (ii-iii). When self-healing agents get in contact with the dye, the color is being deleted and no color remains visible allowing monitoring the self-healing reaction.

3.1.2 Experimental

Materials

Crystal violet lactone (CVL, 97%, Alfa Aesar, USA), phenyl acetate (Sigma-Aldrich, USA). Poly(methyl methacrylate) (M_w is 120000 g·mol^{-1} as determined by GPC, Sigma-Aldrich, USA),

LUDOX® HS-30 (30 wt.% dispersion, Sigma-Aldrich, USA), chloroform (> 99%, Acros Organics, Belgium), aqueous HCl solution (1 mol·L^{-1}, Carl Roth, Germany). For the model coating experiment, a waterborne polymeric coating (Mowilith® DHS S1, Celanese, Germany) was kindly donated by Celanese corporation and was used as the coating matrix material. The trivalent azide and the multivalent alkyne (equimolar ratio) and Cu$^{(I)}$Br(PPh$_3$)$_3$ (1mol%, 98%, Sigma-Aldrich, USA) were used for damage self-healing tests.

Synthesis of healing chemicals

The synthesis of these healing chemicals[201] are shown in **Figure 3.1.2** and **Figure 3.1.3** and briefly described as follows: for the synthesis of the multivalent alkyne (trimethylolpropane tripropargyl ether), trimethylolpropane (97%, Sigma-Aldrich, USA) was converted with propargyl bromide (80% in toluene, Sigma-Aldrich, USA) at 60 °C for 41 h in the presence of sodium hydroxide (99%, Grüssing, Germany) as deprotonating agent and tetra-*n*-butylammonium bromide (99%, TCI, Belgium) as phase transfer catalyst and the crude product was purified by column chromatography. (**Figure 3.1.2**) The structures of multivalent alkyne were determined by SHIMADZU GCMS-QP2010 gas chromatograph mass spectrometer.

(x + y + z = 1, x : y : z = 86:13:1)
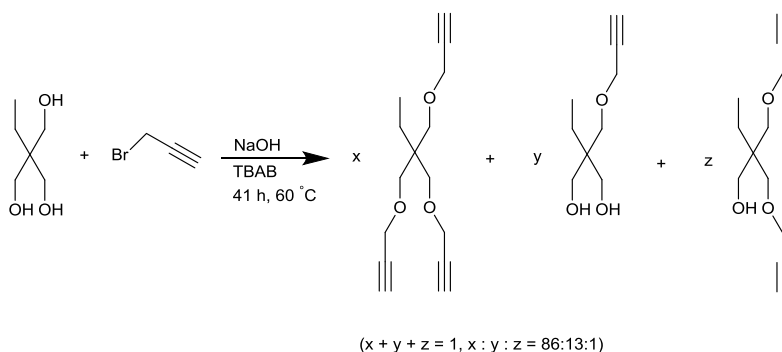
Figure 3.1.2 Synthesis of multivalent alkyne chemicals (with one, two, three alkyne groups).

The preparation of trivalent azide (((2-((2-acetoxy-3-azidopropoxy)methyl)-2-ethylpropane-1,3-diyl)bis(oxy))bis(3-azidopropane-1,2-diyl) diacetate) was in a two-step synthesis. (**Figure 3.1.3**) Therefore, the ring opening of trimethylolpropane triglycidyl ether (technical grade, Sigma-Aldrich USA) and subsequent azidation reaction was performed in methanol (99.8%, Sigma-Aldrich, USA) under refluxing conditions within 24 h in the presence of sodium azide (99.5%, Sigma-Aldrich, USA) followed by acetylation with acetic anhydride (99%, Sigma-Aldrich, USA) proceeding within 89 hours at room temperature in DMF (99%, Grüssing, Germany). Diethylenetriamine (99%, Sigma-Aldrich, USA) and ethanol (> 99.5%, Sigma-Aldrich, USA) were used for color deleting tests.
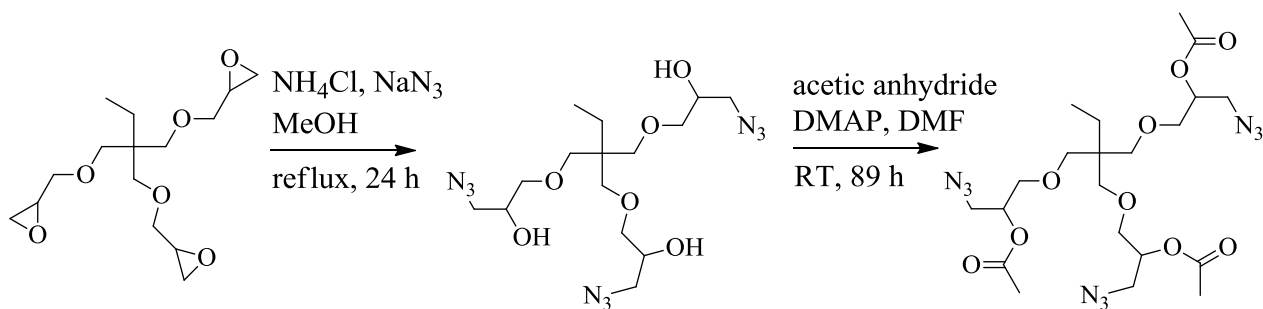
Figure 3.1.3 Synthesis of trivalent azide (((2-((2-acetoxy-3-azidopropoxy)methyl)-2-ethylpropane-1,3-diyl) bis(oxy))bis(3-azidopropane-1,2-diyl) diacetate).

Preparation of damage self-reporting nanocapsules: The three-component nanocapsules were fabricated by combining a Pickering emulsion with the solvent evaporation technique.[202] Varied amount of poly(methyl methacrylate) (PMMA) (300 – 1200 mg, detailed information in **Table 3.1.1**) was first dissolved in 5 g chloroform. Then 100 mg crystal violet lactone (CVL) was dissolved in 1 g phenyl acetate in a separated vessel.

Table 3.1.1 Shell thickness and diameter of capsules with different emulsification parameters.

Sample number	Polymer amount (mg)	Silica colloidal amount (g)	Ultrasound amplitude (%)	Diameter (nm)	Shell thickness* of capsules (nm)
1	300	4.8	50	202 ± 80	8 ± 3
2	300	3.2	50	212 ± 76	8 ± 3
3	300	2.4	50	272 ± 137	10 ± 5
4	300	3.2	30	304 ± 130	12 ± 5
5	400	3.2	50	418 ± 112	20 ± 5
6	500	3.2	50	428 ± 87	25 ± 5
7	600	3.2	50	449 ± 125	30 ± 8
8	700	3.2	50	523 ± 160	39 ± 12

*The shell thickness (d) of capsules was determined by the following equation according to Zhao *et al* [213]:

$$d = R \times \left(1 - \frac{1}{\sqrt[3]{\frac{m_{polymer}}{m_{core}} \times \frac{\rho_{core}}{\rho_{polymer}}}}\right) \text{ (3.1.1)}$$

where R, $m_{polymer}$, m_{core}, $\rho_{polymer}$, ρ_{core} is the radius of the capsule, mass of the polymer, mass of the core, density of the polymer and density of the core, respectively.

The CVL and PMMA solutions were mixed together in a vessel as the oil phase. Varied amount (2.4 g, 3.2 g and 4.8 g) of LUDOX® HS-30 as emulsion stabilizer was added into 16.8 g of distilled water as continuous phase. The combined phases were mixed using vortex for two minutes. The pH of the pre-emulsion was adjusted to 8.0 by adding 1 M HCl solution. An ultrasonification tip was used to form the oil in water emulsion under ice bath cooling (*d* (tip) = ½ inch; 30% or 50% amplitude; 30 s pulse, 10 s pause; 3 min). The resulting emulsion was rapidly transferred in a preheated oil bath at 40 °C and stirred at 1000 rpm for 16 hours to evaporate the chloroform (**Figure 3.1.3**).
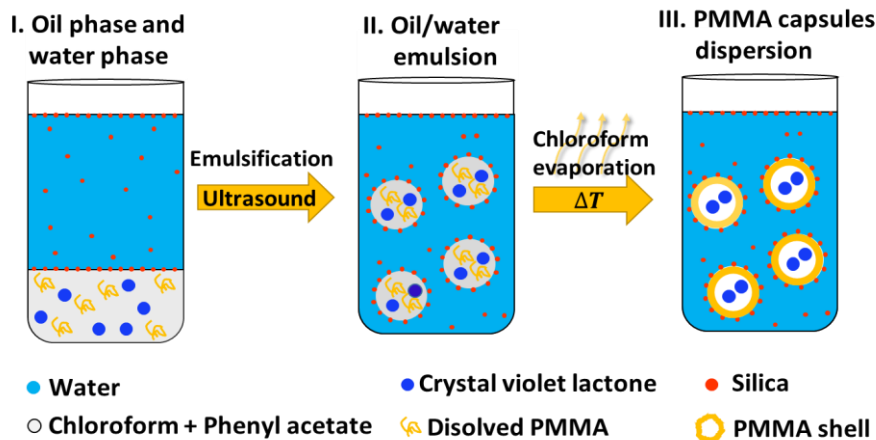
Figure 3.1.3 Schematic picture of the fabrication process of silica / CVL / PMMA nanocapsules *via* a combination of Pickering stabilized miniemulsion and solvent evaporation process.

Coating fabrication: 1 mL of the fabricated nanocapsule dispersion (0.3 g of PMMA and 3.2 g of silica were used, the applied ultrasound amplitude was 50%) was centrifuged at 5000 rpm for 15 min. Then the supernatant was removed and the remaining slurry was coated carefully on the surface of a glass slide. After 1 min of pre-drying (the capsules suspension should not dry completely, otherwise some capsules can already break with the result of a pale blue color in the final coating layer) at room temperature, 1 g of Mowilith® DHS S1 was coated on top of the capsules as a protective layer. Then the coating was dried overnight at room temperature. The coating thickness was normally 96 ± 12 μm (measured by a thickness gage from Mitutoyo company, Japan). For the mechanical damage tests, a razor blade (Stanley 28-510) was used to scratch the coating layer and to form a micro-crack. For the damage healing test the combined healing agents, namely a trivalent azide, a multivalent alkyne and $Cu^{(I)}Br(PPh_3)_3$ as catalyst were added onto the damaged spot to heal the crack for 48 h at room temperature.

Characterizations: The hydrodynamic diameter of the nanocapsules was measured by DLS (Nano-Zetasizer, Malvern Instruments, UK) at 20 °C under a scattering angle of 90° at $\lambda = 633$ nm. The

morphology of the nanocapsules was observed by transmission electron microscopy (TEM, JEOL JEM1400, Japan) and scanning electron microscopy (SEM, Hitachi SU8000, Japan). Before the electron microscopy measurements, 5 μL of diluted dispersions were coated on a silicon wafer (SEM measurement) or 400-mesh copper grid (TEM measurement) and dried at room temperature. The topography of the fabricated capsules in liquid and air environment was measured using JPK Nanowizard 3 AFM (JPK Instruments, Berlin, Germany) using the quantitative imaging mode. In this operation mode, data are taken by recording force vs. distance curves for each image pixel position. From such a data set, the height profile of a sample can be reconstructed by taking the distance at which the repulsive force between tip and sample reaches a fixed value (force set-point). For deformable samples, this will result in an apparent sample height value that depends on the selected force set-point and sample stiffness. This imaging mode was chosen because the adherence of capsules in liquid to the silicon wafer was too weak leading to lateral drift of capsules during intermittent contact (tapping) mode imaging. The spring constant of the cantilevers (OMCL-AC240TS-R3, Olympus, Japan) was determined by the thermal tune method. For the measurement in liquid, a starting set-point force of 5 nN was used and then increased in steps of 5 nN until reaching a critical force at which the capsules collapsed. For the measurements in air, the set-point force was 5 nN. All the experiments were carried out at room temperature (20 °C). For chemical analysis of the capsules´ shell, the SU8000 with an energy dispersive x-ray spectrometer (EDX) was used to measure the content of silicon and carbon. Ultraviolet / visible (UV / Vis) spectra of CVL and CVL^+ with different chemicals (color developing or deleting agents) were obtained by using a Perkin Elmer Lambda 25 spectrometer. The transparency of the coating layer without and with capsules was measured by UV / Vis spectrum (wavelength range is $350 - 800$ nm). Lactone ring opening and closure was studied by Fourier transform infrared spectroscopy

(FTIR) and nuclear magnetic resonance (NMR) spectroscopy. Powder samples and KBr were ground to prepare a pellet for FTIR measurements. Solution ^{1}H NMR spectra were acquired in a Bruker Avance spectrometer operating at 300 MHz. All chemical shifts were referenced to the residual proton signals from acetone-d6 (2.05 ppm). The damage appearance and healing of the coatings were investigated with a Zeiss Axiophot stereomicroscope (Carl-Zeiss Microscopy GmbH, Germany) equipped with a digital camera. Differential scanning calorimetry (DSC) investigations were performed on a 204F1 / ASC Phönix (Netzsch, nitrogen flow of 20 mL·min^{-1}) in a temperature range from - 20 to 250 °C with heating rates of 5, 10, 15 and 20 °C · min^{-1} and crucibles and lids out of alumina were used.

3.1.3 Results and discussion

As color indication dye, crystal violet lactone (CVL) was selected because of its intense color change capabilities through selective reaction with a manifold of compounds able to develop or delete its color.[203, 204] The reversible opening of the lactone ring of the colorless CVL can be induced through hydrogen bonding (*e.g.* through silanol groups of silica, see **Figure 3.1.5**) to form CVL$^+$ with an intensive blue color (**Figure 3.1.6a, photograph (i) and (ii)**).

CVL
(leuco form)

CVL$^+$
(colored form)
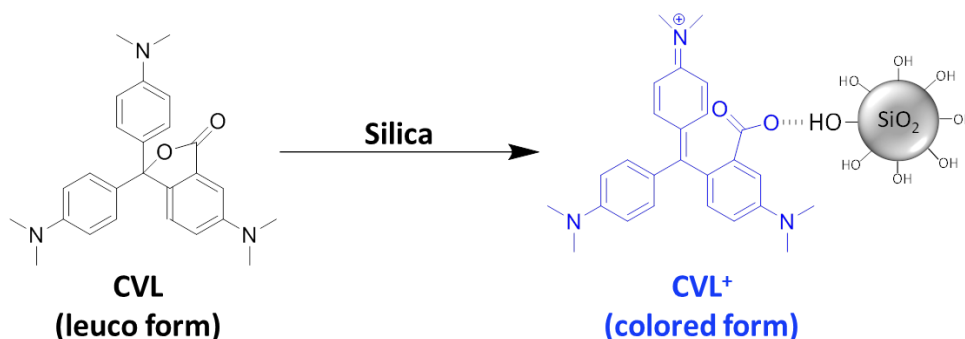
Figure 3.1.5 Chemical structures of CVL and CVL$^+$. The lactone ring of CVL can be opened by the silanol groups of silica. Then the colorless leuco form (CVL) changes its conformation to a colored form (CVL$^+$).
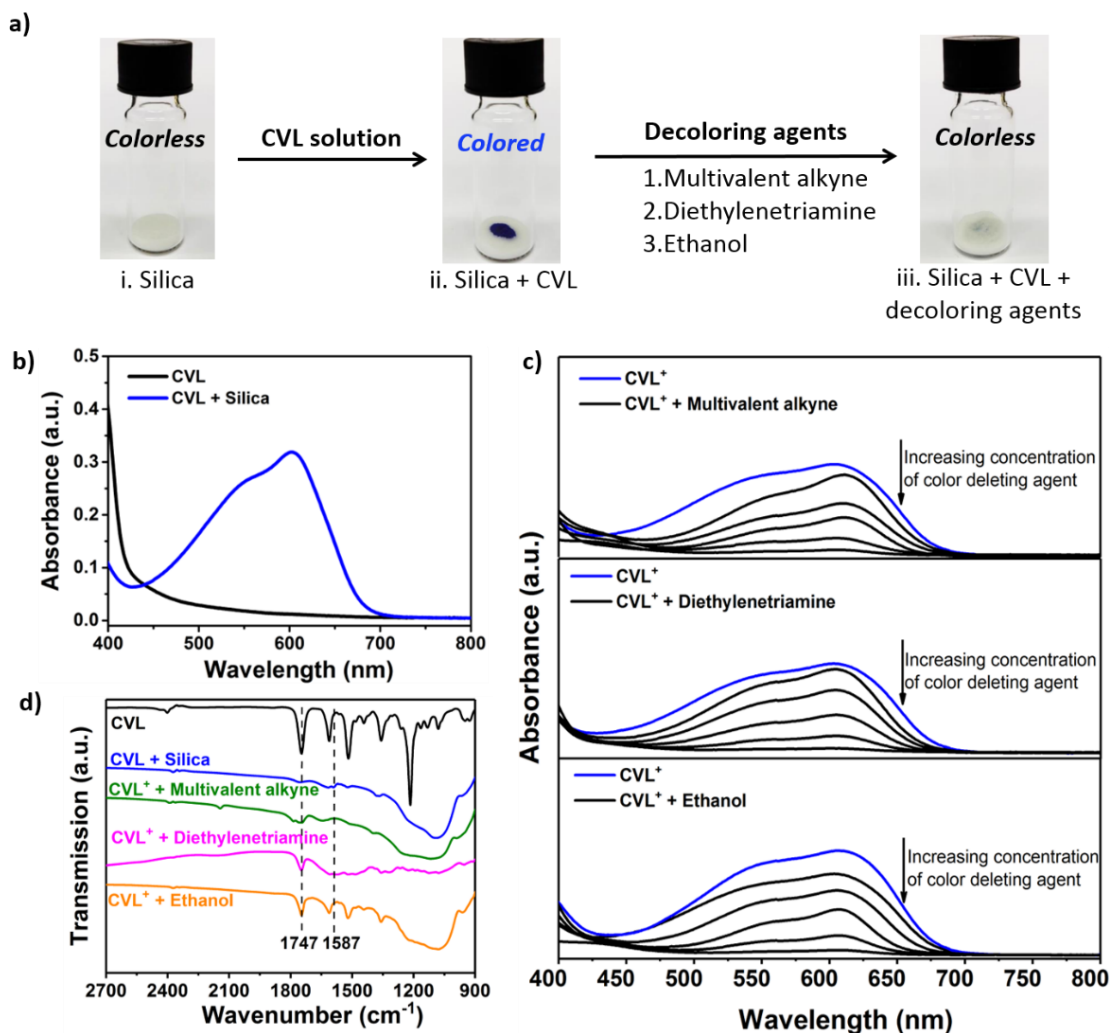
Figure 3.1.6 (a) Photographs of i) silica powder, ii) a mixture of silica and CVL powder after developing of the color and iii) silica and CVL powder after addition of different decoloring agents to delete the blue color. (b) UV / Vis spectra of CVL and CVL mixed with silica nanoparticles. (c) UV / Vis spectra of CVL$^+$ reacted with different amounts of the decoloring agents. (d) FTIR spectra of a CVL powder, a mixture of silica and a CVL powder after developing of the color, and CVL$^+$ with three decoloring agents (multivalent alkyne, diethylenetriamine, and ethanol).

To demonstrate the color development, CVL was dissolved in phenyl acetate and added dropwise onto silica powder. An intense blue color immediately evolved, indicating the conversion of CVL to CVL$^+$ which can be followed by a broad absorption peak with a maximum at $\lambda = 603$ nm *via*

UV / Vis measurements (**Figure 3.1.6b**). Besides the color developing mechanism, the color deleting mechanism in the presence of various decoloring agents was investigated. Ethanol, diethylenetriamine (DETA) and a multivalent alkyne were selected as decoloring reagents since they are common self-healing components[201, 205] or byproducts[206-208] of self-healing reactions. To prove the decoloring feature, different amounts of decoloring agent were mixed with the CVL$^+$, which had previously been developed in the presence of silica powder (**Figure 3.1.6a, photograph (iii)**). The absorption band of the colored CVL$^+$ at 603 nm was lowered with increasing amounts of decoloring agents (**Figure 3.1.6c**). Although all of the three agents showed a color deleting effect on CVL$^+$, their decoloring kinetics were noticeably different: the multivalent alkyne deleted the blue color in two hours while DETA and ethanol deleted the color within minutes.
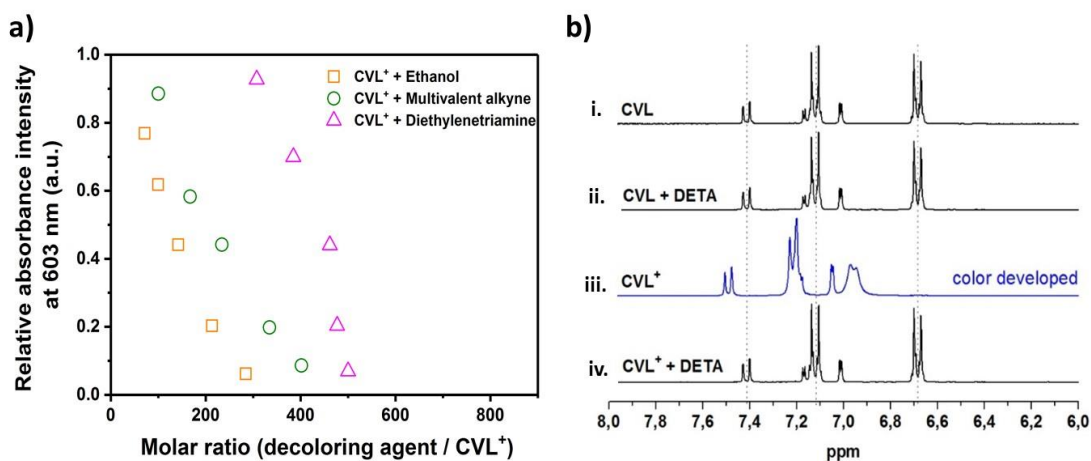
Figure 3.1.7 (a) The relationship between color intensity and the molar ratio of decoloring agents to CVL$^+$. (b) Solution ^{1}H NMR spectra of the aromatic protons in CVL in different conditions: i) CVL before color developing; ii) CVL in presence of DETA (CVL : DETA at 1 : 2 mol ratio), no effect; iii) CVL$^+$ color developing with HCl (CVL : HCl at 2.4 : 1 mol ratio); iv) CVL$^+$ color deleting with DETA (CVL$^+$: DETA at 1:2 mol ratio). All spectra were acquired in acetone-d6 immediately after mixing all components.

Additionally, the amounts of decoloring agents that can initiate the color deleting effects were found to be different (**Figure 3.1.7a**). Thus, variations in the color deleting efficiency between the different decoloring agents and CVL$^+$ or silica were most probably related to different decoloring mechanisms. The strong blue color of CVL$^+$ is initiated by hydrogen bonding of the hydroxyl groups of silica with the carboxylate groups of CVL$^+$.[209] Breakage of these hydrogen bonds, and consequent color fading, can either be achieved by adding polar solvents that insert between the silica and the CVL$^+$,[210] or by bases. The dependence of the color developing on the acid / base equilibrium is apparent from the ^{1}H NMR spectra in solution. As shown in **Figure 3.1.7b**, color developing with HCl causes the expected downfield shift of the aromatic protons signals of CVL due to the opening of the lactone ring. Addition of DETA, on the other hand, immediately neutralizes the effect of HCl and quantitatively restores CVL from CVL$^+$.

Additionally, the hydrogen bonding ability between the dye, the hydroxyl groups of the silica, and the decoloring agents was investigated *via* FTIR spectroscopy (**Figure 3.1.7d**). The pure CVL shows a band at 1747 cm^{-1} due to the vibration of the C=O group of the lactone ring. When silica reacts with CVL, a new band arises in the spectrum of CVL$^+$ at 1587 cm^{-1}, which can be ascribed to the carboxylate group of the opened lactone ring. This band disappears when the color deleting agents interact with CVL$^+$, indicating the closure of the lactone ring.[211] Thus, the color of CVL can be developed with silica and be deleted by self-healing agents or byproducts from the healing reaction.

The damage self-reporting capsule was achieved in a one-step miniemulsion solvent-evaporation process (details in **Experimental**), in which the silica particles function as Pickering stabilizer. At the beginning of the solvent-evaporation process, PMMA and CVL were homogeneously dissolved in a mixture of chloroform and phenylacetate. During the evaporation of the chloroform,

the PMMA becomes insoluble and phase separates from the phenylacetate to form the solid capsule shell, while the CVL stays dissolved in phenyl acetate to consequently create the liquid core. The raspberry-like surface topology of the capsules was observed *via* scanning electron microscope (SEM) imaging (**Figure 3.1.8a**) and their core-shell morphology *via* transmission electron microscope (TEM) imaging (**Figure 3.1.8b-c**). The silica nanoparticles cover the shell of the nanocapsules as shown by the SEM-EDX mapping image (**Figure 3.1.8d**).
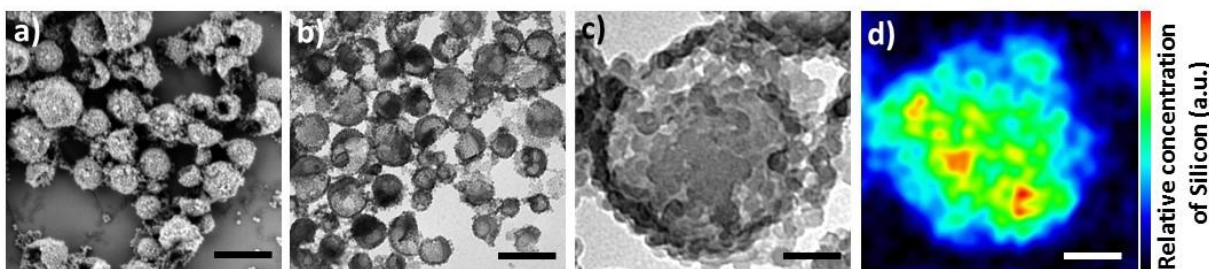
Figure 3.1.8 Tuning of the color response and mechanical stability of the damage self-reporting nanocapsules. (a) SEM image, (b) and (c) TEM images and (d) SEM-EDX silicon mapping of fabricated nanocapsules (scale bars are 300 nm, 300 nm, 100 nm, and 100 nm, respectively).

For successful implementation of the prepared nanocapsules as damage-indication systems in coatings, their mechanical response has to be tuned in a way that they do not break in suspension and during the embedding process into the coating, but exclusively when they are exposed to air (*e.g.* through a crack in the coating). The mechanical stability of micro- /submicrocapsules is related to the critical buckling pressure (p_c) of spherical capsules[212] which mainly relates to the capsules' radius (R) and shell thickness (d) as follows: $p_c \propto \dfrac{d^2}{R^2}$ (**3.1.2**)

To further understand the mechanical stability of the capsules, different submicro- / nanocapsules with different p_c values were prepared. By varying the silica concentration, the amount of PMMA, and the sonication amplitude, the capsules' hydrodynamic diameter can be tuned between

approximately 200 and 1100 nm and the shell thicknesses between approximately 10 and 120 nm (see **Table 3.1.1** in **Experimental**). First, the stability of the capsules was tested by drying the capsules under ambient conditions. The white suspensions of capsules were drop-casted on glass slides and dried for several hours at room temperature. During drying of the dispersions, capillary forces between the particles will occur in two ways. First during recession of the air-water interface from the outmost layer of particles down to the substrate and second during drying out of the remaining menisci. These forces can cause the capsules to collapse during drying depending on their mechanical stability and then develop a blue color. After drying, the capsules with different shell thickness developed varying intensities of a blue color (**Figure 3.1.9a**). **Equation (3.1.2)** was used to evaluate the critical buckling pressure of the capsules[212] and tune the color development. As shown in **Figure 3.1.9b**, the color intensity decreased with increasing the value of $\frac{d^2}{R^2}$. The capsules with $\frac{d^2}{R^2} < 0.030$ developed an intense blue color, indicating that the shells had been damaged during the drying process owing to their weak shell stability. However, capsules with $\frac{d^2}{R^2} > 0.030$ show no blue color and displayed a white color after drying, indicating that the capsules were able to resist the drying process. To further test the robustness of the capsules and to demonstrate their capability to still develop a blue color upon breaking, the dried capsules with higher critical buckling pressure ($\frac{d^2}{R^2} = 0.047$) were subsequently ground with a pestle. After grinding, the submicrocapsules developed a blue color, indicating the shell destruction and the ability of color development (**Figure 3.1.9c**).
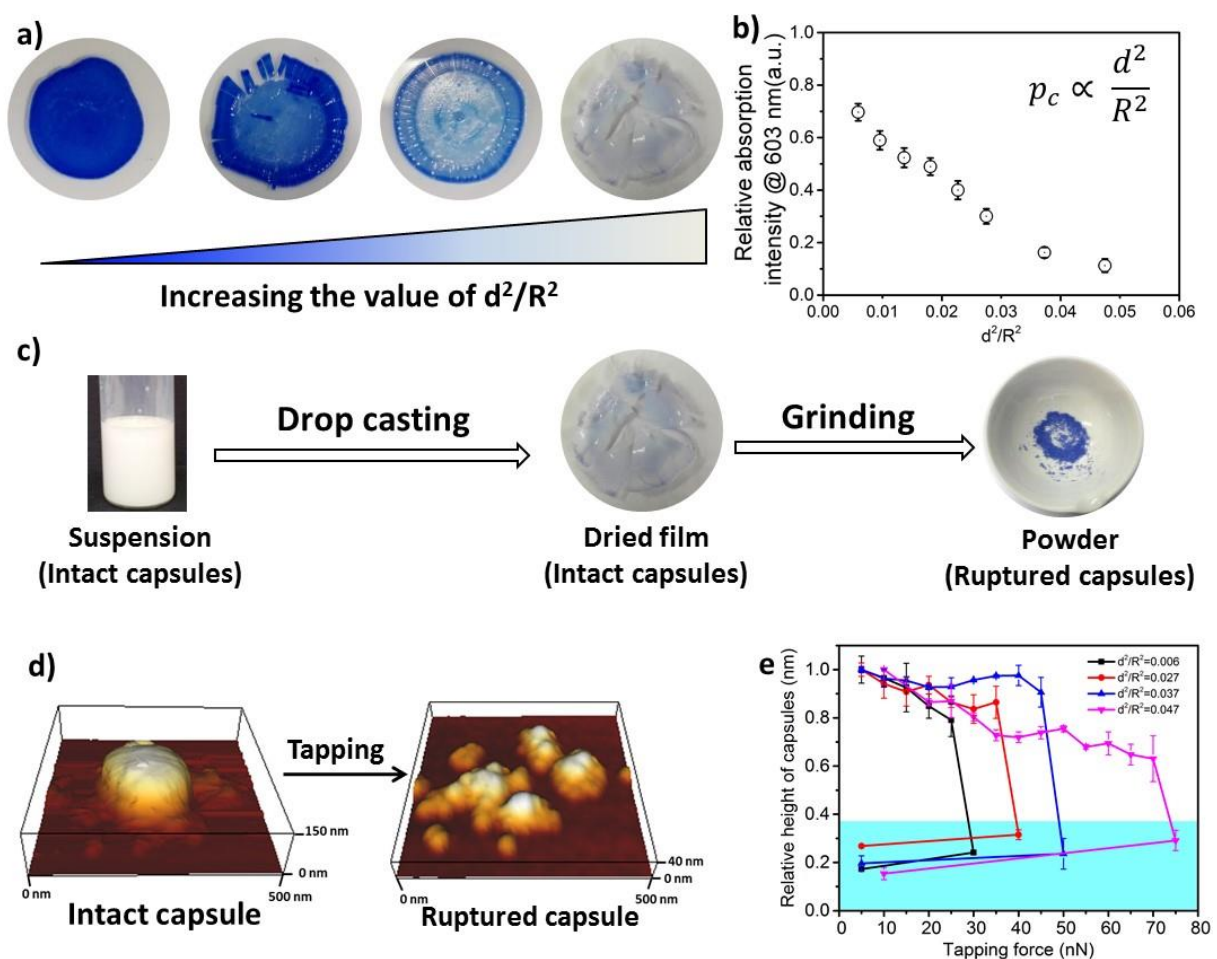
Figure 3.1.9 (a) Optical photographs of dried capsule suspensions with different critical buckling

pressure. (b) Absorption intensities at $\lambda = 603$ nm of dried capsules as a function of their $\frac{d^2}{R^2}$ value

as determined by UV /Vis measurements. (c) The suspension of the capsules with highest critical

buckling pressure ($\frac{d^2}{R^2} = 0.047$) is dried without blue color developing. When these dried capsules

are grinded with a pestle, a strong blue color is developed. (d) AFM height images of a capsule

($\frac{d^2}{R^2} = 0.006$) in suspension before and after rupture. (e) Change of normalized apparent capsules'

height with increasing set-point force. The area with cyan color marks values measured after

capsules rupturing.

To theoretically determine the breaking force during drying, the following calculation is considering. During drying of dispersions, capillary forces between the particles will occur in two ways. First during recession of the air-water interface from the outmost layer of particles down to the substrate and second during drying out of the remaining menisci. Assuming complete wetting of the particles, *i.e.* a contact angle of zero, the capillary force is proportional to the water surface tension γ and the particle radius R for both cases.

$$F_C = A \, \gamma \, R \quad \textbf{(3.1.3)}$$

The proportionality factor A is in both cases in the order of unity. For the case of the meniscus between two spheres, the prefactor equals $A = 2\pi$, whereas, in the case of the receding water front, it is given by:

$$A = \frac{3\sqrt{2}(1-f)^2}{\sqrt{3}-1} \quad \textbf{(3.1.4)}$$

with f being a factor depending on the amount of deformation of the spheres that ranges from 0 to 0.095 and is zero for zero deformation, i.e. $A = 5.8$. Therefore, both prefactors are well approximated by $A = 6$ and the capillary force for both cases takes a value of

$$F_C = 6 \cdot 0.072 \frac{N}{m} \cdot 150 \, nm = 65 \, nN \quad \textbf{(3.1.5)}$$

Exemplarily, the capillary force for capsules with a diameter of 300 nm can be calculated to $F_c = 65$ nN (**Equation 3.1.5**). To investigate if this calculated capillary force is enough to break the capsules, atomic force microscopy (AFM) measurements were used in which a certain force was applied to one capsule in an aqueous environment. With AFM, a defined force can be applied directly with the tip of the cantilever on a single capsule until it breaks (**Figure 3.1.9d**). **Figure 3.1.9e** further shows that the apparent height of the capsules decreases when imaged using

an increasing contact force. When the contact force reached a certain threshold, its apparent height dramatically declined to a very low value, which remained constant after the initial low contact force was applied again, indicating that the capsule had been irreversibly ruptured. Hence, the mechanical response of the investigated capsules can be precisely measured (for the investigated cases 30 - 75 nN) and fine-tuned depending on the shell thickness. The determined forces are well in agreement with the capillary force that occurs on the capsules during drying as calculated in the supporting information.

To demonstrate the capability of the damage self-reporting capsules for micro-crack indication in coatings, nanocapsules with a low critical bulking pressure ($\frac{d^2}{R^2} = 0.006$) that break upon exposure to air were combined with a commercially available waterborne polymer coating (approx. 100 μm thick). Therefore, the nanocapsules suspension was firstly coated on a glass slide, pre-dried and sealed with the commercial coating to avoid breakage of the capsules (details in **Experimental** section). Introduction of the capsules to the commercial coating causes only minor decrease of the transparency of the coating, which retains its optical properties (**Figures 3.1.10**).
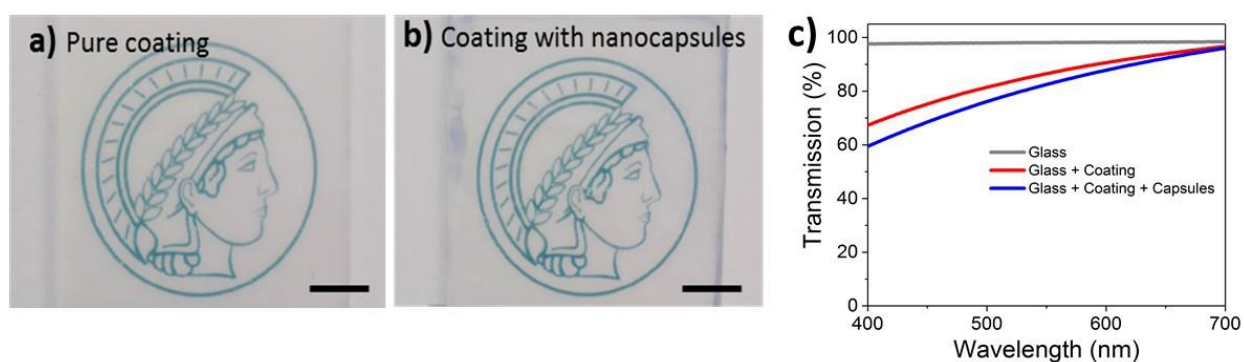
Figure 3.1.10 Optical photographs of translucent coating of water based polymeric coating (a) and the polymeric coating with self-reporting nanocapsules (b) on glass slide, respectively. Scale bars are 5 mm. (c) Optical transmission of glass slide without any coatings (grey line), polymeric coating films without (red line) and with self-reporting nanocapsules (blue line) on glass slides.

Micro-cracks were artificially induced by scratching with a razor blade and were observed by stereomicroscopy and SEM. While the control coating without any nanocapsules showed no color development (**Figure 3.1.11a**); the coating containing nanocapsules highlighted the induced micro-crack *via* a strong blue color appearance (**Figure 3.1.11b**). Hence, the described system autonomously reports the damaging of a coating upon mechanical disintegration. By chemically modifying the release properties of the capsules (*e.g.* redox-responsive release),[213] other types of damages, like redox-disintegration of the coating, could be detected in the future as well.
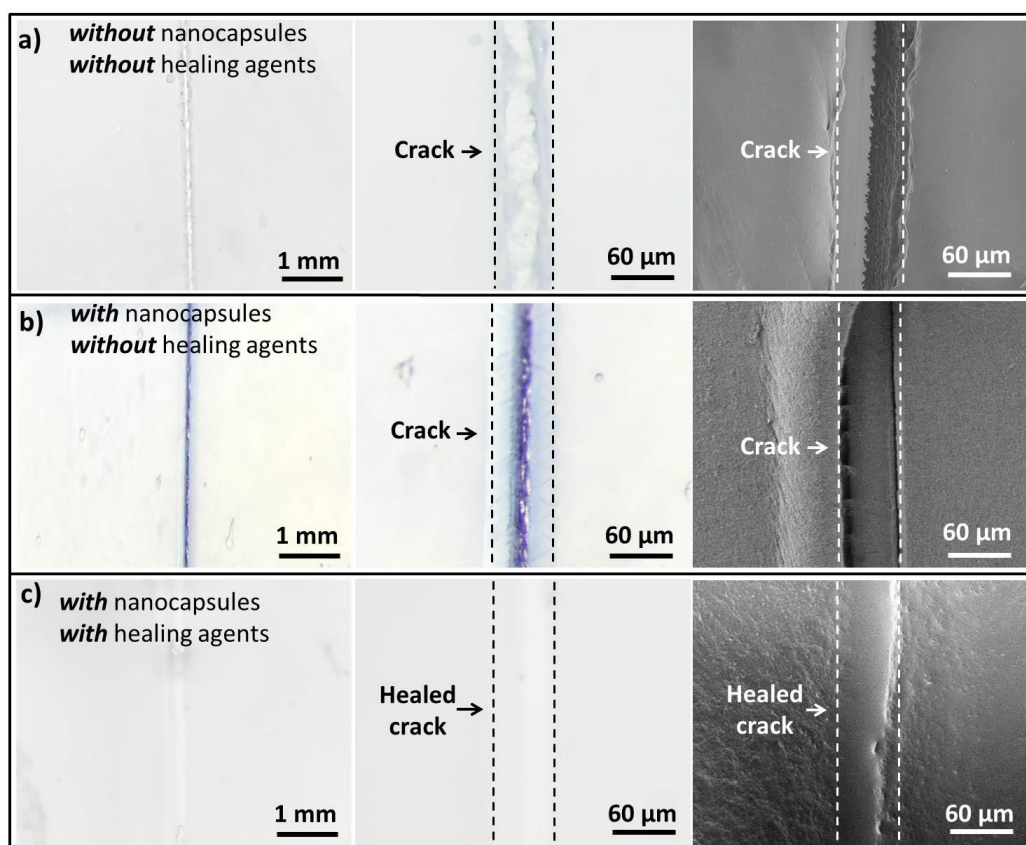
Figure 3.1.11 Autonomous colorimetric indication of cracks appearance and color deletion to report crack healing. Optical photographs (left and middle column) and SEM images (right column) of a micro-crack in a polymeric coating in the (a) absence and (b) presence of damage self-reporting nanocapsules; (c)the colored micro-crack is healed and reversibly becomes colorless when in contact with the self-healing system composed of multivalent alkyne, trivalent azide, and $Cu^{(I)}Br(PPh_3)_3$.

In the next step, the chemical response of the coating system with self-healing compounds was tested to investigate whether only the non-healed damages can be reported. Therefore, the reversibility of the color development process through the reaction with self-healing compounds was demonstrated by analyzing the color deleting properties of CVL^+ in the presence of multivalent alkyne and azide (self-healing monomers) that can form a polymer network suitable for self-healing *via* "click" chemistry at room temperature and achieve a self-healing efficiency of nearly 100% after 48 h.[196] When adding multivalent alkyne, trivalent azide and $Cu^{(I)}Br(PPh_3)_3$ into the strongly blue colored crack, the color slowly vanished in the time frame of two days until it finally completely disappeared. Simultaneously, the crack was being healed (**Figure 3.1.11c**). Hence, the capsule system can be applied to autonomously indicate the "click"-induced healing of the coating when the blue color is reversibly deleted. Besides the "click"-chemistry healing system it was shown, additionally, that other classes of self-healing reactions, including the epoxy-amine[205] and PDMS self-healing[206] systems, can turn off the optical signal and therefore potentially indicate a successful self-healing reaction. In case of the epoxy-amine self-healing system, free amine groups of healing agents delete the color; while in the case of the PDMS self-healing system, the color of CVL^+ is deleted by the ethanol that is produced during the healing reaction.

3.1.4 Conclusions

In this chapter, a reversible damage self-reporting nanocapsular system has been developed and presented, which was subsequently used to monitor crack appearance and healing in coatings. Therefore, a three-component capsule was designed which contains an inactive dye in the liquid core, a protective polymer shell and color developing silica nanoparticles on the surface. Breakage of the shell enables autonomous destruction-reporting *via* an intense blue color development. By

embedding the capsules into coatings, they break upon damaging of the coating and highlight damaged spots. The visually highlighted spots can be erased through interaction of the dye with different self-healing compounds or byproducts of self-healing reactions and subsequent color deletion. Hence, the system can be applied to monitor damage appearance and healing in coatings. It is envisioned that this reversible self-reporting system with high versatility can be applied in a new generation of self-reporting coatings, which has multiple autonomous functions to monitor the whole health-cycle of artificial materials.

3.2 Fabrication of nonequilibrium disentangled polymer in single-chain nanoparticles *via* electrospraying[†]

Chapter 3.1 demonstrate how miniemulsion is an effective and robust method to prepare complex nanostructured hybrid particles. In that case, the system was engineered so the silica nanoparticles used as surfactant would also provide additional functionalities to the polymer nanocapsule. However, in some cases, the presence of surfactant, especially organic molecules, could be a drawback. For example, when casting a film with a latex suspension stabilized with surfactants, the surfactant might act as a plasticizer for the polymer matrix or interfere with the thermal stability of the film. As an alternative to miniemulsion to prepare surfactant-free nanoparticles, electrospraying is an attractive method. Not only electrospraying can be used to make nanoparticles, but the rapid evaporation process during electrospraying also provide a way to trap the polymer chains in out of equilibrium conformation.

In this chapter, electrospraying has been used to fabricate polymer nanoparticles with minimal entanglements of the polymer chains. Entanglement of polymer chains causes industrial problems during polymer processing because of the limited diffusion and movement of the polymer chains. This prevents the use of polymers with very high molecular weight by traditional processing methods for thermoplastic materials such as molding or melt extrusion. The objective, here, was to minimize polymer chain entanglement in linear polystyrene ($M_n = 1.1\times10^6$ g·mol^{-1}) in order to

make it easier processable. The polymer was dissolved at a very dilute concentration, well below the critical concentration of entanglement, and then electrosprayed. The very rapid drying of small droplets of a polymer solution, devoided of entanglements, resulted in the formation of nanoparticles composed one single chain (or very few) without (or with few) entanglements.

3.2.1 Introduction

Polymers have become an essential part of our daily life. In order to use polymers in various applications, it is important not only to synthesize new functional polymers, but also to process synthetic polymers to meet the different requirements of specific applications.[214-216] Processing polymer melts is one of the most appealing industrial processing methods and is used to prepare a variety of everyday thermoplastic product such as packaging and bottles, as well as value added material such as medical implants.[217,218] Polymer melts display a rich viscoelastic behavior in the typical length and time scales relevant to their processing.[219,220] The processing of polymer melts become more difficult with increasing molecular weight due to the increase of viscosity. In a melt of high molecular weight polymers, many long polymer chains have to move in a collective and specific way to flow due to the topological constraints called "entanglements" imposed by neighboring chains.[221, 222] The increase in viscosity observed with increasing molecular weight of the polymer chains is caused by the increasing number of entanglements at high M_n.[223]

In order to facilitate the processing of a polymer with high molecular weight, the most straightforward way would be to minimize the chain entanglements in the melt. It is possible to obtain a less entangled polymer directly during polymerization. By careful synthesis with a single site catalyst, high molecular weight polyethylene with a single chain has been obtained and formed a single crystal.[224] Such polymer crystals can form a heterogeneous melt through slow and careful controlled melting. This heterogeneous melt has a heterogeneous distribution of entanglements

within the melt because of the semi-crystallinity of the polymer, leading to different mechanical and rheological behavior in comparison to an equilibrated melt having a homogeneous distribution of entanglements. The long-lived heterogeneous melt shows less viscosity than the homogeneous entangled melt, which largely improved the processability of this polymer melt. Therefore, being able to easily process a variety of polymers to prepare disentangle polymer formulation would result in an advantageous material for the further processing in the molten state.[225]

Single chain nanoparticles can be prepared using various approaches such as precipitation,[226] freeze-drying[227, 228] and electrospraying.[229] Among these techniques, electrospraying can be scaled-up to produce a large amount of single chain nanoparticles without the use of any additives in one batch. In electrospraying, a polymer solution is pumped out of a capillary nozzle and then an electric field is applied between the nozzle and a target. (**Figure 3.2.1**) The difference of potential is used to accelerate the solution of polymer and leads to the elongation of the solution coming out of the nozzle and the formation of a jet.[230] The charges covering the surface of the jet generate relatively high electrostatic force. Once such force is larger than the surface tension of the material, the jet can further deform and split into unstable micro- or nano-droplets due to the high electrical forces. Once the droplets have detached from the main jet, the solvent in the droplets of polymer solution evaporates and then generate dense and solid particles at micro- or nanometer size that are propelled towards the collector.[231]

In this chapter, nanoparticles containing one single chain were prepared by the electrospraying of a diluted polystyrene solution. The concentration of polystyrene solution was well below the critical concentration of entanglement. After electrospraying, the resulting nanoparticles were collected and the glass transition temperature was determined.
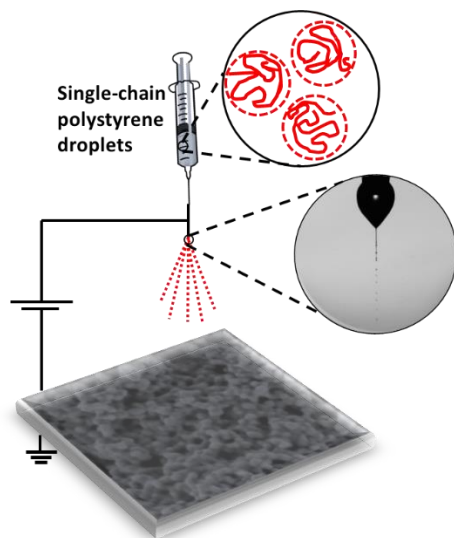
Figure 3.2.1 Schematic picture of fabrication of single chain polystyrene nanoparticles without entanglements by electrospraying process.

3.2.2 Experimental

Electrospraying

Polystyrene ($M_n = 1.1 \times 10^6$ g·mol^{-1}, $M_w = 1.4 \times 10^6$ g·mol^{-1}, PDI $= 1.26$) was dissolved in dimethylformamide or chloroform and mechanically stirred overnight to prepare the polymer solution with different concentrations (from 0.01 wt.% to 10 wt.%). The resulting dispersions were filled into a syringe and then electrosprayed at 20-25% relative humidity and room temperature onto an aluminum foil support. The tip diameter was 0.8 mm. The distance between the collector and tip was fixed to 20 cm. The feeding rate was varied from 0.5 mL·h^{-1} to 2.0 mL·h^{-1}. The applied voltage was varied from 15 kV to 25 kV.

Characterizations

The surface tension of polystyrene solutions was measured with a tensiometer (DCAT 21, DataPhysics, Germany). The hydrodynamic diameter of polymer chains in solutions with different

concentrations was measured at different angles by dynamic light scattering (DLS) using an ALV instrument (ALV, Langen, Germany) with a goniometer and ALV-5001 multiple-tau full-digital correlators with 320 channels. The light source consisted of a helium-neon laser (JDS Uniphase, Milpitas, USA) with 25 mW output power and a laser wavelength of 632.8 nm. The viscosities of the polystyrene solutions were obtained using a Cannon-Fenske viscometer (Cannon, U.S.A.). The morphology of electrosprayed nanoparticles was observed by transmission electron microscopy (TEM; JEOL JEM1400, Japan) and scanning electron microscopy (SEM; Hitachi SU8000, Japan). The samples were collected on 400-mesh copper grids and silicon wafers during electrospraying process for TEM and SEM measurement. The glass transition temperature was measured by differential scanning calorimetry (Perkin-Elmer DSC 8500, USA). The DSC measurements were performed in a nitrogen atmosphere with a heating rate of 10 C min^{-1}, the temperature was first decreased from 20 °C to -140 °C, then the temperature was increased to 200 °C.

3.2.3 Results and discussion

To prepare the polymer solution without entanglement, the concentration was varied from 0.01 wt.% to 10 wt.%. The surface tension of the polymer solutions did not change over the range of concentration, indicating that the polystyrene was well dissolved in both solvents (DMF and chloroform). (**Figure 3.2.2a**) Additionally, the hydrodynamic radius of the polymer chains in the two solvents lightly decreased with the increase of concentration. (**Figure 3.2.2b**)
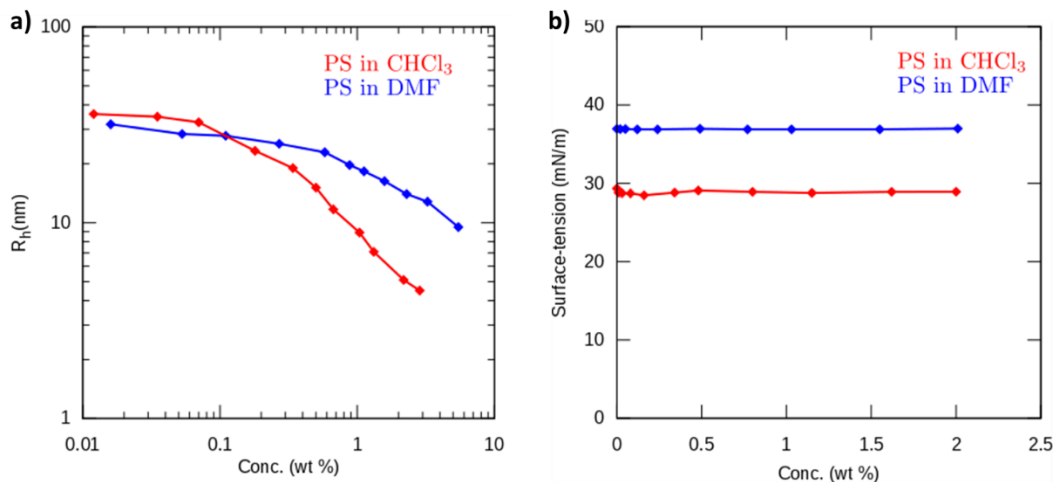
Figure 3.2.2 Characterization of polymer solutions. (a) surface tension and (b) hydrodynamic radius at different concentrations of polystyrene in chloroform (CHCl$_3$) and dimethylformamide (DMF).

In order to know when entanglements are formed in the polystyrene in solution, the viscosity of polymer solutions at different polymer concentrations was measured. **Figure 3.2.3**, shows that over the entire concentration range, the viscosity of the polymer solution increased with increasing concentration. Two different regimes were observed, at low concentration, the viscosity increase moderately with the increase of concentration; however, at higher concentration, the viscosity increased more steeply with increased concentrations. The cross-over between those two regimes occurred at the critical entanglement concentration (C*). Above C*, polymer chains are entangled in solutions.

Figure 3.2.3 shows that in DMF, when the polystyrene concentration was lower than 0.5 wt.%, the increase of viscosity display a relatively small slope because there were no entanglements between polymer chains in solutions in that concentration range. However, when the concentration of polystyrene was increased above 1 wt.% the increase of viscosity was more pronounced due to the presence of entanglements and the increase in the number of entanglement increasing with

increasing concentration and the C* was determined as 0.95 wt.%. In the case of polystyrene

solution in chloroform, the C* was 0.4 wt.%.
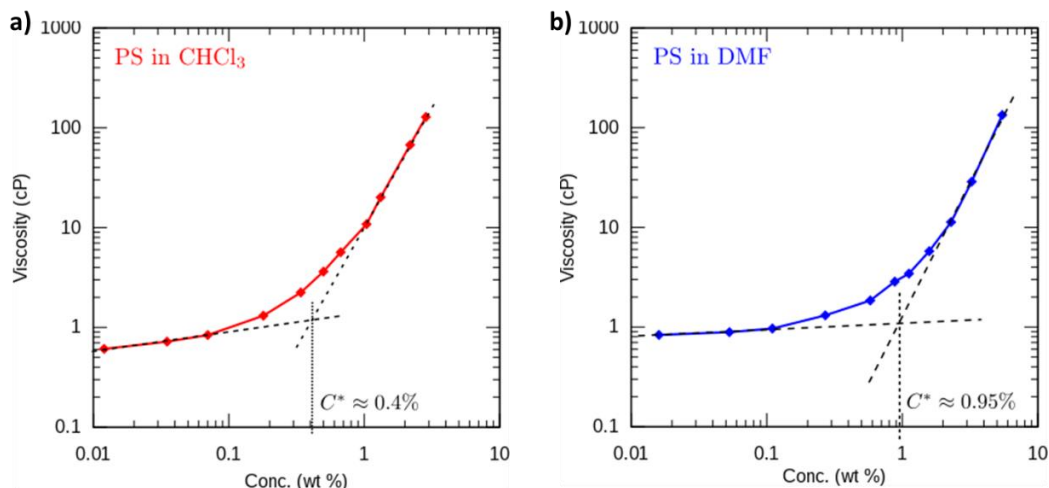
Figure 3.2.3 Viscosity as a function of polymer concentrations. (a) polystyrene solution in DMF. (b) polystyrene solutions in chloroform.

In the electrospraying process, the droplets form only when the surface charge of polymer solution

overcomes the surface tension force, leading to fission of the droplet. The charge and size of the

droplet can be easily controlled to some extent by adjusting the flow rate and voltage applied to

the nozzle. During electrospraying, it is important to control the applied voltage and the flow rate

of the suspension. Those are critical factors to the formation of a stable jet to produce homogeneous

and reproducible nanoparticles.[44] The difference of potential between the nozzle and the collector

is used to accelerate the solution of polymer and leads to the elongation of the solution coming out

of the nozzle and the formation of a jet.[45] Thus, jet formation during electrospraying with various

voltage and flow rate were observed by microscopy. With the polystyrene solution in DMF, a low

voltage of 12.5 kV was insufficient to create the enough potential and form a jet near the nozzle.

The droplet was only elongating by the electrical current when it left the nozzle, resulting in a

discontinuous flow. At 15 kV, formation of a stable jet was observed and the jet was breaking in droplets downstream. At higher voltages, the number of charges at the surface of the solvent was so large that multiple points of instability were observed. (**Figure 3.2.4a**) Similar to the variation of flow rate, the stable jet can be obtained only when the flow rate was 1.5 mL·h^{-1}. Although different flow rates can form the multiple-jet, they would cause the inhomogeneous distribution of droplets and final nanoparticles on the substrate. Additionally, instabilities were observed when the flow rate of the solution was decreased or increased. (**Figure 3.2.4b**) Therefore, the optimal applied voltage and flow rate for forming a stable jet is 15 kV and 1.5 mL·h^{-1}, respectively.
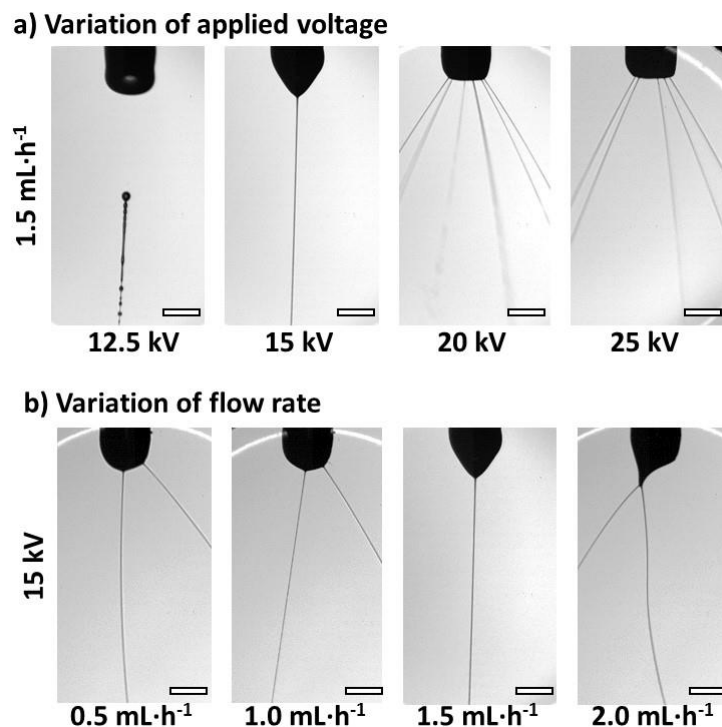
Figure 3.2.4 Variation of (a) applied voltage and (b) flow rate during the electroparying process. Snapshot images of electrospraying process (polystyrene in DMF) obtained by high-speed video. Videos were taken at the beginning of jet. Scale bar = 500 µm.

Electrospraying of polymer solutions below *C**, near *C**, and above *C** was carried out. The choice of solvent and the polymer concentration in solution were both critical in obtaining different morphologies (**Figure 3.2.5**). In both DMF and chloroform, nanofibers (diameter of fibers above 100 nm) were obtained at the concentration above *C** (2.3 wt.% and 1 wt.%, respectively). At intermediated concentration near *C**, a mixture of particles and nanofibers were obtained. At concentration well below C*, large microcapsules were observed when using chloroform as the solvent. However, small nanoparticles were obtained for the electrospray-drying of DMF solutions.
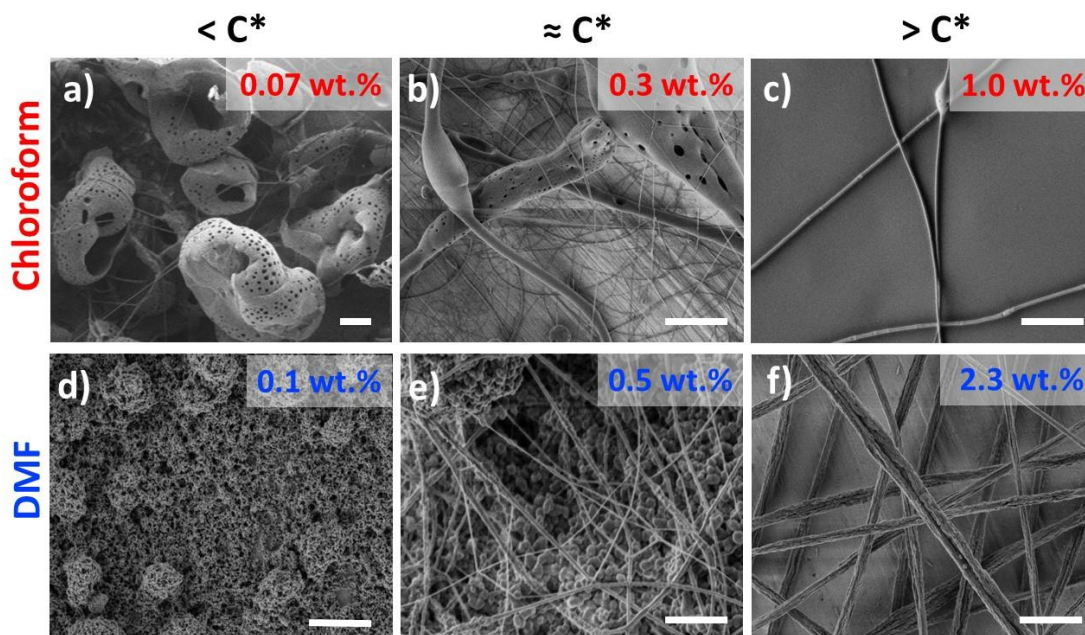
Figure 3.2.5 SEM image of the electrospayed polystyrene microcapsules and micro/submicro-fibers for solution of 0.07 wt.% (a), 0.3 wt.% (b), and 1.0 wt.% (c) in chloroform. Electrospayed polystyrene nanoparticles and nanofibers for solution 0.1 wt.% (d), 0.5 wt.% (e), and 2.3 wt.% (f) in DMF. Scale bar = 1 µm.

The differences of the obtained structures could be attributed to a combination of the state of the polymer in solution and the physical properties of the solution. Above *C**, because of the

entanglements present between the polymer chains, and the viscosity of the polymer solution, continuous jets are formed leading to the electrospinning of long polymer fibers. At concentration below C^*, the viscosity of the polymer solution decreased, consequently, the same shear force created by the difference of potential can lead to a larger deformation. At some point, the steady jet of polymer solution will break to form droplets. However, at intermediate concentration, close to C^*, the system was in a transition state and a mixture of structures was observed by microscopy.
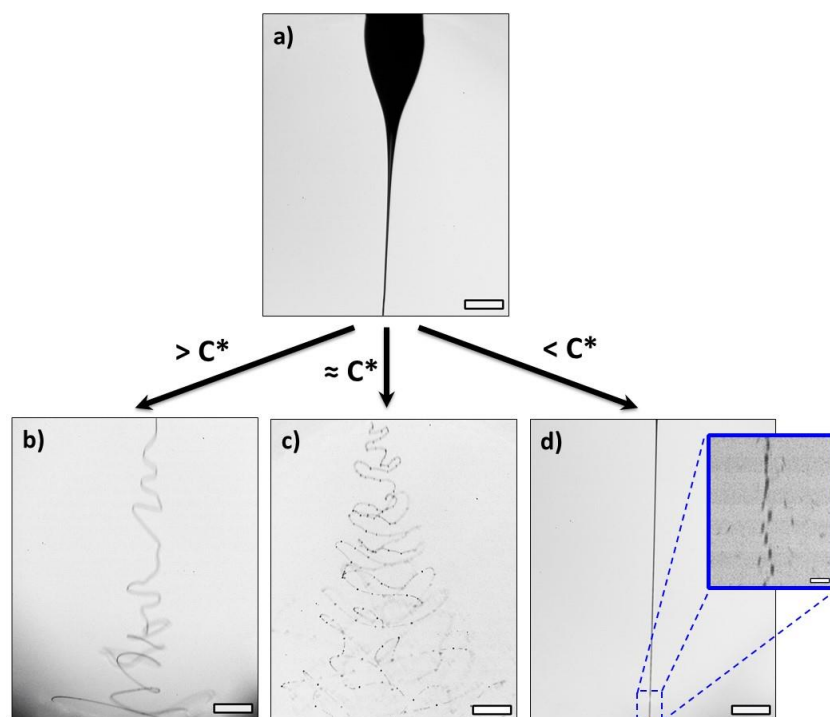
Figure 3.2.6 Snapshot images of electrospraying process (polystyrene in DMF) obtained by high-speed video. Videos were taken (a) at the beginning of jet and at the 3 mm away from the jet with (b) 2%, (c) 0.5%, and (d) 0.1% of polystyrene solution. Scale bar $= 500 \, \mu m$. The scale bar of insect is $100 \, \mu m$.

To study the behavior of the jet of polymer solution during the electro-spinning/spraying process, a high-speed camera was used to monitor the polymer solution in flight (**Figure 3.2.6**). The transition between the electrospinning regime at high concentration to the electrospraying regime

at low concentration could be clearly observed. At high concentrations, one single jet whipping back and forth was observed, in agreement with the formation of long fibers (**Figure 3.2.6b**). In the intermediate regime, the formation of a broken beaded jet was observed (**Figure 3.2.6c**). At low polymer concentration, electrospraying was observed (**Figure 3.2.6d**). Within the first few millimeters from the tip of the needle, the jet quickly broke down in smaller droplets. The size of the droplets formed during the electrospraying of the chloroform solution (ca. 20 - 50 µm) can explain the size of the polymer capsules obtained (ca. 5 - 25 µm). The same was not true for the electrospraying of polystyrene solution in DMF (**Figure 3.2.7**).
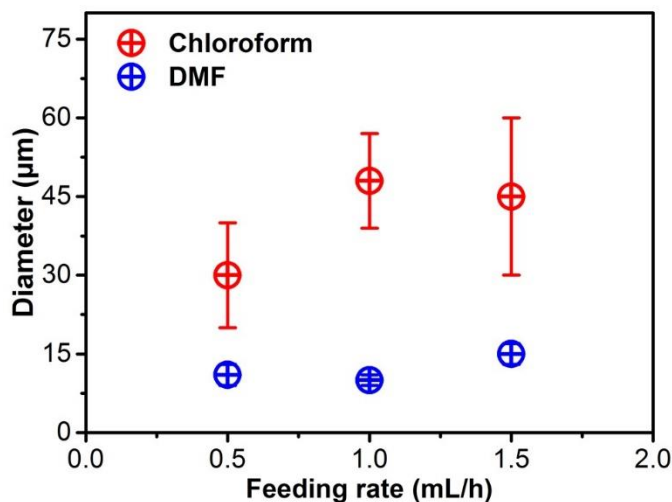
Figure 3.2.7 Average diameter of in-flight droplets with different feeding rates during the electrospraying by using chloroform and DMF as solvents at 15 kV.

The electrospraying of dilute solutions of polystyrene in DMF lead to the formation of droplets of ca. 10-15 µm, but interestingly, particles of ca. 20 nm were collected at the end of the drying process. A droplet of a 0.1 wt% solution of polystyrene in DMF with an initial diameter of 10 µm would contain ca. 0.5 picograms of polymer. By assuming that the density of disentangled polystyrene to be 1.04 g·cm^{-3}, after the complete drying of this droplet, this amount of polystyrene

should be contained in a spherical particle of a diameter of ca. 0.9 µm. This is much larger than the size of the nanoparticles obtained (ca. 20 nm). However, the droplets of DMF could undergo a secondary splitting in-flight, and this phenomenon likely occurred too late in-flight for being observable with the current experimental setup.

In electrospraying, droplets can undergo secondary splaying or splitting.[232] Such splaying effect might cause the initial microdroplets to split into nanometer size droplets in-flight. The parent droplet can split due to Coulombic fission when the electrostatic repulsion surpasses the surface tension.[233] Coulombic fission occurs during the transport of the droplets before the collection because the evaporation of the solvent from the droplets leads to an increase in the concentration of charges on the surface.[234] The effect of this increase in the number of charge per units of surface area depends on the conductivity and dielectric constant of the solvent. The relative dielectric constant of chloroform and DMF are respectively 4.8 and 36.7. Consequently, the increase concentration of charges on the surface of a DMF droplet would lead to a more important destabilization of the droplet surface than in chloroform. The 20 nm nanoparticles obtained during the electrospraying of the DMF polymer solution could be attributed to the in-fight secondary splaying of the droplets caused by Coulombic fission. This is consistent with the use of DMF in electrospraying and electrospinning to increase the conductivity and dielectric strength of polymer solution to produce thinner fiber and smaller particles.[235]

The morphology of the resulting nanoparticles was analyzed by TEM and AFM, the size of the nanoparticles formed by the electrospraying of a 0.1 wt.% solution of polystyrene ($M_n = 1.1 \times 10^6$ Da) in DMF was 20 ± 5 nm (**Figure 3.2.8a**-**b**). This result was compatible with theoretical calculation predicting that a disentangled polystyrene chain of this molecular weight

should occupy a volume with a radius of 19 nm. Therefore, the nanoparticles obtained by electrospraying should be particles composed of one chain without or with few entanglements.
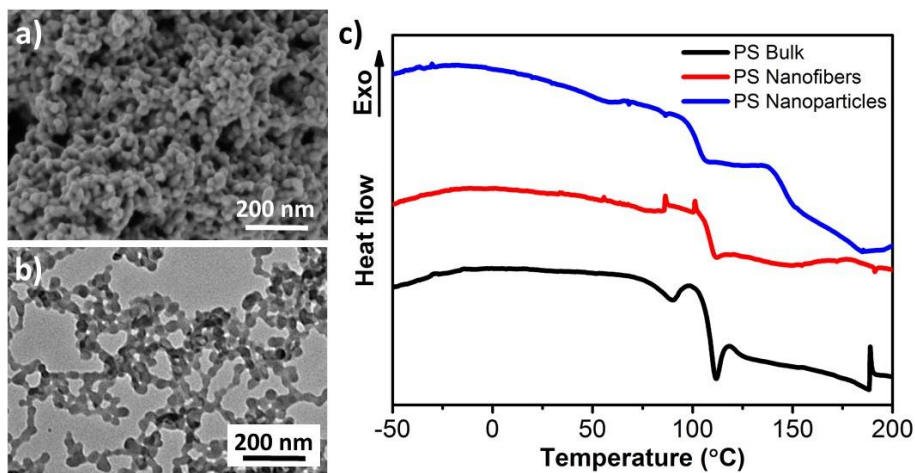
Figure 3.2.8 SEM (a) and TEM (b) image of obtained polystyrene nanoparticles from 0.1 wt.% polymer solution in DMF. (c) Thermogravimetric analysis curves of polystyrene bulk, nanoparticles and nanofibers.

Further evidence of the disentanglement of the polymer chains in the polystyrene nanoparticles was obtained by calorimetry (**Figure 3.2.8c**). The glass transition temperature (T_g) of the nanofibers and nanoparticles was determined by differential scanning calorimetry. **Figure 3.2.8c** shows the thermal behavior of bulk polystyrene, polystyrene nanofibers, and polystyrene nanoparticles. The T_g of polystyrene in bulk was 107 °C and it was similar to the polystyrene nanofibers (109 °C). However, the T_g of electrosprayed nanoparticles was 98 °C, indicating that the mobility of polymer chains increases in keeping with the formation of disentangled polymer chains. However, further evidence of the disentanglement of the polymer chain(s) in the nanoparticles need to be obtained. Rheology experiments will be performed at a temperature above T_g to study the reentanglement of the polymer melt. This type of experiments will demonstrate

how the processing of the polystyrene could be improved by formulation disentangle single chains nanoparticles.

3.2.4 Conclusion

In summary, linear polystyrene with high molecular weight (M_n = 1.1×10^6 g·mol^{-1}) has been used to produce nanoparticles by electrospraying. The diameter of the nanoparticles obtained was 20 nm, which was similar to the size of a disentangle single-chain nanoparticles obtained from theoretical calculation. The nanoparticles had a relatively low glass transition temperature; in comparison to bulk polystyrene, the glass transition temperature of polystyrene nanoparticles decreased from 107 to 98 °C. The decrease in T_g indicates an enhancement of the mobility of polymer chains caused by the disentanglement. Therefore, these nanoparticles maybe use to produce the polymer melt without or with less entanglement, which will be highly useful for the processing of polymer in the industry.

3.3 Fibrous nanozyme dressings with catalase-like activity for H_2O_2 reduction to promote wound healing[†]

Chapter 3.2 showed how electrospraying can be used to produce polymer nanoparticles. Furthermore, when the concentration of polymer in the solution used to prepared nanoparticles was higher than the critical entanglement concentration, fibers were obtained. Hence, electrospraying can be adapted to prepare nanofiber. This technique, called electrospinning, can be used to prepare complex hybrid material. In this chapter, the electrospinning technique has been used to assemble hematite (α-Fe_2O_3) nanoparticles within the polymer fibers. The hematite nanoparticles show catalase-like activity by reducing H_2O_2 and producing O_2. Such catalase-like function is helpful for improving the wound healing process, which requires decreasing the amount of H_2O_2 and sufficient O_2. Therefore, hematite nanozyme particles were integrated into electrospun and cross-linked poly(vinyl alcohol) membranes. Within the dual-compound membrane, the polymeric mesh provides a porous scaffold with high water permeability and the nanozymes acts as a catalyst to efficiently convert H_2O_2 into O_2. The proliferation of fibroblasts at a H_2O_2 concentration of 50 µM showed large differences when comparing the growth with and without application of the nanozyme dressing. Thus, application of the nanozyme dressing can significantly reduce the harmful effect of higher H_2O_2 concentrations. The described catalytic membranes could be used in the future to provide an improved environment for cell proliferation

in wounds and thus applied as advanced wound healing dressings.

3.3.1 Introduction

Wound dressings can accelerate and improve the wound healing process.[236] They provide an environment that allows oxygen permeation, maintains moisture for materials diffusion, prevents infection, and promotes tissue formation.[237] Two important key metabolites involved in the healing process are the redox-pair hydrogen peroxide (H_2O_2) and oxygen (O_2). While a high concentration of H_2O_2 causes a delayed healing *via* preventing the connective tissue formation,[238] O_2 can help to improve the healing efficiency.[239] Therefore, the wound healing process can be promoted by down-regulating H_2O_2 levels and increasing O_2 levels.[240] A contemptuous adjustment of H_2O_2 and O_2 concentrations can be achieved by catalytic conversion of H_2O_2 into H_2O and O_2 through enzymatic catalysis with catalase, a naturally occurring enzyme.

The production of catalase can be achieved by direct synthesis or extraction from natural systems.[241] Such a production process is however accompanied by high production costs and the natural enzyme is highly sensitive to changes in environmental conditions and possesses a short biological half-life.[242] Hence, recent research has focused on the replacement of natural enzymes by synthesizing artificial compounds, so-called enzyme mimics, which can imitate the catalytic behavior of natural enzymes.[243,244] To the present day various enzyme-mimics have been reported such as metal complexes,[245,246] supramolecular chemistry[247] and inorganic nanoparticles (NPs).[248,249] The use of inorganic NPs as enzyme mimics comprises the advantages of cost efficiency and much higher stability than their natural counterparts while possessing comparable sizes.[241,242,250] In addition, the so-called nanozymes exhibit a high number of catalytically active

surface atoms, enabling high activities. It is thus not surprising that they can react more efficient than natural enzymes, which commonly feature only one active center.[241,251,252]

Recently, different classes of nanozymes have been reported to reduce the concentration of H_2O_2.[253] Among them, hematite NPs show a catalase-like activity and have been used to convert H_2O_2 to H_2O.[253,255] Hematite (α-Fe_2O_3) is a weakly magnetic and highly stable iron (III) oxide, which is stable with respect to corrosion, non-toxic, and many simple low-cost synthetic procedures have been described. Template-assisted synthesis[256], forced hydrolysis[257], sol-gel methods[258] and hydrothermal routes[259] in aqueous solution even without organic surfactants and in large quantities are viable routes. This makes hematite an excellent material for applications in wound treatment to mimic catalase and reduce H_2O_2 concentrations.

Integration of iron oxide nanoparticles in nanofibrous membranes can be achieved by either directly assembling the magnetic particles under an external magnetic field[260,261] or electrospinning the particles together with a templating polymer.[262-264] Electrospinning[265-267] or pressurized gyration process[268] can be used to fabricate nanofiber mats for wound dressings. Recently, portable electrospinning devices[269,270] have been used for in situ producing wound dressing materials. The high surface-to-volume ratio and porosity of the electrospun membranes exhibit a promising water absorption ability to meet the requirement of strong oxygen permeation.[271] Additionally, the high surface area membranes are ideal as heterogeneous catalysts. [272,273] However, a catalytically active membrane that can regulate H_2O_2 and O_2 levels to improve the wound environment could not be achieved to date.

In this chapter, an electrospun hybrid nanofibrous material as dressing for wound healing, with a high porosity, wettability and the ability to simultaneously decrease the H_2O_2 and increase the O_2 concentration has been presented. As shown in **Figure 3.3.1**, a polyvinyl alcohol (PVA) solution

and a suspension of hematite nanoparticles were mixed to electrospin the nanozyme containing nanofibers. PVA fibers was used as the scaffold material and the hematite nanoparticles were implemented as the catalytic moieties. After electrospinning and crosslinking, the water-permeable PVA gel possesses a high porosity and good wettability. The encapsulated hematite shows catalase-like activity by reducing the amount of H_2O_2 and producing O_2. When incubating fibroblasts at critically high H_2O_2 concentrations, the catalytically active membrane efficiently reduces the H_2O_2 concentration and enables good cell proliferation. Thanks to this catalase-like activity, the hybrid nanofibrous gel can be used for improving the wound healing process.
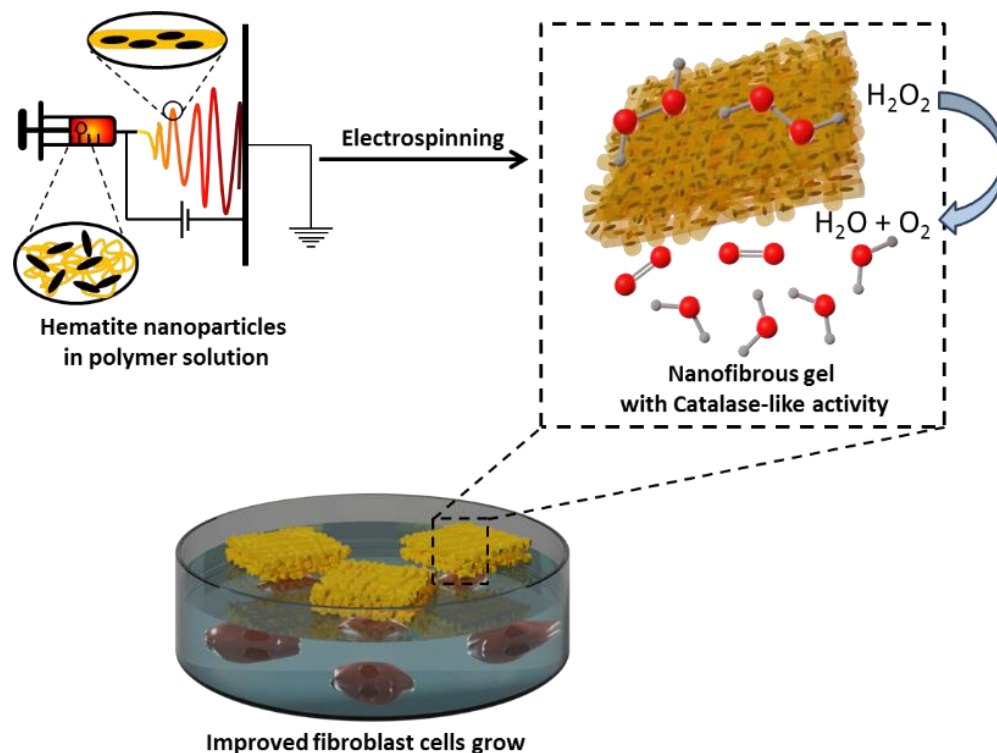
Figure 3.3.1 Schematic illustration of the fabrication procedure of hematite nanofibrous gels *via* electrospinning and their use as catalase mimics to convert hydrogen peroxide into water and oxygen to yield an improved fibroblast growth.

3.3.2 Experimental

Chemicals

$FeCl_3 \cdot 6H_2O$ and tetrahydrofuran (THF) were purchased from Acros Organics (Fisher Scientific), KH_2PO_4 was purchased from Sigma Aldrich (Germany). Polyvinyl alcohol (PVA, Polysciences Inc., $M_w = 125000$ g·mol^{-1}), glutaraldehyde (GA, Merck KGaA, 50% aqueous solution), and hydrochloric acid (HCl, Sigma-Aldrich, 37 wt.%, AR grade) were used for electrospinning and crosslinking.

Nanoparticle synthesis

20 mmol $FeCl_3$ and 0.4 mmol KH_2PO_4 were added to 1 L of water (MilliQ) to form a clear yellowish solution that was magnetically stirred and heated under reflux for 72 h. The resulting brown, turbid dispersion was then filtered through a 3.1 µm syringe filter (CME, Roth Germany). Portions of 20 mL were precipitated using THF (volume ratio 1:2) and collected by centrifugation. The brown powder was dried at 70 °C in air. Solutions for electrospinning experiments of 5 wt.%, 15 wt.% and 25 wt.% were prepared by dispersing hematite nanopowder in water (MilliQ) by sonicated for 20 min.

Electrospinning and cross-linking

The different concentrations of hematite nanoparticle dispersions (5 wt.%, 15 wt.% and 25 wt.%) were combined with the 15 wt.% PVA solution at a ratio of 1:2 for a total polymer concentration of 10 wt.% and mixed by mechanical stirring through vortex until a homogenous dispersion was obtained. The resulting dispersion was filled into a 1 mL syringe and electrospun at 20-25% relative humidity and room temperature onto an aluminum foil support (20 cm distance, 0.3 mL · h^{-1} feed rate, 0.8 mm tip diameter, +18 and 0 kV). During the electrospinning, a TEM

grid was used to collect samples for TEM measurement. Afterward, the electrospun mats were reacted with 1 mL of 50 wt.% glutaraldehyde (GA) and 20 µL of 37 wt.% HCl in a vacuum oven. The acetal bridges can be formed between aldehyde groups of GA and the hydroxyl groups of PVA. HCl was the catalyst for this crosslinking reaction. Afterward, the crosslinked nanofibrous mats were put in the fume hood for 24 h to evaporate the unreacted GA and HCl.

Wettability and water stability of cross-linked electrospun mats

The wettability of the PVA mats was measured on a static contact angle measuring system equipped with a side camera (IDS uEye camera) and a goniometer. To test the water stability of the PVA mats, the mats were immersed in water for 1 h and transferred into the fume hood to evaporate excess water overnight. The morphology of the PVA mats before and after water immersion was observed by scanning electron microscopy (SEM; Hitachi SU8000, Japan).

Tests for catalytic activity

To measure catalytic activities europium(III) chloride hexahydrate and 3-(N-morpholino)propanesulfonic acid (MOPS) sodium salt (98%) from Alfa Aesar, tetracycline hydrochloride, catalase enzyme (3000-5000 $U \cdot mg^{-1}$) and hydrogen peroxide (H_2O_2) from Sigma-Aldrich were used. All chemicals were used without further purification and reactions were conducted with MilliQ water. The catalase-like activity of the tested materials was investigated similarly to the fluorescence assay reported by Wu et al.[274] The procedure is briefly described as followed: in a first step, the PVA fibers were washed several times with MilliQ water to remove free NPs that were possibly not completely cocooned in the polymer matrix. The fibers were added into the wells of a 96 well plate, which was placed in a temperature controlled (25 °C) 96 well plate reader. In free wells, the fluorescently active EuTc-HP complex was generated by mixing 65 µL EuTc solution, 20 µL H_2O_2 solution (5 $mmol \cdot L^{-1}$) and 165 µL MOPS buffer solution

(10 mmol$\cdot$L^{-1}) The detailed step is described as followed:

A) MOPS buffer solution (10 mmol$\cdot$L^{-1}): The appropriate amount of MOPS sodium salt was dissolved in 800 mL of MilliQ water and the pH was set to 6.9. The volumetric flask was filled up to 1 L with MilliQ water and the solution was homogenized.

B) EuCl$_3$ solution (6.3 mmol$\cdot$L^{-1} of Eu^{3+}): 115.3 mg of EuCl$_3\cdot$6 H$_2$O were dissolved in 50 mL of A)

C) Tetracycline hydrochloride solution (2.1 mmol$\cdot$L^{-1}): 50.5 mg of tetracycline hydrochloride were dissolved in 50 mL of A)

D) EuTc solution: 5 mL of solution B) and 5 mL C) were mixed and filled up to 50 mL with A).

The fibers were placed in a 96 well plate, and the assay was conducted following the procedure described below. In addition, control measurements were done with native catalase. In this case, A solution of native catalase (0.1 mg$\cdot$mL^{-1}) was used. The mixture was incubated at 25 °C for 10 min. To start the reaction, the EuTc-HP solution was added to the fiber containing wells. The reaction process was observed for 10 min based on the decrease of fluorescence intensity. Control measurements were conducted by varying the concentration of native urease

Cell-viability experiments

50 mg of PVA membranes without hematite nanoparticles and PVA membranes with high loading of hematite nanoparticles were incubated separately with H$_2$O$_2$ at 50 µM for 10 min in the shaking bed. Then the membranes and H$_2$O$_2$ solutions were mixed with the fibroblast cell line NIH-3T3 for overnight incubation. After 16 h incubation, the cells were washed with a phosphate-buffered saline solution and detached from the culture vessel with 2.5% trypsin (Gibco, Germany). Before measuring on the CyFlow ML cytometer (Partec, Germany), the cells were stained with 650 µL of propidium iodide solution (diluted in phosphate-buffered saline solution to a final concentration of 2.0 µg$\cdot$mL^{-1}) to assess the cell viability. To compare the significant difference between different

samples, an unpaired student´s t-test assuming equal variances was performed. Calculated p values were considered to be significant for *$p < 0.05$, **$p < 0.01$, ***$p < 0.001$.

Characterizations

Plate reader. Plate reader measurements were conducted using an Infinite 200 Pro Plate reader from TECAN. Additionally, flat bottom 96 well plates black from Greiner bio-one were used for the catalase assay. The excitation filter was set to 405 nm and the emission filter to 620 nm.

Electron microscopy (EM). The morphology of the PVA meshes was observed by transmission electron microscopy (TEM; JEOL JEM1400, Japan) and scanning electron microscopy (SEM; Hitachi SU8000, Japan). The PVA meshes were electrospun on a 400-mesh copper grid and silicon wafer for the TEM and SEM measurement, respectively.

TEM images of the pure NP were taken with a Tecnai G2 Spirit from FEI (Hilsboro, USA) with LaB6 cathode crystal, twin objective and a US 1000 CCD camera from Gatan (Pleasanton, USA). For sample preparation, the particles were dispersed in water or ethanol and one drop of the dispersion was dried on a carbon coated copper grids.

The size of nanofibers was obtained by analyzing SEM images of electrospun samples with IMAGE J software. Each sample was measured 100 times to calculate the average number and standard deviation.

Fourier-transform infrared spectroscopy (FTIR). The functional groups of crosslinked PVA meshes were measured by Fourier-transform infrared spectroscopy (FTIR) in the 400 - 4000 cm^{-1} range. 20 mg of the individual samples were mixed with KBr powder to make a pellet.

Powder X-ray diffraction (XRD). The crystal structure and the crystallinity were analyzed on a D8 Advance diffractometer equipped with a Sol-X energy dispersive detector using molybdenum Kα-radiation ($\lambda = 0.72$ Å). The nanoparticle powder was dispersed on a scotch[TM] tape (which causes a broad reflection at low Bragg angles).

Thermogravimetry (TGA). Thermogravimetric measurements of the nanoparticles were performed on a Pyris TGA 6 with nitrogen atmosphere in a corundum crucible at a heating rate of 5 °C·min^{-1} for functionalized particles from 50 to 700 °C after 20 min at 50 °C. At 700 °C the temperature was held for 1 min.

3.3.3 Results and discussion

Spindle-shaped nanoparticles were prepared by forced hydrolysis of ferric chloride in water.[257] The solution was refluxed for three days in the presence of catalytic amounts of KH_2PO_4. The resulting particles were not coated with a surfactant layer, and are self-stabilized in water, allowing a direct and unhindered accessibility for substrate molecules to the catalytically active particle surface. High solid contents of the particles in aqueous PVA solution were achieved by centrifugation.

Analysis of the shape and morphology of the iron oxide nanoparticles was performed by transmission electron microscopy (TEM, **Figure 3.3.2**). The nanoparticles have an anisotropic shape (**Figure 3.3.2a-b**), and their aspect ratio was determined from the TEM images to be approximately 5:1 (**Figure 3.3.2c**). The particles are highly crystalline as seen from the electron diffraction pattern (**Figure 3.3.2d**). Powder XRD analysis revealed the phase of the particles to be pure α-Fe_2O_3 (hematite).
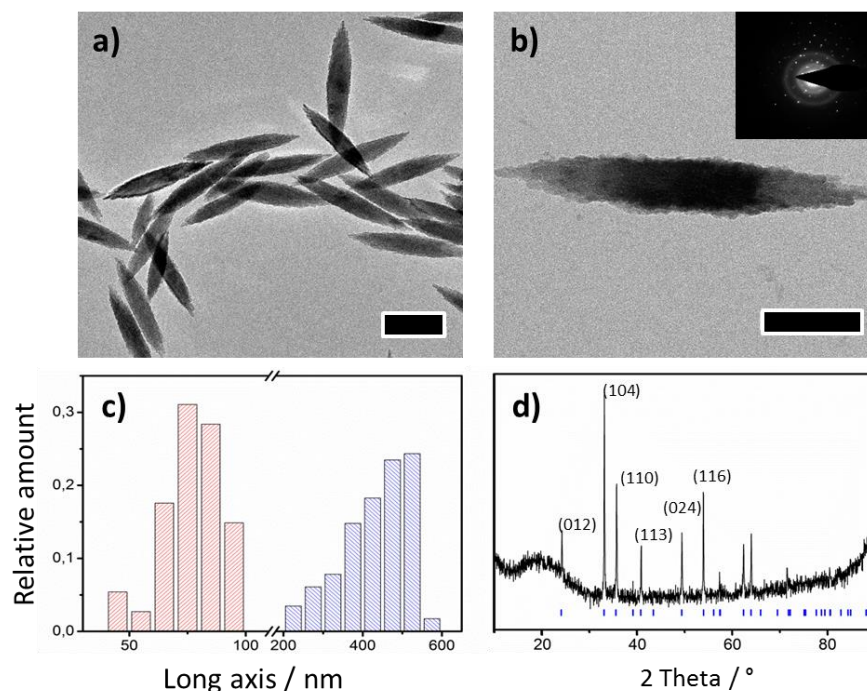
Figure 3.3.2. TEM pictures of α -Fe$_2$O$_3$ spindle-shaped particles (scale bar is 200 nm and 100 nm in a) and b) respectively. Size distribution of long and short axis of the particles as determined from TEM images (c). All reflections of the powder XRD pattern can be assigned to hematite (d).

To integrate the hematite nanoparticles in non-woven fabric mats, they were electrospun together with poly(vinyl alcohol) (PVA). Simple mixing of a PVA solution and a hematite suspension and subsequent electrospinning allowed a homogeneous integration of different amounts of hematite in the resulting fibers (**Figure 3.3.3a-d**). The hematite nanoparticles were oriented in the fiber axis-direction after the electrospinning process. Without loading the nanoparticles, the size of the fiber is 299 ± 34 nm. When the loading amount of the hematite nanoparticles increased, the viscosity of the electrospun solution increased. It resulted in producing thicker fiber (the average size of nanofibers is 305 ± 33 nm, 351 ± 41 nm, and 412 ± 64 nm, respectively). After washing away loosely bound nanoparticles and cross-linking, the concentrations of the PVA mats were determined by TGA (**Figure 3.3.3e**). With increasing amounts of hematite nanoparticles, the color

of the electrospun mats turns from light to darker brown (inset photos in **Figure 3.3.3**). To determine the particle loading inside the cross-linked PVA fibers, the mass loss in TGA heating curves up to 700 °C was used from each sample and normalized between 0 and 100% for pure PVA and pure nanoparticles, respectively. All samples showed similar behavior when they heated under nitrogen. A small weight loss below 250 °C could be observed, which corresponds to the evaporation of water. The major mass loss for all samples was observed between 250 °C and 450 °C, which can be correlated to the decomposition and evaporation of most of the PVA. After that, the mass is still constantly decreasing which may be explained by remnants of the decomposition products that evaporate.
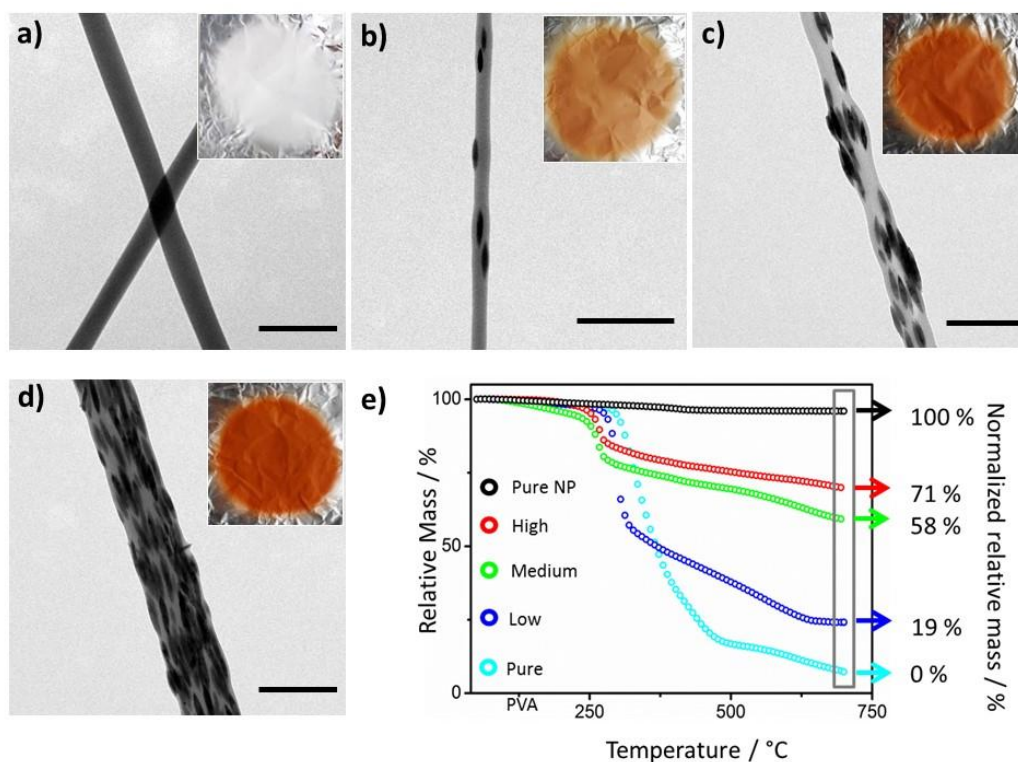
Figure 3.3.3. Characterization of hematite/PVA nanofibrous mats. TEM images of the PVA nanofibers loaded with 0% (a), 19% (b), 58% (c), 71% (d) of hematite nanoparticles (scale bar = 1 µm) and the corresponding photographs of the PVA mats (insets). TGA (e) curves of the nanoparticles and the crosslinked PVA mats with different nanoparticle loading.

In order to apply the PVA mats as wound dressings, they were covalently cross-linked after electrospinning to retain the structural integrity of the fibers in an aqueous environment. To demonstrate the stability of the cross-linked fibers towards water treatment, scanning electron microscopy (SEM) images of the cross-linked fibers before (**Figure 3.3.4a**) and after (**Figure 3.3.4b**) water immersion were analyzed. The SEM images showed no change of the fibrous structure after washing, indicating that the PVA scaffold was maintained. The fiber mesh showed a high porosity, which is ideal for wound dressing materials.
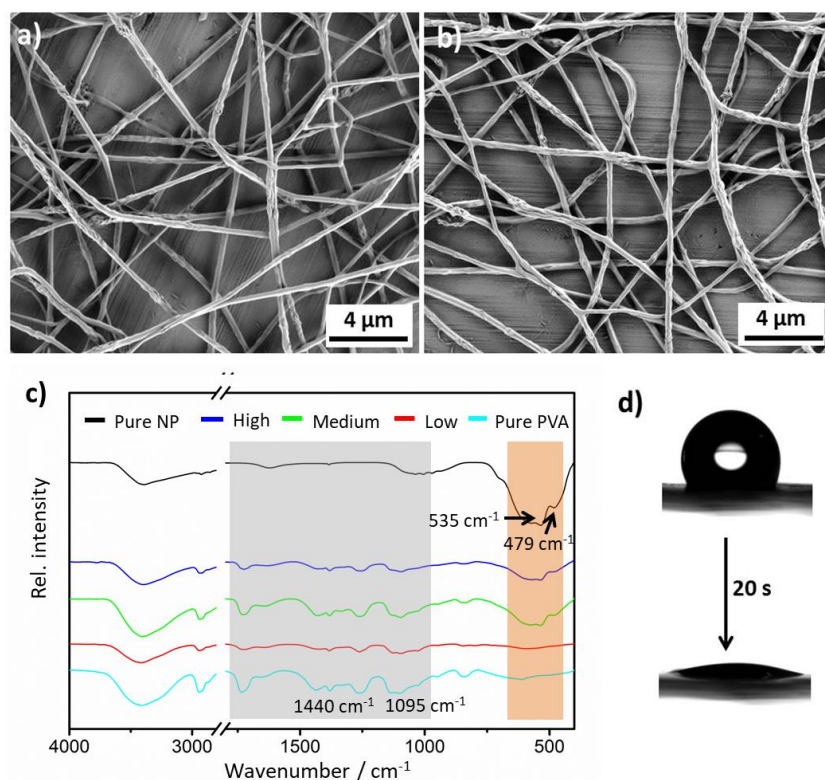
Figure 3.3.4 Characterization of cross-linked hematite/PVA nanofibrous mats. SEM images of the PVA mat containing 71% of hematite nanoparticles before (a) and after (b) water immersion. FTIR spectra of cross-linked PVA mats containing different amounts of hematite nanoparticles (c). Dynamic wettability of the PVA mat containing 71% of hematite nanoparticles (d).

The permanent entrapment of the hematite particles within the fibers after washing was investigated by FTIR spectroscopy (**Figure 3.3.4c**). Therefore, pure hematite nanoparticles, pure PVA fibers and hybrids of both with varying ratios were investigated. The appearance of the characteristic bands for hematite at 479 cm^{-1} and 535 cm^{-1} corresponding to the Fe-O vibration[275] in all hematite/PVA fiber samples confirmed the permanent embedment of the particles inside the PVA fibers. The PVA component of the fibers is represented by bands at 1095 cm^{-1} (C-O-C vibrations of aldehyde crosslinked PVA) as well as at 1437 cm^{-1} (C-H bending vibration)[276]. Furthermore, the wettability of the cross-linked PVA mats was tested by adding a water droplet on the membrane surfaces. Due to the good wettability of the PVA membrane, the water droplet could spread completely on the PVA mat within 20 s (**Figure 3.3.4d** and **Figure 3.3.5**).
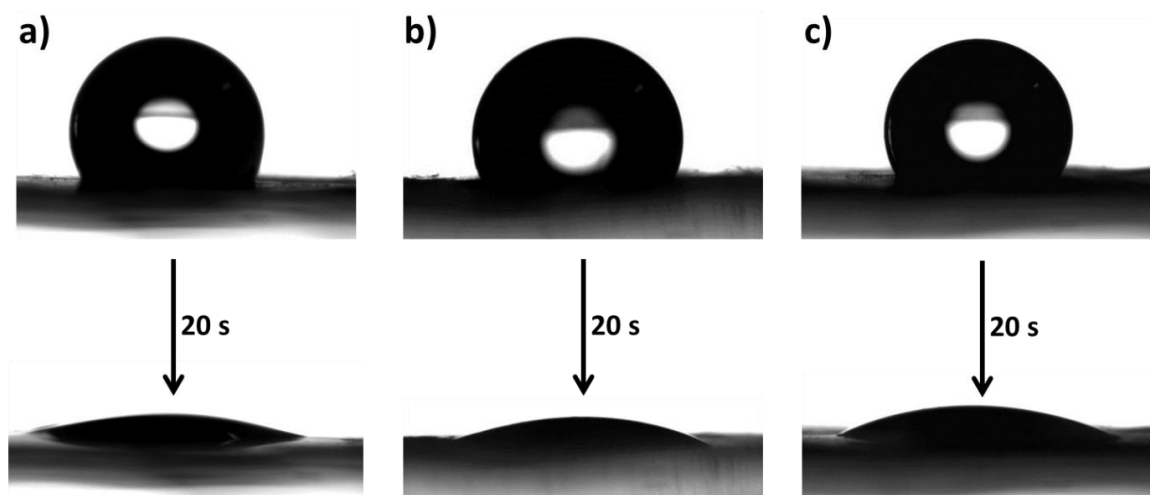
Figure 3.3.5 Dynamic wettability of the crosslinked PVA mat containing 0% (a), 19% (b), and 58% (c) of hematite nanoparticles.

The enzyme-like activity of hematite PVA fiber meshes was investigated with a europium tetracycline (EuTc) based fluorescence catalase assay.[274] While EuTc alone is not fluorescent, H_2O_2 binding to the metal center leads to a strong increase of the fluorescence intensity (**Figure**

3.3.6a). The fluorescent europium tetracycline hydrogen peroxide complex (EuTc-HP) complex is formed by incubating EuTc and H_2O_2 for several minutes. A decomposition of H_2O_2 rapidly shifts the equilibrium between the complexes EuTc-HP and EuTc (**Equation 3.3.1**). Thus, it is possible to directly monitor the reduction of the H_2O_2 level based on the change of the fluorescence intensity. [274]

$$EuTc + H_2O_2 \leftrightarrow EuTc\text{-}HP \quad (\textbf{3.3.1})$$
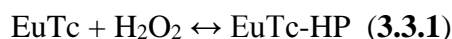
To investigate a catalase-like activity of the hematite fiber meshes, they were placed in a 96 well plate and treated with an EuTc-HP solution in 3-(*N*-morpholino)propanesulfonic acid (MOPS) buffer. The change of the fluorescence intensity at 620 nm (with $\lambda_{ex} = 405$ nm) was monitored over a period of 10 min. Control measurements were conducted using the hematite NPs and the native catalase enzyme. Comparison of the fluorescence spectra of EuTc and EuTc-HP demonstrate the effect of H_2O_2 binding to the EuTc complex (**Figure 3.3.6a**). In the presence of native catalase, the present H_2O_2 was decomposed, which resulted in the expected decrease of fluorescence intensity (**Figure 3.3.6b**). A similar behavior could be observed for hematite NPs. Variation of the particle concentration led to a decrease of the fluorescence intensity (**Figure 3.3.6c**). Based on the determined catalase-like activity of the hematite NPs the catalytic activity of hematite PVA fiber meshes was investigated. While pure PVA fibers without NPs exhibited no significant effect, the iron oxide loaded fibers showed lower H_2O_2 levels with increasing hematite loading, demonstrating the use of the nanozyme-in-fiber meshes as catalase mimics for the degradation of H_2O_2 (**Figure 3.3.6d**).
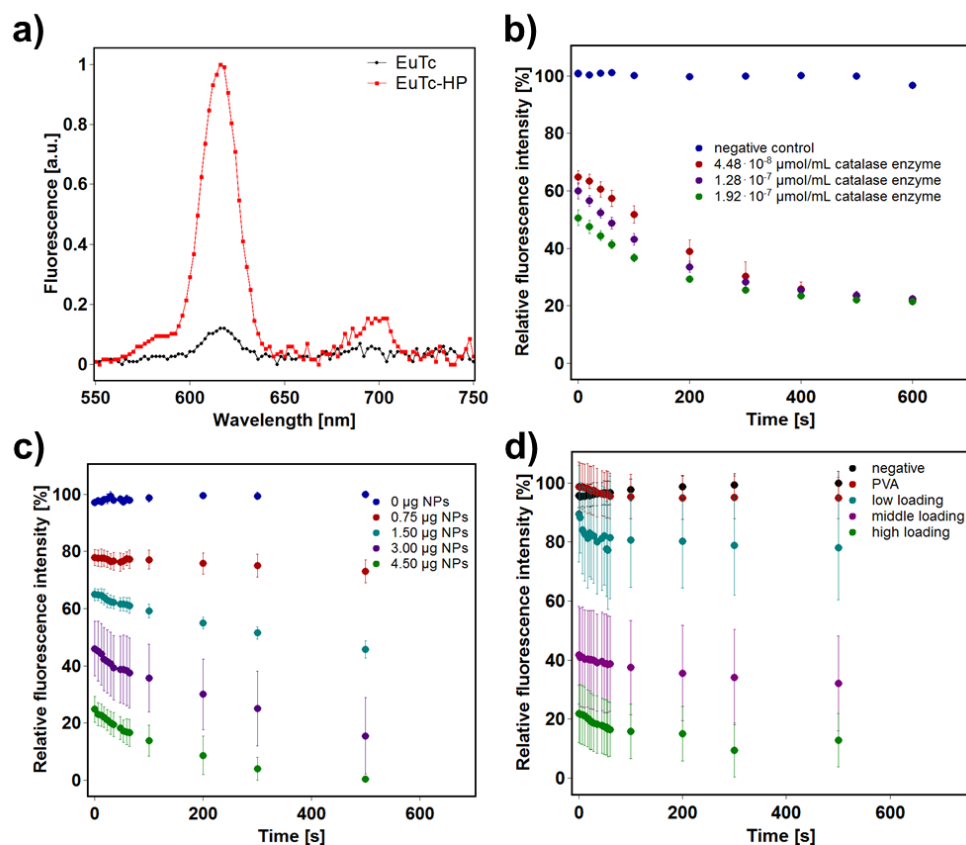
Figure 3.3.6 (a) Fluorescence spectra of EuTc and EuTc-HP recorded with $\lambda_{ex} = 405$ nm. Decomposition of H_2O_2 catalyzed by (b) native catalase, (c) hematite NPs, and (d) hematite loaded PVA fiber meshes (observed with the fluorescence signal at 605 nm of EuTc-HP).

The iron oxide NPs and the loaded fiber meshes showed a similar concentration dependency of their catalytic activity (**Figure 3.3.7a-b**). In all cases, an increasing amount of catalyst leads to a higher decomposition of H_2O_2. With the highest hematite loading of the hematite PVA fiber meshes, a reduction of the fluorescence intensity down to 9.5% - related to 100% control - was achieved. To demonstrate the catalase-like activity, the decomposition products were investigated. Elemental oxygen was found to be one of the key reaction products (**Figure 3.3.7c**). With increasing hematite loading, higher formation rates of oxygen were observed, which is in agreement with the determined catalytic activities.
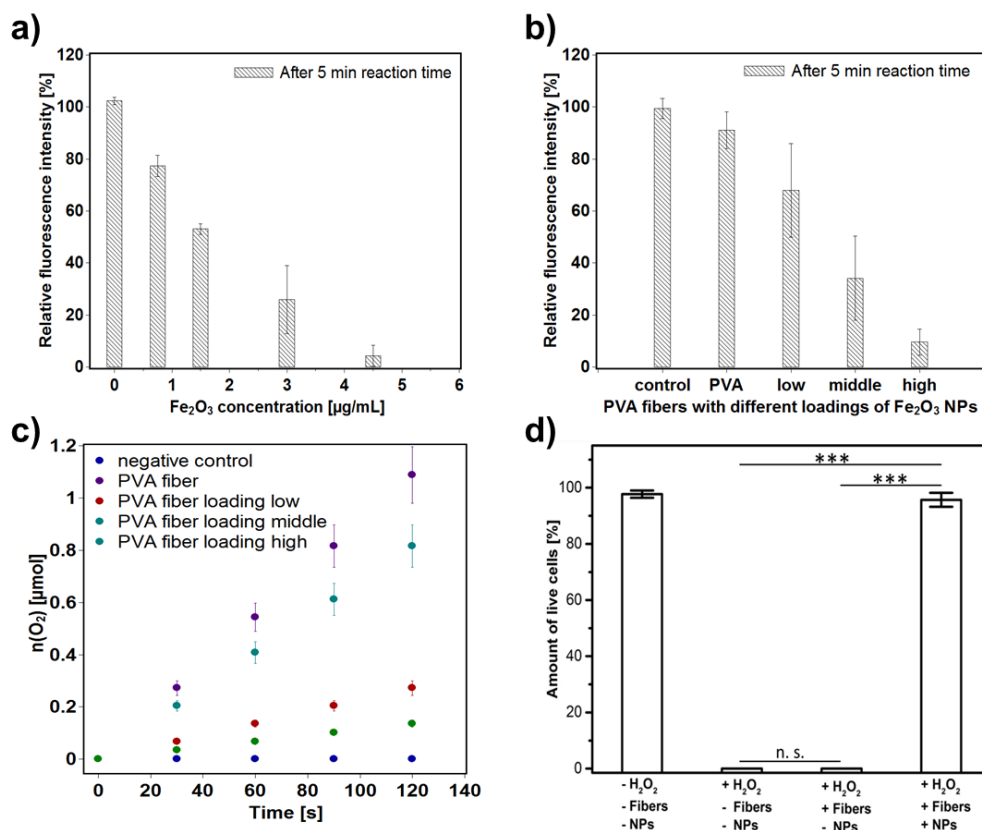
Figure 3.3.7 Analysis of the catalytic activity and the resulting products. H_2O_2 level after a reaction time of 5 min in the sample solution is shown for (a) hematite NPs and (b) for the hematite containing PVA fibers. (c) To establish the reaction mechanism of the hematite PVA fiber meshes, the formation of elemental oxygen, which is one of the key reaction products in a catalase-like reaction, was monitored using an oxygen sensitive electrode. Increasing hematite loadings show higher formation rates of oxygen. (d) Hematite PVA fibers protect cells against cell death triggered by extensive H_2O_2 levels. Control measurements conducted without hematite PVA fibers, or pure PVA fibers exhibit no cell protection. n. s. is not significantly different. *p < 0.05, **p < 0.01, ***p < 0.001.

To further investigate the H_2O_2 conversion ability of hematite PVA fibers in bio-applications. The fibroblast cells were used as *in vitro* model. All the cells were died after overnight culturing when 50 µM of H_2O_2 was applied into cell media, indicating that such concentration of H_2O_2 causes apoptosis of fibroblast cells. However, more than 90% of the cells were survived when the PVA

fibers with hematite nanoparticles were cultured together with H_2O_2 in cell media. It showed that the hematite PVA fibers were able to mediate the H_2O_2 concentration to the non-toxic level (**Figure 3.3.7d**).

3.3.4 Conclusion

In summary, the fabrication and use of an electrospun nanofibrous membrane with a high porosity, wettability and the catalytic capability to simultaneously decrease the H_2O_2 and increase the O_2 level was demonstrated. Therefore, hematite nanozymes were integrated in various concentrations into PVA membranes *via* electrospinning. To retain the fiber scaffold in the presence of water, the membrane was cross-linked to form a stable fibrous gel. After cross-linking, the membrane showed high water permeability and hence, provided a good accessibility of hydrophilic compounds to the embedded hematite nanozyme particles. The encapsulated hematite showed a high catalase-like activity and quickly converted H_2O_2 into O_2. When incubating fibroblasts at critically high H_2O_2 concentrations, the catalytically active membrane efficiently reduced the H_2O_2 concentration and enabled undiminished cell proliferation. Thanks to this catalase-like activity, the hybrid nanofibrous gel could be used for improving the wound healing process.

3.4 Nanozymes in nanofibrous mats with haloperoxidase-like activity to combat biofouling[†]

In the previous chapter, electrospinning has been used to assemble hematites nanoparticles within the polymer fibers and keep their catalytic activity in the electrospun polymer mats. However, a variety of functional nanoparticle could be included inside the nanofibers to produce an array of functional materials. For example, in many environments the polymer nanofibers prepared by electrospinning suffer from biofouling during long-term usage, resulting in persistent infections and device damage. In this chapter, the fabrication of polymer mats with CeO_{2-x} nanorods that can prevent biofouling in aqueous environment is described. The embedded CeO_{2-x} nanorods are functional mimics of natural haloperoxidases that catalyze the oxidative bromination of Br^- and H_2O_2 to HOBr. The generated HOBr, a natural signaling molecule, disrupted the bacterial quorum sensing,a critical step in biofilm formation. The polymer fibers provide porous structures with high water wettability, and the embedded cerium oxide nanozymes act as a catalyst that can efficiently trigger oxidative bromination, as shown by a haloperoxidase assay. Additionally, the embedded nanozymes enhance the mechanical property of polymer mats, as shown by a single-fiber bending test using atomic force microscopy. It can be envisioned that the fabricated polymer mats with CeO_{2-x} nanorods may be used to provide mechanically robust coatings and membranes with anti-biofouling properties.

3.4.1 Introduction

Recently, biomimetic strategies have been developed to replicate the role of natural enzymes, and a variety of nanozymes – inorganic nanoparticle-based artificial enzymes – have been prepared and displayed an array of functions depending on the chemical composition.[277,278] Several of those nanozymes have shown an unmatched potential to reduce biofouling.[278-280] However, the key challenge remains to formulate those inorganic nanoparticles into functional, versatile and easy to use materials. Electrospinning has been shown to be an efficient, practical and scalable method to prepare robust hybrid materials including of polymer and nanozymes,[281] and could be beneficial to the formulation of hybrid materials with anti-biofouling nanozymes.

Electrospinning is a scalable and versatile technique to obtain nanofibrous materials with variable porous structures and controllable fiber diameters.[282,283] Electrospinning of polymer and polymer hybrids has already been implemented in roll-to-roll processes,[284] and other industrial processes[285,286] for the formation of self-standing fibers and mat as well as coatings. The nanofibrous materials can be further functionalized and mechanically enhanced by integrating nano-objects, e.g. nanoparticles and nanocapsules, during or after the electrospinning process.[287,288] Additionally, the electrospun nanofibers can orderly arrange into hierarchical structures by controlling their alignment.[289] These attributes make electrospun nanofibers attractive for applications such as tissue engineering,[290-292] wound healing,[281,293] and water purification.[294] Furthermore, electrospun fibers can be used either in their fibrous state or as coatings, self-standing mats or membranes.[295,296]

Biofouling is a critical phenomenon, especially when the materials are used in an environment containing microorganisms. Biofouling is the nonspecific surface adhesion of microorganisms.[297] This can be detrimental to the performance of the materials and reduce the efficiency of

membranes,[298] leading to corrosion on metallic surfaces[299] and bacterial infections on implanted medical devices.[300] Cleaning the nanofibrous surfaces to remove the adhered layer is difficult and sometimes is even impossible. Thus, it is essential to develop surfaces that are not susceptible to biofouling.

In the last decade, many strategies have been developed to reduce or avoid bacterial adhesion.[301] A number of antimicrobial or antibiotic compounds have been integrated into electrospun mats to release toxic agents into aqueous environments to kill the surrounding bacteria.[302,303] This strategy is highly efficient but will lead to the development of antibiotic-resistant bacteria strains.[304] As an alternative, silver nanoparticles have been widely used as antibacterial compounds. These nanoparticles can form on the nanofiber surface by post-reaction after electrospinning, or be embedded into the electrospun fibers.[305,306] A problem common to the use of silver nanoparticles or antibiotics is the decrease of the antifouling activity due to the release of the active compound with time, leading to materials with a limited lifespan. Besides the biocidal strategy, one of the most common methods to combat biofouling is to develop surfaces to which bacteria and cells cannot adhere. For example, surfaces coated with zwitterionic polymers are known to suppress nonspecific protein adsorption and bacterial adhesion.[307,308]

Another alternative in creating anti-fouling surfaces is to draw inspiration from nature. For example, seaweeds have developed a unique chemical strategy against biofouling. Seaweeds secrete a group of enzymes, the vanadium haloperoxidases, that catalyze the oxidation of halides (Cl^- and Br^-) with hydrogen peroxide (H_2O_2) to form hypohalous acids (HOCl and HOBr).[309,310] The presence of hypohalous acids is known to disrupt the quorum sensing of microorganisms, a process that cells and bacteria use to regulate biofilm formation, the first step in the permanent

biofouling of a surface. Thus, the release of hypohalous acids prevents the biofouling of seaweeds.[311]

Vanadium- and cerium- based nanomaterials have shown great potential to mimic the activity of haloperoxidase to reduced biofouling to produce material with long-term stability in harsh environments.[277,278] Several nanozymes are promised to preventing biofouling in marine environments.[279] For example, vanadium pentoxide nanowires were able to catalyze the oxidation of Br^- to HOBr in presence of H_2O_2.[312] Similarly, cerium oxide nanorods displaying haloperoxidase-like activity have been used to prepare anti-biofouling coatings.[280] Such nanozyme displayed a sustained and long-term activity to produce enough hypohalous acids to prevent biofouling in aqueous environments using only the concentration of peroxide and halides bioavailable. Cerium oxide nanorods were recently used to disrupt the quorum sensing of bacteria and thus prevent the bacterial adhesion only using the halogens atoms and the hydrogen peroxide naturally present in fresh water.[279,280] Given that similar or even higher concentration of both halogen ions and peroxide are present in the human body similar behavior could also potentially be observed coating used on implants or on wound-dressing.[313,314] Additionally, the nanoceria is generally considered as a biologically benign material.[315,316]

Furthermore, the catalytic activity and stability of nanozymes can be preserved by immobilizing them into polymer materials. Compared with nanozyme dispersions, polymer-embedded nanozymes are more convenient for handling, continuous processing, and avoiding product contamination. The main supporting materials for nanozymes are microgels,[317] metal-organic frameworks,[318] and nanofibrous materials.[281,319] Among these different supporting materials, polymer fibrous mats have attracted sustained research interest, because the fibrous morphology provides a high specific surface area, which is ideal for catalytic reactions. For example,

immobilized gold nanoparticles within polymer nanofibrous mats catalyze the reaction of 4-nitrophenol to 4-aminophenol over multiple cycles[320] and electrospun Fe_3O_4 nanofibers showed a better peroxidase-like catalytic activity than commercial Fe_3O_4 nanoparticles.[321] Recently, electrospun PVA mats with hematite nanoparticles showed the catalase-like activity. These hybrid mats can be used as a wound dressing material to regulate the H_2O_2 concentration in wound sites.[281]

Here, CeO_{2-x} nanorods (NRs) were electrospun with polyvinyl alcohol (PVA) to fabricate free-standing nanofibrous mats. After crosslinking, the water-swellable PVA mats embedding CeO_{2-x} NRs mimicked the haloperoxidase activity in aqueous media. The activity of the CeO_{2-x} embedded in the PVA fibers was quantified by the bromination of phenol red to demonstrate that the activity of the nanozyme was preserved after their processing inside the polymer matrix. The mechanically robust hybrid mats catalyzed the oxidation of Br^- and H_2O_2 to HOBr, like natural haloperoxidase. To demonstrate the anti-biofouling properties of this novel hybrid material, the effect of embedded CeO_{2-x} NRs on the fouling of *E. Coli* was studied in an aqueous environment. Thanks to their haloperoxidase-like activity, PVA/CeO_{2-x} such nanofibrous mats are potential candidates as new anti-biofouling coating materials for application in biological or marine environments (**Figure 3.4.1**) used either on water filtration membranes or on any immersed surfaces. These new polymer hybrid mats offer a new method to prepare stable materials where the inorganic active component provides a sustained anti-biofouling behavior that is not the result of the dissolution of the inorganic part, as observed with silver or copper containing materials, but rather act as a catalyst for the production of analytes able to disrupt bacterial quorum sensing. Such material would find application as coatings from the biomedical field to water purification.
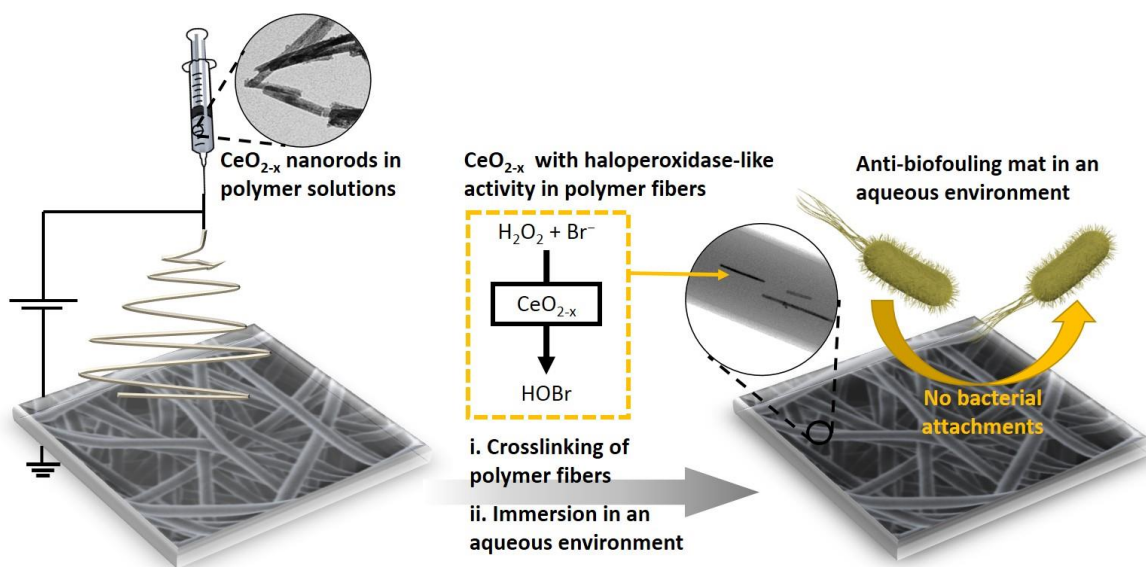
Figure 3.4.1 Fabrication of ceria nanorods (CeO_{2-x}) nanofibrous mats by electrospinning. The hybrid mat can catalyze Br^- with H_2O_2 to HOBr to prevent bacterial adhesion on its surface.

3.4.2 Experimental

Materials

Fomblin® Y, cerium(III) nitrate hexahydrate, sodium hydroxide, phenol red and hydrochloric acid (HCl, 37 wt.%, AR grade) were purchased from Sigma-Aldrich (Germany), ammonium bromide was from ABCR GmbH (Germany), hydrogen peroxide solution (30%) from Roth (Germany), polyvinyl alcohol (PVA, M_w = 125000 g·mol^{-1}) from Polysciences Inc and glutaraldehyde (GA, 50% aqueous solution) from Merck KGaA (Germany). All syntheses, experiments and catalytic tests were conducted using MilliQ water (pH = 6.90, 18.2 MΩ).

Synthesis of CeO$_{2-x}$ nanorods

Cerium(III) nitrate hexahydrate (2 mmol) was dissolved in 5 mL of water under an argon atmosphere. Then, 20 mL of a 6 M NaOH solution were added and the reaction mixture was stirred for 30 min. The mixture was transferred to the Teflon® inlay of a stainless-steel autoclave. The

autoclave was placed in an electric oven and heated to 373 K for 24 h. After the natural cooling to room temperature, the precipitate was isolated by centrifugation (9000 rpm, 10 min) and washed several times with water and ethanol. The product was dried for 24 h in an electric oven at 35 °C.[322]

Electrospinning and cross-linking of PVA/CeO$_{2-x}$ nanorods composites

Dispersions with varying concentrations of nanorods were prepared by combining CeO$_{2-x}$ nanorods suspensions with a PVA solution to yield a suspension containing 10 wt.% of PVA and CeO$_{2-x}$ nanorods for electrospinning. An ultrasonic tip was used to disperse the nanorods in the PVA solution (d (tip) = 6 mm; 50% amplitude; 5 s pulse, 5 s pause; 3 min). Afterward, the mixtures were stirred mechanically overnight at 900 rpm to obtain a homogenous dispersion. 1 mL syringe was filled with the nanorod/PVA mixture. The electrospinning process was conducted at room temperature with a relative humidity of 20-25% onto an aluminum foil carrier placed at a distance of 20 cm from the nozzle (diameter: 0.8 mm). The feeding rate was 0.3 mL h^{-1} and the applied voltages were +18 kV and 0 kV. Fibers without CeO$_{2-x}$ nanorods were prepared under same conditions. The fibers were crosslinked by treating the fibers with 1 mL of a 50 wt.% glutaraldehyde (GA) solution and 20 µL of a 37 wt.% HCl solution. The crosslinking reaction was conducted in a vacuum oven at room temperature and 1 mbar for 24 h. Finally, unreacted GA and HCl were removed by drying the samples for 24 h at room temperature. Samples for TEM analysis were prepared by placing a TEM grid (copper, 300 mesh) on the aluminum foil to collect the fiber sample for 30 s.

Powder X-ray diffraction (XRD)

Solid-state analysis of the pure CeO$_{2-x}$ nanorods was conducted on a STOE Stadi P (Germany) diffractometer using the Ag K$_{\alpha 1}$ radiation. The sample was prepared on a perfluoropolyether film with Fomblin® Y. The data were analyzed with the EVA software package from Bruker.

Swelling ratio of hybrid PVA mats

The water absorption ratio of the hybrid PVA mats was defined as the swelling ratio in this study. To determine the swelling ratio, the mats were dried at 50 °C under vacuum overnight. Then the dried mats were soaked in demineralized water in a mixer (HLC MKR 23, Ditabis, Germany) at room temperature for 24 h. The weights of the swollen samples were measured after removing the excessive water on the mats by gently patting the polymer mat with a filter paper. The swelling ratios of the PVA mats were calculated from **Equation (3.4.1)**:

$$Swelling\ ratio = \frac{W_S - W_D}{W_D} \times 100\% \quad (\textbf{3.4.1})$$

where W_S and W_D are the weights of the swollen and dried samples, respectively. All samples were triplicate in the experiments.

Contact angle measurement

The static contact angle of water on PVA fiber meshes was analyzed using a goniometer coupled to an IDS uEye camera. For the measurement, 5 µL droplets of water were deposited on the mats surfaces and the contact angle measured after 1 min.

Morphology of the CeO_{2-x} nanorods and of the hybrid mats

The CeO_{2-x} nanorods were imaged by transmission electron microscopy using a Tecnai G2 Spirit TEM (FEI, Hilsboro, USA) using LaB_6 crystal as the cathode, a twin objective and a CCD camera (US 1000, Gatan Pleasanton, USA). The sample was prepared by dispersing the nanorods in ethanol and dropping one drop of the dispersion onto a carbon coated copper grid from Science Services. The morphology of the PVA mats was analyzed with a JEM1400 transmission electron microscope (JEOL, Japan) and a SU8000 scanning electron microscope (Hitachi, Japan).

Thermogravimetry (TGA).

The nanorod content in the PVA mats was determined by thermogravimetric analysis (TGA). The measurements were conducted using a Mettler-Toledo TGA/SDTA-851 thermo-balance (50 to 700 °C, heating rate of 5 °C·min^{-1}, nitrogen atmosphere, the sample weight was about 10 mg). To measure the leakage of the nanoparticles from the PVA fibers, thermogravimetric analysis was conducted on samples having been immersed into water for two weeks and dried overnight in a vacuum oven.

Young's modulus of crosslinked fibers determined by atomic force microscopy (AFM)

The Young's modulus of single fibers was determined by measuring their resistance against bending by applying point loads onto freely suspended fibers. For this purpose, the fibers were electrospun onto microstructured silicon wafers (HS-500MG height calibration standard, Budget Sensors, Sofia, Bulgaria), which contained regular arrays of square holes with 5 µm length and 0.5 µm depth. A Nanowizard IV AFM (JPK Instruments, Berlin, Germany) was used to image the sample in tapping mode to find places where a single fiber spanned one of the square holes. Once such a freely suspended fiber was located, it was imaged in QI mode, where a force distance curve with defined maximum load of 100 nN was recorded for each of the 256×256 pixels of the image. For a circular fiber clamped at both ends, the stiffness $k_F(x)$ at position x along the fiber axis is related to its Young's modulus E by

$$k_F(x) = \frac{3L^3 EI}{(L-[x-x_0])^3(x-x_0)^3} \quad (\textbf{3.4.2})$$

where L is the length of the suspended fiber segment and $I = \pi R^4/4$ is the moment of inertia of a fiber with radius R. From the QI images, the individual fiber radius R could be extracted as well as the values of $k_F(x)$ for each image pixel along the freely suspended part with length L. By fitting this experimental curve of with **Equation (3.4.2)**, the Young's modulus of individual fiber was

obtained. The offset x_0 is a fitting parameter to account of the small uncertainty in determining the position of end points of the suspended segment. The use of a clamped boundary condition is justified as the fibers showed strong adhesion to the silicon substrate. The same AFM cantilever was used for all experiments to exclude any relative error between experiments due to variation in spring constants. The spring constant of this cantilever was determined by both Sader method[323] and thermal noise method[324] integrated into JPK AFM software giving a value of 49.9 ± 3.6 N·m^{-1}.

Haloperoxidase-like activity of PVA/CeO$_{2-x}$ nanorods composites

The catalytic activity of the materials was analyzed using a previously reported method.[305,316,317] Briefly, the kinetic studies were conducted with pure cerium oxide nanoparticles, PVA fibers without cerium oxide nanorods, and PVA fibers with low (6 wt.%), medium (14 wt.%) and high (22 wt.%) loading of cerium oxide nanorods. The PVA fibers were fixed on the bottom of the cuvette with a magnetic stir bar, preventing the fiber mats to float in the path of the UV beam, which would directly influence and distort the UV-Vis signal.

For each measurement, the cuvette contained 4.4×10^{-3} mol·L^{-1} of ammonium bromide, 2.8×10^{-5} mol·L^{-1} of phenol red, 4.2×10^{-4} mol·L^{-1} of hydrogen peroxide and the 18 cm^2 of the CeO$_{2-x}$ containing mats. All solutions were prepared in water, and the cuvette contained a final volume of 2.5 mL. In all cases, the hydrogen peroxide solution (30%) was added directly before the measurements. Absorption scans were recorded in intervals of one minute for a total duration of 5 h.

Bacterial adhesion tests of PVA/CeO$_{2-x}$ nanorods composites

To determine whether the incorporation of CeO$_{2-x}$ nanorods can impede bacterial adhesion, 2.5 cm $\times$ 2.5 cm pieces of PVA mats with a loading of cerium oxide nanorods (22 wt.%) were compared to PVA mats without cerium oxide nanorods. *Escherichia coli* (*E. coli*) were grown in

a liquid culture overnight. Then PVA mats were incubated with 4.4 mM NH$_4$Br and 0.42 mM H$_2$O$_2$ and a defined number of bacteria for 16 hours in standard lysogeny broth (LB) medium at 37 °C on a horizontal shaker. Afterwards PVA fibers were removed and gently rinsed with distillated water to wash away all non-adherent bacteria. To quantify the amount of adherent bacteria, the washed PVA mats were transferred to fresh LB medium (without NH$_4$Br and H$_2$O$_2$) where adherent bacteria were able to proliferate. After 2 h proliferation, the bacteria amount was determined by measuring the optical density at 600 nm with a spectrophotometer. Those experiments were repeated 3 times.

3.4.3 Results and discussion

The CeO$_{2-x}$ nanorods (NRs), functional mimics of natural haloperoxidases, were prepared by hydrothermal synthesis. After the reaction, the products showed a rod-like morphology. Powder XRD revealed the nanorods to consist of pure CeO$_{2-x}$ (**Figure 3.4.2a**), the CeO$_{2-x}$ crystalized in a fluorite structure and no impurities or additional crystalline phases were observed. The resulting nanoparticles were not functionalized with any surfactants, allowing a direct accessibility for substrate molecules to the catalytic sites of particle surfaces.To integrate the nanorods in polymer materials, the suspension of CeO$_{2-x}$ NRs were mixed in a PVA solution. Ultrasonication ensured complete dispersion of the CeO$_{2-x}$ NRs in the PVA solution.

Table 3.4.1 Swelling ratios of PVA mats with different loading of CeO$_{2-x}$ nanorods

CeO$_{2-x}$ loading in PVA mats	0%	6%	14%	22%
Swelling ratio	188%	196%	188%	195%

To allow the use of water-soluble PVA fibers in aqueous systems, the electrospun fibers were crosslinked covalently with glutaraldehyde. The swelling of pure PVA mats was 188% and the

addition of CeO$_{2-x}$ NRs did not significantly change the swelling of the mats (**Table 3.4.1**). The high swelling ratio allows the absorption of water and water-soluble substrates penetrate into the PVA fibers to contact with the embedded CeO$_{2-x}$ NRs.
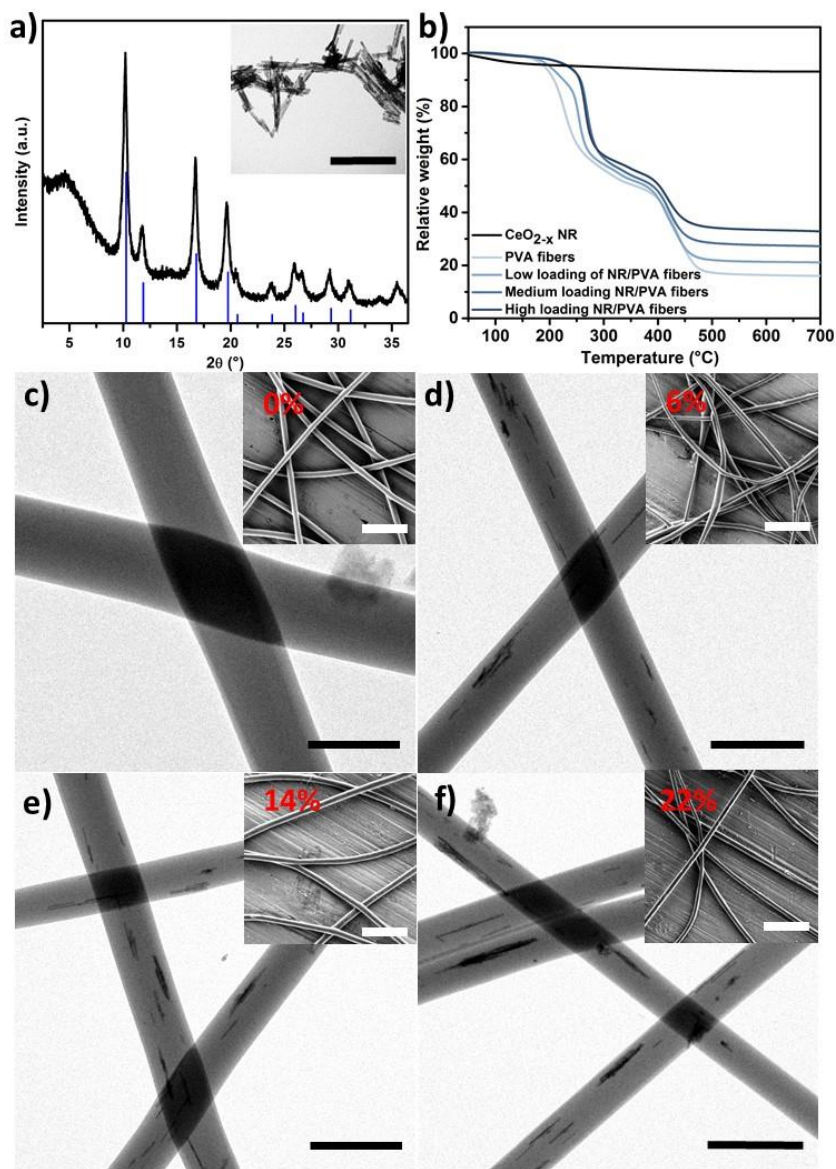
Figure 3.4.2 (a) XRD pattern of synthesized CeO$_{2-x}$ nanorods (NRs). The inset shows a TEM image of NR (scale bar = 200 nm). (b) TGA curves of the hybrid PVA/CeO$_{2-x}$ mats with different NR loading. (The curves from top to bottom are presented the pure CeO$_{2-x}$ NR, pure PVA, PVA with 6%, 14% and 22% of CeO$_{2-x}$ NR.) TEM images of PVA fibers with (c) 0%, (d) 6%, (e) 14%, and (f) 22% of CeO$_{2-x}$ NRs (c-f: scale bar = 500 nm, insets: scale bar = 2 µm).

Additionally, the nanofibrous network and the porous structure of PVA mats were maintained even after two weeks of immersion in water. The mats retained their physical integrity and no leakage of the NRs was observed (**Figure 3.4.3**). This indicates that the PVA/CeO$_{2-x}$ nanofibrous mats are promising hybrid materials for long-term use in aqueous environments.
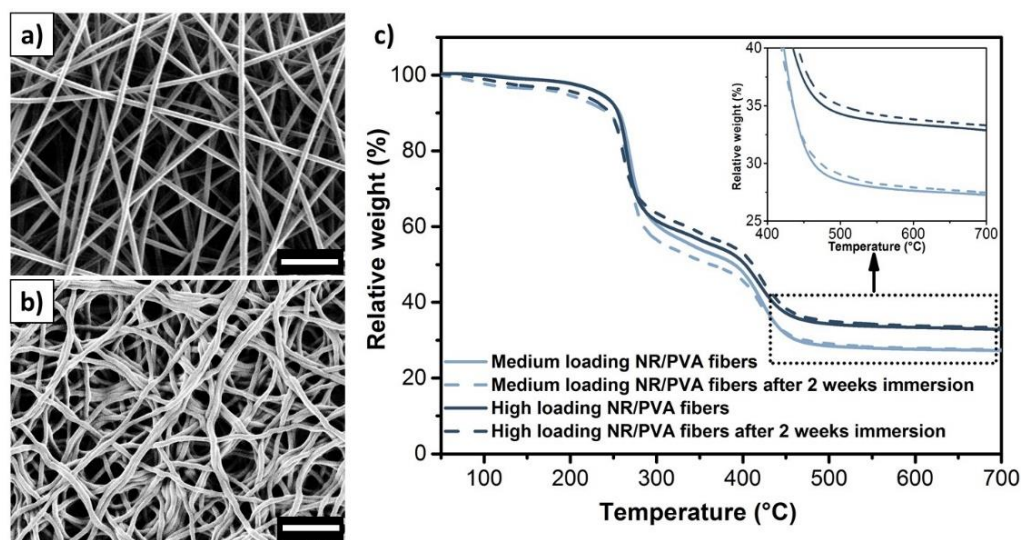
Figure 3.4.3 SEM images of the PVA mat containing 6% of CeO$_{2-x}$ NRs before (a) and after (b) water immersion for two weeks. (c) TGA curves of the CeO$_{2-x}$ NR/PVA mats with different NR loadings (14% and 22%) before and after immersion in water for two weeks.

The loading of CeO$_{2-x}$ NRs in PVA mats was measured by TGA (**Figure 3.4.2b**). The results show that pure CeO$_{2-x}$ NRs are stable in the investigated temperature range. However, pure PVA fibers without CeO$_{2-x}$ NRs underwent thermal decomposition between 250 °C and 450 °C with the typical two-step decomposition mechanism of PVA.[327] Above 500 °C, the decomposition stopped; this indicated the formation of stable carbonaceous residues representing ca. 20% of the original PVA weight. All samples containing PVA and CeO$_{2-x}$ NRs showed similar behavior when heated under nitrogen, although the presence of the inorganic nanoparticles slightly improved the thermal stability of the hybrid material. The main difference observed in the decomposition curve is the

solid fraction of material remaining after complete decomposition of PVA. The composition of the solid residue was used to calculate the original loading of CeO_{2-x} NRs in hybrid PVA mats with low, medium, and high amount (respectively 6%, 14%, and 22%). The TEM images (**Figure 3.4.2c - f**) of the electrospun fibers showed that the CeO_{2-x} NRs were successfully incorporated into the nanofibers and did not show the presence of any large aggregates. The nanorods were embedded in the fiber and distributed throughout the fiber.
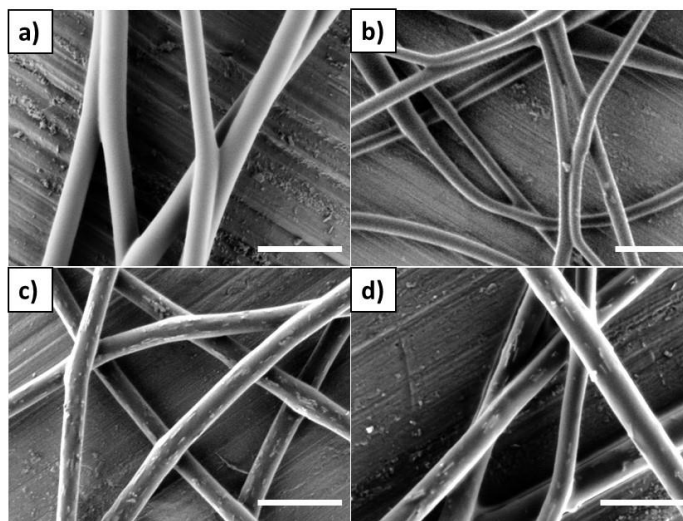
Figure 3.4.4 SEM images of CeO_{2-x} NR/PVA mats with different NR loadings. (a) 0%, (b) 6%, (c) 14%, (d) 22%. Scale bar = 1 µm.

SEM images of the fibers show the NR almost protruding out of the fiber at medium and high NRs loading (**Figure 3.4.4**). However, TEM tomography (**Figure 3.4.5**) clearly demonstrated that the NRs were located within the fibers.
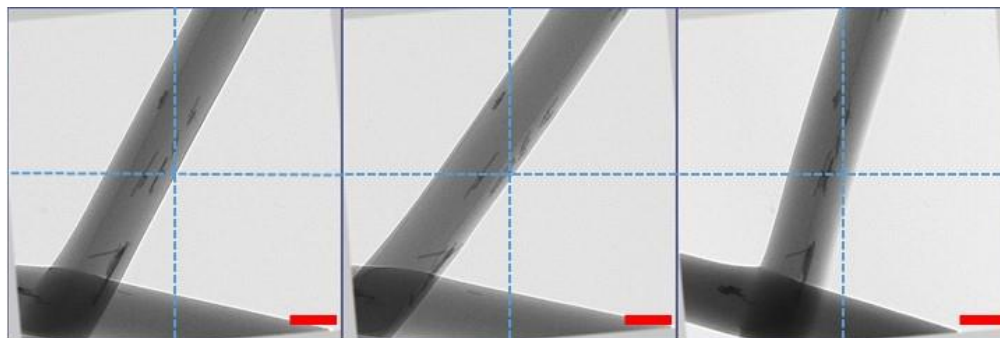
Figure 3.4.5 TEM projection of CeO$_{2-x}$ NR/PVA fiber containing 22% of NR used for the TEM tomography reconstruction. Scale bar = 200 nm.

Additionally, the NRs were oriented along the fiber axis direction. The alignment of NRs in PVA nanofibers can be attributed to the strong shear forces generated on the NRs/PVA suspension during the electrospinning process. The suspension was elongated by the electrical force and then the NRs were oriented with the direction of elongated polymer flow.[328,329]

The long-term stability of the PVA/CeO$_{2-x}$ hybrid mats can be influenced not only by the leakage of the NRs but also by the mechanical properties of the fibers themselves. Therefore, the Young's modulus of PVA fibers with different loading of CeO$_{2-x}$ NRs was measured by atomic force microscopy (AFM). AFM has become a key method to obtained quantitative mechanical information about nanomaterials and nanofibers using force spectroscopy.[330,331] To measure the mechanical properties of the hybrid PVA/CeO$_{2-x}$ fibers, vertical point loads were applied along freely suspended fiber segments by AFM to locally probe their bending stiffness. (**Figure 3.4.6a**). From a fit of the stiffness profiles with **Equation 3.4.2**, the Young's modulus of the fibers was obtained.
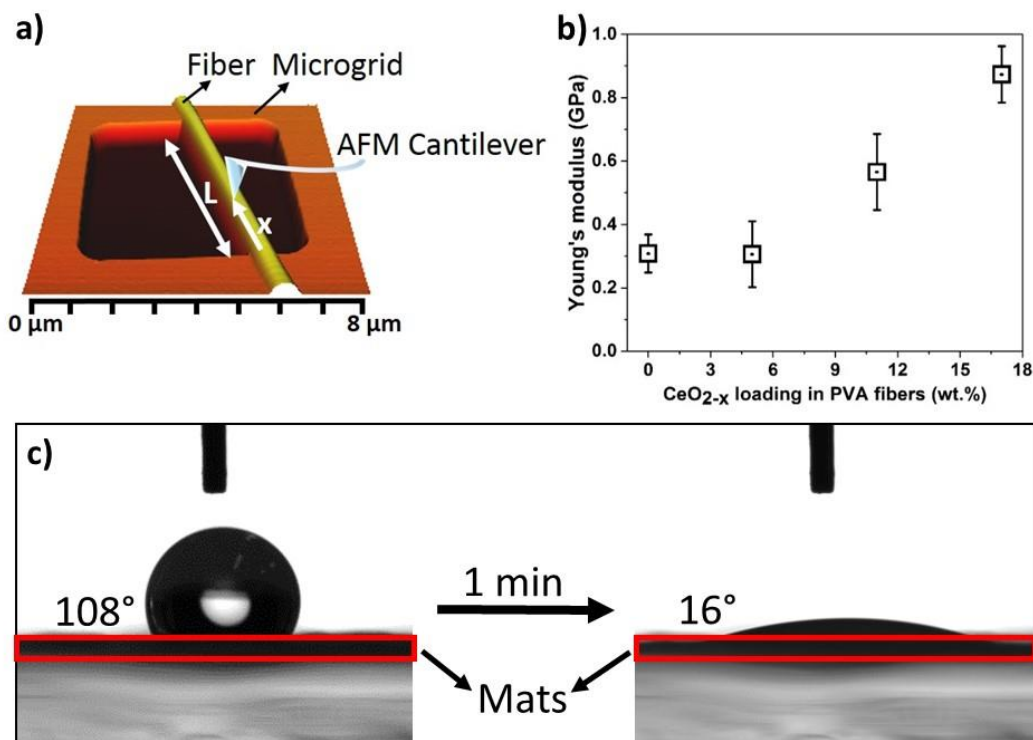
Figure 3.4.6 (a) Schematics of the AFM bending experiment. A point load is applied by the AFM tip onto the fiber that spanned a microgrid. (b) Young's modulus of the PVA mats measured by the AFM bending experiment. (c) Dynamic wettability of the mats containing 22% of CeO_{2-x} NRs.

PVA fibers without nanorods displayed a Young's modulus of 0.31 ± 0.06 GPa. The addition of 6% of CeO_{2-x} NRs did not lead to a modification of the mechanical property of fibers. However, a significant mechanical enhancement was observed in the presence of 14% and 22% of nanorods, (**Figure 3.4.6b**). These results demonstrate that the addition of CeO_{2-x} NRs to the PVA fibers leads to the formation of a composite material with improved mechanical properties.

The wettability of the PVA mats was tested by adding a droplet of water (5 µL) on the surface. All mats displayed similar wettability; within less than a minute, the contact angle of the water droplet on the electrospun mat decreased from 108° to 16°. This almost instantaneous absorption of the water indicated that the electrospun mats have a good wettability and hydrophilicity (**Figure 3.4.6c**

and **Figure 3.4.7**). The hydrophilic character of the PVA mats allowed the fibers to swell in presence of water, improving further the access of the molecular substrates to the embedded CeO_{2-x} NRs in the PVA fibers.
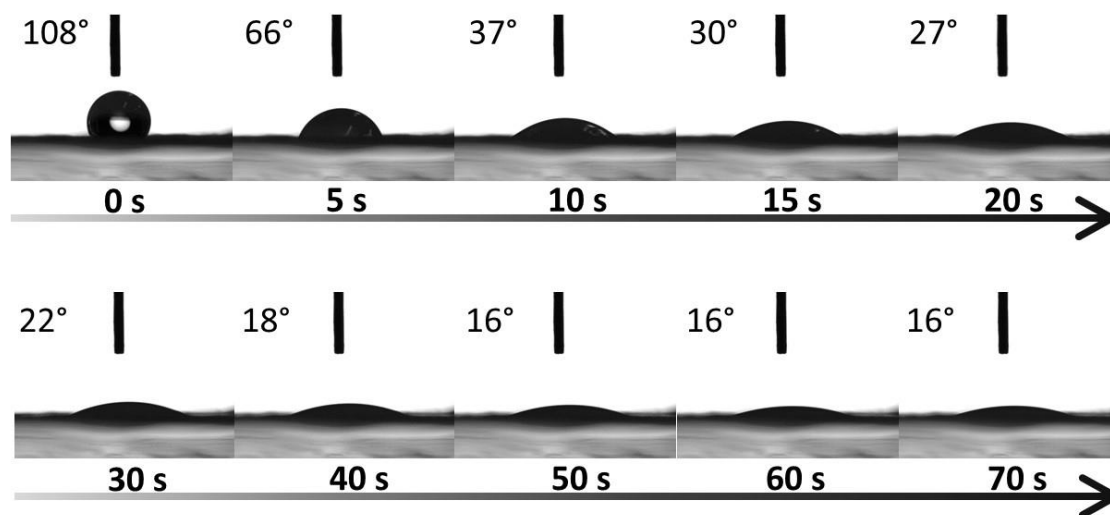
Figure 3.4.7 Images of the water contact angle of PVA mats with 22% NRs at different contact times.

The haloperoxidase-like activity of PVA/CeO_{2-x} NRs mats was demonstrated with the phenol red bromination assay. The phenol red ($\lambda_{max} = 432$ nm) can be brominated with hypobromous acid (HOBr) to form bromophenol blue ($\lambda_{max} = 590$ nm) (**Figure 3.4.8a**). However, hypobromous acid is not present in the system, it is rather formed *in situ* by the reaction of ammonium bromide (NH_4Br) and hydrogen peroxide (H_2O_2) at the surface of the ceria nanorods. First, a molecule of H_2O_2 needs to coordinate with a Ce(III) atom at the 110 surface of the nanorod, the oxidation of the cerium atom into Ce(IV) is then accompanied by the cleavage of the O-O bond to form two ligands, a hydroxyl anion and a hydroxyl radical. The hydroxyl radical ligand can then react with a bromide anion, the following reorganization will result in the release of a hypobromite anion and the coordination of a water molecule to a regenerated Ce(III) atom.[280] The resulting hypobromite

can then diffuse away from the ceria nanorods and the PVA fibers to take part in further reactions in the vicinity of the hybrid mat. For example, the stepwise bromination of phenol red to bromophenol red and finally to bromophenol blue was catalyzed by the hybrid mats and the reaction was monitored spectrophotometrically.[332] The haloperoxidase-like reaction leads to a decrease of the absorption maximum at 432 nm and simultaneously to an increase in the absorption at 590 nm (**Figure 3.4.8b**).
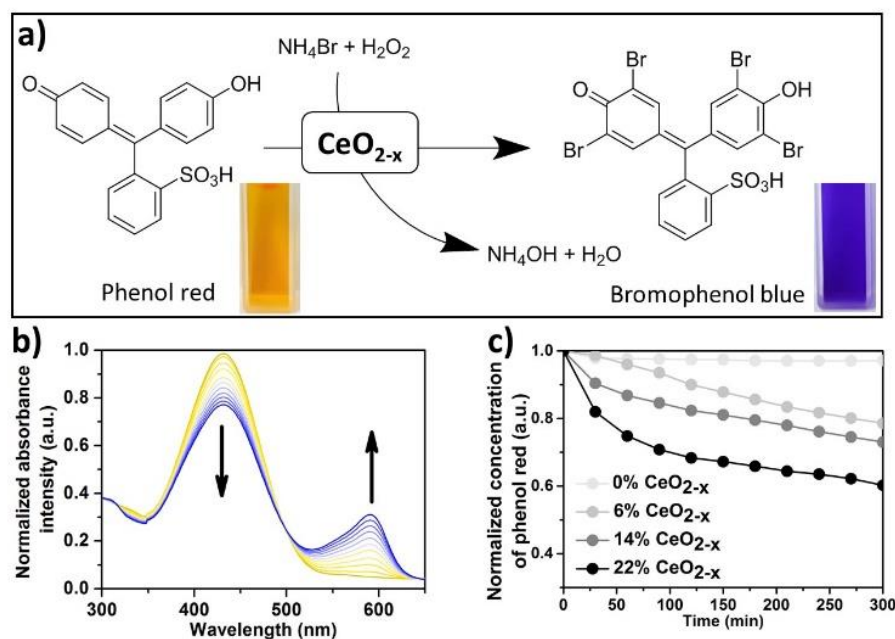
Figure 3.4.8 (a) Schematic illustration of the oxidation of phenol red to bromophenol blue catalyzed by CeO_{2-x} NRs. Insets are the digital images of phenol red before and after reaction. (b) Time-dependent UV/vis spectra of PVA mats loaded with 6% CeO_{2-x} (2.8×10^{-5} mol·L^{-1} of phenol red, 4.4×10^{-3} mol·L^{-1} of NH_4Br, 4.2×10^{-4} mol·L^{-1} of H_2O_2, 300 min, 23 - 25 °C). (c) Changes of phenol red with time on different PVA mats.

Additionally, control measurements were conducted for PVA mats without CeO_{2-x} NRs. This control experiment did not show any change in the absorption spectra, and the concentration of

phenol red remained constant throughout the experiment, indicating that the mat itself did not catalyze the phenol red bromination (**Figure 3.4.9a**).
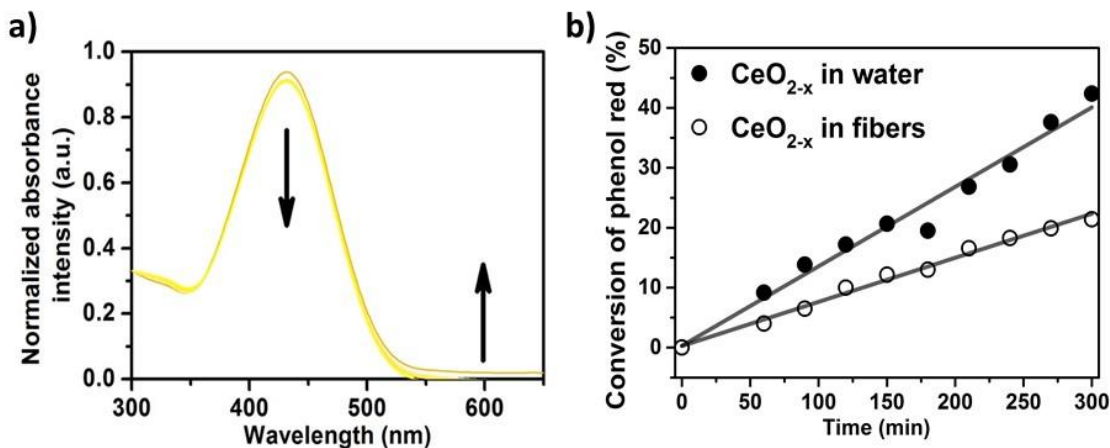
Figure 3.4.9 (a) Time-dependent UV/vis spectra of PVA membranes without CeO_{2-x} nanorods. (b) Conversion of phenol red measured by UV/vis spectroscopy for bare CeO_{2-x} nanorods and PVA membranes with 6% of CeO_{2-x} nanorods (2.8×10^{-5} mol·L^{-1} of phenol red, 4.4×10^{-3} mol·L^{-1} of NH_4Br, 4.2×10^{-4} mol·L^{-1} of H_2O_2, 300 min, 23 - 25 °C).

In contrast, PVA mats containing CeO_{2-x} NRs exhibited haloperoxidase-like activity and facilitated the bromination reaction. The reduction in the concentration of phenol red ($\lambda_{max} = 432$ nm) and the simultaneous increase in the concentration of bromophenol blue ($\lambda_{max} = 590$ nm) increased with increased loading of CeO_{2-x} NRs (**Figure 3.4.8c**). The results show that the reaction rate increased with increasing concentration of CeO_{2-x} NRs in the PVA fibers. This indicated that the haloperoxidase-like activity of PVA mats depends on the loading with CeO_{2-x} NRs. The activity of the embedded CeO_{2-x} NRs was largely preserved in comparison to free CeO_{2-x} NRs (**Figure 3.4.9b**). The moderate decrease in the rate of conversion of phenol red into bromophenol blue can be attributed the fact that the reaction is controlled by the diffusion of Br^-, H_2O_2 and HOBr through the PVA fiber.
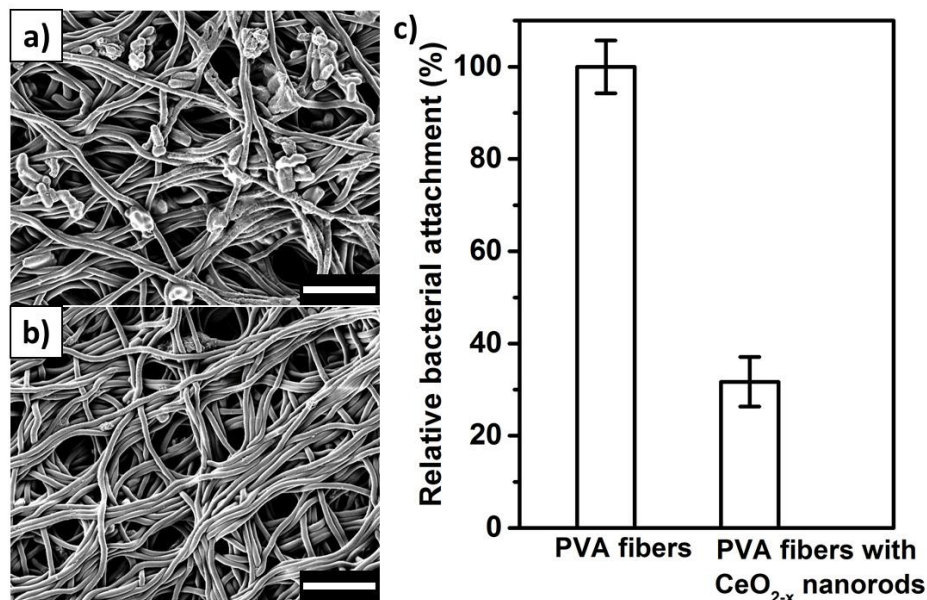
Figure 3.4.10 Inhibition of bacterial adhesion on electrospun PVA mats with 22% of CeO_{2-x} NRs in presence of H_2O_2 and NH_4Br. SEM image of (a) PVA mats without NRs and (b) PVA mats with 22% of CeO_{2-x} NRs after 16 h incubation. Scale bar = 5 µm (c) Normalized bacterial attachment of PVA mats with CeO_{2-x} NRs compared to the PVA mats without NRs after 16 h of culture and 2 h of proliferation.

The PVA mats with CeO_{2-x} NRs mimic the vanadium haloperoxidases to catalyze the oxidation of Br^- to form HOBr. The phenol red assay allows quantifying the reactivity, which is important for anti-bacterial adhesion. To test the anti-adhesion ability of the PVA/CeO_{2-x} mats, they were immersed in a *E. coli* suspension for 16 h at 37 °C with the substrates, Br^- and H_2O_2. **Figure 3.4.10a** shows that the PVA mats without CeO_{2-x} NRs were covered by a large number of bacteria. In contrast, very few bacteria were attached to the PVA mats containing 22% of CeO_{2-x} NRs (**Figure 3.4.10b**). The amount of the adherent bacteria was quantified by rinsing the PVA mats after 16 h incubation with the *E. coli* follow by 2 h of proliferation in media without Br^- and H_2O_2. After 2 h of incubation, the number of bacteria was determined by the optical density of the media. Loading the PVA mats with 22% of CeO_{2-x} NRs reduced the bacterial adhesion by 69% in

comparison to pure PVA mats (**Figure 3.4.10c**) in agreement with the SEM analysis of the mats. Therefore, the PVA mat loaded with CeO_{2-x} is a potential candidate for combating bacterial adhesion in humid or marine environments.

3.4.4 Conclusions

In summary, the electrospun PVA mats with high wettability, high mechanical stability, and the catalytic capability of producing HOBr for preventing bacterial adhesion has been fabricated. Various concentrations of cerium oxide nanorods were integrated into polymer fibers by electrospinning. To improve the stability of PVA fibers in aqueous media, the fibers were crosslinked to form a water-swellable PVA mat. The PVA mats showed a high water swellability; therefore, the hydrophilic compounds can easily access to the embedded cerium oxide nanozymes to trigger the catalytic reaction. The embedded nanozymes showed a haloperoxidase-like activity and were able to convert Br^- and H_2O_2 to HOBr efficiently, allowing the prevention of bacterial adhesion. Thanks to this haloperoxidase-like activity in the PVA mats, they could be used as the robust coatings with anti-biofouling property in humid and marine environments.

3.5 Shaping the assembly of superparamagnetic nanoparticles[†]

In the previous chapters, different techniques including solvent evaporation combined Pickering emulsion (chapter 3.1), electrospraying (chapter 3.2), and electrospinning (chapter 3.3 and 3.4) have been applied to fabricated functional materials from the 0D to 1D assemblies of nanoparticles and polymer. However, the fabrication of the functional materials with a more complex 3D microstructure, it is still a challenge. In this chapter, the evaporation-guided assembly was used to produce superparamagnetic supraparticles by drying ferrofluid droplets on a superamphiphobic substrate in the presence of an external magnetic field. By tuning the concentration of ferrofluid droplets and controlling the magnetic field, barrel-like, cone-like, and two-towers-like supraparticles were obtained. These assembled supraparticles preserved the superparamagnetism of the original nanoparticles. Moreover, other colloids can easily be integrated into the ferrofluid suspension to produce, by co-assembly, anisotropic binary supraparticles with additional functions. Additionally, the magnetic and anisotropic nature of the resulting supraparticles were harnessed to prepare magnetically actuable microswimmers.

3.5.1 Introduction

Superparamagnetic materials display high magnetization only in the presence of a magnetic field, and they do not retain any magnetization once the magnetic field is removed.[333,334] This reversible magnetization allows to manipulate superparamagnetic materials by applying magnetic fields, resulting in numerous attractive applications such as micro-actuators,[335-337] magnetic separation,[338-340] and drug delivery.[341-343] However, superparamagnetism is strongly size-dependent and only exists in nanocrystals. In the case of iron oxide nanoparticles (NP), superparamagnetism is mostly observed in particles with a diameter smaller than c.a. 30 nm.[344,345]

To build micro/macro-size superparamagnetic materials for further applications, superparamagnetic nanoparticles have to be assembled into more complex hierarchical structures.[344,346] However, the uncontrolled aggregation associated with strong dipole-dipole interaction could lead to a loss of the superparamagnetism due to the formation of larger polycrystalline magnetic domains. Therefore, the controlled assembly of superparamagnetic nanoparticles is required. Such structures have been prepared by the direct formation of 1D arrays[347, 348] or by the formation of controlled hybrid clustered beads.[344,349,350] Those clustered-beads can themselves undergo further assembly leading to the formation of more complex structures, e.g. necklace-like chains.[351-353]

In comparison to those simples structures, 3D-structured magneto-responsive materials, especially materials with an anisotropic magnetic response, would display an even larger array of potential applications such as flexible integrated sensors[354,355] or biomimetic soft-robots.[356,357] In order to obtain 3D-structured magneto-responsive materials, techniques such as self-assembly[358-360] and lithography[361-363] have been used. For example, the self-assembly of magnetite nanocubes into helical superstructure was realized by solvent evaporation at the liquid-air interface in the presence

of an external magnetic field.[358] Similarly, lithography has been used to prepare complex 3D structures containing iron oxide nanoparticles. For example, iron oxide nanoparticles embedded in a monomer solution were used to produce superparamagnetic 3D-structured microrobots with a helical shape. These helical microrobots were able to mimic bacterial movements and swim under remote magnetic guidance in low flows with low Reynolds numbers, e.g. in blood.[364-366] Even though those processing methods have shown a range of potential applications for 3D-structured magneto-responsive materials, they still suffer from limited scalability and heavy use of non-ecofriendly conditions.

Recently, evaporation-guided colloidal assembly has been proposed as a new method for the preparation of 3D mesoscopic nanoparticle assemblies.[367,368] In this approach, droplets of nanoparticle suspension were dried on liquid-repellent surfaces to form supraparticles.[367-369] After evaporation guided-assembly, the fabricated supraparticles can be easily collected without further processing step which prevents the use of toxic solvents.[367] Moreover, various sizes and shapes of supraparticles can be obtained. Only by tuning the concentration of the suspension and the volume of the drops, the size of the supraparticles can be varied from several microns to several millimeters. Supraparticles with various shapes, such as hemispherical,[370] doughnut-like,[371] and boat-like[372,373], have been fabricated with the simple control of the wettability of the colloidal suspension on the substrates. Additionally, the composition of supraparticles can be varied by changing or mixing different types of colloids.[368] For example, suspensions of iron-nickel alloy particles were mixed into droplets of silica nanoparticles and led to the formation of patchy supraparticles.[371]

An alternative method for the formation of large 3D superparamagnetic structures is to make use of the natural properties of ferrofluids. Colloidal suspensions of magnetic nanoparticles, known as

ferrofluid, can form a variety of transient structures when placed in a magnetic field. Ferrofluids produce reversible structures under the guidance of a magnetic field, such as Rosensweig pattern[374] or separated cone-like microdroplets when placed on non-wetting solid surfaces.[375] However, those shapes have never been used to purposely template solid materials.

In this chapter, a suspension of hybrid Fe_3O_4/polystyrene nanoparticles (mgPS NPs) was dried in the presence of a magnetic field on a superamphiphobic surface (**Figure 3.5.1**) to trap the transient shape of the suspension droplets during evaporation. By controlling the magnetic strength, magnetic orientation and the initial concentration of nanoparticles, supraparticles with distinct anisotropic shapes were obtained.
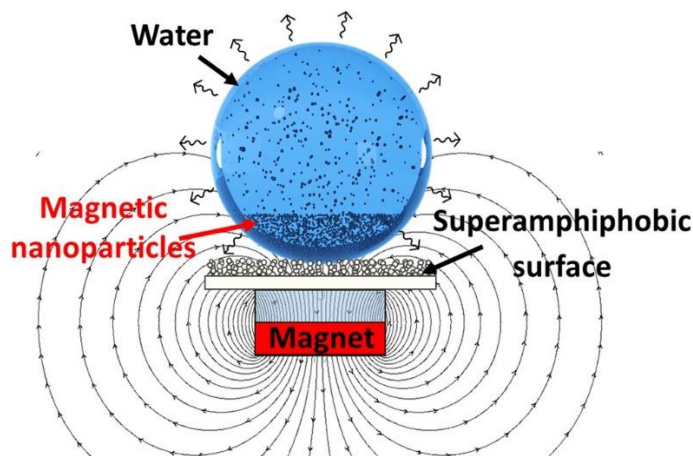
Figure 3.5.1 Experimental system used for the production of supraparticles by evaporation-guided assembly of a magnetic nanoparticles dispersion on a superamphiphobic surface.

3.5.2 Experimental

Synthesis of oleate-coated iron oxide nanoparticles (Fe$_3$O$_4$ NPs)

Oleate-coated iron oxide nanoparticles (Fe_3O_4 NPs) were synthesized by co-precipitation.[351,353] Iron(III) chloride hexahydrate (24.36 g, 90 mmol) and Iron(II) chloride tetrahydrate (12.01 g,

60 mmol) were dissolved in 100 mL water. Then, an aqueous ammonia solution (40 mL, 28 wt.%) was added dropwise under vigorous stirring and oleic acid (4.00 g, 14 mmol) was added to the solution. Subsequently, the solution was heated in an oil bath to 70 °C for one hour and then stirred at 110 °C for two hours. After the synthesis, the oleate-capped iron oxide nanoparticles were precipitated and rinsed with distilled water five times and dried in an oven at 65 °C overnight. In order to remove the excess oleate, the oleate-capped iron oxide nanoparticles were dispersed in ethanol (technical grade), separated from the solvent with a permanent magnet (NdFeB, $30 \times 30 \times 15$ mm) and redispersed in fresh ethanol, this procedure was repeated three times. **Figure 3.5.2a** shows the morphology of synthesized Fe_3O_4 NPs, their average diameter was 13 ± 4 nm (**Figure 3.5.2b**). The crystal structure of synthesized Fe_3O_4 NPs was consistent with the structure of magnetite in X-ray diffraction (XRD) spectrum (**Figure 3.5.2c**).
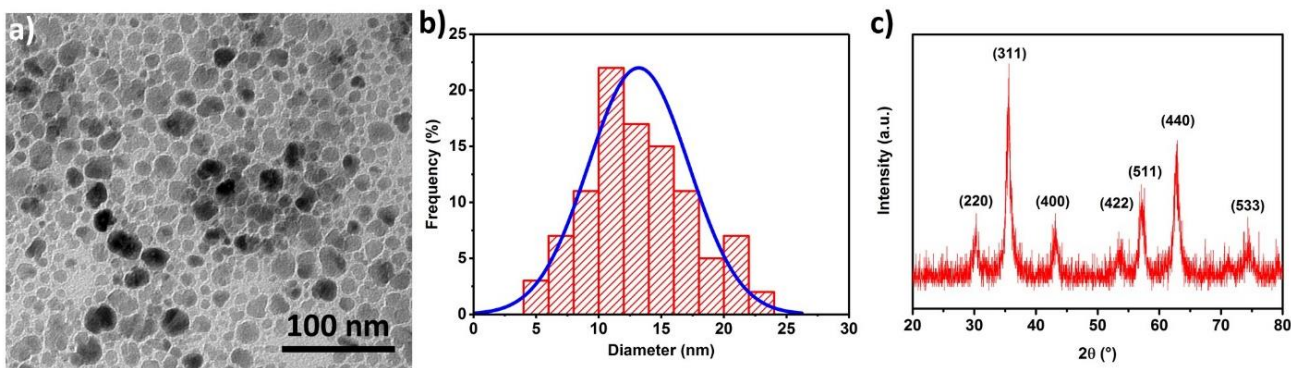
Figure 3.5.2 (a) TEM image of iron oxide nanoparticles (Fe_3O_4 NPs). (b) Histogram of the size distribution of Fe_3O_4 NPs (>100 NPs). (c) XRD spectrum of synthesized Fe_3O_4 NPs.

Synthesis of hybrid Fe_3O_4/polystyrene nanoparticles (mgPS NPs)

The Fe_3O_4 NPs (below 20 nm) were immobilized inside polystyrene nanoparticles by emulsion polymerization.[353] Briefly, 1 g of Fe_3O_4 NPs was dispersed in 0.5 g of n-octane for 30 min in a sonication bath followed by the addition of 24 g of an aqueous solution containing 24 mg of

sodium dodecyl sulfate (SDS). The two-phase suspension was sonicated with a tip (d (tip) = ½, Branson 450 Digital Sonifier, U.S.) for 3 min under ice cooling (70% amplitude, 5 s pulse, 5 s pause) and stirred using a mechanical stirrer (KPG) at room temperature. Separately, 1.2 g of styrene was mixed with 20 mg of n-hexadecane and 24 g of water containing 60 mg of SDS. An emulsion was prepared by the sonication of the water/styrene mixture with a tip (d (tip) = ½, Branson 450 Digital Sonifier, U.S.) for 1 min under ice cooling (10% amplitude, 5 s pulse, 5 s pause). The iron oxide-in-water dispersion and the styrene-in-water dispersion were mixed and then nitrogen was bubbled in the combined dispersions for of 10 min. Then, 35 mg potassium persulfate (KPS) and 30 mg of sodium styrenesulfonate were added, and the reaction mixture was heated to 80 °C under stirring for 14 h. Purification of the superparamagnetic polystyrene particles was carried out magnetically and by centrifugation. The final surface tension of the suspension was adjusted to 49 mN/m by controlling the SDS concentration.

Figure 3.5.3 shows the morphology of the synthesized hybrid Fe_3O_4/polystyrene nanoparticles (mgPS NPs) obtained by TEM, the average diameter was 93 ± 16 nm. The hydrodynamic diameter of the mgPS NPs measured by DLS (Nicomp, UK) was 110 ± 30 nm, and their Zeta potential (Zeta Nanosizer, Malvern Instruments, UK) was -67 ± 13 mV. The resulting hybrid mgPS NPs were supraparamagnetic has evidence by the variation of the magnetization in magnetic fields of different strength (**Figure 3.5.3c**).
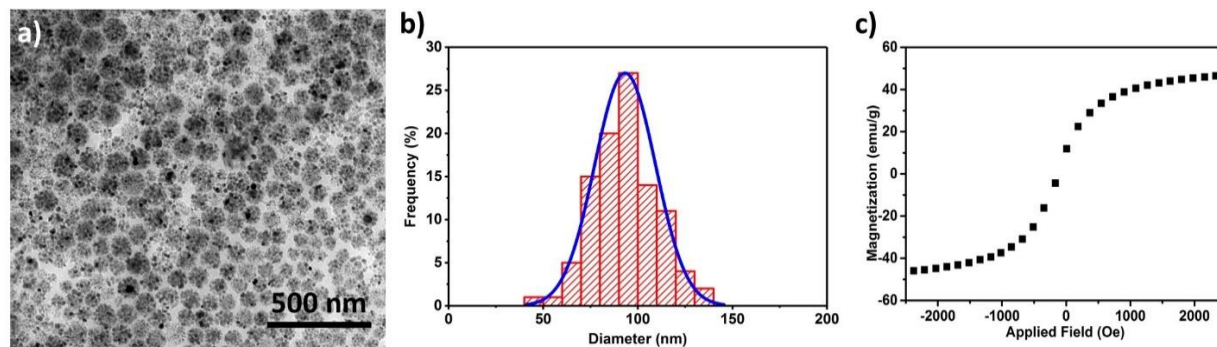
Figure 3.5.3 (a) TEM image of Fe_3O_4/polystyrene nanoparticles (mgPS NPs). (b) Histogram of the size distribution of mgPS NPs (> 100 NPs). (c) Magnetization of mgPS NPs in a magnetic field of decreasing strength at room temperature.

Fabrication of superparamagnetic supraparticles on superamphiphobic surfaces

First, soot-templated superamphiphobic surfaces were prepared following the previously described method.[379] Briefly, soot particles were deposited on the glass substrate by the candle-soot deposition method. Then 10-20 nm SiO_2 layer was coated on those particles by chemical vapor deposition of tetraethoxysilane catalyzed with ammonia. The soot particles were removed by heating at 550 °C, resulting in a fractal-like structure of SiO_2 with overhangs. The superamphiphobic surface was finally obtained by surface modification with trichloro(1H,1H,2H,2H-perfluorooctyl)silane which lowered the surface energy.

To fabricate the supraparticles, droplets of an aqueous suspension of mgPS NPs (from 0.3 wt% to 30 wt%) were deposited using a micropipette on the superamphiphobic surface. To generate the magnetic field, a permanent magnet (NdFeB, $30 \times 30 \times 15$ mm) was placed under the superamphiphobic surface. By controlling the distance between the magnet and the surface, it was possible to tune the strength of the magnetic field. The magnetic field was measured at the surface

119

of the superamphiphobic substrate. Unless noted otherwise, the supraparticles were formed using 5 uL of suspension dried at a temperature of 23 °C under a humidity of 25%.

To obtain binary supraparticles, titanium dioxide nanoparticles (TiO_2 NPs, 25 nm, Aldrich, Germany) and polystyrene nanoparticles (PS NPs, 270 nm) were dispersed in distilled water to reach different concentrations and then mixed with a concentrated suspension of mgPS NPs in order to obtain a final nanoparticles concentration of 6 wt%.

Investigation of supraparticles magnetically-controlled movement

The supraparticles were put in a petri dish with distilled water. The movement of those supraparticles was controlled by displacing a permanent magnet (NdFeB, $50 \times 10 \times 10$ mm) at different positions. The trajectory, moving speed, and orientation of the supraparticle over time in distilled water were analyzed with ImageJ.

Characterizations

The drying process of droplets was monitored with a goniometer equipped with a side-camera (OCA 35, DataPhysics, Germany). The movie of drying droplets was recorded at 12 frames/min and for ca. 1 h. The movie was extracted and analyzed to obtain the contact angle and contact line over time using MATLAB. The morphologies of the supraparticles were obtained with a stereomicroscope (M80, Leica, Germany) equipped with a digital camera (IC80 HD, Leica, Germany). To observed the inner structures of supraparticles, they were first embedded in epoxy resin and then sliced (slice thickness of 500 nm) with an ultramicrotome (EM UC7, Leica, Germany). The magnetic properties of mgPS NPs and supraparticles were obtained with a vibrating-sample magnetometer (Cryogenic Ltd. UK). The morphologies of the nanoparticles and supraparticles were observed by transmission electron microscopy (TEM, JEOL JEM1400, Japan)

and scanning electron microscopy (SEM, Hitachi SU8000, Japan). For the chemical analysis of

the supraparticles´ surface and interior, the SU8000 with an energy dispersive x-ray spectrometer

(EDX) was used to measure the elemental composition.

3.5.3 Results and discussion

The use of superamphiphobic substrates was critical to obtained 3D supraparticles. When, instead,

only hydrophobic substrates were used, film-like structures were observed due to the strong

pinning effect caused by the more important wetting of the substrate by the colloidal suspension

(**Figure 3.5.4**).
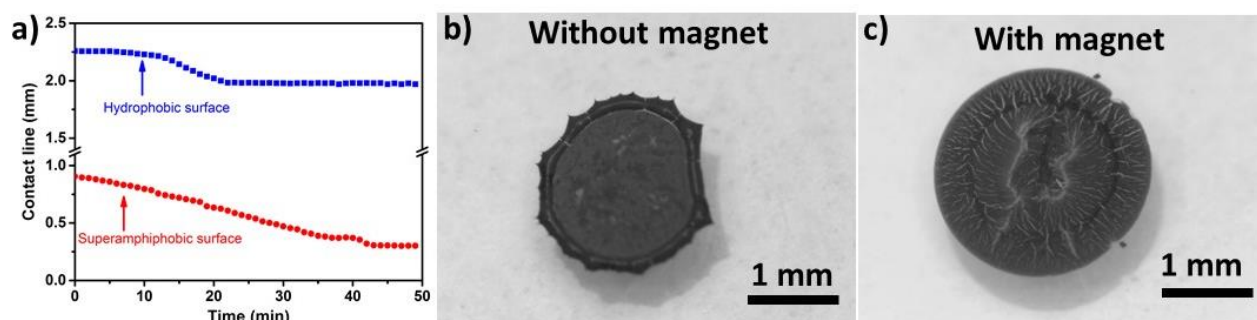
Figure 3.5.4 (a) Comparison between the drying kinetic of ferrofluid droplets (3 wt.%) on a
hydrophobic fluorinated surface (blue) and a superamphiphobic (red) surfaces. Drying of a 3 wt.%
droplet of ferrofluid on the hydrophobic fluorinated surfaces without (b) and with (c) a magnetic
field of 2 kOe.

To fully understand the effect of the presence of a magnetic field on the supraparticles formation,

the drying process of superparamagnetic NPs suspensions with and without magnetic field was

observed under the same drying conditions. **Figure 3.5.5** shows that in the absence of a magnetic

field, the spherical droplet shrunk symmetrically as a consequence of water evaporation. After

35 min, the shape of the droplet changed through a buckling mechanism, i.e. after reaching a

critical composition, a sudden deformation of the droplet occurred. The resulting anisotropic

structure, shaped like a deflating ball, subsequently shrunk further without notable alteration in its shape during the final part of the drying process. This buckling behavior was caused by the non-uniform distribution of mgPS NPs and surfactant molecules within the droplet.
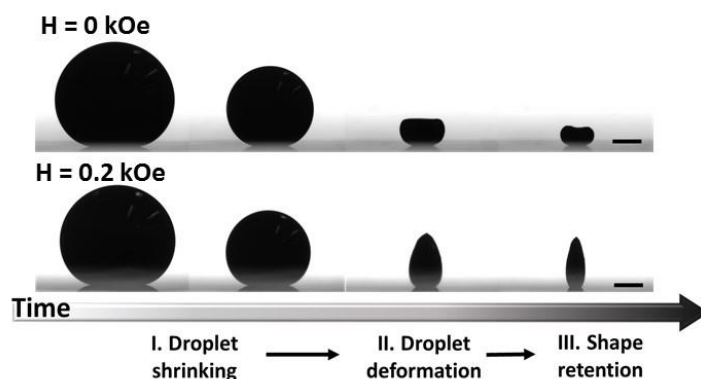
Figure 3.5.5 Evolution of a 3 wt.% droplet during drying without (upper panel) and with (bottom panel) magnetic field. Scale bars are 0.5 mm.

Energy dispersive X-ray spectroscopy was used to analyze the distribution of surfactant and mgPS NP across the volume of the supraparticle (**Figure 3.5.6**). The concentrations of sulfur and iron were used as respective indicators for the concentration of surfactant and mgPS NPs (**Table 3.5.1**).
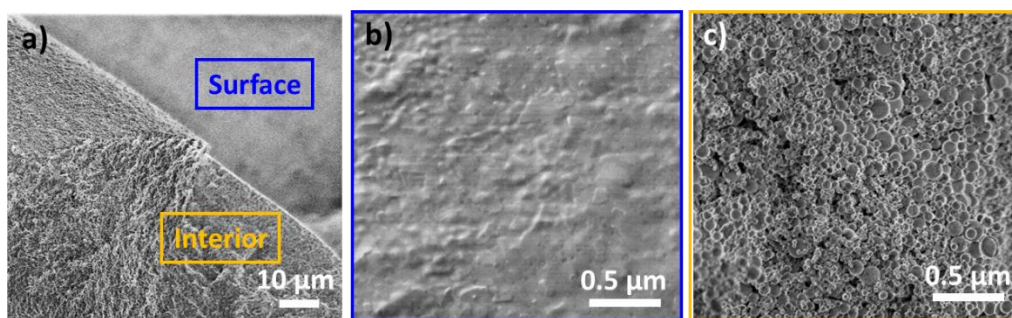
Figure 3.5.6 Inner structure of a supraparticles. The particle was obtained by drying a 21 wt.% suspension of ferrofluid. (a) SEM images of the cross-section of the supraparticle. And zoomed-in SEM images of (b) surface and (c) interior of the supraparticle.

Table 3.5.1 Elemental composition of different areas of the cross-sections of supraparticle.

Atom %	Surface	Interior
C	61.47	53.07
O	25.54	32.49
Na	2.05	0
S	3.63	0.4
Fe	7.31	14.04

The results show that the surface of the supraparticles was enriched in surfactant in comparison to the bulk which was richer in mgPS NPs. During the evaporation, the concentration of NPs and surfactants at the air/water interface increased, leading to the formation of a shell. As the amount of water in the droplet kept decreasing, a mechanical stress built up in the shell. To release this stress, the shell rapidly deformed and the droplet buckled. As a result, the contact line remained constant while the surface of the drop wrinkled (**Figure 3.5.7a**). This buckling behaviour was similar to what has been previously observed for suspension of silica or polystyrene NPs drying on the superhydrophobic surfaces,[371,372] and reminiscent of what has been observed during spray drying of microdroplets of colloidal suspension.[376]
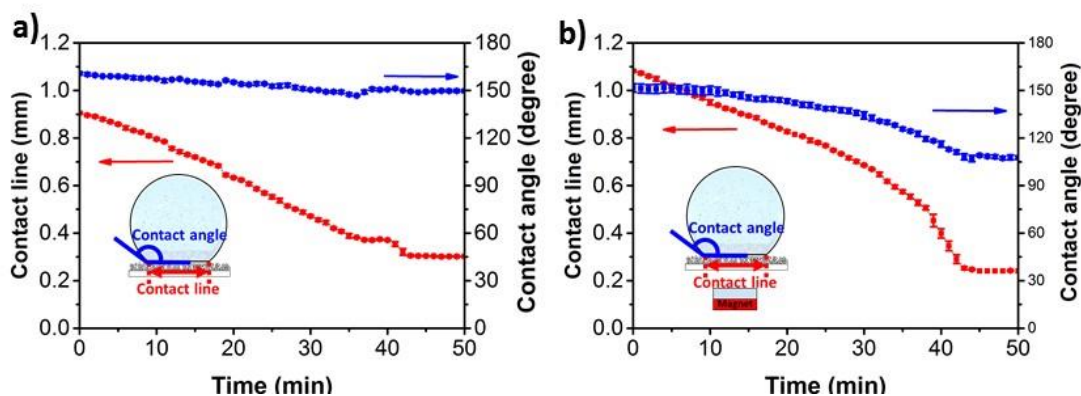
Figure 3.5.7 Drying curve of the droplet (a) without and (b) with magnetic field. Insets represent the dimensions measured during drying.

In the presence of a magnetic field of 0.2 kOe, the initial contact line was larger than that observed without magnetic field since the magnetic attractive force is driving the NPs to partially segregate at the bottom of the droplet. Initially, the volume of the droplet decreased symmetrically by evaporation preserving the original aspect ratio. However, after 30 - 40 min, the aspect ratio of the droplet started to change; the droplet became narrower and more elongated over the following 2 - 10 min, the height of the droplet quickly increased, and the droplet formed a cone-like structure. After this point, the shape and aspect ratio of the supraparticles was preserved until evaporation of the remaining water. Ultimately, the final shape of the supraparticle was reached and preserved after ca. 45 min (**Figure 3.5.7b**).

To control the shape of the ferrofluid droplets, the magnetization of the droplets has to be considered. The net magnetization of mgPS NPs changes with the applied magnetic field (*H*) and is described by:[374]

$$M(H) = \chi(H)H \quad (\textbf{3.5.1})$$

where χ is the volume magnetic susceptibility of materials. Furthermore, the magnetization (*M*) of the ferrofluid suspension depends on the NP concentration, as it is proportional to the volume fraction of superparamagnetic material in the suspension. According to the Rosensweig theory:[374,377]

$$M \propto \frac{V_{Fe_3O_4NPs}}{V_{Droplet}} \quad (\textbf{3.5.2})$$

where $V_{Fe_3O_4NPs}$ is the volume of iron oxide nanoparticles and $V_{Droplet}$ is the volume of the droplet. Consequently, the initial concentration of nanoparticles (c_{NP}) in the ferrofluid droplet and the applied magnetic field were varied to investigate the relationship between the final shape of the supraparticle and conditions under which drying was performed.

The initial c_{NP} was varied from 0.3 wt.% to 30 wt.%, and the droplet dried in a magnetic field of 0.2 kOe. The initial contact angle decreased and the initial contact line increased with increasing c_{NP}, since at higher concentration a larger number of nanoparticles was dragged to the interface. This led to an increase in the apparent wetting of the surface by the suspension, characterized by a lower contact angle and higher contact line (**Figure 3.5.8a**).
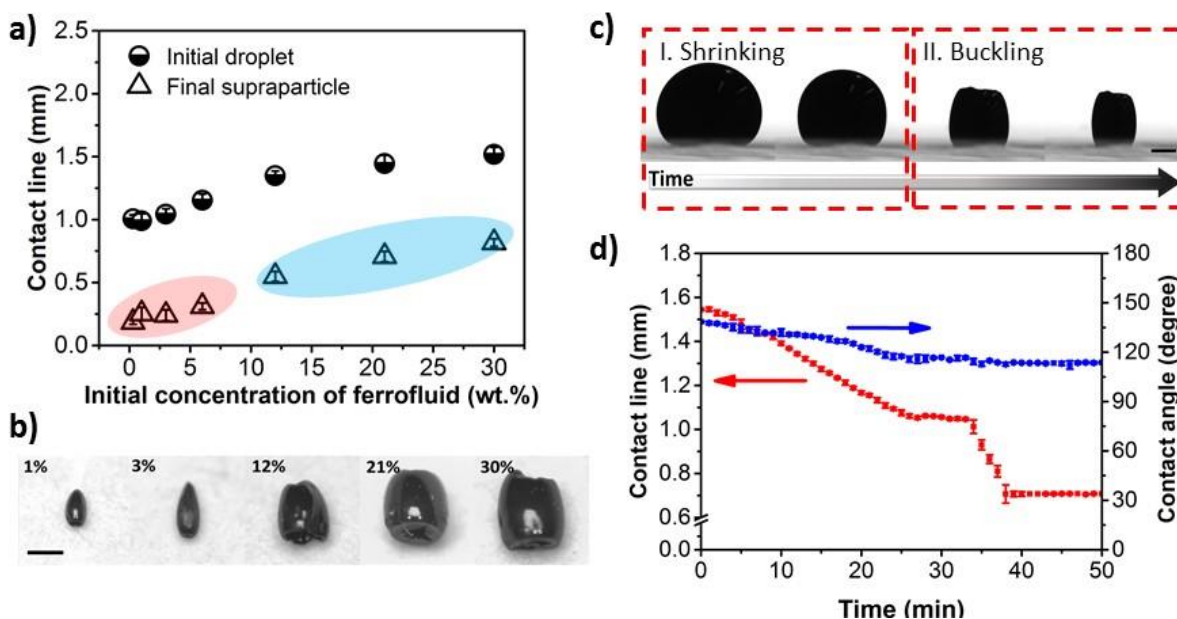
Figure 3.5.8 Drying kinetics of ferrofluid droplets in magnetic fields of 0.2 kOe. (a) Contact lines of the initial droplets and of the resulting supraparticles as a function of initial concentration of nanoparticles (c_{NP}). The red regime indicates cone-like structures. The blue regime indicates barrel-like structures. (b) Optical photos of supraparticles prepared with different initial c_{NP}. Scale bar is 0.5 mm. (c) Side-view pictures of the drying process for $c_{NP} = 21$ wt.%. Scale bar is 0.5 mm. (d) Evolution of contact angle and contact line during the drying of initial $c_{NP} = 21$ wt.%.

The drying of suspensions with different c_{NP} resulted in the formation of supraparticles with distinct shapes. In a magnetic field of 0.2 kOe, two populations of supraparticles were observed: cone-like structures at low c_{NP} (≤ 6 wt.%) and barrel-like structures at high c_{NP} (**Figure 3.5.8b**).

The cones were partially empty; a cavity was formed at the interface between the droplet and the superamphiphobic surface. The formation of this cavity can be attributed to a buckling effect directed by the magnetic field and the presence of the superamphiphobic surface. Particles jamming created by the combined effect of solvent evaporation and magnetic field led to the formation of a stiff layer of particle at the droplet/surface interface, when this layer was unable to shrink further, buckling happened creating the cavity. Conversely, suspensions with high c_{NP} (≥ 12 wt.%) resulted in supraparticles with barrel-like structures. The inner part was completely empty and was opened from top-to-bottom; the result of the combined effect of the buckling and dewetting (**Figure 3.5.9**).
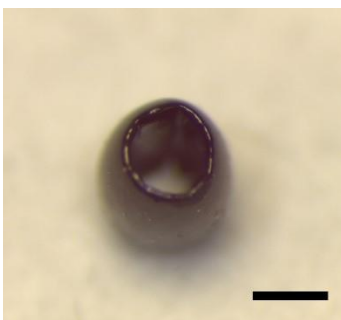
Figure 3.5.9 Top view of the barrel-like supraparticle (prepared in a 0.2 kOe magnetic field and $c_{NP} = 21$ wt.%). Scale bar is 0.5 mm.

Initially, the ferrofluid droplet was spherical and shrunk symmetrically during the water evaporation. Then the aspect ratio of the droplet started to increase, which is similar to what was observed for lower c_{NP} leading to the formation of a conical droplet (**Figure 3.5.8c** and **Figure 3.5.10a**).
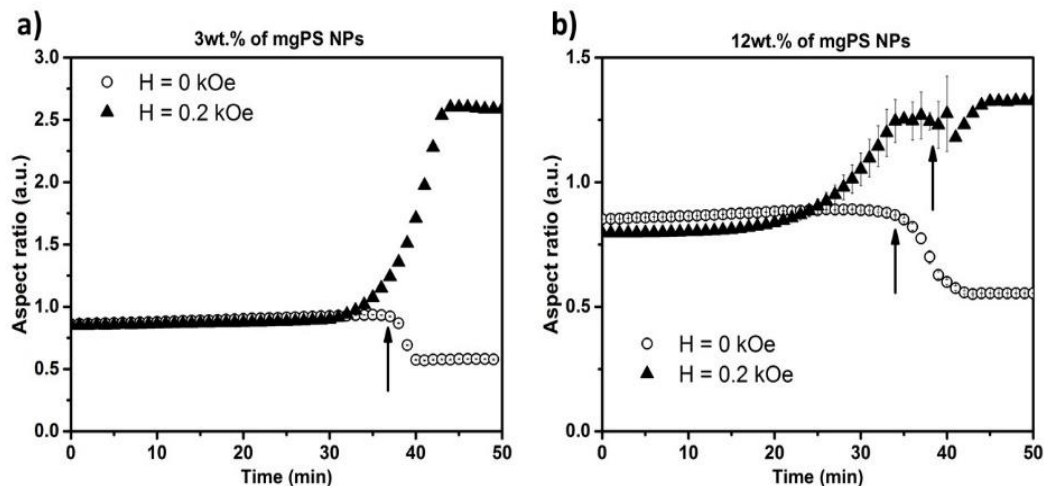
Figure 3.5.10 Change in the aspect ratio of the droplet during evaporation without and with magnetic field (H = 0.2 kOe). The initial concentration is (a) 3 wt.% and (b) 12 wt.%. The arrows indicate the beginning of droplet buckling.

Afterward, the height of the conical ferrofluid droplet increased until it reached a critical point where buckling happened, resulting in the formation of a barrel-like structure within minutes. This buckling effect was also observable in the variation of the contact line over time (**Figure 3.5.10b**). The buckling happened where a strong discontinuity was monitored toward the end of the drying process. For example, during the drying of a suspension with $c_{NP} = 21$ wt.% in a magnetic field of 0.2 kOe, the contact line decreased during the first 25 min. Then, the contact line and the width of the droplet remained constant for ca. 5 min, and only the height of the droplet decreased until the droplet buckled. Following the buckling of the droplet, a rapid decrease in the contact line was observed and the final barrel-like supraparticle was obtained. The barrel like-structure is the stretched version of toroid formed with non-magnetic suspension drops.[371]

To investigate further the influence of the strength of the magnetic field a series of experiments at 2.0 kOe was conducted. Similarly to the behavior observed in *H* = 0.2 kOe, the contact line of the

droplets increased with increasing c_{NP}, but, in every case, the contact line at 2.0 kOe was larger than at 0.2 kOe. In a field of 2.0 kOe, especially at higher c_{NP}, the effect of the strong field led of an increase of the contact line of the droplets on the surface (**Figure 3.5.11a**), since the magnetic attraction forces acting on the nanoparticles were stronger and dragged the mgPS NPs to the substrate, increasing the apparent wetting of the superamphiphobic surface.
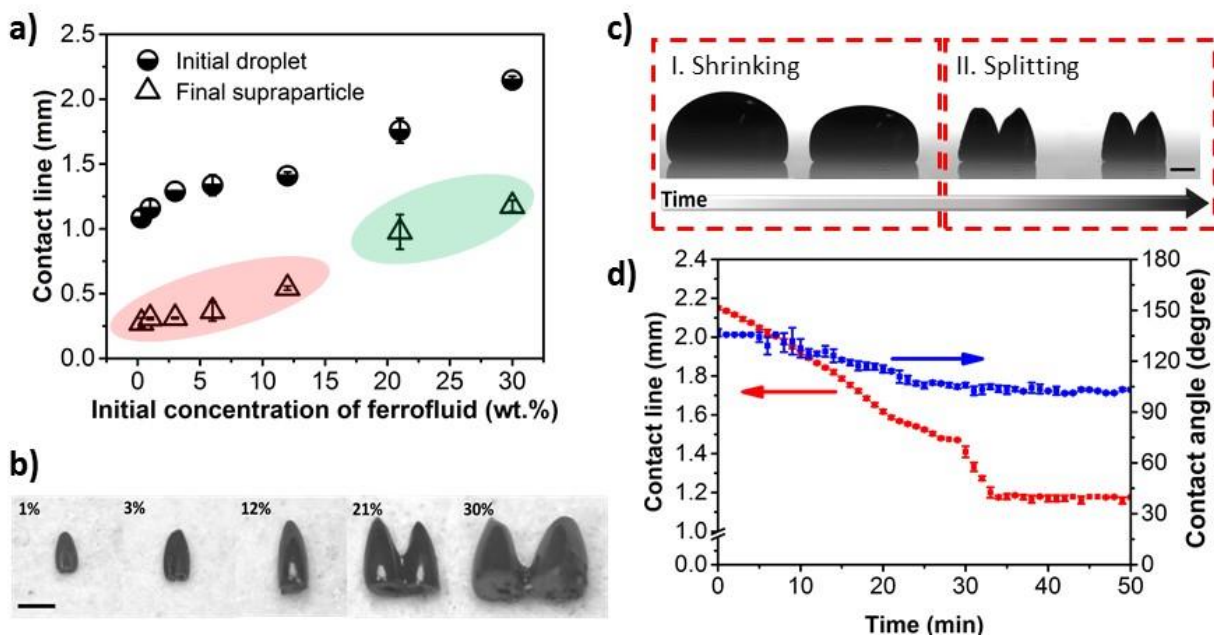
Figure 3.5.11 (a) Contact lines of the initial droplet and of the resulting supraparticle as a function of initial c_{NP}. The red regime indicates cone-like structures. The green regime indicates two-tower-like structures. (b) Optical photos of supraparticles prepared with different initial c_{NP}. Scale bar is 0.5 mm. (c) Side-view pictures of drying process for $c_{NP} = 30$ wt.%. Scale bar is 0.5 mm. (d) Time evolution of contact angle and contact line of initial $c_{NP} = 30$ wt.% during evaporation.

In a magnetic field of $H = 2$ kOe two different types of shapes, either cone-like structure or two-tower-like structures, were observed. Similarly to what was observed with $H = 0.2$ kOe, lower c_{NP} (≤ 12 wt.%) led to the formation of empty cone-like structures. However, at higher c_{NP} (≥ 21 wt.%), the nanoparticles formed two-tower-like structures instead of barrel-like shapes. (**Figure 3.5.11b**)

At high H and high c_{NP}, the ferrofluid droplets did not buckle into a barrel-like structures, but rather split into two cone-like shapes during evaporation (**Figure 3.5.11c**). This splitting effect was observed in the variation of the contact line over time. For example, during the drying of a suspension with $c_{NP} = 30$ wt.% in a magnetic field of 2.0 kOe, the contact line first decreased for ca. 25 min. Then the contact line remained constant, during that time, the top part of the droplet split into two separated fractions (**Figure 3.5.11d**).

This behavior was similar to what has been observed for the splitting of ferrofluid droplets on superhydrophobic substrates under variable magnetic fields.[375] It is known that ferrofluid drops can spontaneously split into several smaller droplets when the drop size (contact line of the droplet) is larger than a critical wavelength (λ_C):[375]

$$\lambda_C \approx 2\pi \sqrt{\frac{\sigma}{\frac{d}{dz}(\mu_0 HM)}} \quad \textbf{(3.5.3)}$$

where, σ is surface tension, μ_0 is vacuum permeability, H is the total magnetic field intensity and M is the magnetization of the drop, d/dz is the change in z-direction (normal to the surface). In the present case, the splitting phenomenon was more complex, because during evaporation, both σ and M are changing since those parameters are concentration dependent. During the drying of the droplets, the change of σ was moderate and similar for all samples with different c_{NP} because the initial concentration of surfactant molecules was the same in all samples. However, the change of magnetization over time, $M(t)$, was not the same at every c_{NP}. As the water evaporated, $V_{Droplet}$ decreased over time resulting in an increase of the magnetization during drying, which finally led to a decrease in λ_C. Consequently, even if, initially, at high c_{NP} the system was below the λ_C, droplet splitting could be observed during the drying process as the concentration and consequently the magnetization increased. The critical concentration where the magnetization was large enough

129

to induce a splitting of the droplet was reached after ca. 30 min at 21 wt.% and 26 min at 30 wt.%

(**Figure 3.5.12**).
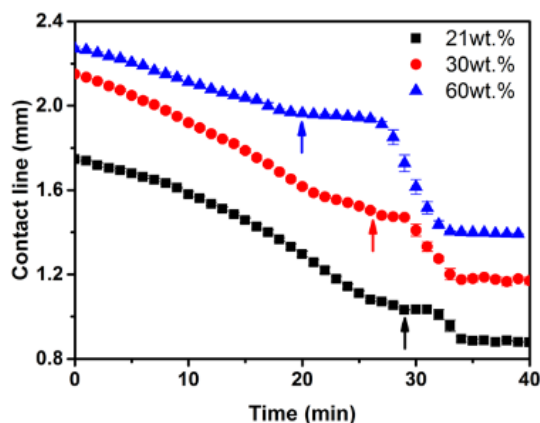
Figure 3.5.12. Drying kinetics of ferrofluid droplets with different initial concentrations (21 wt.%, 30 wt.%, and 60 wt.%) in a magnetic field of 2 kOe. The arrows indicate the beginning of droplet splitting.

The relation between the size of the contact line and the splitting of the droplet was also corroborated by using droplets of different volume with $c_{NP} = 21$ wt% (**Figure 3.5.13**). During the drying kinetics, droplets of different volume have the same magnetization and surface tension, but the contact line decreases with the initial volume of the droplet while λ_C stayed constant.
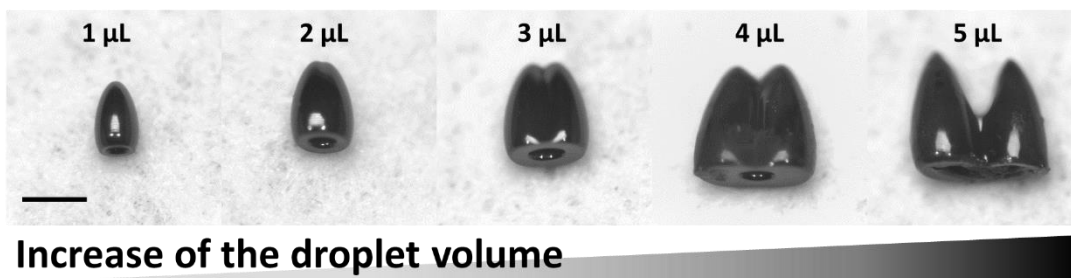
Figure 3.5.13 Microscopic images of supraparticles fabricated from drying 21 wt.% of ferrofluid droplet with different volumes (from 1 µL to 5 µL) in a magnetic field of 2 kOe. Scale bar is 0.5 mm.

Thus, smaller droplets, having smaller initial contact lines, did not experience splitting because the contact line remained constantly smaller than λ_C.

Figure 3.5.14a summarizes the diversity of supraparticle shapes obtained as a pseudo-phase diagram of the initial NPs concentrations and applied magnetic fields. Four different shapes were obtained for the resulting supraparticles: deflating-ball, cone, barrel and two-tower. The difference in the final structure adopted by the drying droplet depended on the complex balance of the forces present in the system, where wetting, buckling and magnetic force all influence through different mechanism the final structure observed.

Figure 3.5.14b shows that the shapes of the supraparticles can be adjusted by changing the direction of the applied magnetic field during the drying process. When the direction of the magnetic field was changed from 90° to 60°, the resulting supraparticles showed similar structures but have different orientation following the directions of the magnetic field. Furthermore, complex heterostructures can be prepared by drying co-suspension of mgPS NPs and other nanoparticles.[371,379]

 For examples, cone-shape supraparticles were prepared by drying a mixture of TiO_2 NPs and mgPS NPs (**Figure 3.5.14c**). Similarly, anisotropic supraparticles were also obtained when mgPS NPs were mixed with pure polystyrene NPs (**Figure 3.5.14d**). In both cases, the mgPS NPs droved the droplet to form anisotropic supraparticles when the concentration of mgPS NPs was above a threshold ratio to actively act as a templating agent. Since the magnetization of the droplet is a function of the concentration of magnetic iron oxide in the droplet, as the ratio of non-magnetic particles increased, the shape selectivity was lost. The formation of supraparticles by the evaporation of co-suspension droplets shows the flexibility of magnetic templating to form complex supraparticles with different architectures, chemical compositions and functions.
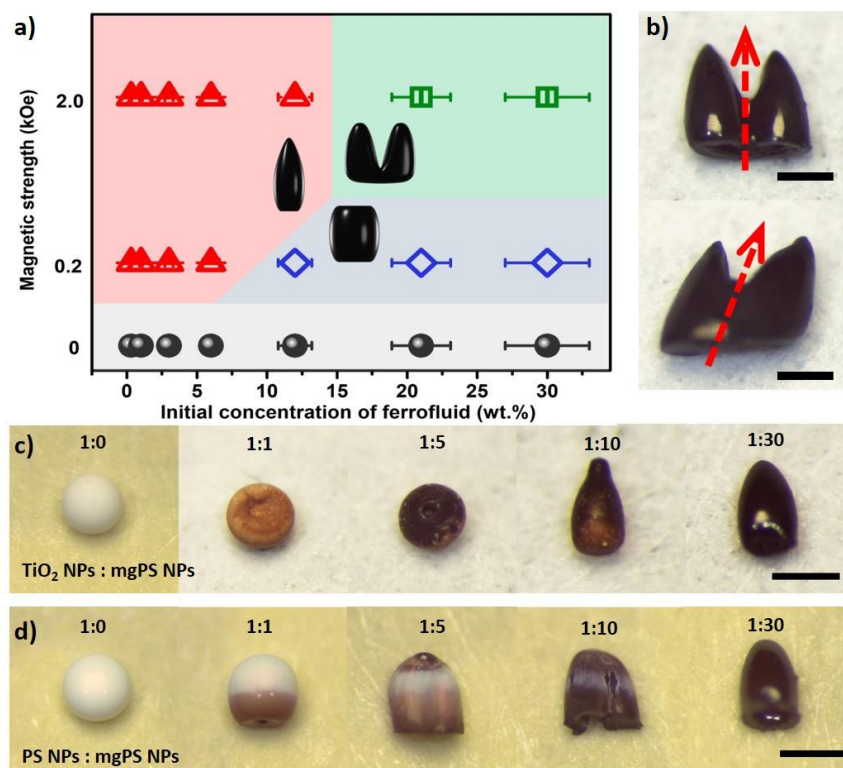
Figure 3.5.14 (a) Pseudo-phase diagram of the supraparticles obtained with the variation of the magnetic strength and initial concentration of ferrofluid. The regime in grey, red, blue and green indicates supraparticle with, respectively, deflated-ball, cone, barrel, two-tower shape. (b) Two-towers-shape supraparticles with different tower orientations by drying the 21 wt.% of ferrofluid under different directions of the magnetic field (left one with the vertical direction and the right one with non-vertical direction, both were under a magnetic field of 2 kOe). Scale bars are 0.5 mm. (c-d) Binary supraparticles fabricated by drying a co-suspension of mgPS NPs with (c) titanium dioxide NPs and (d) hybrid Fe_3O_4/polystyrene NPs. The weight ratio of titanium dioxide nanoparticles and ferrofluid was varied from 1:0 (left) to 1:30 (right). In c and d, the total initial NPs concentration is 6 wt.% and the magnetic field is 2 kOe. Scale bars are 0.5 mm.

The anisotropic supraparticles obtained by drying mgPS NPs preserved the superparamagnetism of the building blocks. The saturated magnetization of mgPS NPs and supraparticles was 55 emu/g

and 52 emu/g, respectively (**Figure 3.5.15a**). Thus, their magneto-responsive behavior could be harnessed to magnetically control the supraparticles.
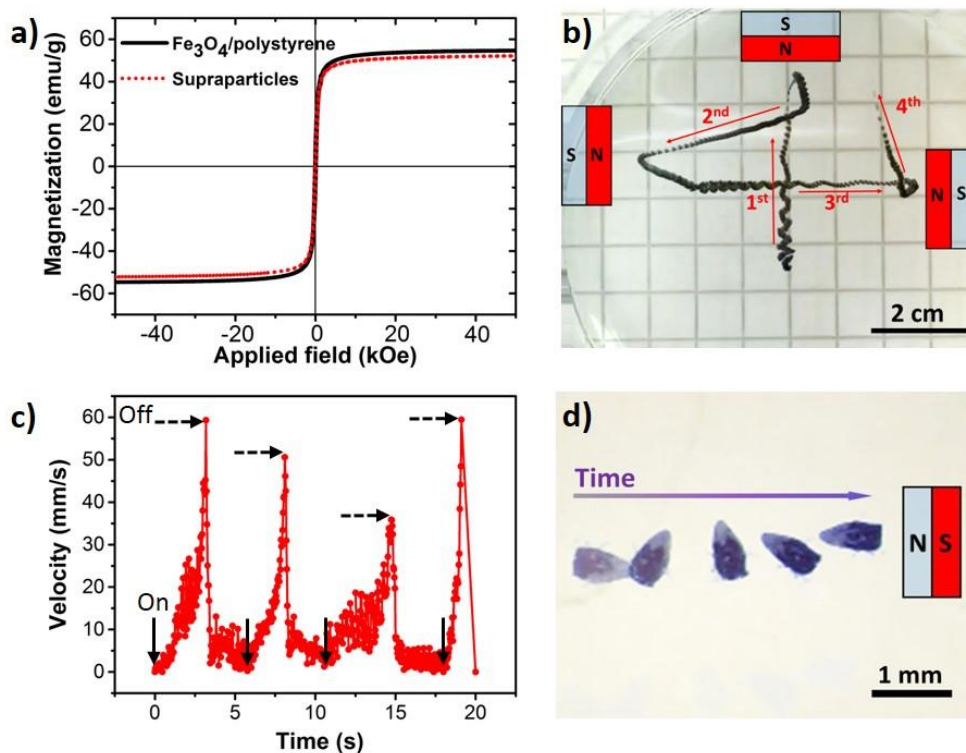
Figure 3.5.15. Supraparticle in a remote magnetic field. (a) Magnetic property of the supraparticles characterized by vibrating-sample magnetometer. (b) Trajectory of a cone-like supraparticle in suspension in water with varied magnetic fields. Insets cartoons indicate the positions of magnets. The order of applied magnetic fields was top, left, right, and top. (c) Velocity of the cone-like supraparticle shown in figure 3.5.15b. The arrows indicate the time of the on/off triggering of the magnetic field. (d) Time-lapse image of the reorientation of a cone-shaped supraparticle in distilled water under the influence of a magnet located on the right side.

Figure 3.5.15b shows the behavior of a cone-like supraparticle in a magnetic field acting as an active microswimmer. First, the movement of the supraparticle in suspension in water was controlled by applying selected magnetic fields. The trajectory of this supraparticle was tailored by the on/off triggering the magnetic field at different locations. The response speed of the

supraparticle was fast, immediately when the magnetic field was turned on, the supraparticle moved and quickly stopped when the magnetic field was removed (**Figure 3.5.15c**). The supraparticle not only followed the magnetic field but also reoriented itself in response to the application of the magnetic field. The bottom part of the cone-like supraparticle was always facing the magnet due to the anisotropy of the supraparticle (**Figure 3.5.15d**). Similar behavior was also observed in a rotational magnetic field.

3.5.4 Conclusion

In summary, the superparamagnetic supraparticles have been successfully prepared by the evaporation-guided assembly of ferrofluid droplets on a superamphiphobic surface in presence of a magnetic field. These magneto-responsive supraparticles have well-defined structures such as deflated-ball, cone, barrel, and two-tower shapes. The final 3D architecture of the supraparticles can be tuned by systematically varying the initial concentration of superparamagnetic nanoparticles and the applied magnetic field. Moreover, the ferrofluid suspension can be used as the driving force to template the assembly of co-suspension of superparamagnetic nanoparticles and other functional nanoparticles to fabricate functional anisotropic binary supraparticles. Thus, this flexible fabrication process offers the possibility for creating anisotropic and magneto-responsive supraparticles with various materials. Since these anisotropic supraparticles are magneto-responsive, their orientation and motion can be spatially controlled by magnetic fields.

4. Summary and outlook

4.1 Summary

In summary, this thesis highlights promising hybrid functional materials based on the combination of nano-objects and polymer. A library of new functional nano-objects have been successfully developed and used to prepared functional hybrid materials: silica/polymer nanocapsules with self-reporting function, iron oxide/polystyrene hybrid nanoparticles with superparamagnetism assembled in anisotropic supraparticles, disentangled single-chain polystyrene nanoparticles, spindle-shaped hematite (α-Fe_2O_3) nanoparticles with catalase-like activity embedded in polymer fibers, and cerium oxide (CeO_{2-x}) nanorods with haloperoxidase-like activity embedded in a crosslinked polymer matrix.

In **Chapter 3.1**, a self-reporting nanocapsule-based system, which was subsequently used to monitor the appearance of micro-cracks in coatings as well as the healing of those micro-cracks, has been successfully fabricated. To do so, a three-component capsule was designed which contains an inactive dye in the liquid core, a protective polymer shell and color-developing silica nanoparticles on its surface. Breakage of the shell enables autonomous damage-reporting *via* development of an intense blue color. When the capsules were assembled into polymer coatings, they broke upon the formation of micro-damages due to mechanical stresses in the coating and thus highlighted the damaged spots. The visually highlighted spots were removed through the interaction of the dye with different self-healing compounds or byproducts of self-healing reactions leading to the subsequent color deletion. Hence, the system can be applied to monitor the appearance and healing of damages in coatings by introducing a second type of capsular or vascular systems to release the healing compounds. Such a reversible self-reporting system with

high versatility could be applied in a new generation of self-reporting coatings which have multiple autonomous functions to monitor the whole health cycle of artificial materials.

In **Chapter 3.2**, linear polystyrene with high molecular weight (M_n=1.1×10^6) has been used to produce nanoparticles by electrospraying. The diameter of the nanoparticles obtained was 20 nm, which was similar to the size of a disentangled single-chain nanoparticles predicted by theoretical calculation. Those nanoparticles had a lower glass transition temperature in comparison to the bulk material. Compared with the bulk polystyrene, the glass transition temperature of polystyrene nanoparticles decreased from 107 to 98 °C, indicating the enhancement of mobility of the polymer chains. Therefore, these nanoparticles may be used to produce the polymer melt without or with fewer entanglements, which would be highly useful for the polymer processing in the industry.

In **Chapter 3.3**, spindle-shaped hematite (α-Fe$_2$O$_3$) nanoparticles with catalase-like activity have been prepared by forced hydrolysis of ferric chloride in water. These hematite nanoparticles were integrated at various concentrations in water-soluble polymer mats *via* electrospinning. To retain the fibrous scaffold in the presence of water, the membranes were crosslinked to form a stable fibrous gel. After cross-linking, the membranes showed high water permeability and hence provided a good accessibility of hydrophilic compounds to the embedded hematite particles. The encapsulated hematite showed a high catalase-like activity and quickly converted H$_2$O$_2$ into O$_2$. When incubating fibroblasts at an H$_2$O$_2$ concentration of 50 μM, the catalytically active material efficiently reduced the H$_2$O$_2$ concentration and enabled undiminished cell proliferation. Thanks to this catalase-like activity, the hybrid nanofibrous gel could be used for improving the wound healing process.

In **Chapter 3.4**, anisotropic cerium oxide (CeO$_{2-x}$) nanorods with haloperoxidase-like activity have been synthesized by hydrothermal synthesis. Various concentrations of cerium oxide nanorods

were integrated into polymer fibers by electrospinning. To improve the stability of polyvinyl alcohol (PVA) fibers in aqueous media, the fibers were crosslinked to form a water-swellable PVA mat. The PVA mats showed a high water swellability; therefore, the hydrophilic compounds can easily access the embedded cerium oxide nanorods to trigger the catalytic reaction. The embedded nanoparticles showed a haloperoxidase-like activity and were able to convert Br^- and H_2O_2 to HOBr efficiently, allowing the prevention of bacterial adhesion. Thanks to this haloperoxidase-like activity in the PVA mats, they could be used as robust coatings with anti-biofouling property in humid and marine environments.

In **Chapter 3.5**, a new bottom-up assembly approach has been introduced. The superparamagnetic supraparticles with various anisotropic micro-structures have been fabricated by the evaporation-guided assembly of ferrofluid droplets on a superamphiphobic surface in presence of a magnetic field. These magneto-responsive supraparticles had various well-defined structures such as deflated-ball, cone, barrel, and two-tower shapes depending on the conditions used for their preparation. The final 3D architecture of the supraparticles can be tuned by systematically varying the initial concentration of superparamagnetic nanoparticles and the applied magnetic field. Moreover, the ferrofluid suspension can be used as the driving force to template the assembly of co-suspension of superparamagnetic nanoparticles and other functional nanoparticles to fabricate functional anisotropic binary supraparticles. Thus, this flexible fabrication process offers the possibility of creating anisotropic and magneto-responsive supraparticles with various materials. Since these anisotropic supraparticles were magneto-responsive, their orientation and motion can be spatially controlled by external magnetic fields.

Overall, the hybrid functional materials have been successfully developed by two strategies: either the fabrication of new functional nano-building-blocks (nano-objects) or the processing of nano-

building-blocks into hierarchical structured polymer/nanoparticle hybrid materials. Following the first strategy, new functional nano-building-blocks, including hybrid nanocapsules (**Chapter 3.1 and 3.5**), polymer nanoparticles (**Chapter 3.2**), and inorganic nanoparticles (**Chapter 3.3 and 3.4**), have been fabricated. By assembling these functional nano-objects in polymer matrices, materials with "self-reporting", wound healing and anti-biofouling functions have been produced. Moreover, a new assembly method, which combined evaporation-guided assembly and magnetic assembly, has been developed to generate 3D anisotropic microstructures with superparamagnetic function. These new assemblies were successfully remotely controlled by magnetic field and could find potential applications in micro-robotics (**Chapter 3.5**).

4.2 Outlook

This thesis showed the promising perspectives and possibilities of assembling functional nano-building-blocks into hierarchical structures to provide the resulting materials with new functions. It explores the possibility of using such attractive hybrid functional materials in applications such as coatings, wound healing and micro-robotics. But the new functional assembled materials are not limited to those described assembled structures and application fields. There are still more to be explored.

Specifically, nanocapsules with self-reporting functions (**Chapter 3.1**) can be developed further to broaden the scope of potential applications. It is clear that such functional nanocapsules can indicate damage or exposure to excessive stress with an optical signal. Moreover, the damage-visualization effect could be realized with different types of dyes (from visible dye to fluorescent one) and different mechanism of activation (from mechanical stress to pH or temperature stimuli). This could be helpful to remotely monitor the health of surfaces that are difficult to access.

In **Chapter 3.2**, single-chain nanoparticles without entanglement were developed. This kind of material will be helpful for the polymer processing due to the large decrease of the viscosity of the polymer melt. The polystyrene has been used as a model polymer to show the possibility of fabricating such nanoparticles by electrospraying. However, other polymers that are widely used in our daily life could be fabricated into disentangled polymer nanoparticles to improve their processing. This would allow the use of high molecular weight polymers in traditional processing method which would lead to the fabrication of plastic-based consumer products with better mechanical properties.

Besides fabrication nanoparticles by electrospraying, the same process can be used for the electrospinning of one-dimensional nanofibers. In **Chapter 3.3 and 3.4**, it has been shown that the inorganic nanoparticles with enzyme-like activities have been successfully integrated into polymer nanofiber by electrospinning and were able to catalyze the reaction. It is not limited to the inorganic nanoparticles, polymer nanoparticles or hybrid nanoparticles could be integrated easily into nanofibers by electrospinning. The electrospinning process can not only immobilize the nano-object inside the fibers, but also align them into a specific order. Therefore, anisotropic functional membranes could be prepared. More generally, electrospinning of nanoparticles/polymer hybrids was shown to be a convenient method to embedded nanoparticles into a robust and easy to use materials.

In **Chapter 3.5**, materials with anisotropic microstructure have been fabricated by the combination of evaporation-guided assembly and magnetic assembly. This new assembly method shows the possibility of fabricating supraparticles with various shapes and components. Moreover, it could be easily applied this method to inject printing or 3D printing. Such supraparticles with a magnetic response can be used as micro-swimmers or actuators in robotics in the near future.

With this thesis, a library of hybrid functional materials composed of nano-objects and polymer have been successfully fabricated and developed, but it only "scratches" the surface of this field. This approach, based on the purposeful combination of polymer and nanoparticle where function and structure unite to produce new functional materials with improved functionalities and ease of use, could be used in an almost limitless number of applications.

5. Acknowledgements

First, I would like to thank Prof. Dr. Katharina Landfester for her supervision of my Ph.D. thesis. It is my pleasure and privilege of conducting such a fascinating research topic for three years at Max Planck Institute for Polymer Research.

I would like to express my sincere gratitude to Dr. Héloïse Thérien-Aubin and Dr. Markus B. Bannwarth. Without their experienced guidance and continuous support, I could not complete my research with such fruitful and inspiring results. In the first two years of my Ph.D., Markus invested a lot of his time and efforts on me to explore the world of colloid chemistry. In the last year of my Ph.D., Héloïse gave me numerous encouragement and critical suggestions for improving my research to a better level than that I cannot reach by myself. Apart from that, I benefit a lot from her valuable suggestions on scientific writing and presentation.

I would like to thank all my collaborators in my Ph.D. projects. They are: Prof. Dr. Wolfgang Tremel, Dr. Karsten Korschelt, Dr. Phillip Daniel and Melanie Viel (Johannes Gutenberg University Mainz), Prof. Dr. Sanghyuk Wooh (Chung-Ang University), Prof. Dr. Hans-Jürgen Butt, Dr. Michael Kappl, Stefan Peil, Dr. Lucas Caire da Silva, Dr. Yaowen Xing, Prof. Kurt Kremer, and Dr. Manjesh Singh (Max Planck Institute for Polymer Research), Prof. Dr. Wolfgang Binder and Dr. Diana Döhler (Martin Luther University Halle-Wittenberg), Prof. Dr. Jürgen Brieger and Nadine Wiesmann (University Medical Center Mainz). In last three years, they have been continuously making great contribution to my Ph.D. projects. I could not manage this multi-discipline and cutting-edge research without their indispensable support.

Many people I met at Max Planck Institute for Polymer Research have made my stay enjoyable and unforgettable. I would like to thank all of them. Specifically, I would like to give my many

thanks to my friends, including Rebecca Momper, Dr. Jie Liu, Dr. Shuai Jiang, Dr. Lucas Caire da Silva, Dr. Carole Champanhac, Prof. Zhijun Chen, Dr. Johanna Simon, Dr. Seong-Min Jo, Prof. Dr. Sanghyuk Wooh, Ke Zhang, and Xuelin Yao, for their support and giving me courage to pass through the tough moments in my study and life.

Additionally, I would like to thank my friends Shilong Lu, Prof. Dr. Xiaodong Yan, Shuo Huang, Dr. Xinxin Zhou, and Ran He. Although they are living in China, they have been giving me numerous encouragement and support regardless of distance and time difference.

Finally, my most sincere thanks go to my fiancée, Dr. Yang Yao, and my parents. They have been supporting and motivating me to be a better man. Thus, I would like to dedicate my thesis to them.

Minghan Hu (胡明翰)

Mainz, 10th November 2018

6. Curriculum vitae

Minghan Hu
Doctoral Candidate in Chemistry
Max Planck Institute for Polymer Research
Date of birth: 15th Mar. 1988
Place of birth: Nanning, China
Email: hum@mpip-mainz.mpg.de
Telephone: +49 6131 379-723
Office Address: Ackermannweg 10, 55128, Mainz, Germany
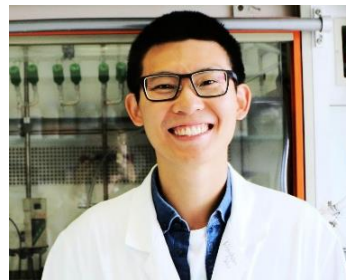
Education

Dec. 2015 – present	Ph.D. Candidate in Chemistry, **Max Planck Institute for Polymer Research**, Johannes Gutenberg-Universität Mainz
Sep. 2011 – Jun. 2014	M.S. in Material Science and Engineering, Beijing University of Chemical Technology
Sep. 2007 – Jun. 2011	B.S. in Material Science and Engineering, Beijing University of Chemical Technology

Research Experiences

Dec. 2015 – present	Ph.D. student in **Max Planck Institute for Polymer Research** Supervised by Prof. Dr. Katharina Landfester, co-supervised by Dr. Héloïse Thérien-Aubin and Dr. Markus B. Bannwarth Thesis: Assembling nano-objects into polymers: from hybrid nanoarchitecture to smart materials Co-supervising one bachelor thesis and two internships
Sep. 2015 – Nov. 2015	Research Assistant in Institute of Microbiology, Universität Stuttgart Supervised by Prof. Dr. Dieter Jendrossek Topic: A novel type of rubber oxygenase for enzymatic cleavage of rubbers
Sep. 2014 – Oct. 2015	Research Associate in the Center of Advanced Elastomer Materials, Beijing University of Chemical Technology Supervised by Prof. Dr. Suhe Zhao Topic: Biodesulfurization of vulcanized rubber by enzymes induced from *Gordonia amicalisa* Co-supervising one bachelor thesis
Sep. 2011 – Jun. 2014	Master student in the Center of Advanced Elastomer Materials, Beijing University of Chemical Technology. Supervised by Prof. Dr. Suhe Zhao

	Thesis: Desulfurization and regeneration of waste rubber *via* microbial method
Sep. 2010 – Jun. 2011	Bachelor student in the Center of Advanced Elastomer Materials,
	Beijing University of Chemical Technology
	Supervised by Prof. Dr. Suhe Zhao
	Thesis: Degradation of waste latex rubber by chemical way

Research Interests

1. Self-reporting coatings
2. Membranes for biomedical applications
3. Evaporation of magnetic fluids on superamphiphobic surfaces
4. Preparation of nanocapsules and nanoparticles from mini-emulsions

Research Methods and Scientific Techniques

Micro/nano-materials fabrication techniques	• Fabrication of supraparticles by evaporation guided self-assembly • Preparation of hybrid multifunctional nanoparticles/nanocapsules by mini-emulsion polymerization/solvent evaporation techniques. • Fabrication of functional micro/nano-fibrous membrane by colloidal electrospinning.
Materials characterizations	TEM, SEM, AFM, optical microscope, contact angle goniometer, dynamic light scattering, DSC, FTIR, GPC *etc*.

Honors and Awards

2015-2018	Graduates Scholarship of Chinese Scholarship Council
Jun. 2014	Excellent Master Graduate Student in Beijing University of Chemical Technology
Jun. 2014	Award for Outstanding Master Thesis in Beijing University of Chemical Technology
Dec. 2013	Industrial Scholarship of Beijing University of Chemical Technology
Jun. 2012	The Golden Prize in 3rd National College of Environmental Science and Technology Design Competition, Guangzhou, China

Languages

English (Fluent), Chinese (Native), German (Elementary)

7. Scientific publications and academic presentations

7.1 Publications

Peer-reviewed papers related to PhD thesis:

1. M. Hu, H.-J. Butt, K. Landfester, M. B. Bannwarth, S. Wooh, H. Thérien-Aubin, Shaping the assembly of superparamagnetic nanoparticles, *ACS Nano*, under review.

2. M. Hu,* K. Korschelt,* M. Viel,* N. Wiesmann, M. Kappl, J. Brieger, K. Landfester, H. Thérien-Aubin, W. Tremel, Nanozymes in Nanofibrous Mats with Haloperoxidase-Like Activity to Combat Biofouling, *ACS Applied Materials and Interfaces*, accepted, doi: 10.1021/acsami.8b16307, 2018.

3. M. Hu, S. Peil, Y. Xing, D. Döhler, L. C. da Silva, W. H. Binder, M. Kappl, M. B. Bannwarth, Monitoring Crack Appearance and Healing in Coatings with Damage Self-Reporting Nanocapsules, *Materials Horizons*, 5(1): 51-58, 2018.

4. M. Hu,* K. Korschelt,* P. Daniel,* K. Landfester, W. Tremel, M. B. Bannwarth, Fibrous Nanozyme Dressings with Catalase-Like Activity for H_2O_2 Reduction to Promote Wound Healing, *ACS Applied Materials and Interfaces*, 9(43): 38024-38031, 2017.

(∗ contributed equally)

Peer-reviewed papers related to Master thesis:

5. M. Hu, S. Zhao, C. Li, B. Wang, Y. Fu, Y. Wang, Biodesulfurization of Vulcanized Rubber by Enzymes Induced from *Gordonia Amicalisa*, *Polymer Degradation and Stability*, 128: 8-14, 2016.

6. C. Yao, S. Zhao, M. Hu, B. Wang, L. Zhang, Half-Submerged Cultivation Method for the Microbial Desulfurization of Waste Latex Rubber, *Journal of Applied Polymer Science*, 131(21): 41039, 2014.

7. M. Hu, S. Zhao, C. Li, B. Wang, C. Yao, Y. Wang, The Influence of Different Tween Surfactants on Biodesulfurization of Ground Tire Rubber by *Sphingomonas sp*. *Polymer Degradation and Stability*, 107: 91-97, 2014.

8. C. Yao, S. Zhao, Y. Wang, B. Wang, M. Wei, M. Hu, Microbial Desulfurization of Waste Latex Rubber with *Alicyclobacillus sp. Polymer Degradation and Stability*, 98(9): 1724-1730, 2013

7.2 Academic Presentations

Oral presentations:

1. Hu M., Butt H.-J., Wooh S., Bannwarth M.B., Thérien-Aubin H., Landfester K., Anisotropic Superparamagnetic Supraparticles Prepared by Controlled-Evaporation of Nanoparticle Suspensions, *Annual Meeting of European Colloid and Interface Society*, Sept. 3rd, 2018, Ljubljana, Slovenia

2. Hu M., Butt H.-J., Wooh S., Bannwarth M.B., Thérien-Aubin H., Landfester K., Supraparticles Assembled by Evaporation of Ferrofluid Droplets, *Annual Meeting of Max Planck-University of Twente Center for Complex Fluid Dynamics*, Jun. 25th, 2018, Enschede, Netherlands

3. Hu M., Landfester K., Bannwarth M.B., From Miniemulsions to Versatile Nanocapsules, *Annual Meeting of Max Planck-University of Twente Center for Complex Fluid Dynamics*, Jun. 15th, 2017, Göttingen, Germany

4. Hu M., Peil S., Kappl M., Xing Y., Landfester K., Bannwarth M. B., Damage Self-reporting Capsules Indicating Crack Appearance and Healing in Coatings, *13th Zsigmondy colloquium of the German Colloid Society*, Apr. 5th, 2017, Saarbrücken, Germany

Poster presentations:

1. Hu M., Butt H.-J., Wooh S., Bannwarth M.B., Thérien-Aubin H., Landfester K., Directing Supraparticles Architecture by Controlled Evaporation and Dewetting of Magnetic Nanoparticle Suspensions on Superamphiphobic Surfaces, *14th Zsigmondy colloquium of the German Colloid Society*, Apr. 9th – 11th, 2018, Mainz, Germany

2. Hu M., Butt H.-J., Wooh S., Bannwarth M.B., Thérien-Aubin H., Landfester K., Directing Supraparticles Architecture by Controlled Evaporation and Dewetting of Magnetic Nanoparticle Suspensions on Superamphiphobic Surfaces, *Annual Meeting of Max Planck-University of Twente Center for Complex Fluid Dynamics*, Jan. 31st – Feb. 2nd, 2018, Mainz, Germany

3. Hu M., Peil S., Xing Y., da Silva L.C., Kappl M., Landfester K., Bannwarth M.B., Self-Reporting Nanocapsules for Monitoring the Health State of Materials: from Occurring Damages to Successful Healing, *Annual Poster Day of Max Planck Institute for Polymer Research*, Oct. 11th 2017, Mainz, Germany

4. Hu M., Landfester K., Bannwarth M. B., Ellipsoid-Shaped Superparamagnetic Nanoclusters through Emulsion Electrospinning, *Summer School of "Self-Assembly in Soft Matter and Biosystems"*, Sept. 25th – 30th, 2016, Bad Honnef, Germany

8. Literature

1.   Kumar, A.; Vemula, P. K.; Ajayan, P. M.; John, G., Silver-Nanoparticle-Embedded Antimicrobial Paints Based on Vegetable Oil. *Nat. Mater.* **2008,** *7* (3), 236.

2.   Law, M.; Greene, L. E.; Johnson, J. C.; Saykally, R.; Yang, P., Nanowire Dye-Sensitized Solar Cells. *Nat. Mater.* **2005,** *4* (6), 455.

3.   Someya, T.; Bao, Z.; Malliaras, G. G., The Rise of Plastic Bioelectronics. *Nature* **2016,** *540* (7633), 379.

4.   Bao, J.; Chen, W.; Liu, T.; Zhu, Y.; Jin, P.; Wang, L.; Liu, J.; Wei, Y.; Li, Y., Bifunctional Au-Fe3o4 Nanoparticles for Protein Separation. *ACS Nano.* **2007,** *1* (4), 293-298.

5.   Gao, J.; Gu, H.; Xu, B., Multifunctional Magnetic Nanoparticles: Design, Synthesis, and Biomedical Applications. *Acc. Chem. Res.* **2009,** *42* (8), 1097-1107.

6.   Abu-Reziq, R.; Wang, D.; Post, M.; Alper, H., Platinum Nanoparticles Supported on Ionic Liquid-Modified Magnetic Nanoparticles: Selective Hydrogenation Catalysts. *Adv. Synth. Catal.* **2007,** *349* (13), 2145-2150.

7.   Li, P.; Li, Y.; Zhou, Z. K.; Tang, S.; Yu, X. F.; Xiao, S.; Wu, Z.; Xiao, Q.; Zhao, Y.; Wang, H., Evaporative Self-Assembly of Gold Nanorods into Macroscopic 3d Plasmonic Superlattice Arrays. *Adv. Mater.* **2016,** *28* (13), 2511-2517.

8.   Rong, Y.; Song, L.; Si, P.; Zhang, L.; Lu, X.; Zhang, J.; Nie, Z.; Huang, Y.; Chen, T., Macroscopic Assembly of Gold Nanorods into Superstructures with Controllable Orientations by Anisotropic Affinity Interaction. *Langmuir.* **2017,** *33* (48), 13867-13873.

9.   Nie, Z.; Petukhova, A.; Kumacheva, E., Properties and Emerging Applications of Self-Assembled Structures Made from Inorganic Nanoparticles. *Nat. Nanotechnol.* **2010,** *5* (1), 15.

10.   Thorkelsson, K.; Bai, P.; Xu, T., Self-Assembly and Applications of Anisotropic Nanomaterials: A Review. *Nano Today* **2015,** *10* (1), 48-66.

11.   Grzelczak, M.; Vermant, J.; Furst, E. M.; Liz-Marzán, L. M., Directed Self-Assembly of Nanoparticles. *ACS Nano.* **2010,** *4* (7), 3591-3605.

12.   Landfester, K., The Generation of Nanoparticles in Miniemulsions. *Adv. Mater.* **2001,** *13* (10), 765-768.

13.   Anton, N.; Benoit, J.-P.; Saulnier, P., Design and Production of Nanoparticles Formulated from Nano-Emulsion Templates—a Review. *J. Control. Release* **2008,** *128* (3), 185-199.

14.   Rao, J. P.; Geckeler, K. E., Polymer Nanoparticles: Preparation Techniques and Size-Control Parameters. *Prog. Polym. Sci.* **2011,** *36* (7), 887-913.

15.   Landfester, K., Miniemulsion Polymerization and the Structure of Polymer and Hybrid Nanoparticles. *Angew. Chem. Int. Ed.* **2009,** *48* (25), 4488-4507.

16.   Voorhees, P. W., The Theory of Ostwald Ripening. *J. Stat. Phys.* **1985,** *38* (1-2), 231-252.

17.   Taylor, P., Ostwald Ripening in Emulsions. *Adv. Colloid Interface Sci.* **1998,** *75* (2), 107-163.

18.   Landfester, K., Polyreactions in Miniemulsions. *Macromol. Rapid Commun.* **2001,** *22* (12), 896-936.

19.   Antonietti, M.; Landfester, K., Polyreactions in Miniemulsions. *Prog. Polym. Sci.* **2002,** *27* (4), 689-757.

20.   Asua, J. M., Miniemulsion Polymerization. *Prog. Polym. Sci.* **2002,** *27* (7), 1283-1346.

21.   Holzapfel, V.; Musyanovych, A.; Landfester, K.; Lorenz, M. R.; Mailänder, V., Preparation of Fluorescent Carboxyl and Amino Functionalized Polystyrene Particles by Miniemulsion Polymerization as Markers for Cells. *Macromol. Chem. Phys.* **2005,** *206* (24), 2440-2449.

22.   Kobitskaya, E.; Ekinci, D.; Manzke, A.; Plettl, A.; Wiedwald, U.; Ziemann, P.; Biskupek, J.; Kaiser, U.; Ziener, U.; Landfester, K., Narrowly Size Distributed Zinc-Containing Poly (Acrylamide) Latexes Via Inverse Miniemulsion Polymerization. *Macromolecules* **2010,** *43* (7), 3294-3305.

23.   Lorenz, S.; Hauser, C. P.; Autenrieth, B.; Weiss, C. K.; Landfester, K.; Mailänder, V., The Softer and More Hydrophobic the Better: Influence of the Side Chain of Polymethacrylate Nanoparticles for Cellular Uptake. *Macromol. Biosci.* **2010,** *10* (9), 1034-1042.

24.   Landfester, K., Synthesis of Colloidal Particles in Miniemulsions. *Annu. Rev. Mater. Res.* **2006,** *36*, 231-279.

25.   Kriwet, B.; Walter, E.; Kissel, T., Synthesis of Bioadhesive Poly (Acrylic Acid) Nano-and Microparticles Using an Inverse Emulsion Polymerization Method for the Entrapment of Hydrophilic Drug Candidates. *J. Control. Release* **1998,** *56* (1-3), 149-158.

26.   Schork, F. J.; Luo, Y.; Smulders, W.; Russum, J. P.; Butté, A.; Fontenot, K., Miniemulsion Polymerization. *Polymer particles* **2005**, 129-255.

27.   Crespy, D.; Landfester, K., Anionic Polymerization of E-Caprolactam in Miniemulsion: Synthesis and Characterization of Polyamide-6 Nanoparticles. *Macromolecules* **2005,** *38* (16), 6882-6887.

28.   Landfester, K.; Tiarks, F.; Hentze, H. P.; Antonietti, M., Polyaddition in Miniemulsions: A New Route to Polymer Dispersions. *Macromol. Chem. Phys.* **2000,** *201* (1), 1-5.

29.   Tiarks, F.; Landfester, K.; Antonietti, M., One-Step Preparation of Polyurethane Dispersions by Miniemulsion Polyaddition. *J. Polym. Sci. A Polym. Chem.* **2001,** *39* (14), 2520-2524.

30.   Zanetti-Ramos, B. G.; Lemos-Senna, E.; Soldi, V.; Borsali, R.; Cloutet, E.; Cramail, H., Polyurethane Nanoparticles from a Natural Polyol Via Miniemulsion Technique. *Polymer* **2006,** *47* (24), 8080-8087.

31.   Piradashvili, K.; Fichter, M.; Mohr, K.; Gehring, S.; Wurm, F. R.; Landfester, K., Biodegradable Protein Nanocontainers. *Biomacromolecules* **2015,** *16* (3), 815-821.

32.   Fichter, M.; Piradashvili, K.; Pietrzak-Nguyen, A.; Pretsch, L.; Kuhn, G.; Strand, S.; Knuf, M.; Zepp, F.; Wurm, F. R.; Mailänder, V., Polymeric Hepatitis C Virus Non-Structural Protein 5a Nanocapsules Induce Intrahepatic Antigen-Specific Immune Responses. *Biomaterials* **2016,** *108*, 1-12.

33.   Piradashvili, K.; Simon, J.; Paßlick, D.; Höhner, J. R.; Mailänder, V.; Wurm, F. R.; Landfester, K., Fully Degradable Protein Nanocarriers by Orthogonal Photoclick Tetrazole–Ene Chemistry for the Encapsulation and Release. *Nanoscale Horiz.* **2017,** *2* (5), 297-302.

34. Staff, R. H.; Landfester, K.; Crespy, D., Recent Advances in the Emulsion Solvent Evaporation Technique for the Preparation of Nanoparticles and Nanocapsules. In *Hierarchical Macromolecular Structures: 60 Years after the Staudinger Nobel Prize Ii*, Springer: 2013; pp 329-344.

35. Staff, R. H.; Schaeffel, D.; Turshatov, A.; Donadio, D.; Butt, H. J.; Landfester, K.; Koynov, K.; Crespy, D., Particle Formation in the Emulsion-Solvent Evaporation Process. *Small.* **2013,** *9* (20), 3514-3522.

36. Musyanovych, A.; Schmitz-Wienke, J.; Mailänder, V.; Walther, P.; Landfester, K., Preparation of Biodegradable Polymer Nanoparticles by Miniemulsion Technique and Their Cell Interactions. *Macromol. Biosci.* **2008,** *8* (2), 127-139.

37. Urban, M.; Musyanovych, A.; Landfester, K., Fluorescent Superparamagnetic Polylactide Nanoparticles by Combination of Miniemulsion and Emulsion/Solvent Evaporation Techniques. *Macromol. Chem. Phys.* **2009,** *210* (11), 961-970.

38. Zhao, Y.; Fickert, J.; Landfester, K.; Crespy, D., Encapsulation of Self-Healing Agents in Polymer Nanocapsules. *Small.* **2012,** *8* (19), 2954-2958.

39. Tanaka, T.; Nakatsuru, R.; Kagari, Y.; Saito, N.; Okubo, M., Effect of Molecular Weight on the Morphology of Polystyrene/Poly (Methyl Methacrylate) Composite Particles Prepared by the Solvent Evaporation Method. *Langmuir.* **2008,** *24* (21), 12267-12271.

40. Landfester, K., Miniemulsion Polymerization and the Structure of Polymer and Hybrid Nanoparticles. *Angew. Chem. Int. Ed.* **2009,** *48* (25), 4488-4507.

41. Sakai, T., Surfactant-Free Emulsions. *Curr. Opin. Colloid Interface Sci.* **2008,** *13* (4), 228-235.

42. Sridhar, R.; Lakshminarayanan, R.; Madhaiyan, K.; Barathi, V. A.; Lim, K. H. C.; Ramakrishna, S., Electrosprayed Nanoparticles and Electrospun Nanofibers Based on Natural Materials: Applications in Tissue Regeneration, Drug Delivery and Pharmaceuticals. *Chem. Soc. Rev.* **2015,** *44* (3), 790-814.

43. Jaworek, A.; Sobczyk, A. T., Electrospraying Route to Nanotechnology: An Overview. *J. Electrostat.* **2008,** *66* (3-4), 197-219.

44. Jaworek, A., Micro-and Nanoparticle Production by Electrospraying. *Powder Technol.* **2007,** *176* (1), 18-35.

45. Taylor, G. I., Disintegration of Water Drops in an Electric Field. *Proc. R. Soc. Lond. A* **1964,** *280* (1382), 383-397.

46. Bock, N.; Woodruff, M. A.; Hutmacher, D. W.; Dargaville, T. R., Electrospraying, a Reproducible Method for Production of Polymeric Microspheres for Biomedical Applications. *Polymers* **2011,** *3* (1), 131-149.

47. Gañán-Calvo, A. M., Cone-Jet Analytical Extension of Taylor's Electrostatic Solution and the Asymptotic Universal Scaling Laws in Electrospraying. *Phys. Rev. Lett.* **1997,** *79* (2), 217.

48. Almería, B.; Deng, W.; Fahmy, T. M.; Gomez, A., Controlling the Morphology of Electrospray-Generated Plga Microparticles for Drug Delivery. *J. Colloid Interf. Sci.* **2010,** *343* (1), 125-133.

49. Chang, M.-W.; Stride, E.; Edirisinghe, M., A New Method for the Preparation of Monoporous Hollow Microspheres. *Langmuir.* **2010,** *26* (7), 5115-5121.

50.   Kango, S.; Kalia, S.; Celli, A.; Njuguna, J.; Habibi, Y.; Kumar, R., Surface Modification of Inorganic Nanoparticles for Development of Organic–Inorganic Nanocomposites—a Review. *Prog. Polym. Sci.* **2013,** *38* (8), 1232-1261.

51.   Wu, Z.; Yang, S.; Wu, W., Shape Control of Inorganic Nanoparticles from Solution. *Nanoscale* **2016,** *8* (3), 1237-1259.

52.   Tang, F.; Li, L.; Chen, D., Mesoporous Silica Nanoparticles: Synthesis, Biocompatibility and Drug Delivery. *Adv. Mater.* **2012,** *24* (12), 1504-1534.

53.   Chang, C.-L.; Fogler, H. S., Controlled Formation of Silica Particles from Tetraethyl Orthosilicate in Nonionic Water-in-Oil Microemulsions. *Langmuir.* **1997,** *13* (13), 3295-3307.

54.   Lentz, C. W., Silicate Minerals as Sources of Trimethylsilyl Silicates and Silicate Structure Analysis of Sodium Silicate Solutions. *Inorg. Chem.* **1964,** *3* (4), 574-579.

55.   Stöber, W.; Fink, A.; Bohn, E., Controlled Growth of Monodisperse Silica Spheres in the Micron Size Range. *J. Colloid Interf. Sci.* **1968,** *26* (1), 62-69.

56.   Cai, Q.; Luo, Z.-S.; Pang, W.-Q.; Fan, Y.-W.; Chen, X.-H.; Cui, F.-Z., Dilute Solution Routes to Various Controllable Morphologies of Mcm-41 Silica with a Basic Medium. *Chem. Mater.* **2001,** *13* (2), 258-263.

57.   Hoffmann, F.; Cornelius, M.; Morell, J.; Fröba, M., Silica-Based Mesoporous Organic–Inorganic Hybrid Materials. *Angew. Chem. Int. Ed.* **2006,** *45* (20), 3216-3251.

58.   Caputo, F.; Mameli, M.; Sienkiewicz, A.; Licoccia, S.; Stellacci, F.; Ghibelli, L.; Traversa, E., A Novel Synthetic Approach of Cerium Oxide Nanoparticles with Improved Biomedical Activity. *Sci. Rep.* **2017,** *7* (1), 4636.

59.   Ragg, R.; Tahir, M. N.; Tremel, W., Solids Go Bio: Inorganic Nanoparticles as Enzyme Mimics. *Eur. J. Inorg. Chem.* **2016,** *2016* (13-14), 1906-1915.

60.   Lee, S. S.; Song, W.; Cho, M.; Puppala, H. L.; Nguyen, P.; Zhu, H.; Segatori, L.; Colvin, V. L., Antioxidant Properties of Cerium Oxide Nanocrystals as a Function of Nanocrystal Diameter and Surface Coating. *ACS Nano.* **2013,** *7* (11), 9693-9703.

61.   Colon, J.; Herrera, L.; Smith, J.; Patil, S.; Komanski, C.; Kupelian, P.; Seal, S.; Jenkins, D. W.; Baker, C. H., Protection from Radiation-Induced Pneumonitis Using Cerium Oxide Nanoparticles. *Nanomedicine* **2009,** *5* (2), 225-231.

62.   Ho, C.; Yu, J. C.; Kwong, T.; Mak, A. C.; Lai, S., Morphology-Controllable Synthesis of Mesoporous Ceo2 Nano-and-Microstructures. *Chem. Mater.* **2005,** *17* (17), 4514-4522.

63.   Mai, H.-X.; Sun, L.-D.; Zhang, Y.-W.; Si, R.; Feng, W.; Zhang, H.-P.; Liu, H.-C.; Yan, C.-H., Shape-Selective Synthesis and Oxygen Storage Behavior of Ceria Nanopolyhedra, Nanorods, and Nanocubes. *J. Phys. Chem. B* **2005,** *109* (51), 24380-24385.

64.   Lee, H.; Kim, J.; Kim, J.; Chung, S. E.; Choi, S.-E.; Kwon, S., Programming Magnetic Anisotropy in Polymeric Microactuators. *Nat. Mater.* **2011,** *10* (10), 747.

65.   Guzmán-Lastra, F.; Kaiser, A.; Löwen, H., Fission and Fusion Scenarios for Magnetic Microswimmer Clusters. *Nat. Commun.* **2016,** *7*, 13519.

66.   Xu, H.; Aguilar, Z. P.; Yang, L.; Kuang, M.; Duan, H.; Xiong, Y.; Wei, H.; Wang, A., Antibody Conjugated Magnetic Iron Oxide Nanoparticles for Cancer Cell Separation in Fresh Whole Blood. *Biomaterials.* **2011,** *32* (36), 9758-9765.

67. Shao, M.; Ning, F.; Zhao, J.; Wei, M.; Evans, D. G.; Duan, X., Preparation of Fe3o4@ Sio2@ Layered Double Hydroxide Core–Shell Microspheres for Magnetic Separation of Proteins. *J. Am. Chem. Soc.* **2012,** *134* (2), 1071-1077.

68. Huber, D. L., Synthesis, Properties, and Applications of Iron Nanoparticles. *Small.* **2005,** *1* (5), 482-501.

69. Peters, C.; Hoop, M.; Pané, S.; Nelson, B. J.; Hierold, C., Degradable Magnetic Composites for Minimally Invasive Interventions: Device Fabrication, Targeted Drug Delivery, and Cytotoxicity Tests. *Adv. Mater.* **2016,** *28* (3), 533-538.

70. Sun, S.; Zeng, H., Size-Controlled Synthesis of Magnetite Nanoparticles. *J. Am. Chem. Soc.* **2002,** *124* (28), 8204-8205.

71. Sharifi Dehsari, H.; Harris, R. A.; Ribeiro, A. H.; Tremel, W.; Asadi, K., Optimizing the Binding Energy of the Surfactant to Iron Oxide Yields Truly Monodisperse Nanoparticles. *Langmuir.* **2018,** *34* (22), 6582-6590.

72. Sun, S.; Zeng, H.; Robinson, D. B.; Raoux, S.; Rice, P. M.; Wang, S. X.; Li, G., Monodisperse Mfe2o4 (M= Fe, Co, Mn) Nanoparticles. *J. Am. Chem. Soc.* **2004,** *126* (1), 273-279.

73. Peng, S.; Wang, C.; Xie, J.; Sun, S., Synthesis and Stabilization of Monodisperse Fe Nanoparticles. *J. Am. Chem. Soc.* **2006,** *128* (33), 10676-10677.

74. Murray, C. B.; Sun, S.; Gaschler, W.; Doyle, H.; Betley, T. A.; Kagan, C. R., Colloidal Synthesis of Nanocrystals and Nanocrystal Superlattices. *IBM J. Res. Dev.* **2001,** *45* (1), 47-56.

75. Sun, S.; Murray, C. B.; Weller, D.; Folks, L.; Moser, A., Monodisperse Fept Nanoparticles and Ferromagnetic Fept Nanocrystal Superlattices. *Science* **2000,** *287* (5460), 1989-1992.

76. Shevchenko, E. V.; Talapin, D. V.; Rogach, A. L.; Kornowski, A.; Haase, M.; Weller, H., Colloidal Synthesis and Self-Assembly of Copt3 Nanocrystals. *J. Am. Chem. Soc.* **2002,** *124* (38), 11480-11485.

77. Laurent, S.; Forge, D.; Port, M.; Roch, A.; Robic, C.; Vander Elst, L.; Muller, R. N., Magnetic Iron Oxide Nanoparticles: Synthesis, Stabilization, Vectorization, Physicochemical Characterizations, and Biological Applications. *Chem. Rev.* **2008,** *108* (6), 2064-2110.

78. Woo, K.; Hong, J.; Choi, S.; Lee, H.-W.; Ahn, J.-P.; Kim, C. S.; Lee, S. W., Easy Synthesis and Magnetic Properties of Iron Oxide Nanoparticles. *Chem. Mater.* **2004,** *16* (14), 2814-2818.

79. Paul, B. K.; Moulik, S. P., Uses and Applications of Microemulsions. *Curr. Sci.* **2001**, 990-1001.

80. Daou, T.; Pourroy, G.; Bégin-Colin, S.; Greneche, J.; Ulhaq-Bouillet, C.; Legaré, P.; Bernhardt, P.; Leuvrey, C.; Rogez, G., Hydrothermal Synthesis of Monodisperse Magnetite Nanoparticles. *Chem. Mater.* **2006,** *18* (18), 4399-4404.

81. Lu, A. H.; Salabas, E. L.; Schüth, F., Magnetic Nanoparticles: Synthesis, Protection, Functionalization, and Application. *Angew. Chem. Int. Ed.* **2007,** *46* (8), 1222-1244.

82. Bannwarth, M. B.; Kazer, S. W.; Ulrich, S.; Glasser, G.; Crespy, D.; Landfester, K., Well-Defined Nanofibers with Tunable Morphology from Spherical Colloidal Building Blocks. *Angew. Chem. Int. Ed.* **2013,** *52* (38), 10107-10111.

83.   Mari, M.;   Müller, B.;   Landfester, K.;   Munoz-Espi, R., Ceria/Polymer Hybrid Nanoparticles as Efficient Catalysts for the Hydration of Nitriles to Amides. *ACS Appl. Mater. Interfaces* **2015,** *7* (20), 10727-10733.

84.   Fischer, V.; Bannwarth, M. B.; Jakob, G.; Landfester, K.; Munoz-Espi, R., Luminescent and Magnetoresponsive Multifunctional Chalcogenide/Polymer Hybrid Nanoparticles. *J. Phys. Chem. C* **2013,** *117* (11), 5999-6005.

85.   Benedetti, C.; Cazzolaro, A.; Carraro, M.; Graf, R.; Landfester, K.; Gross, S.; Munoz-Espi, R., Dual Role of Zirconium Oxoclusters in Hybrid Nanoparticles: Cross-Linkers and Catalytic Sites. *ACS Appl. Mater. Interfaces* **2016,** *8* (39), 26275-26284.

86.   Benedetti, C.; Flouda, P.; Antonello, A.; Rosenauer, C.; Pérez-Pla, F. F.; Landfester, K.; Gross, S.; Muñoz-Espí, R., Zirconium Oxocluster/Polymer Hybrid Nanoparticles Prepared by Photoactivated Miniemulsion Copolymerization. *Nanotechnology* **2017,** *28* (36), 365603.

87.   Schrade, A.;   Cao, Z.;   Landfester, K.;   Ziener, U., Preparation of Raspberry-Like Nanocapsules by the Combination of Pickering Emulsification and Solvent Displacement Technique. *Langmuir.* **2011,** *27* (11), 6689-6700.

88.   Chen, T.;   Colver, P. J.; Bon, S. A., Organic–Inorganic Hybrid Hollow Spheres Prepared from Tio2-Stabilized Pickering Emulsion Polymerization. *Adv. Mater.* **2007,** *19* (17), 2286-2289.

89.   Schrade, A.;   Landfester, K.;   Ziener, U., Pickering-Type Stabilized Nanoparticles by Heterophase Polymerization. *Chem. Soc. Rev.* **2013,** *42* (16), 6823-6839.

90.   Galati, E.; Tebbe, M.; Querejeta-Fernández, A.; Xin, H. L.; Gang, O.; Zhulina, E. B.; Kumacheva, E., Shape-Specific Patterning of Polymer-Functionalized Nanoparticles. *ACS Nano.* **2017,** *11* (5), 4995-5002.

91.   Klinkova, A.;   Thérien-Aubin, H.;   Ahmed, A.;   Nykypanchuk, D.;   Choueiri, R. M.; Gagnon, B.;   Muntyanu, A.;   Gang, O.;   Walker, G. C.; Kumacheva, E., Structural and Optical Properties of Self-Assembled Chains of Plasmonic Nanocubes. *Nano Lett.* **2014,** *14* (11), 6314-6321.

92.   Liu, Y.; He, J.; Yang, K.; Yi, C.; Liu, Y.; Nie, L.; Khashab, N. M.; Chen, X.; Nie, Z., Folding up of Gold Nanoparticle Strings into Plasmonic Vesicles for Enhanced Photoacoustic Imaging. *Angew. Chem. Int. Ed.* **2015,** *54* (52), 15809-15812.

93.   Liu, K.; Lukach, A.; Sugikawa, K.; Chung, S.; Vickery, J.; Therien-Aubin, H.; Yang, B.;   Rubinstein, M.; Kumacheva, E., Copolymerization of Metal Nanoparticles: A Route to Colloidal Plasmonic Copolymers. *Angew. Chem. Int. Ed.* **2014,** *53* (10), 2648-2653.

94.   Karakoti, A.;   Kuchibhatla, S. V.;   Babu, K. S.; Seal, S., Direct Synthesis of Nanoceria in Aqueous Polyhydroxyl Solutions. *J. Phys. Chem. C* **2007,** *111* (46), 17232-17240.

95.   Karakoti, A. S.; Singh, S.; Kumar, A.; Malinska, M.; Kuchibhatla, S. V.; Wozniak, K.; Self, W. T.; Seal, S., Pegylated Nanoceria as Radical Scavenger with Tunable Redox Chemistry. *J. Am. Chem. Soc.* **2009,** *131* (40), 14144-14145.

96.   Mandoli, C.; Pagliari, F.; Pagliari, S.; Forte, G.; Di Nardo, P.; Licoccia, S.; Traversa, E., Stem Cell Aligned Growth Induced by Ceo2 Nanoparticles in Plga Scaffolds with Improved Bioactivity for Regenerative Medicine. *Adv. Func. Mater.* **2010,** *20* (10), 1617-1624.

97. Pagliari, F.; Mandoli, C.; Forte, G.; Magnani, E.; Pagliari, S.; Nardone, G.; Licoccia, S.; Minieri, M.; Di Nardo, P.; Traversa, E., Cerium Oxide Nanoparticles Protect Cardiac Progenitor Cells from Oxidative Stress. *ACS Nano.* **2012,** *6* (5), 3767-3775.

98. Ko, F.; Gogotsi, Y.; Ali, A.; Naguib, N.; Ye, H.; Yang, G.; Li, C.; Willis, P., Electrospinning of Continuous Carbon Nanotube-Filled Nanofiber Yarns. *Adv. Mater.* **2003,** *15* (14), 1161-1165.

99. Zhang, C. L.; Lv, K. P.; Cong, H. P.; Yu, S. H., Controlled Assemblies of Gold Nanorods in Pva Nanofiber Matrix as Flexible Free-Standing Sers Substrates by Electrospinning. *Small.* **2012,** *8* (5), 648-653.

100. Xue, J.; Xie, J.; Liu, W.; Xia, Y., Electrospun Nanofibers: New Concepts, Materials, and Applications. *Acc. Chem. Res.* **2017,** *50* (8), 1976-1987.

101. Jiang, S.; Lv, L.-P.; Landfester, K.; Crespy, D., Nanocontainers in and onto Nanofibers. *Acc. Chem. Res.* **2016,** *49* (5), 816-823.

102. Choi, S. K.; Kim, S.; Lim, S. K.; Park, H., Photocatalytic Comparison of Tio2 Nanoparticles and Electrospun Tio2 Nanofibers: Effects of Mesoporosity and Interparticle Charge Transfer. *J. Phys. Chem. C* **2010,** *114* (39), 16475-16480.

103. Chen, S.; Chi, M.; Zhu, Y.; Gao, M.; Wang, C.; Lu, X., A Facile Synthesis of Superparamagnetic Fe3o4 Nanofibers with Superior Peroxidase-Like Catalytic Activity for Sensitive Colorimetric Detection of L-Cysteine. *Appl. Surf. Sci.* **2018,** *440*, 237-244.

104. Friedemann, K.; Corrales, T.; Kappl, M.; Landfester, K.; Crespy, D., Facile and Large-Scale Fabrication of Anisometric Particles from Fibers Synthesized by Colloid-Electrospinning. *Small.* **2012,** *8* (1), 144-153.

105. Jiang, S.; Lieberwirth, I.; Landfester, K.; Muñoz-Espí, R.; Crespy, D., Nanofibrous Photocatalysts from Electrospun Nanocapsules. *Nanotechnology* **2017,** *28* (40), 405601.

106. Xue, J.; Niu, Y.; Gong, M.; Shi, R.; Chen, D.; Zhang, L.; Lvov, Y., Electrospun Microfiber Membranes Embedded with Drug-Loaded Clay Nanotubes for Sustained Antimicrobial Protection. *ACS Nano.* **2015,** *9* (2), 1600-1612.

107. Prevo, B. G.; Kuncicky, D. M.; Velev, O. D., Engineered Deposition of Coatings from Nano-and Micro-Particles: A Brief Review of Convective Assembly at High Volume Fraction. *Colloids Surf. A Physicochem. Eng. Asp.* **2007,** *311* (1-3), 2-10.

108. Erbil, H. Y., Evaporation of Pure Liquid Sessile and Spherical Suspended Drops: A Review. *Adv. Colloid Interface Sci.* **2012,** *170* (1-2), 67-86.

109. Sperling, M.; Gradzielski, M., Droplets, Evaporation and a Superhydrophobic Surface: Simple Tools for Guiding Colloidal Particles into Complex Materials. *Gels* **2017,** *3* (2), 15.

110. Good, R. J., A Thermodynamic Derivation of Wenzel's Modification of Young's Equation for Contact Angles; Together with a Theory of Hysteresis. *J. Am. Chem. Soc.* **1952,** *74* (20), 5041-5042.

111. Adam, N., Use of the Term 'Young's Equation'for Contact Angles. *Nature* **1957,** *180* (4590), 809.

112. Deegan, R. D.; Bakajin, O.; Dupont, T. F.; Huber, G.; Nagel, S. R.; Witten, T. A., Capillary Flow as the Cause of Ring Stains from Dried Liquid Drops. *Nature* **1997,** *389* (6653), 827.

113.   Layani, M.; Gruchko, M.; Milo, O.; Balberg, I.; Azulay, D.; Magdassi, S., Transparent Conductive Coatings by Printing Coffee Ring Arrays Obtained at Room Temperature. *ACS Nano.* **2009,** *3* (11), 3537-3542.

114.   Rastogi, V.; Melle, S.; Calderon, O. G.; García, A. A.; Marquez, M.; Velev, O. D., Synthesis of Light-Diffracting Assemblies from Microspheres and Nanoparticles in Droplets on a Superhydrophobic Surface. *Adv. Mater.* **2008,** *20* (22), 4263-4268.

115.   Wooh, S.; Huesmann, H.; Tahir, M. N.; Paven, M.; Wichmann, K.; Vollmer, D.; Tremel, W.; Papadopoulos, P.; Butt, H. J., Synthesis of Mesoporous Supraparticles on Superamphiphobic Surfaces. *Adv. Mater.* **2015,** *27* (45), 7338-7343.

116.   Sekido, T.; Wooh, S.; Fuchs, R.; Kappl, M.; Nakamura, Y.; Butt, H.-J.; Fujii, S., Controlling the Structure of Supraballs by Ph-Responsive Particle Assembly. *Langmuir.* **2017,** *33* (8), 1995-2002.

117.   Sperling, M.; Kim, H. J.; Velev, O. D.; Gradzielski, M., Active Steerable Catalytic Supraparticles Shuttling on Preprogrammed Vertical Trajectories. *Adv. Mater. Int.* **2016,** *3* (15), 1600095.

118.   Rastogi, V.; García, A. A.; Marquez, M.; Velev, O. D., Anisotropic Particle Synthesis inside Droplet Templates on Superhydrophobic Surfaces. *Macromol. Rapid Commun.* **2010,** *31* (2), 190-195.

119.   Sperling, M.; Velev, O. D.; Gradzielski, M., Controlling the Shape of Evaporating Droplets by Ionic Strength: Formation of Highly Anisometric Silica Supraparticles. *Angew. Chem. Int. Ed.* **2014,** *53* (2), 586-590.

120.   Wang, M.; He, L.; Yin, Y., Magnetic Field Guided Colloidal Assembly. *Mater. Today* **2013,** *16* (4), 110-116.

121.   Rosensweig, R. E., *Ferrohydrodynamics*. 2nd ed.; Dover Publications: Mineola (NY), 1997; p 333.

122.   Timonen, J. V.; Latikka, M.; Leibler, L.; Ras, R. H.; Ikkala, O., Switchable Static and Dynamic Self-Assembly of Magnetic Droplets on Superhydrophobic Surfaces. *Science* **2013,** *341* (6143), 253-257.

123.   Latikka, M.; Backholm, M.; Timonen, J. V.; Ras, R. H., Wetting of Ferrofluids: Phenomena and Control. *Curr. Opin. Colloid Interface Sci.* **2018**.

124.   Bannwarth, M. B.; Utech, S.; Ebert, S.; Weitz, D. A.; Crespy, D.; Landfester, K., Colloidal Polymers with Controlled Sequence and Branching Constructed from Magnetic Field Assembled Nanoparticles. *ACS Nano.* **2015,** *9* (3), 2720-2728.

125.   Singh, G.; Chan, H.; Baskin, A.; Gelman, E.; Repnin, N.; Král, P.; Klajn, R., Self-Assembly of Magnetite Nanocubes into Helical Superstructures. *Science.* **2014**, 1254132.

126.   Malik, V.; Petukhov, A. V.; He, L.; Yin, Y.; Schmidt, M., Colloidal Crystallization and Structural Changes in Suspensions of Silica/Magnetite Core–Shell Nanoparticles. *Langmuir.* **2012,** *28* (41), 14777-14783.

127.   Yuan, H.; Zvonkina, I. J.; Al-Enizi, A. M.; Elzatahry, A. A.; Pyun, J.; Karim, A., Facile Assembly of Aligned Magnetic Nanoparticle Chains in Polymer Nanocomposite Films by Magnetic Flow Coating. *ACS Appl. Mater. Interfaces* **2017,** *9* (12), 11290-11298.

128.   Kralj, S.; Makovec, D., Magnetic Assembly of Superparamagnetic Iron Oxide Nanoparticle Clusters into Nanochains and Nanobundles. *ACS Nano.* **2015,** *9* (10), 9700-9707.

129.   Zhang, Q.; Janner, M.; He, L.; Wang, M.; Hu, Y.; Lu, Y.; Yin, Y., Photonic Labyrinths: Two-Dimensional Dynamic Magnetic Assembly and in Situ Solidification. *Nano Lett.* **2013,** *13* (4), 1770-1775.

130.   Velez, C.; Torres-Díaz, I.; Maldonado-Camargo, L.; Rinaldi, C.; Arnold, D. P., Magnetic Assembly and Cross-Linking of Nanoparticles for Releasable Magnetic Microstructures. *ACS Nano.* **2015,** *9* (10), 10165-10172.

131.   Patrick, J. F.; Robb, M. J.; Sottos, N. R.; Moore, J. S.; White, S. R., Polymers with Autonomous Life-Cycle Control. *Nature* **2016,** *540* (7633), 363.

132.   Mura, S.; Nicolas, J.; Couvreur, P., Stimuli-Responsive Nanocarriers for Drug Delivery. *Nat. Mater.* **2013,** *12* (11), 991.

133.   Vogel, N.; Utech, S.; England, G. T.; Shirman, T.; Phillips, K. R.; Koay, N.; Burgess, I. B.; Kolle, M.; Weitz, D. A.; Aizenberg, J., Color from Hierarchy: Diverse Optical Properties of Micron-Sized Spherical Colloidal Assemblies. *Proc. Natl. Acad. Sci. U. S. A.* **2015,** *112* (35), 10845-10850.

134.   Wintzheimer, S.; Granath, T.; Oppmann, M.; Kister, T.; Thai, T.; Kraus, T.; Vogel, N.; Mandel, K., Supraparticles: Functionality from Uniform Structural Motifs. *ACS Nano.* **2018**.

135.   Glotzer, S. C.; Solomon, M. J., Anisotropy of Building Blocks and Their Assembly into Complex Structures. *Nat. Mater.* **2007,** *6* (8), 557.

136.   Shchukin, D.; Möhwald, H., A Coat of Many Functions. *Science* **2013,** *341* (6153), 1458-1459.

137.   Lv, L.-P.; Zhao, Y.; Vilbrandt, N.; Gallei, M.; Vimalanandan, A.; Rohwerder, M.; Landfester, K.; Crespy, D., Redox Responsive Release of Hydrophobic Self-Healing Agents from Polyaniline Capsules. *J. Am. Chem. Soc.* **2013,** *135* (38), 14198-14205.

138.   Cho, S. H.; Andersson, H. M.; White, S. R.; Sottos, N. R.; Braun, P. V., Polydimethylsiloxane-Based Self-Healing Materials. *Adv. Mater.* **2006,** *18* (8), 997-1000.

139.   Vimalanandan, A.; Lv, L. P.; Tran, T. H.; Landfester, K.; Crespy, D.; Rohwerder, M., Redox-Responsive Self-Healing for Corrosion Protection. *Adv. Mater.* **2013,** *25* (48), 6980-6984.

140.   Doan, T. Q.; Leslie, L. S.; Kim, S. Y.; Bhargava, R.; White, S. R.; Sottos, N. R., Characterization of Core-Shell Microstructure and Self-Healing Performance of Electrospun Fiber Coatings. *Polymer* **2016,** *107*, 263-272.

141.   Park, J. H.; Braun, P. V., Coaxial Electrospinning of Self-Healing Coatings. *Adv. Mater.* **2010,** *22* (4), 496-499.

142.   Jiang, S.; Lv, L.; Li, Q.; Wang, J.; Landfester, K.; Crespy, D., Tailoring Nanoarchitectonics to Control the Release Profile of Payloads. *Nanoscale* **2016,** *8* (22), 11511-11517.

143.   Jiang, S.; Lv, L.-P.; Landfester, K.; Crespy, D., Dual-Responsive Multicompartment Nanofibers for Controlled Release of Payloads. *Rsc Adv.* **2016,** *6* (49), 43767-43770.

144.   Fitridge, I.; Dempster, T.; Guenther, J.; de Nys, R., The Impact and Control of Biofouling in Marine Aquaculture: A Review. *Biofouling* **2012,** *28* (7), 649-669.

145.   Kolewe, K. W.; Dobosz, K. M.; Rieger, K. A.; Chang, C.-C.; Emrick, T.; Schiffman, J. D., Antifouling Electrospun Nanofiber Mats Functionalized with Polymer Zwitterions. *ACS Appl. Mater. Interfaces* **2016,** *8* (41), 27585-27593.

146.   Jiang, S.; Cao, Z., Ultralow-Fouling, Functionalizable, and Hydrolyzable Zwitterionic Materials and Their Derivatives for Biological Applications. *Adv. Mater.* **2010,** *22* (9), 920-932.

147.   Xu, X.; Yang, Q.; Wang, Y.; Yu, H.; Chen, X.; Jing, X., Biodegradable Electrospun Poly (L-Lactide) Fibers Containing Antibacterial Silver Nanoparticles. *Eur. Polym. J.* **2006,** *42* (9), 2081-2087.

148.   Liu, C.; Shen, J.; Yeung, K. W. K.; Tjong, S. C., Development and Antibacterial Performance of Novel Polylactic Acid-Graphene Oxide-Silver Nanoparticle Hybrid Nanocomposite Mats Prepared by Electrospinning. *ACS Biomater. Sci. Eng.* **2017,** *3* (3), 471-486.

149.   Patrick, J. F.; Robb, M. J.; Sottos, N. R.; Moore, J. S.; White, S. R., Polymers with Autonomous Life-Cycle Control. *Nature* **2016,** *540* (7633), 363-370.

150.   Cho, S. H.; White, S. R.; Braun, P. V., Self-Healing Polymer Coatings. *Adv. Mater.* **2009,** *21* (6), 645-649.

151.   Ulbrich, K.; Hola, K.; Subr, V.; Bakandritsos, A.; Tucek, J.; Zboril, R., Targeted Drug Delivery with Polymers and Magnetic Nanoparticles: Covalent and Noncovalent Approaches, Release Control, and Clinical Studies. *Chem. Rev.* **2016,** *116* (9), 5338-5431.

152.   Brannon-Peppas, L.; Blanchette, J. O., Nanoparticle and Targeted Systems for Cancer Therapy. *Adv. Drug Deliv. Rev.* **2012,** *64*, 206-212.

153.   Bannwarth, M. B.; Ebert, S.; Lauck, M.; Ziener, U.; Tomcin, S.; Jakob, G.; Münnemann, K.; Mailänder, V.; Musyanovych, A.; Landfester, K., Tailor-Made Nanocontainers for Combined Magnetic-Field-Induced Release and Mri. *Macromol. Biosci.* **2014,** *14* (9), 1205-1214.

154.   Vernikouskaya, I.; Fekete, N.; Bannwarth, M.; Erle, A.; Rojewski, M.; Landfester, K.; Schmidtke-Schrezenmeier, G.; Schrezenmeier, H.; Rasche, V., Iron-Loaded Plla Nanoparticles as Highly Efficient Intracellular Markers for Visualization of Mesenchymal Stromal Cells by Mri. *Contrast Media Mol. Imaging* **2014,** *9* (2), 109-121.

155.   Corr, S. A.; Byrne, S. J.; Tekoriute, R.; Meledandri, C. J.; Brougham, D. F.; Lynch, M.; Kerskens, C.; O'Dwyer, L.; Gun'ko, Y. K., Linear Assemblies of Magnetic Nanoparticles as Mri Contrast Agents. *J. Am. Chem. Soc.* **2008,** *130* (13), 4214-4215.

156.   Park, J. H.; von Maltzahn, G.; Zhang, L.; Schwartz, M. P.; Ruoslahti, E.; Bhatia, S. N.; Sailor, M. J., Magnetic Iron Oxide Nanoworms for Tumor Targeting and Imaging. *Adv. Mater.* **2008,** *20* (9), 1630-1635.

157.   He, C. W.; Parowatkin, M.; Mailänder, V.; Flechtner-Mors, M.; Ziener, U.; Landfester, K.; Crespy, D., Sequence-Controlled Delivery of Peptides from Hierarchically Structured Nanomaterials. *ACS Appl. Mater. Interfaces* **2017,** *9* (4), 3885-3894.

158.   Zahedi, P.; Rezaeian, I.; Ranaei-Siadat, S. O.; Jafari, S. H.; Supaphol, P., A Review on Wound Dressings with an Emphasis on Electrospun Nanofibrous Polymeric Bandages. *Polym. Adv. Technol.* **2010,** *21* (2), 77-95.

159.   Rieger, K. A.; Birch, N. P.; Schiffman, J. D., Designing Electrospun Nanofiber Mats to Promote Wound Healing–a Review. *J. Mater. Chem. B* **2013,** *1* (36), 4531-4541.

160. Ghavami Nejad, A.; Rajan Unnithan, A.; Ramachandra Kurup Sasikala, A.; Samarikhalaj, M.; Thomas, R. G.; Jeong, Y. Y.; Nasseri, S.; Murugesan, P.; Wu, D.; Hee Park, C., Mussel-Inspired Electrospun Nanofibers Functionalized with Size-Controlled Silver Nanoparticles for Wound Dressing Application. *ACS Appl. Mater. Interfaces* **2015,** *7* (22), 12176-12183.

161. Jiang, S.; Ma, B. C.; Huang, W.; Kaltbeitzel, A.; Kizisavas, G.; Crespy, D.; Zhang, K. A. I.; Landfester, K., Visible Light Active Nanofibrous Membrane for Antibacterial Wound Dressing. *Nanoscale Horiz.* **2018**.

162. Nie, S.; Emory, S. R., Probing Single Molecules and Single Nanoparticles by Surface-Enhanced Raman Scattering. *Science* **1997,** *275* (5303), 1102-1106.

163. Hao, E.; Schatz, G. C., Electromagnetic Fields around Silver Nanoparticles and Dimers. *J. Phys. Chem.* **2004,** *120* (1), 357-366.

164. Graham, D.; Thompson, D. G.; Smith, W. E.; Faulds, K., Control of Enhanced Raman Scattering Using a DNA-Based Assembly Process of Dye-Coded Nanoparticles. *Nat. Nanotechnol.* **2008,** *3* (9), 548.

165. Yang, G.-Z.; Bellingham, J.; Dupont, P. E.; Fischer, P.; Floridi, L.; Full, R.; Jacobstein, N.; Kumar, V.; McNutt, M.; Merrifield, R., The Grand Challenges of Science Robotics. *Sci. Robot.* **2018,** *3* (14), eaar7650.

166. Sitti, M., Miniature Devices: Voyage of the Microrobots. *Nature* **2009,** *458* (7242), 1121.

167. Hu, W.; Lum, G. Z.; Mastrangeli, M.; Sitti, M., Small-Scale Soft-Bodied Robot with Multimodal Locomotion. *Nature* **2018,** *554* (7690), 81.

168. Chen, X.-Z.; Hoop, M.; Mushtaq, F.; Siringil, E.; Hu, C.; Nelson, B. J.; Pané, S., Recent Developments in Magnetically Driven Micro-and Nanorobots. *Appl. Mater. Today.* **2017,** *9*, 37-48.

169. Chen, X. Z.; Jang, B.; Ahmed, D.; Hu, C.; De Marco, C.; Hoop, M.; Mushtaq, F.; Nelson, B. J.; Pané, S., Small-Scale Machines Driven by External Power Sources. *Adv. Mater.* **2018,** *30* (15), 1705061.

170. Vimalanandan, A.; Lv, L. P.; Tran, T. H.; Landfester, K.; Crespy, D.; Rohwerder, M., Redox-Responsive Self-Healing for Corrosion Protection. *Adv. Mater.* **2013,** *25* (48), 6980-6984.

171. Tran, T. H.; Vimalanandan, A.; Genchev, G.; Fickert, J.; Landfester, K.; Crespy, D.; Rohwerder, M., Regenerative Nano-Hybrid Coating Tailored for Autonomous Corrosion Protection. *Adv. Mater.* **2015,** *27* (25), 3825-3830.

172. Shchukin, D.; Möhwald, H., A Coat of Many Functions. *Science.* **2013,** *341* (6153), 1458-1459.

173. Leslie, D. C.; Waterhouse, A.; Berthet, J. B.; Valentin, T. M.; Watters, A. L.; Jain, A.; Kim, P.; Hatton, B. D.; Nedder, A.; Donovan, K., A Bioinspired Omniphobic Surface Coating on Medical Devices Prevents Thrombosis and Biofouling. *Nature Biotechnol.* **2014,** *32* (11), 1134-1140.

174. Patrick, J. F.; Robb, M. J.; Sottos, N. R.; Moore, J. S.; White, S. R., Polymers with Autonomous Life-Cycle Control. *Nature.* **2016,** *540* (7633), 363-370.

175. Di Credico, B.; Griffini, G.; Levi, M.; Turri, S., Microencapsulation of a Uv-Responsive Photochromic Dye by Means of Novel Uv-Screening Polyurea-Based Shells for Smart Coating Applications. *ACS Appl. Mater. Interfaces* **2013,** *5* (14), 6628-6634.

176.   Song, Y.-K.; Lee, K.-H.; Kim, D.-M.; Chung, C.-M., A Microcapsule-Type Fluorescent Probe for the Detection of Microcracks in Cementitious Materials. *Sens. Actuator B-Chem.* **2016,** *222*, 1159-1165.

177.   Odom, S. A.; Jackson, A. C.; Prokup, A. M.; Chayanupatkul, S.; Sottos, N. R.; White, S. R.; Moore, J. S., Visual Indication of Mechanical Damage Using Core–Shell Microcapsules. *ACS Appl. Mater. Interfaces* **2011,** *3* (12), 4547-4551.

178.   Li, W.; Matthews, C. C.; Yang, K.; Odarczenko, M. T.; White, S. R.; Sottos, N. R., Autonomous Indication of Mechanical Damage in Polymeric Coatings. *Adv. Mater.* **2016.**

179.   Döhler, D.; Rana, S.; Rupp, H.; Bergmann, H.; Behzadi, S.; Crespy, D.; Binder, W. H., Qualitative Sensing of Mechanical Damage by a Fluorogenic "Click" Reaction. *Chem. Commun.* **2016,** *52* (74), 11076-11079.

180.   Robb, M. J.; Li, W.; Gergely, R. C.; Matthews, C. C.; White, S. R.; Sottos, N. R.; Moore, J. S., A Robust Damage-Reporting Strategy for Polymeric Materials Enabled by Aggregation-Induced Emission. *ACS Cent. Sci.* **2016,** *2* (9), 598-603.

181.   Song, Y. K.; Kim, B.; Lee, T. H.; Kim, J. C.; Nam, J. H.; Noh, S. M.; Park, Y. I., Fluorescence Detection of Microcapsule-Type Self-Healing, Based on Aggregation-Induced Emission. *Macromol. Rapid Comm.* **2017,** *38* (6).

182.   Davis, D. A.; Hamilton, A.; Yang, J.; Cremar, L. D.; Van Gough, D.; Potisek, S. L.; Ong, M. T.; Braun, P. V.; Martínez, T. J.; White, S. R., Force-Induced Activation of Covalent Bonds in Mechanoresponsive Polymeric Materials. *Nature.* **2009,** *459* (7243), 68.

183.   Gossweiler, G. R.; Hewage, G. B.; Soriano, G.; Wang, Q.; Welshofer, G. W.; Zhao, X.; Craig, S. L., Mechanochemical Activation of Covalent Bonds in Polymers with Full and Repeatable Macroscopic Shape Recovery. *ACS Macro Lett.* **2014,** *3* (3), 216-219.

184.   Ramachandran, D.; Liu, F.; Urban, M. W., Self-Repairable Copolymers That Change Color. *RSC Adv.* **2012,** *2* (1), 135-143.

185.   Samadzadeh, M.; Boura, S. H.; Peikari, M.; Kasiriha, S.; Ashrafi, A., A Review on Self-Healing Coatings Based on Micro/Nanocapsules. *Prog. Org. Coat.* **2010,** *68* (3), 159-164.

186.   Diesendruck, C. E.; Sottos, N. R.; Moore, J. S.; White, S. R., Biomimetic Self-Healing. *Angew. Chem. Int. Ed.* **2015,** *54* (36), 10428-10447.

187.   Michael, P.; Doehler, D.; Binder, W. H., Improving Autonomous Self Healing Via Combined Chemical/Physical Principles. *Polymer.* **2015,** *69*, 216-227.

188.   Roy, N.; Bruchmann, B.; Lehn, J.-M., Dynamers: Dynamic Polymers as Self-Healing Materials. *Chem. Soc. Rev.* **2015,** *44* (11), 3786-3807.

189.   Herbst, F.; Döhler, D.; Michael, P.; Binder, W. H., Self-Healing Polymers Via Supramolecular Forces. *Macromol. Rapid Comm.* **2013,** *34* (3), 203-220.

190.   Chen, X.; Dam, M. A.; Ono, K.; Mal, A.; Shen, H.; Nutt, S. R.; Sheran, K.; Wudl, F., A Thermally Re-Mendable Cross-Linked Polymeric Material. *Science.* **2002,** *295* (5560), 1698-1702.

191.   Chen, S.; Binder, W. H., Dynamic Ordering and Phase Segregation in Hydrogen-Bonded Polymers. *Acc. Chem. Res.* **2016,** *49* (7), 1409-1420.

192.   Cordier, P.; Tournilhac, F.; Soulié-Ziakovic, C.; Leibler, L., Self-Healing and Thermoreversible Rubber from Supramolecular Assembly. *Nature.* **2008,** *451* (7181), 977.

193.   Burnworth, M.; Tang, L.; Kumpfer, J. R.; Duncan, A. J.; Beyer, F. L.; Fiore, G. L.; Rowan, S. J.; Weder, C., Optically Healable Supramolecular Polymers. *Nature.* **2011,** *472* (7343), 334.

194.   Wang, Z.; Urban, M. W., Facile Uv-Healable Polyethylenimine–Copper (C 2 H 5 N–Cu) Supramolecular Polymer Networks. *Polym. Chem.* **2013,** *4* (18), 4897-4901.

195.   Wang, Z.; Yang, Y.; Burtovyy, R.; Luzinov, I.; Urban, M. W., Uv-Induced Self-Repairing Polydimethylsiloxane–Polyurethane (Pdms–Pur) and Polyethylene Glycol–Polyurethane (Peg–Pur) Cu-Catalyzed Networks. *J. Mater. Chem. A* **2014,** *2* (37), 15527-15534.

196.   Rana, S.; Döhler, D.; Nia, A. S.; Nasir, M.; Beiner, M.; Binder, W. H., "Click"-Triggered Self-Healing Graphene Nanocomposites. *Macromol. Rapid Comm.* **2016,** *37* (21), 1715-1722.

197.   An, S. Y.; Arunbabu, D.; Noh, S. M.; Song, Y. K.; Oh, J. K., Recent Strategies to Develop Self-Healable Crosslinked Polymeric Networks. *Chem. Commun.* **2015,** *51* (66), 13058-13070.

198.   Jin, H.; Mangun, C. L.; Griffin, A. S.; Moore, J. S.; Sottos, N. R.; White, S. R., Thermally Stable Autonomic Healing in Epoxy Using a Dual-Microcapsule System. *Adv. Mater.* **2014,** *26* (2), 282-287.

199.   Ghosh, B.; Urban, M. W., Self-Repairing Oxetane-Substituted Chitosan Polyurethane Networks. *Science.* **2009,** *323* (5920), 1458-1460.

200.   Guo, Y.; Chen, L.; Xu, D.; Zhong, J.; Yue, G.; Astruc, D.; Shuai, M.; Zhao, P., A Dual Functional Epoxy Material with Autonomous Damage Indication and Self-Healing. *RSC Adv.* **2016,** *6* (69), 65067-65071.

201.   Nia, A. S.; Rana, S.; Döhler, D.; Osim, W.; Binder, W. H., Nanocomposites Via a Direct Graphene-Promoted "Click"-Reaction. *Polymer.* **2015,** *79*, 21-28.

202.   Schrade, A.; Cao, Z.; Landfester, K.; Ziener, U., Preparation of Raspberry-Like Nanocapsules by the Combination of Pickering Emulsification and Solvent Displacement Technique. *Langmuir.* **2011,** *27* (11), 6689-6700.

203.   Panák, O.; Držková, M.; Kaplanová, M.; Novak, U.; Gunde, M. K., The Relation between Colour and Structural Changes in Thermochromic Systems Comprising Crystal Violet Lactone, Bisphenol a, and Tetradecanol. *Dyes Pigm.* **2017,** *136*, 382-389.

204.   Raditoiu, A.; Raditoiu, V.; Nicolae, C. A.; Raduly, M. F.; Amariutei, V.; Wagner, L. E., Optical and Structural Dynamical Behavior of Crystal Violet Lactone–Phenolphthalein Binary Thermochromic Systems. *Dyes Pigm.* **2016,** *134*, 69-76.

205.   Jin, H.; Mangun, C. L.; Stradley, D. S.; Moore, J. S.; Sottos, N. R.; White, S. R., Self-Healing Thermoset Using Encapsulated Epoxy-Amine Healing Chemistry. *Polymer.* **2012,** *53* (2), 581-587.

206.   Cho, S. H.; Andersson, H. M.; White, S. R.; Sottos, N. R.; Braun, P. V., Polydimethylsiloxane-Based Self-Healing Materials. *Adv. Mater.* **2006,** *18* (8), 997-1000.

207.   Keller, M. W.; White, S. R.; Sottos, N. R., A Self-Healing Poly (Dimethyl Siloxane) Elastomer. *Adv. Func. Mater.* **2007,** *17* (14), 2399-2404.

208.   Cho, S. H.; White, S. R.; Braun, P. V., Self-Healing Polymer Coatings. *Adv. Mater.* **2009,** *21* (6), 645-649.

209.   Ichimura, K.; Funabiki, A.; Aoki, K.-i.; Akiyama, H., Solid Phase Adsorption of Crystal Violet Lactone on Silica Nanoparticles to Probe Mechanochemical Surface Modification. *Langmuir.* **2008,** *24* (13), 6470-6479.

210.   Zhang, Y.; Dong, J.; Sun, H.; Yu, B.; Zhu, Z.; Zhang, J.; Wang, A., Solvatochromic Coatings with Self-Cleaning Property from Palygorskite@ Polysiloxane/Crystal Violet Lactone. *ACS Appl. Mater. Interfaces* **2016,** *8* (40), 27346-27352.

211.   MacLaren, D. C.; White, M. A., Dye–Developer Interactions in the Crystal Violet Lactone–Lauryl Gallate Binary System: Implications for Thermochromism. *J. Mater. Chem.* **2003,** *13* (7), 1695-1700.

212.   Fery, A.; Weinkamer, R., Mechanical Properties of Micro-and Nanocapsules: Single-Capsule Measurements. *Polymer.* **2007,** *48* (25), 7221-7235.

213.   Zhao, Y.; Zhao, Y.; Fickert J., Landfester, K.; Crespy, D., Encapsulation of Self-Healing Agents in Polymer Nanocapsules. *Small.* **2012,** *8* (19), 2954-2958.

214.   Bauer, K. N.; Tee, H. T.; Velencoso, M. M.; Wurm, F. R., Main-Chain Poly (Phosphoester) S: History, Syntheses, Degradation, Bio-and Flame-Retardant Applications. *Prog. Polym. Sci.* **2017,** *73*, 61-122.

215.   Binder, W. H., The Past 40 Years of Macromolecular Sciences: Reflections on Challenges in Synthetic Polymer and Material Science. *Macromol. Rapid Comm.* **2018**, 1800610.

216.   Wang, X.; Jiang, M.; Zhou, Z.; Gou, J.; Hui, D., 3d Printing of Polymer Matrix Composites: A Review and Prospective. *Compos. Part B-Eng.* **2017,** *110*, 442-458.

217.   Hussain, F.; Hojjati, M.; Okamoto, M.; Gorga, R. E., Polymer-Matrix Nanocomposites, Processing, Manufacturing, and Application: An Overview. *J. Compos. Mater.* **2006,** *40* (17), 1511-1575.

218.   Thakur, V. K.; Thakur, M. K., Processing and Characterization of Natural Cellulose Fibers/Thermoset Polymer Composites. *Carbohyd. Polym.* **2014,** *109*, 102-117.

219.   Colby, R. H.; Fetters, L. J.; Graessley, W. W., The Melt Viscosity-Molecular Weight Relationship for Linear Polymers. *Macromolecules.* **1987,** *20* (9), 2226-2237.

220.   Gupta, P.; Elkins, C.; Long, T. E.; Wilkes, G. L., Electrospinning of Linear Homopolymers of Poly (Methyl Methacrylate): Exploring Relationships between Fiber Formation, Viscosity, Molecular Weight and Concentration in a Good Solvent. *Polymer.* **2005,** *46* (13), 4799-4810.

221.   Tsenoglou, C., Molecular Weight Polydispersity Effects on the Viscoelasticity of Entangled Linear Polymers. *Macromolecules.* **1991,** *24* (8), 1762-1767.

222.   Fetters, L. J.; Lohse, D. J.; Milner, S. T.; Graessley, W. W., Packing Length Influence in Linear Polymer Melts on the Entanglement, Critical, and Reptation Molecular Weights. *Macromolecules.* **1999,** *32* (20), 6847-6851.

223.   Rotzinger, B. P.; Chanzy, H. D.; Smith, P., High Strength/High Modulus Polyethylene: Synthesis and Processing of Ultra-High Molecular Weight Virgin Powders. *Polymer.* **1989,** *30* (10), 1814-1819.

224.   Rastogi, S.; Lippits, D. R.; Peters, G. W. M.; Graf, R.; Yao, Y.; Spiess, H. W., Heterogeneity in Polymer Melts from Melting of Polymer Crystals. *Nat. Mater.* **2005,** *4* (8), 635.

225.   Lippits, D. R.; Rastogi, S.; Höhne, G. W. H.; Mezari, B.; Magusin, P. C. M. M., Heterogeneous Distribution of Entanglements in the Polymer Melt and Its Influence on Crystallization. *Macromolecules.* **2007,** *40* (4), 1004-1010.

226.   Boyer, R. F.; Heidenreich, u. R. D., Molecular Weight Studies on High Polymers with the Electron Microscope. *J. Appl. Phys.* **1945,** *16* (10), 621-639.

227.   Teng, C.; Gao, Y.; Wang, X.; Jiang, W.; Zhang, C.; Wang, R.; Zhou, D.; Xue, G., Reentanglement Kinetics of Freeze-Dried Polymers above the Glass Transition Temperature. *Macromolecules.* **2012,** *45* (16), 6648-6651.

228.   Kebarle, P.; Tang, L., From Ions in Solution to Ions in the Gas Phase-the Mechanism of Electrospray Mass Spectrometry. *Anal. Chem.* **1993,** *65* (22), 972A-986A.

229.   Festag, R.; Alexandratos, S. D.; Cook, K. D.; Joy, D. C.; Annis, B.; Wunderlich, B., Single-and Few-Chain Polystyrene Particles by Electrospray. *Macromolecules.* **1997,** *30* (20), 6238-6242.

230.   Taylor, G. I., Disintegration of Water Drops in an Electric Field. *Proc. R. Soc. Lond. A* **1964,** *280* (1382), 383-397.

231.   Bock, N.; Woodruff, M. A.; Hutmacher, D. W.; Dargaville, T. R., Electrospraying, a Reproducible Method for Production of Polymeric Microspheres for Biomedical Applications. *Polymers.* **2011,** *3* (1), 131-149.

232.   Deitzel, J. M.; Kleinmeyer, J.; Harris, D. E. A.; Tan, N. C. B., The Effect of Processing Variables on the Morphology of Electrospun Nanofibers and Textiles. *Polymer.* **2001,** *42* (1), 261-272.

233.   Duft, D.; Achtzehn, T.; Müller, R.; Huber, B. A.; Leisner, T., Coulomb Fission: Rayleigh Jets from Levitated Microdroplets. *Nature.* **2003,** *421* (6919), 128.

234.   Guo, Q.; Mather, J. P.; Yang, P.; Boden, M.; Mather, P. T., Fabrication of Polymeric Coatings with Controlled Microtopographies Using an Electrospraying Technique. *PloS One.* **2015,** *10* (6), e0129960.

235.   Lee, K. H.; Kim, H. Y.; Khil, M. S.; Ra, Y. M.; Lee, D. R., Characterization of Nano-Structured Poly (E-Caprolactone) Nonwoven Mats Via Electrospinning. *Polymer.* **2003,** *44* (4), 1287-1294.

236.   Griffin, D. R.; Weaver, W. M.; Scumpia, P. O.; Di Carlo, D.; Segura, T. Accelerated Wound Healing by Injectable Microporous Gel Scaffolds Assembled from Annealed Building Blocks. *Nat Mater* **2015**, *14* (7), 737–744.

237.   Fan, Z.; Liu, B.; Wang, J.; Zhang, S.; Lin, Q.; Gong, P.; Ma, L.; Yang, S. A Novel Wound Dressing Based on Ag/graphene Polymer Hydrogel: Effectively Kill Bacteria and Accelerate Wound Healing. *Adv. Funct. Mater.* **2014**, *24* (25), 3933–3943.

238.   Loo, A. E. K.; Wong, Y. T.; Ho, R.; Wasser, M.; Du, T.; Ng, W. T.; Halliwell, B. Effects of Hydrogen Peroxide on Wound Healing in Mice in Relation to Oxidative Damage. *PLoS One* **2012***, 7* (11), 49215–49228.

239.   Sen, C. Wound Healing Essentials: Let There Be Oxygen. *Wound Repair Regen*. **2009,** *17* (1), 1–18.

240.   Kanta, J. The Role of Hydrogen Peroxide and Other Reactive Oxygen Species in Wound Healing. *Acta Medica (Hradec Kralove)* **2011,** *54*, 97–101.

241.   Wei, H.; Wang, E. Nanomaterials with Enzyme-like Characteristics (Nanozymes): Next-Generation Artificial Enzymes. *Chem. Soc. Rev.* **2013,** *42* (14), 6060–6093.

242.   Grunwald, P. Biocatalysis and Nanotechnology; *Pan Stanford Publishing Pte. Ltd*, **2017**.

243.   Gao, L.; Zhuang, J.; Nie, L.; Zhang, J.; Zhang, Y.; Gu, N.; Wang, T.; Feng, J.; Yang, D.; Perrett, S.; Yan, X. Intrinsic Peroxidase-like Activity of Ferromagnetic Nanoparticles. *Nat. Nanotechnol.* **2007,** *2* (9), 577–583.

244.   Fan, K.; Cao, C.; Pan, Y.; Lu, D.; Yang, D.; Feng, J.; Song, L.; Liang, M.; Yan, X. Magnetoferritin Nanoparticles for Targeting and Visualizing Tumour Tissues. *Nat. Nanotechnol.* **2012,** *7* (7), 459–464.

245.   Que Jr, L.; Tolman, W. B. Biologically Inspired Oxidation Catalysis. *Nature* **2008,** *455* (7211), 333–340.

246.   Comba, P.; Gahan, L. R.; Hanson, G. R.; Westphal, M. Phosphatase Reactivity of a dicopper(II) Complex of a Patellamide Derivative--Possible Biological Functions of Cyclic Pseudopeptides. *Chem. Commun.* **2012,** *48* (75), 9364–9366.

247.   Wiester, M. J.; Ulmann, P. A.; Mirkin, C. A. Enzyme Mimics Based upon Supramolecular Coordination Chemistry. *Angew. Chem. Int. Ed.* **2011,** *50* (1), 114–137.

248.   André, R.; Natálio, F.; Humanes, M.; Leppin, J.; Heinze, K.; Wever, R.; Schröder, H. C.; Müller, W. E. G.; Tremel, W. V_2O_5 Nanowires with an Intrinsic Peroxidase-like Activity. *Adv. Funct. Mater.* **2011,** *21* (3), 501–509.

249.   Korsvik, C.; Patil, S.; Seal, S.; Self, W. T. Superoxide Dismutase Mimetic Properties Exhibited by Vacancy Engineered Ceria Nanoparticles. *Chem. Commun.* **2007,** *10*, 1056–1058.

250.   Wang, X.; Hu, Y.; Wei, H. Nanozymes in Bionanotechnology: From Sensing to Therapeutics and beyond. *Inorg. Chem. Front.* **2016,** *3* (1), 41–60.

251.   Kim, C. K.; Kim, T.; Choi, I. Y.; Soh, M.; Kim, D.; Kim, Y. J.; Jang, H.; Yang, H. S.; Kim, J. Y.; Park, H. K.; Park, S. P.; Park, S.; Yu, T.; Yoon, B. W.; Lee, S. H.; Hyeon, T. Ceria Nanoparticles That Can Protect against Ischemic Stroke. *Angew. Chem. Int. Ed.* **2012,** *51* (44), 11039–11043.

252.   Korschelt, K.; Ragg, R.; Metzger, C. S.; Kluenker, M.; Oster, M.; Barton, B.; Panthöfer, M.; Strand, D.; Kolb, U.; Mondeshki, M.; Strand, S.; Brieger, J.; Nawaz Tahir, M.; Tremel, W. Glycine-Functionalized copper(II) Hydroxide Nanoparticles with High Intrinsic Superoxide Dismutase Activity. *Nanoscale* **2017,** *9* (11), 3952–3960.

253.   Ragg, R.; Tahir, M. N.; Tremel, W. Solids Go Bio: Inorganic Nanoparticles as Enzyme Mimics. *Eur. J. Inorg. Chem.* **2016,** *2016* (13–14), 1906–1915.

254.   Chaudhari, K. N.; Chaudhari, N. K.; Yu, J.-S. Peroxidase Mimic Activity of Hematite Iron Oxides (Alpha-Fe_2O_3) with Different Nanostructres. *Catal. Sci. Technol.* **2012,** *2* (1), 119–124.

255.   Dutta, A. K.; Maji, S. K.; Srivastava, D. N.; Mondal, A.; Biswas, P.; Paul, P.; Adhikary, B. Peroxidase-like Activity and Amperometric Sensing of Hydrogen Peroxide by Fe 2O 3 and Prussian Blue-Modified Fe_2O_3 Nanoparticles. *J. Mol. Catal. A Chem.* **2012,** *360*, 71–77.

256.   Chen, J.; Xu, L.; Li, W.; Gou, X. α-Fe_2O_3 Nanotubes in Gas Sensor and Lithium-Ion Battery Applications. *Adv. Mater.* **2005,** *17* (5), 582–586.

257.   Ozaki, M.; Kratohvil, S.; Matijević, E. Formation of Monodispersed Spindle-Type Hematite Particles. *J. Colloid Interface Sci.* **1984,** *102* (1), 146–151.

258.   Woo, K.; Lee, H. J.; Ahn, J. P.; Park, Y. S. Sol-Gel Mediated Synthesis of Fe_2O_3 Nanorods. *Adv. Mater.* **2003,** *15* (20), 1761–1764.

259.   Wang, X.; Chen, X.; Gao, L.; Zheng, H.; Ji, M.; Tang, C.; Shen, T.; Zhang, Z. Synthesis of β-FeOOH and α-Fe_2O_3 Nanorods and Electrochemical Properties of β-FeOOH. *J. Mater. Chem.* **2004,** *14* (5), 905–907.

260.   Bannwarth, M. B.; Kazer, S. W.; Ulrich, S.; Glasser, G.; Crespy, D.; Landfester, K. Well-Defined Nanofibers with Tunable Morphology from Spherical Colloidal Building Blocks. *Angew. Chemie Int. Ed.* **2013,** *52* (38), 10107–10111.

261.   Bannwarth, M. B.; Utech, S.; Ebert, S.; Weitz, D. A.; Crespy, D.; Landfester, K. Colloidal Polymers with Controlled Sequence and Branching Constructed from Magnetic Field Assembled Nanoparticles. *ACS Nano* **2015,** *9* (3), 2720–2728.

262.   Bannwarth, M.; Crespy, D. Combining the Best of Two Worlds: Nanoparticles and Nanofibers. *Chem. - An Asian J.* **2014,** *9* (8), 2030–2035.

263.   Bannwarth, M. B.; Camerlo, A.; Ulrich, S.; Jakob, G.; Fortunato, G.; Rossi, R. M.; Boesel, L. F. Ellipsoid-Shaped Superparamagnetic Nanoclusters through Emulsion Electrospinning. *Chem. Commun.* **2015,** *51* (18), 3758–3761.

264.   Ulrich, S.; Hirsch, C.; Diener, L.; Wick, P.; Rossi, R. M.; Bannwarth, M. B.; Boesel, L. F. Preparation of Ellipsoid-Shaped Supraparticles with Modular Compositions and Investigation of Shape-Dependent Cell-Uptake. *RSC Adv.* **2016,** *6* (92), 89028–89039.

265.   Greiner, A.; Wendorff, J. H. Electrospinning: A Fascinating Method for the Preparation of Ultrathin Fibers. *Angew. Chem. Int. Ed.* **2007,** *46* (30), 5670–5703.

266.   Abrigo, M.; McArthur, S. L.; Kingshott, P. Electrospun Nanofibers as Dressings for Chronic Wound Care: Advances, Challenges, and Future Prospects. *Macromol. Biosci.* **2014,** *14* (6), 772–792.

267.   Jiang, S.; Ma, B. C.; Reinholz, J.; Li, Q.; Wang, J.; Zhang, K. A. I.; Landfester, K.; Crespy, D. Efficient Nanofibrous Membranes for Antibacterial Wound Dressing and UV Protection. *ACS Appl. Mater. Interfaces* **2016,** *8* (44), 29915–29922.

268.   Mahalingam, S.; Edirisinghe, M. Forming of Polymer Nanofibers by a Pressurised Gyration Process. Macromol. *Rapid Commun.* **2013,** *34* (14), 1134–1139.

269. Sofokleous, P.; Stride, E.; Bonfield, W.; Edirisinghe, M. Design, Construction and Performance of a Portable Handheld Electrohydrodynamic Multi-Needle Spray Gun for Biomedical Applications. *Mater. Sci. Eng. C* **2013,** *33* (1), 213–223.

270. Dong, R.-H.; Jia, Y.-X.; Qin, C.-C.; Zhan, L.; Yan, X.; Cui, L.; Zhou, Y.; Jiang, X.; Long, Y.-Z. In Situ Deposition of a Personalized Nanofibrous Dressing via a Handy Electrospinning Device for Skin Wound Care. *Nanoscale* **2016,** *8* (6), 3482–3488.

271. Mi, F. L.; Shyu, S. S.; Wu, Y. B.; Lee, S. T.; Shyong, J. Y.; Huang, R. N. Fabrication and Characterization of a Sponge-like Asymmetric Chitosan Membrane as a Wound Dressing. *Biomaterials* **2001***, 22* (2), 165–173.

272. Koo, W. T.; Choi, S. J.; Kim, S. J.; Jang, J. S.; Tuller, H. L.; Kim, I. D. Heterogeneous Sensitization of Metal-Organic Framework Driven Metal@Metal Oxide Complex Catalysts on an Oxide Nanofiber Scaffold Toward Superior Gas Sensors. *J. Am. Chem. Soc.* **2016,** *138* (40), 13431–13437.

273. Finnegan, J. R.; Gwyther, J.; Manners, I. Enabling Heterogeneous Gold Catalysis with Patchy Micelles. *Angew. Chemie Int. Ed.* **2017,** *56* (11), 2842–2844.

274. Wu, M.; Lin, Z.; Wolfbeis, O. S. Determination of the Activity of Catalase Using a europium(III)-Tetracycline-Derived Fluorescent Substrate. *Anal. Biochem.* **2003,** *320* (1), 129–135.

275. Zhang, X.; Liu, H.; Wei, Y. Catalytic Synthesis and Characterization of Spindle-Type α–Fe_2O_3 Particles. *J. Mater. Res.* **2011,** *20* (3), 628–635.

276. Mansur, H. S.; Sadahira, C. M.; Souza, A. N.; Mansur, A. A. P. FTIR Spectroscopy Characterization of Poly (Vinyl Alcohol) Hydrogel with Different Hydrolysis Degree and Chemically Crosslinked with Glutaraldehyde. *Mater. Sci. Eng. C* **2008**, *28* (4), 539–548.

277. Wei, H.; Wang, E., Nanomaterials with Enzyme-Like Characteristics (Nanozymes): Next-Generation Artificial Enzymes. *Chem. Soc. Rev.* **2013,** *42* (14), 6060-6093.

278. Korschelt, K.; Tahir, M. N.; Tremel, W., A Step into the Future: Applications of Nanoparticle Enzyme Mimics. *Chem. Eur. J.* **2018,** *24* (39), 9703-9713.

279. Herget, K.; Frerichs, H.; Pfitzner, F.; Tahir, M. N.; Tremel, W., Functional Enzyme Mimics for Oxidative Halogenation Reactions That Combat Biofilm Formation. *Adv. Mater.* **2018**, 1707073.

280. Herget, K.; Hubach, P.; Pusch, S.; Deglmann, P.; Götz, H.; Gorelik, T. E.; Gural'skiy, I. y. A.; Pfitzner, F.; Link, T.; Schenk, S.; Panthöfer, M.; Ksenofontov, V.; Kolb, U.; Opatz, T.; André, R.; Tremel, W., Haloperoxidase Mimicry by CeO_{2-x} Nanorods Combats Biofouling. *Adv. Mater.* **2017,** *29* (4), 1603823.

281. Hu, M.; Korschelt, K.; Daniel, P.; Landfester, K.; Tremel, W.; Bannwarth, M. B., Fibrous Nanozyme Dressings with Catalase-Like Activity for H_2O_2 Reduction to Promote Wound Healing. *ACS Appl. Mater. Interfaces* **2017,** *9* (43), 38024-38031.

282. Xue, J.; Xie, J.; Liu, W.; Xia, Y., Electrospun Nanofibers: New Concepts, Materials, and Applications. *Acc. Chem. Res.* **2017,** *50* (8), 1976-1987.

283.   Yang, G.; Li, X.; He, Y.; Ma, J.; Ni, G.; Zhou, S., From Nano to Micro to Macro: Electrospun Hierarchically Structured Polymeric Fibers for Biomedical Applications. *Prog. Polym. Sci.* **2017**.

284.   Xu, J.; Liu, C.; Hsu, P.-C.; Liu, K.; Zhang, R.; Liu, Y.; Cui, Y., Roll-to-Roll Transfer of Electrospun Nanofiber Film for High-Efficiency Transparent Air Filter. *Nano Lett.* **2016,** *16* (2), 1270-1275.

285.   Agarwal, S.; Greiner, A.; Wendorff, J. H., Functional Materials by Electrospinning of Polymers. *Prog. Polym. Sci.* **2013,** *38* (6), 963-991.

286.   Dvir, T.; Timko, B. P.; Kohane, D. S.; Langer, R., Nanotechnological Strategies for Engineering Complex Tissues. *Nat. Nanotechnol.* **2010,** *6*, 13.

287.   Zhang, C.-L.; Yu, S.-H., Nanoparticles Meet Electrospinning: Recent Advances and Future Prospects. *Chem. Soc. Rev.* **2014,** *43* (13), 4423-4448.

288.   Jiang, S.; Lv, L.-P.; Landfester, K.; Crespy, D., Nanocontainers in and onto Nanofibers. *Acc. Chem. Res.* **2016,** *49* (5), 816-823.

289.   Xie, J.; Liu, W.; MacEwan, M. R.; Bridgman, P. C.; Xia, Y., Neurite Outgrowth on Electrospun Nanofibers with Uniaxial Alignment: The Effects of Fiber Density, Surface Coating, and Supporting Substrate. *ACS Nano.* **2014,** *8* (2), 1878-1885.

290.   Jiang, T.; Carbone, E. J.; Lo, K. W.-H.; Laurencin, C. T., Electrospinning of Polymer Nanofibers for Tissue Regeneration. *Prog. Polym. Sci.* **2015,** *46*, 1-24.

291.   Deng, H.; Zhou, X.; Wang, X.; Zhang, C.; Ding, B.; Zhang, Q.; Du, Y., Layer-by-Layer Structured Polysaccharides Film-Coated Cellulose Nanofibrous Mats for Cell Culture. *Carbohyd. Polym.* **2010,** *80* (2), 474-479.

292.   Chen, J.; Cheng, G.; Liu, R.; Zheng, Y.; Huang, M.; Yi, Y.; Shi, X.; Du, Y.; Deng, H., Enhanced Physical and Biological Properties of Silk Fibroin Nanofibers by Layer-by-Layer Deposition of Chitosan and Rectorite. *J. Colloid Interf. Sci.* **2018,** *523*, 208-216.

293.   Huang, R.; Li, W.; Lv, X.; Lei, Z.; Bian, Y.; Deng, H.; Wang, H.; Li, J.; Li, X., Biomimetic Lbl Structured Nanofibrous Matrices Assembled by Chitosan/Collagen for Promoting Wound Healing. *Biomaterials.* **2015,** *53*, 58-75.

294.   Ray, S. S.; Chen, S.-S.; Li, C.-W.; Nguyen, N. C.; Nguyen, H. T., A Comprehensive Review: Electrospinning Technique for Fabrication and Surface Modification of Membranes for Water Treatment Application. *RSC Adv.* **2016,** *6* (88), 85495-85514.

295.   Doan, T. Q.; Leslie, L. S.; Kim, S. Y.; Bhargava, R.; White, S. R.; Sottos, N. R., Characterization of Core-Shell Microstructure and Self-Healing Performance of Electrospun Fiber Coatings. *Polymer* **2016,** *107*, 263-272.

296.   Vahedi, V.; Pasbakhsh, P.; Piao, C. S.; Seng, C. E., A Facile Method for Preparation of Self-Healing Epoxy Composites: Using Electrospun Nanofibers as Microchannels. *Journal of Materials Chemistry A* **2015,** *3* (31), 16005-16012.

297.   Garrett, T. R.; Bhakoo, M.; Zhang, Z., Bacterial Adhesion and Biofilms on Surfaces. *Pro. Nat. Sci.-Mater.* **2008,** *18* (9), 1049-1056.

298.   Kochkodan, V.; Hilal, N., A Comprehensive Review on Surface Modified Polymer Membranes for Biofouling Mitigation. *Desalination* **2015,** *356*, 187-207.

299.   Tesler, A. B.; Kim, P.; Kolle, S.; Howell, C.; Ahanotu, O.; Aizenberg, J., Extremely Durable Biofouling-Resistant Metallic Surfaces Based on Electrodeposited Nanoporous Tungstite Films on Steel. *Nat. Commun.* **2015,** *6*, 8649.

300.   Costerton, J. W.; Stewart, P. S.; Greenberg, E. P., Bacterial Biofilms: A Common Cause of Persistent Infections. *Science.* **1999,** *284* (5418), 1318-1322.

301.   Banerjee, I.; Pangule, R. C.; Kane, R. S., Antifouling Coatings: Recent Developments in the Design of Surfaces That Prevent Fouling by Proteins, Bacteria, and Marine Organisms. *Adv. Mater.* **2011,** *23* (6), 690-718.

302.   Zhang, Z.; Tang, J.; Wang, H.; Xia, Q.; Xu, S.; Han, C. C., Controlled Antibiotics Release System through Simple Blended Electrospun Fibers for Sustained Antibacterial Effects. *ACS Appl. Mater. Interfaces* **2015,** *7* (48), 26400-26404.

303.   Zirehpour, A.; Rahimpour, A.; Arabi Shamsabadi, A.; Sharifian Gh, M.; Soroush, M., Mitigation of Thin-Film Composite Membrane Biofouling Via Immobilizing Nano-Sized Biocidal Reservoirs in the Membrane Active Layer. *Environ. Sci. Technol.* **2017,** *51* (10), 5511-5522.

304.   Romero, D.; Kolter, R., Will Biofilm Disassembly Agents Make It to Market? *Trends Microbiol.* **2011,** *19* (7), 304-306.

305.   De Faria, A. F.; Perreault, F. o.; Shaulsky, E.; Arias Chavez, L. H.; Elimelech, M., Antimicrobial Electrospun Biopolymer Nanofiber Mats Functionalized with Graphene Oxide–Silver Nanocomposites. *ACS Appl. Mater. Interfaces* **2015,** *7* (23), 12751-12759.

306.   GhavamiNejad, A.; Rajan Unnithan, A.; Ramachandra Kurup Sasikala, A.; Samarikhalaj, M.; Thomas, R. G.; Jeong, Y. Y.; Nasseri, S.; Murugesan, P.; Wu, D.; Hee Park, C., Mussel-Inspired Electrospun Nanofibers Functionalized with Size-Controlled Silver Nanoparticles for Wound Dressing Application. *ACS Appl. Mater. Interfaces* **2015,** *7* (22), 12176-12183.

307.   Ozcan, S.; Kaner, P.; Thomas, D.; Cebe, P.; Asatekin, A., Hydrophobic Antifouling Electrospun Mats from Zwitterionic Amphiphilic Copolymers. *ACS Appl. Mater. Interfaces* **2018,** *10* (21), 18300-18309.

308.   Yang, W.; Sundaram, H. S.; Ella, J.-R.; He, N.; Jiang, S., Low-Fouling Electrospun Plla Films Modified with Zwitterionic Poly (Sulfobetaine Methacrylate)-Catechol Conjugates. *Acta Biomater.* **2016,** *40*, 92-99.

309.   Sandy, M.; Carter-Franklin, J. N.; Martin, J. D.; Butler, A., Vanadium Bromoperoxidase from Delisea Pulchra: Enzyme-Catalyzed Formation of Bromofuranone and Attendant Disruption of Quorum Sensing. *Chem. Commun.* **2011,** *47* (44), 12086-12088.

310.   Kristensen, J. B.; Meyer, R. L.; Laursen, B. S.; Shipovskov, S.; Besenbacher, F.; Poulsen, C. H., Antifouling Enzymes and the Biochemistry of Marine Settlement. *Biotechnol. Adv.* **2008,** *26* (5), 471-481.

311.   Dobretsov, S.; Teplitski, M.; Paul, V., Mini-Review: Quorum Sensing in the Marine Environment and Its Relationship to Biofouling. *Biofouling* **2009,** *25* (5), 413-427.

312.   Natalio, F.; André, R.; Hartog, A. F.; Stoll, B.; Jochum, K. P.; Wever, R.; Tremel, W., Vanadium Pentoxide Nanoparticles Mimic Vanadium Haloperoxidases and Thwart Biofilm Formation. *Nat. Nanotechnol.* **2012,** *7* (8), 530.

313.   Price, D.; Worsfold, P. J.; C. Mantoura, R. F., Hydrogen Peroxide in the Marine Environment: Cycling and Methods of Analysis. *Trends Analyt. Chem.* **1992,** *11* (10), 379-384.

314.   Halliwell, B.; Clement, M. V.; Long, L. H., Hydrogen Peroxide in the Human Body. *FEBS Lett.* **2000,** *486* (1), 10-13.

315.   Yokel, R. A.; Hussain, S.; Garantziotis, S.; Demokritou, P.; Castranova, V.; Cassee, F. R., The Yin: An Adverse Health Perspective of Nanoceria: Uptake, Distribution, Accumulation, and Mechanisms of Its Toxicity. *Environ. Sci. Nano* **2014,** *1* (5), 406-428.

316.   Xu, C.; Qu, X., Cerium Oxide Nanoparticle: A Remarkably Versatile Rare Earth Nanomaterial for Biological Applications. *Npg Asia Materials* **2014,** *6*, e90.

317.   Zhang, Z.; Liu, Y.; Zhang, X.; Liu, J., A Cell-Mimicking Structure Converting Analog Volume Changes to Digital Colorimetric Output with Molecular Selectivity. *Nano Lett.* **2017,** *17* (12), 7926-7931.

318.   Liang, H.; Lin, F.; Zhang, Z.; Liu, B.; Jiang, S.; Yuan, Q.; Liu, J., Multicopper Laccase Mimicking Nanozymes with Nucleotides as Ligands. *ACS Appl. Mater. Interfaces* **2017,** *9* (2), 1352-1360.

319.   Breitwieser, M.; Klose, C.; Hartmann, A.; Büchler, A.; Klingele, M.; Vierrath, S.; Zengerle, R.; Thiele, S., Cerium Oxide Decorated Polymer Nanofibers as Effective Membrane Reinforcement for Durable, High-Performance Fuel Cells. *Adv. Energy Mater.* **2017,** *7* (6).

320.   Fang, X.; Ma, H.; Xiao, S.; Shen, M.; Guo, R.; Cao, X.; Shi, X., Facile Immobilization of Gold Nanoparticles into Electrospun Polyethyleneimine/Polyvinyl Alcohol Nanofibers for Catalytic Applications. *J. Mater. Chem.* **2011,** *21* (12), 4493-4501.

321.   Chen, S.; Chi, M.; Zhu, Y.; Gao, M.; Wang, C.; Lu, X., A Facile Synthesis of Superparamagnetic Fe_3O_4 Nanofibers with Superior Peroxidase-Like Catalytic Activity for Sensitive Colorimetric Detection of L-Cysteine. *Appl. Surf. Sci.* **2018,** *440*, 237-244.

322.   Mai, H.-X.; Sun, L.-D.; Zhang, Y.-W.; Si, R.; Feng, W.; Zhang, H.-P.; Liu, H.-C.; Yan, C.-H., Shape-Selective Synthesis and Oxygen Storage Behavior of Ceria Nanopolyhedra, Nanorods, and Nanocubes. *J. Phys. Chem. B* **2005,** *109* (51), 24380-24385.

323.   Sader, J. E.; Larson, I.; Mulvaney, P.; White, L. R., Method for the Calibration of Atomic Force Microscope Cantilevers. *Rev. Sci. Instrum.* **1995,** *66* (7), 3789-3798.

324.   Hutter, J. L.; Bechhoefer, J., Calibration of Atomic-Force Microscope Tips. *Rev. Sci. Instrum.* **1993,** *64* (7), 1868-1873.

325.   Colpas, G. J.; Hamstra, B. J.; Kampf, J. W.; Pecoraro, V. L., Functional Models for Vanadium Haloperoxidase: Reactivity and Mechanism of Halide Oxidation. *J. Am. Chem. Soc.* **1996,** *118* (14), 3469-3478.

326.   Chen, C.; Sun, Q.; Ren, D.-X.; Zhang, R.; Bai, F.-Y.; Xing, Y.-H.; Shi, Z., Bromoperoxidase Mimic as Catalysts for Oxidative Bromination—Synthesis, Structures and Properties of the Diversified Oxidation State of Vanadium (Iii, Iv and V) Complexes with Pincer N-Heterocycle Ligands. *Cryst. Eng. Comm.* **2013,** *15* (27), 5561-5573.

327.   Yang, C.-C.; Lee, Y.-J.; Yang, J. M., Direct Methanol Fuel Cell (Dmfc) Based on Pva/Mmt Composite Polymer Membranes. *J. Power Sources* **2009,** *188* (1), 30-37.

328.   Zhang, C. L.; Lv, K. P.; Cong, H. P.; Yu, S. H., Controlled Assemblies of Gold Nanorods in Pva Nanofiber Matrix as Flexible Free-Standing Sers Substrates by Electrospinning. *Small.* **2012,** *8* (5), 648-653.

329.   Roskov, K. E.; Kozek, K. A.; Wu, W.-C.; Chhetri, R. K.; Oldenburg, A. L.; Spontak, R. J.; Tracy, J. B., Long-Range Alignment of Gold Nanorods in Electrospun Polymer Nano/Microfibers. *Langmuir.* **2011,** *27* (23), 13965-13969.

330.   Corrales, T. P.; Friedemann, K.; Fuchs, R.; Roy, C. m.; Crespy, D.; Kappl, M., Breaking Nano-Spaghetti: Bending and Fracture Tests of Nanofibers. *Langmuir.* **2016,** *32* (5), 1389-1395.

331.   Stachewicz, U.; Bailey, R. J.; Wang, W.; Barber, A. H., Size Dependent Mechanical Properties of Electrospun Polymer Fibers from a Composite Structure. *Polymer* **2012,** *53* (22), 5132-5137.

332.   Terrón, M. C.; Verhagen, F. J.; Franssen, M. C.; Field, J. A., Chemical Bromination of Phenol Red by Hydrogen Peroxide Is Possible in the Absence of Haloperoxidases. *Chemosphere* **1998,** *36* (6), 1445-1452.

333.   Laurent, S.; Forge, D.; Port, M.; Roch, A.; Robic, C.; Vander Elst, L.; Muller, R. N., Magnetic Iron Oxide Nanoparticles: Synthesis, Stabilization, Vectorization, Physicochemical Characterizations, and Biological Applications. *Chem. Rev.* **2008,** *108* (6), 2064-2110.

334.   Wu, L.; Mendoza-Garcia, A.; Li, Q.; Sun, S., Organic Phase Syntheses of Magnetic Nanoparticles and Their Applications. *Chem. Rev.* **2016,** *116* (18), 10473-10512.

335.   Lee, H.; Kim, J.; Kim, J.; Chung, S. E.; Choi, S.-E.; Kwon, S., Programming Magnetic Anisotropy in Polymeric Microactuators. *Nat. Mater.* **2011,** *10* (10), 747.

336.   Guzmán-Lastra, F.; Kaiser, A.; Löwen, H., Fission and Fusion Scenarios for Magnetic Microswimmer Clusters. *Nat. Commun.* **2016,** *7*, 13519.

337.   Chen, X.-Z.; Hoop, M.; Mushtaq, F.; Siringil, E.; Hu, C.; Nelson, B. J.; Pané, S., Recent Developments in Magnetically Driven Micro-and Nanorobots. *Appl. Mater. Today.* **2017,** *9*, 37-48.

338.   Perez, J. M., Iron Oxide Nanoparticles: Hidden Talent. *Nat. Nanotechnol.* **2007,** *2* (9), 535.

339.   Xu, H.; Aguilar, Z. P.; Yang, L.; Kuang, M.; Duan, H.; Xiong, Y.; Wei, H.; Wang, A., Antibody Conjugated Magnetic Iron Oxide Nanoparticles for Cancer Cell Separation in Fresh Whole Blood. *Biomaterials.* **2011,** *32* (36), 9758-9765.

340.   Shao, M.; Ning, F.; Zhao, J.; Wei, M.; Evans, D. G.; Duan, X., Preparation of Fe3o4@ Sio2@ Layered Double Hydroxide Core–Shell Microspheres for Magnetic Separation of Proteins. *J. Am. Chem. Soc.* **2012,** *134* (2), 1071-1077.

341.   Li, J.; de Ávila, B. E.-F.; Gao, W.; Zhang, L.; Wang, J., Micro/Nanorobots for Biomedicine: Delivery, Surgery, Sensing, and Detoxification. *Sci. Robot.* **2017,** *2* (4), eaam6431.

342.   Ulbrich, K.; Hola, K.; Subr, V.; Bakandritsos, A.; Tucek, J.; Zboril, R., Targeted Drug Delivery with Polymers and Magnetic Nanoparticles: Covalent and Noncovalent Approaches, Release Control, and Clinical Studies. *Chem. Rev.* **2016,** *116* (9), 5338-5431.

343.   Peters, C.; Hoop, M.; Pané, S.; Nelson, B. J.; Hierold, C., Degradable Magnetic Composites for Minimally Invasive Interventions: Device Fabrication, Targeted Drug Delivery, and Cytotoxicity Tests. *Adv. Mater.* **2016,** *28* (3), 533-538.

344.   Ge, J.; Hu, Y.; Biasini, M.; Beyermann, W. P.; Yin, Y., Superparamagnetic Magnetite Colloidal Nanocrystal Clusters. *Angew. Chem. Int. Ed.* **2007,** *46* (23), 4342-4345.

345.   Teja, A. S.; Koh, P.-Y., Synthesis, Properties, and Applications of Magnetic Iron Oxide Nanoparticles. *Prog. Cryst. Growth Ch.* **2009,** *55* (1-2), 22-45.

346.   Klünker, M.; Nawaz Tahir, M.; Dören, R.; Deuker, M.; Komforth, P.; Plana-Ruiz, S.; Barton, B.; Shylin, S. I.; Ksenofontov, D. V.; Panthöfer, M., Iron Oxide Superparticles with Enhanced Mri Performance by Solution Phase Epitaxial Growth. *Chem. Mater.* **2018**.

347.   Sim, S.; Miyajima, D.; Niwa, T.; Taguchi, H.; Aida, T., Tailoring Micrometer-Long High-Integrity 1d Array of Superparamagnetic Nanoparticles in a Nanotubular Protein Jacket and Its Lateral Magnetic Assembling Behavior. *J. Am. Chem. Soc.* **2015**, *137* (14), 4658-4661.

348.   Gao, M.; Kuang, M.; Li, L.; Liu, M.; Wang, L.; Song, Y., Printing 1d Assembly Array of Single Particle Resolution for Magnetosensing. *Small.* **2018**, 1800117.

349.   Bannwarth, M. B.; Camerlo, A.; Ulrich, S.; Jakob, G.; Fortunato, G.; Rossi, R. M.; Boesel, L. F., Ellipsoid-Shaped Superparamagnetic Nanoclusters through Emulsion Electrospinning. *Chem. Commun.* **2015**, *51* (18), 3758-3761.

350.   Maity, D.; Chandrasekharan, P.; Pradhan, P.; Chuang, K.-H.; Xue, J.-M.; Feng, S.-S.; Ding, J., Novel Synthesis of Superparamagnetic Magnetite Nanoclusters for Biomedical Applications. *J. Mater. Chem.* **2011**, *21* (38), 14717-14724.

351.   Bannwarth, M. B.; Kazer, S. W.; Ulrich, S.; Glasser, G.; Crespy, D.; Landfester, K., Well‑Defined Nanofibers with Tunable Morphology from Spherical Colloidal Building Blocks. *Angew. Chem. Int. Ed.* **2013**, *52* (38), 10107-10111.

352.   Kralj, S.; Makovec, D., Magnetic Assembly of Superparamagnetic Iron Oxide Nanoparticle Clusters into Nanochains and Nanobundles. *ACS Nano.* **2015**, *9* (10), 9700-9707.

353.   Bannwarth, M. B.; Utech, S.; Ebert, S.; Weitz, D. A.; Crespy, D.; Landfester, K., Colloidal Polymers with Controlled Sequence and Branching Constructed from Magnetic Field Assembled Nanoparticles. *ACS Nano.* **2015**, *9* (3), 2720-2728.

354.   Zang, Y.; Zhang, F.; Huang, D.; Di, C. a.; Zhu, D., Sensitive Flexible Magnetic Sensors Using Organic Transistors with Magnetic‑Functionalized Suspended Gate Electrodes. *Adv. Mater.* **2015**, *27* (48), 7979-7985.

355.   Xu, X.; Li, H.; Zhang, Q.; Hu, H.; Zhao, Z.; Li, J.; Li, J.; Qiao, Y.; Gogotsi, Y., Self-Sensing, Ultralight, and Conductive 3d Graphene/Iron Oxide Aerogel Elastomer Deformable in a Magnetic Field. *ACS Nano.* **2015**, *9* (4), 3969-3977.

356.   Hu, W.; Lum, G. Z.; Mastrangeli, M.; Sitti, M., Small-Scale Soft-Bodied Robot with Multimodal Locomotion. *Nature.* **2018**, *554* (7690), 81.

357.   Diller, E.; Sitti, M., Three‑Dimensional Programmable Assembly by Untethered Magnetic Robotic Micro‑Grippers. *Adv. Func. Mater.* **2014**, *24* (28), 4397-4404.

358.   Singh, G.; Chan, H.; Baskin, A.; Gelman, E.; Repnin, N.; Král, P.; Klajn, R., Self-Assembly of Magnetite Nanocubes into Helical Superstructures. *Science.* **2014**, 1254132.

359.   Chen, W.; Li, S.; Chen, C.; Yan, L., Self‑Assembly and Embedding of Nanoparticles by in Situ Reduced Graphene for Preparation of a 3d Graphene/Nanoparticle Aerogel. *Adv. Mater.* **2011**, *23* (47), 5679-5683.

360.   Brunner, J.; Baburin, I. A.; Sturm, S.; Kvashnina, K.; Rossberg, A.; Pietsch, T.; Andreev, S.; Sturm, E.; Cölfen, H., Self‑Assembled Magnetite Mesocrystalline Films: Toward Structural Evolution from 2d to 3d Superlattices. *Adv. Mater. Int.* **2017,** *4* (1), 1600431.

361.   Chen, Y.; Wang, H.; Yao, Q.; Fan, B.; Wang, C.; Xiong, Y.; Jin, C.; Sun, Q., Biomimetic Taro Leaf-Like Films Decorated on Wood Surfaces Using Soft Lithography for Superparamagnetic and Superhydrophobic Performance. *J. Mater. Sci.* **2017,** *52* (12), 7428-7438.

362.   Diller, E.; Miyashita, S.; Sitti, M., Remotely Addressable Magnetic Composite Micropumps. *Rsc Adv.* **2012,** *2* (9), 3850-3856.

363.   Tavacoli, J. W.; Bauër, P.; Fermigier, M.; Bartolo, D.; Heuvingh, J.; du Roure, O., The Fabrication and Directed Self-Assembly of Micron-Sized Superparamagnetic Non-Spherical Particles. *Soft Matter.* **2013,** *9* (38), 9103-9110.

364.   Servant, A.; Qiu, F.; Mazza, M.; Kostarelos, K.; Nelson, B. J., Controlled in Vivo Swimming of a Swarm of Bacteria‑Like Microrobotic Flagella. *Adv. Mater.* **2015,** *27* (19), 2981-2988.

365.   Qiu, F.; Fujita, S.; Mhanna, R.; Zhang, L.; Simona, B. R.; Nelson, B. J., Magnetic Helical klMicroswimmers Functionalized with Lipoplexes for Targeted Gene Delivery. *Adv. Func. Mater.* **2015,** *25* (11), 1666-1671.

366.   Huang, H.-W.; Sakar, M. S.; Petruska, A. J.; Pané, S.; Nelson, B. J., Soft Micromachines with Programmable Motility and Morphology. *Nat. Commun.* **2016,** *7*, 12263.

367.   Rastogi, V.; Melle, S.; Calderon, O. G.; García, A. A.; Marquez, M.; Velev, O. D., Synthesis of Light‑Diffracting Assemblies from Microspheres and Nanoparticles in Droplets on a Superhydrophobic Surface. *Adv. Mater.* **2008,** *20* (22), 4263-4268.

368.   Wooh, S.; Huesmann, H.; Tahir, M. N.; Paven, M.; Wichmann, K.; Vollmer, D.; Tremel, W.; Papadopoulos, P.; Butt, H. J., Synthesis of Mesoporous Supraparticles on Superamphiphobic Surfaces. *Adv. Mater.* **2015,** *27* (45), 7338-7343.

369.   Sekido, T.; Wooh, S.; Fuchs, R.; Kappl, M.; Nakamura, Y.; Butt, H.-J. r.; Fujii, S., Controlling the Structure of Supraballs by Ph-Responsive Particle Assembly. *Langmuir.* **2017,** *33* (8), 1995-2002.

370.   Park, J.; Moon, J.; Shin, H.; Wang, D.; Park, M., Direct-Write Fabrication of Colloidal Photonic Crystal Microarrays by Ink-Jet Printing. *J. Colloid Interf. Sci.* **2006,** *298* (2), 713-719.

371.   Rastogi, V.; García, A. A.; Marquez, M.; Velev, O. D., Anisotropic Particle Synthesis inside Droplet Templates on Superhydrophobic Surfaces. *Macromol. Rapid Comm.* **2010,** *31* (2), 190-195.

372.   Sperling, M.; Velev, O. D.; Gradzielski, M., Controlling the Shape of Evaporating Droplets by Ionic Strength: Formation of Highly Anisometric Silica Supraparticles. *Angew. Chem. Int. Ed.* **2014,** *53* (2), 586-590.

373.   Sperling, M.; Spiering, V. J.; Velev, O. D.; Gradzielski, M., Controlled Formation of Patchy Anisometric Fumed Silica Supraparticles in Droplets on Bent Superhydrophobic Surfaces. *Part. Part. Syst. Char.* **2017,** *34* (1).

374.   Rosensweig, R. E., *Ferrohydrodynamics*. Courier Corporation: 2013.

375.   Timonen, J. V.; Latikka, M.; Leibler, L.; Ras, R. H.; Ikkala, O., Switchable Static and Dynamic Self-Assembly of Magnetic Droplets on Superhydrophobic Surfaces. *Science.* **2013,** *341* (6143), 253-257.

376.   Biswas, P.; Sen, D.; Mazumder, S.; Basak, C. B.; Doshi, P., Temperature Mediated Morphological Transition During Drying of Spray Colloidal Droplets. *Langmuir.* **2016,** *32* (10), 2464-2473.

377.   Rosensweig, R. E., Heating Magnetic Fluid with Alternating Magnetic Field. *J. Magn. Magn. Mater.* **2002,** *252*, 370-374.

378.   Sperling, M.; Kim, H.-J.; Velev, O. D.; Gradzielski, M., Active Steerable Catalytic Supraparticles Shuttling on Preprogrammed Vertical Trajectories. *Adv. Mater. Int.* **2016,** *3* (15), 1600095.

379.   Deng, X.; Mammen, L.; Butt, H.-J.; Vollmer, D., Candle Soot as a Template for a Transparent Robust Superamphiphobic Coating. *Science.* **2012,** *335* (6064), 67-70.